Simulations of Physics and Chemistry of Polar Stratospheric Clouds with a General Circulation Model

Dissertation
zur Erlangung des Grades
„Doktor der Naturwissenschaften“

am Fachbereich Physik
der Johannes Gutenberg-Universität
in Mainz

Joachim Buchholz
geb. in Offenburg

Mainz, den 20. April 2005

Datum der mündlichen Prüfung: 22. Juli 2005

Abstract

A polar stratospheric cloud submodel has been developed and incorporated in a general circulation model including atmospheric chemistry (ECHAM5/-MESSy). The formation and sedimentation of polar stratospheric cloud (PSC) particles can thus be simulated as well as heterogeneous chemical reactions that take place on the PSC particles.

For solid PSC particle sedimentation, the need for a tailor-made algorithm has been elucidated. A sedimentation scheme based on first order approximations of vertical mixing ratio profiles has been developed. It produces relatively little numerical diffusion and can deal well with divergent or convergent sedimentation velocity fields.

For the determination of solid PSC particle sizes, an efficient algorithm has been adapted. It assumes a monodisperse radii distribution and thermodynamic equilibrium between the gas phase and the solid particle phase. This scheme, though relatively simple, is shown to produce particle number densities and radii within the observed range. The combined effects of the representations of sedimentation and solid PSC particles on vertical H_2O and HNO_3 redistribution are investigated in a series of tests.

The formation of solid PSC particles, especially of those consisting of nitric acid trihydrate, has been discussed extensively in recent years. Three particle formation schemes in accordance with the most widely used approaches have been identified and implemented. For the evaluation of PSC occurrence a new data set with unprecedented spatial and temporal coverage was available. A quantitative method for the comparison of simulation results and observations is developed and applied. It reveals that the relative PSC sighting frequency can be reproduced well with the PSC submodel whereas the detailed modelling of PSC events is beyond the scope of coarse global scale models.

In addition to the development and evaluation of new PSC submodel components, parts of existing simulation programs have been improved, e. g. a method for the assimilation of meteorological analysis data in the general circulation model, the liquid PSC particle composition scheme, and the calculation of heterogeneous reaction rate coefficients. The interplay of these model components is demonstrated in a simulation of stratospheric chemistry with the coupled general circulation model. Tests against recent satellite data show that the model successfully reproduces the Antarctic ozone hole.

Zusammenfassung

Im Rahmen der vorliegenden Arbeit wurde ein Modell zur Simulation polarer Stratosphärenwolken entwickelt und an ein globales Chemie-Zirkulationsmodell (ECHAM5/MESSy) gekoppelt. Die Bildung und Sedimentation polarer Stratosphärenwolken sowie chemische Reaktionen auf den Wolkenteilchen können damit simuliert werden.

Hinsichtlich der Modellierung der Sedimentation polarer Stratosphärenwolken besteht ein Bedarf an verbesserten Algorithmen. Daher wurde ein Sedimentationsverfahren entworfen und untersucht, welches auf linearen Näherungen des vertikalen Eis- und HNO_3-Gehalts der Luft basiert. Es ist vergleichsweise wenig diffusiv und herkömmlichen Methoden bei der Behandlung divergenter und konvergenter Geschwindigkeitsfelder überlegen.

Für die Bestimmung der Wolkenteilchenradien wurde Wert auf ein effizientes Verfahren gelegt. Die Radienverteilung wird im Modell als monodispers angenommen; zwischen der Gasphase und den festen Wolkenteilchen herrscht thermodynamisches Gleichgewicht. Trotz seiner Einfachheit führt dieser Modellansatz zu Wolkenteilchenzahldichten und -radien, die mit Beobachtungen verträglich sind. In einer Testreihe wird die vertikale Umverteilung von H_2O und HNO_3 infolge der in der vorliegenden Arbeit verwendeten Sedimentations- und Teilchengrößenmodellierungsverfahren untersucht.

Die Bildung polarer Stratosphärenwolken, insbesondere solcher aus Salpetersäuretrihydratteilchen, wurde in den vergangenen Jahren intensiv diskutiert. Drei konkurrierende Modellansätze wurden in das Stratosphärenwolkenmodell aufgenommen und hinsichtlich ihrer Auswirkungen verglichen. Für den quantitativen Vergleich des simulierten Vorkommens polarer Stratosphärenwolken mit Beobachtungen stand ein neuer und beispiellos umfangreicher, auf Satellitenmessungen basierender Datensatz zur Verfügung. Die Auswertung ergibt, dass die beobachtete relative Häufigkeit des Auftretens polarer Stratosphärenwolken in Simulationen gut reproduziert werden kann. Die detaillierte Simulation einzelner polarer Stratosphärenwolken mit einem großskaligen, globalen Modell ist dagegen kaum möglich.

Neben der Entwicklung und Auswertung neuer Modellkomponenten beinhaltete die vorliegende Arbeit auch die Verbesserung bestehender Programmteile. Hierzu gehört das Verfahren zur Assimilation meteorologischer Analysedaten ins globale Chemie-Zirkulationsmodell, die Parametrisierung der Zusammensetzung flüssiger, stratosphärischer Aerosolteilchen und die Berechnung der Reaktionskonstanten heterogener chemischer Reaktionen. Das Zusammenspiel dieser Modellkomponenten wird anhand einer Stratosphärenchemiesimulation mit dem globalen Chemie-Zirkulationsmodell demonstriert. Ein Vergleich mit neuen Satellitenmessungen belegt die erfolgreiche Modellierung des antarktischen Ozonloches.

Contents

Chapter 1

Motivation

The goal of this work was the development of a polar stratospheric cloud submodel for a general circulation model including chemistry (ECHAM5/MESSy).

Polar stratospheric clouds (PSCs) occur in the winter at high latitutes between 12 km and 24 km geometric height. They are mainly composed of water, nitric acid, and sulphuric acid. Their presence triggers chemical processes that can lead to massive ozone destruction in the Antarctic spring stratosphere ("ozone hole") and, to a lesser degree, also in the Arctic spring. After its discovery in the mid-1980s, the Antarctic ozone hole quickly gained great scientific and even public interest. Within a few years worldwide political action was taken to ban the production of halocarbon gases that, via a complex chain of processes, cause polar ozone depletion. Since then polar ozone chemistry and thus polar stratospheric clouds have stayed an important issue in stratospheric research.

Progress in PSC research has been made by theoretical considerations, laboratory work, in situ measurements, remote sensing, and computer simulations. As far as the latter are concerned, comprehensive computer models for detailed PSC studies and simplified ones for use in long-term simulations can be distinguished. The requirement for the PSC submodel described in this thesis was to efficiently calculate the most important features of PSCs, taking into account the limited spatial and temporal resolution of the input data from the global scale general circulation model.

The representation of PSCs is essential for simulations of polar stratospheric dynamics and chemistry. Examples of scientific questions that can be investigated with general circulation models capable of simulating PSCs and atmospheric chemistry are: the future development of the ozone hole, the interaction of the ozone hole and the increased "greenhouse effect", the influence of atmospheric chemistry on the dynamics of the polar stratosphere, and the influence of polar stratosphere dynamics on tropospheric climate.

As far as solid PSC particle formation, growth and evaporation are concerned, it has been necessary to find approaches that reproduce the essence of these microphysical processes in a simplified way, i. e. related to parameters calculated at the typical global model grid scale of several hundred kilometers.

Similarly, the proper simulation of solid PSC particle sedimentation in a coarse vertical grid can be challenging. In the past, special characteristics of this type of transport have not always been taken into account in the formulation of sedimentation schemes. Since the vertical redistribution of H_2O and especially of HNO_3 due to PSC particle sedimentation has attracted considerable interest in recent years, close attention has been payed in the current work to the modelling of this process.

For the simulation of liquid particle composition and of heterogeneous chemical reactions on PSC particles, previously existing program code from a box model could be reused. However, the requirements for a liquid particle scheme and for a PSC chemistry scheme in a general circulation model differ from those in a box model. Thus the transfer of the respective program components led to improvements and the development of new modelling concepts.

Due to the high complexity of chemistry-climate models, their evaluation is a major challenge. In the past, the availability of observational data for comparison with model results has not always been satisfactory. Fortunately, opportunities for model evaluation are improving. New impulses for polar stratospheric chemistry research come, for example, from the satellite instrument MIPAS on board ENVISAT, operational from July 2002 to January 2004. For this thesis, a new dataset derived from MIPAS observations was available, which contains information about polar stratospheric cloud occurrence in the Antarctic winter of 2003 with unprecedented spatial and temporal coverage.

Background information about the stratosphere, polar stratospheric clouds, and polar stratospheric chemistry is given in chapter 2 (Introduction). Chapter 3 (Model Overview) supplements the introduction with an overview of atmospheric modelling. A brief explanation of contributions to the data assimilation technique available in the general circulation model is also included in chapter 3.

The model components designed and evaluated during the course of this work are presented in chapters 4 (Solid PSC Particle Sedimentation), 5 (Solid PSC Particle Modelling), and 6 (PSC Simulations and Evaluation), including detailed literature reviews on PSC microphysics and sedimentation.

Chapter 7 (Notes on Model Temperatures) summarises information about the important model variable temperature. Chapters 8 (Liquid PSC Particle Scheme) and 9 (PSC Chemistry and Ozone Depletion) describe certain aspects of previously existing program routines that had to be adapted for use in ECHAM5/MESSy. Chapter 9 also contains results of a simulation run of the Antarctic winter of 2003, documenting the implications of the PSC submodel within ECHAM5/MESSy simulations of the stratosphere. Abbreviations, Symbols and Notation are explained in the appendix.

Chapter 2

Introduction

2.1 The Polar Stratosphere

The stratosphere is the atmospheric layer above the troposphere and below the mesosphere. Whereas the troposphere and the mesosphere are characterised by negative vertical temperature gradients, the temperature in the stratosphere increases with height. The heating process responsible for this temperature inversion is the absorption of solar radiation by stratospheric ozone, which has its maximum number concentration of about $7 \cdot 10^{18}\,\frac{1}{\mathrm{m}^3}$ at a geometric height of 22 km and its maximum amount-of-substance ratio[1] of about $10\,\frac{\mu\mathrm{mol}}{\mathrm{mol}}$ at 35 km (Andrews et al., 1987). The interface layer between troposphere and stratosphere is called tropopause; mesosphere and stratosphere are separated by the stratopause.

Near the poles the stratosphere extends from about 8 km geometric height (which corresponds to a pressure of about 250 hPa) to about 50 km (1 hPa). In the tropics, the lower boundary of the stratosphere, the tropopause, has an approximate altitude of about 18 km (100 hPa). Due to the temperature increase with height, the stratosphere is stably stratified; motions in the stratosphere are horizontal rather than vertical.

Fundamental ideas about stratosphere dynamics were developed in the middle of the 20th century by Brewer (1949) and Dobson (1956). More recent reviews of this subject can be found in Andrews et al. (1987) and Holton (1992).

Tropospheric air enters the stratosphere mainly in the tropics. As the tropical tropopause is very cold, most of the water vapour contained in the ascending air freezes and precipitates during this process. Therefore, the stratosphere is relatively dry (amount-of-substance ratios of water to air from $1.5\,\frac{\mu\mathrm{mol}}{\mathrm{mol}}$ to $8\,\frac{\mu\mathrm{mol}}{\mathrm{mol}}$, e. g. Nedoluha et al. (2003)). After reaching the tropical stratosphere, the formerly tropospheric air is transported upwards and later polewards by the Brewer-Dobson circulation. In the lower and middle stratosphere, transport to the summer pole is stronger than transport to the winter pole. In the upper stratosphere and in the mesosphere, air flows from the summer pole to the winter pole. The time scale for this pole to pole transport is of the order of a few months.

---

[1] Section B.2 defines and discusses the quantity “amount-of-substance ratio of X to air”.

The Brewer-Dobson circulation is wave driven, i. e. it is largely caused by momentum deposition by breaking waves that have vertically propagated from the troposphere (planetary waves and gravity waves). Over the winter pole, the Brewer-Dobson circulation leads to a downward air motion. Its velocity is roughly $3\,\frac{\mathrm{km}}{\mathrm{month}}$ in the upper stratosphere and $1\,\frac{\mathrm{km}}{\mathrm{month}}$ in the lower stratosphere (Newman et al., 2003). The downward motion is associated with adiabatic warming.

For a study of polar stratospheric clouds and polar ozone chemistry, the most important feature of stratospheric dynamics is the polar vortex. During wintertime, air in the polar night region experiences radiative cooling and downward motion. Temperature and pressure gradients cause air flow from mid-latitudes into the polar region. Due to the balance between the Coriolis force and the pressure gradient force this meridional wind turns into a "polar night jet", which circulates around the pole in eastern direction with wind velocities of more than $100\,\frac{\mathrm{m}}{\mathrm{s}}$.

The polar night jet constitutes a dynamical barrier that separates air inside from air outside the vortex. If it is stable (which is the normal state in the southern hemisphere), in the interior of the polar vortex solar heating is absent for several months. Thus temperatures can become especially low (as low as 180 K over Antarctica). The polar vortex can be observed in wind velocity patterns, by means of potential vorticity calculations, or via characteristic differences in trace gas concentrations inside and outside the vortex.

Differences between the orography at high latitudes in the northern and southern hemisphere have important implications for both polar vortices. Zonally asymmetric mountain ranges at high latitudes on the northern hemisphere cause vertically propagating waves. The stronger wave activity enhances the Brewer-Dobson circulation on the northern hemisphere and disturbs the polar night jet around the vortex. As a consequence of the more rapid downward flow, adiabatic heating is stronger in the Arctic winter stratosphere than in the Antarctic winter stratosphere. The disturbation of the polar night jet causes the northern polar vortex to be less centered around the pole. Furthermore, mixing of air inside and outside the vortex is stronger in the northern hemisphere. As a consequence, temperatures in the northern polar vortex are about 10 K above temperatures in the southern polar vortex.

In the winter stratosphere, zonal temperatures normally decrease polewards of ca. 60° latitude. Exceptions to this rule are sudden stratospheric warmings. In a major warming the zonal mean temperature increases polewards of 60° and below 10 Pa. Moreover, the zonal mean wind becomes easterly instead of westerly. Minor warmings are defined by a reversal of the temperature gradient without the zonal mean flow turning easterly.

Note that the sudden stratospheric warming events are not necessarily zonally symmetric despite the fact that they are defined in terms of zonal mean atmospheric variables.

In the Arctic, major stratospheric warmings occur approximately in one out of two winters. In the Antarctic, the vortex split in September 2002 is the only major warming that has been observed so far. On both hemispheres, minor warmings can happen several times each winter.

2.2 Polar Stratospheric Clouds

In the relatively dry stratosphere, clouds form in very cold regions only, i. e. above the tropical tropopause and inside the polar vortex between about 12 km to 24 km. This thesis is entirely devoted to the latter cloud type, for which McCormick et al. (1982) coined the term "polar stratospheric clouds" (PSCs).

From early LIDAR (LIght Detection And Ranging) observations it was concluded that there are two distinct PSC particle types ("type I PSCs" and "type II PSCs"). Later measurements revealed that type I PSC particles are sometimes solid ("type Ia"), and sometimes liquid ("type Ib"). Type II PSC particles are always solid.

It is widely accepted that PSCs mainly consist of H_2O, HNO_3, and H_2SO_4. Some details of PSC particle formation, composition and phase changes, however, are subject of ongoing research.

Water Ice

From laboratory data (Washburn, 1924) it has been known for a long time that ice can exist in the polar winter stratosphere.

Steele et al. (1983) concluded from theoretical considerations and from the Stratospheric Aerosol Measurement II (SAM II) observations that PSCs consist of ice. Hofmann et al. (1989) actually found ice particles in airborne in situ PSC measurements.

Current knowledge about ice PSC formation is discussed in further detail in section 6.1. Briefly, ice particles come to existence where temperatures drop below the ice frost point. This happens every winter on a synoptic scale in Antarctica. Ice PSCs in the northern hemisphere are more rare due to the higher average temperatures of the Artic winter polar stratosphere. There they form preferentially in lee waves of mountain ranges, where adiabatic cooling leads to sufficiently cold temperatures. Ice PSCs are thought to also contain some HNO_3 and other trace gases.

Chapter 6 presents simulations of ice particle occurrence in the Antarctic winter 2003.

Nitric Acid Trihydrate

Crutzen and Arnold (1986) and Toon et al. (1986) first suggested from theoretical consideratins that PSC particles might sometimes be composed of nitric acid trihydrate (NAT). The laboratory work of Hanson and Mauersberger (1988) confirmed that NAT is indeed thermodynamically stable under polar winter stratospheric conditions. However, it took twelve more years until direct measurements could be attributed to NAT with high probability for the first time (Voigt et al., 2000).

NAT is mainly relevant because the NAT equilibrium temperature is about 7 K higher than the ice frost point so that NAT particles can exist in conditions where ice evaporates. The process of NAT formation is still uncertain. Possible NAT formation mechanisms include homogeneous nucleation (Salcedo et al., 2001; Drdla and Browell, 2004), heterogeneous nucleation on SAT (sulfuric acid tetrahydrate), heterogeneous nucleation on ice (Koop et al., 1997; Waibel et al., 1999), gas-to-solid nucleation on meteoritic debris (Biermann et al., 1996), and surface induced nucleation of liquid aerosols (Tabazadeh et al., 2002). A detailed review of NAT formation theories can be found in section 6.1.

Chapter 6 shows simulation results for NAT particle occurrence in the Antarctic winter 2003.

Supercooled Ternary Solutions

Between 15 km and 30 km height, an aerosol layer of H_2SO_4/H_2O binary solution droplets (SSA – stratospheric sulfate aerosols) is observed around the globe ("Junge layer"; Junge et al. (1961)). Stratospheric H_2SO_4 mainly originates from tropospheric carbonyl sulfide (OCS) and sulfur dioxide (SO_2). Major volcanic eruptions, too, can inject sulfate into the stratosphere, e. g. Mount Pinatubo in 1991.

In the early 1990s, analysis of balloon- and rocket-borne mass spectrometer measurements stimulated speculations about HNO_3 condensation in supercooled SSA (Arnold, 1992).

In the middle 1990s, the laboratory work of Molina et al. (1993) and comparisons with thermodynamic models (Carslaw et al., 1994; Drdla et al., 1994; Tabazadeh et al., 1994) confirmed the assumption that PSC particles sometimes consist of liquid supercooled solutions of HNO_3 and H_2SO_4 in water. The supercooled ternary solutions (STS) grow from H_2SO_4/H_2O binary solution droplets (SSA) by the uptake of HNO_3.

Del Negro et al. (1997) show in a detailed analysis of in situ PSC particle observations that particles measured by them probably consisted of STS. In a more direct chemical analysis of PSC particles, also Schreiner et al. (1999) found STS composition.

In the current work, the Carslaw et al. (1994) model has been adapted (chapter 8) and applied in simulations (chapter 6).

Other Polar Stratospheric Cloud Components

Based on LIDAR results and thermodynamic considerations, Poole and McCormick (1988) suggested a three stage concept for PSC formation. It assumes that upon cooling, SSA freezes to SAT. SAT particles then serve as nuclei for NAT condensation. When temperatures decrease further below the ice frost point, water ice condenses on the NAT coated SAT particles. In this picture, type I PSCs consist of NAT, type II PSCs of ice particles.

Meanwhile, the STS concept has been recognised as superior to the classical three stage hypothesis (Peter, 1997). Part of the difficulties involved with SAT are its rather complicated phase transitions, as it deliquesces at low temperatures (Koop and Carslaw, 1996; Iraci et al., 1998); the deliquescence temperature depends on the availability of HNO_3. However, even though SAT is probably less important for PSC formation than previously assumed, it could still play a minor role in PSC formation.

Metastable phases of potential importance for PSCs include nitric acid dihydrate (NAD) (Worsnop et al., 1993) and sulfuric acid hemihexahydrate.

The PSC submodel presented in this thesis does not consider PSC particle compositions other than ice, NAT and STS (this choice is explained in section 6.1).

2.3 Sedimentation, Denitrification, Dehydration

Evidence of vertical HNO_3 redistribution by PSCs was found soon after the discovery of the ozone hole (Toon et al., 1986; Crutzen and Arnold, 1986). This effect is called "denitrification". Typical amount-of-substance ratios of HNO_3 to air at 20 km height are $10\,\frac{\mathrm{nmol}}{\mathrm{mol}}$ before denitrification, i. e. at the beginning of an Antarctic winter, and $2\,\frac{\mathrm{nmol}}{\mathrm{mol}}$ after denitrification, i. e. at the end of an Antarctic winter. Meanwhile it is widely accepted that denitrification is due to sedimentation of NAT particles and of ice particles containing HNO_3 (Newman et al., 2003).

Denitrification is observed above both winter poles. However, as PSC events in the northern polar stratosphere normally last shorter than those in the southern polar stratosphere, the typical depth of the denitrified air layer differs in both atmospheric regions. According to Tabazadeh et al. (2000, 2001) and Newman et al. (2003), typical vertical denitrification extents are $\gtrsim 10$ km over Antarctica and a few km over the Arctic.

Similarly to denitrification, dehydration is the vertical redistribution of H_2O due to sedimentation of ice PSCs. Typical amount-of-substance ratios of H_2O to air at 20 km are $5\,\frac{\mu\mathrm{mol}}{\mathrm{mol}}$ before dehydration and $2\,\frac{\mu\mathrm{mol}}{\mathrm{mol}}$ after dehydration (Nedoluha et al., 2003).

Dehydration, which requires temperatures low enough for ice particle formation, is widespread in Antarctic winters but not in the warmer Arctic winters. Nedoluha et al. (2003) show severe dehydration over an altitude range of 10 km in Antarctica. For the Arctic polar stratosphere, Newman et al. (2003) conclude that, even in cold winters, ice PSC occurrence is not widespread and persistent enough for noticeable dehydration.

The redistribution of H_2O affects PSC formation and the radiative properties of the polar stratosphere. Furthermore, H_2O is a reactant in several chemical reactions in the stratosphere. Denitrification increases ozone depletion, since the lack of HNO_3 reduces the conversion of reactive chlorine species into inactive $ClONO_2$.

Chapter 4 concentrates on sedimentation modelling, chapter 5 on the interplay of solid PSC size modelling and sedimentation.

2.4 Polar Ozone Chemistry

Reaction Cycles

At the heart of stratospheric ozone chemistry are the photolytic oxygen reactions shown in table 2.1 and table 2.2 (Chapman, 1930). Note that M in reaction 2 and later on is a third body, usually a N_2 or an O_2 molecule, that removes excess energy from the reaction products by collisional deactivation.

$$\begin{array}{lcll}
O_2 + h\nu & \longrightarrow & O + O & \text{(R1)} \\
2\,(O + O_2) & \xrightarrow{M} & 2\,O_3 & \text{(R2)} \\
\text{net: } 3\,O_2 & \longrightarrow & 2\,O_3 & \text{(R3)}
\end{array}$$

Table 2.1: Ozone production

$$\begin{array}{lcll}
O + O_3 & \longrightarrow & 2\,O_2 & \text{(R4)} \\
O_3 + h\nu & \longrightarrow & O_2 + O & \text{(R5)} \\
\text{net: } 2\,O_3 & \longrightarrow & 2\,O_3 & \text{(R6)}
\end{array}$$

Table 2.2: Ozone loss

Stratospheric ozone is also influenced by reactions with nitrogen oxides[2], e. g. the ones shown in table 2.3 (Crutzen, 1970). These are mainly relevant above 30 km and in sunlight conditions, as NO is photochemically related to NO_2 and largely depleted during nighttime. The main source of NO in the stratosphere is tropospheric N_2O via its reaction with excited oxygen atoms $O(^1D)$.

$$\begin{array}{lcll}
NO + O_3 & \longrightarrow & NO_2 + O_2 & \text{(R7)} \\
O_3 + h\nu & \longrightarrow & O_2 + O & \text{(R5)} \\
NO_2 + O & \longrightarrow & NO + O_2 & \text{(R8)} \\
\text{net: } 2\,O_3 & \longrightarrow & 3\,O_2 & \text{(R9)}
\end{array}$$

Table 2.3: NO_x reaction cycle

HO_x, too, reduces stratospheric ozone.[3] The reaction cycle given in table 2.4 is most relevant in the lower stratosphere (below 20 km). However, HO_x reactions of relevance for ozone chemistry do also take place in other parts of the atmosphere.

For this thesis, ozone destruction by reactions involving chlorine and bromine are of greatest interest, as they are linked to polar stratospheric clouds. The most prominent example in this context is given in table 2.5 (Molina and Molina, 1987). It involves the formation of the chlorine dimer in reaction (R13), which is effective only at very low temperatures. Furthermore, the reactants ClO are provided by photolytic reactions. Therefore, the reaction cycle of table 2.5 is only effective in the springtime polar stratosphere.

A second reaction cycle involving ClO was proposed by Molina and Rowland (1974); see table 2.6. It is most effective at about 40 km height. At lower altitudes the concentration of oxygen radicals decreases, which renders reaction (R19) inefficient. Therefore, the reactions in table 2.6 contribute to ozone

---

[2] Reactive nitrogen species are summarised as NO_x, which is defined as the sum of N, NO, NO_2, NO_3, and two times N_2O_5

[3] HO_x are reactive hydrogen species; in the context of this work, HO_x is the sum of H, OH, and HO_2.

$$\begin{array}{lcll}
\mathrm{OH} + \mathrm{O_3} & \longrightarrow & \mathrm{HO_2} + \mathrm{O_2} & \mathrm{(R10)} \\
\mathrm{HO_2} + \mathrm{O_3} & \longrightarrow & \mathrm{OH} + 2\,\mathrm{O_2} & \mathrm{(R11)} \\
\text{net: } 2\,\mathrm{O_3} & \longrightarrow & 3\,\mathrm{O_2} & \mathrm{(R12)}
\end{array}$$

Table 2.4: HO_x reaction cycle

$$\begin{array}{lcll}
\mathrm{ClO} + \mathrm{ClO} & \xrightarrow{M} & \mathrm{Cl_2O_2} & \mathrm{(R13)} \\
\mathrm{Cl_2O_2} + h\nu & \longrightarrow & \mathrm{Cl} + \mathrm{ClOO} & \mathrm{(R14)} \\
\mathrm{ClOO} & \xrightarrow{M} & \mathrm{Cl} + \mathrm{O_2} & \mathrm{(R15)} \\
2\,(\mathrm{Cl} + \mathrm{O_3} & \longrightarrow & \mathrm{ClO} + \mathrm{O_2}) & \mathrm{(R16)} \\
\text{net: } 2\,\mathrm{O_3} & \longrightarrow & 3\,\mathrm{O_2} & \mathrm{(R17)}
\end{array}$$

Table 2.5: ClO reaction cycle

destruction only at the upper end of the “ozone layer” where about 90 % of atmospheric ozone is located (roughly in between 15 km and 40 km).

$$\begin{array}{lcll}
\mathrm{Cl} + \mathrm{O_3} & \longrightarrow & \mathrm{ClO} + \mathrm{O_2} & \mathrm{(R18)} \\
\mathrm{O_3} + h\nu & \longrightarrow & \mathrm{O_2} + \mathrm{O} & \mathrm{(R5)} \\
\mathrm{ClO} + \mathrm{O} & \longrightarrow & \mathrm{Cl} + \mathrm{O_2} & \mathrm{(R19)} \\
\text{net: } 2\,\mathrm{O_3} & \longrightarrow & 3\,\mathrm{O_2} & \mathrm{(R20)}
\end{array}$$

Table 2.6: Cl_x reaction cycle

There are more complex catalytic cycles involving chlorine and reactants from other families (HO_x, NO_x, Cl_x)[4].

Bromine has reaction cycles similar to chlorine. They contribute significantly to ozone desctruction in the polar stratosphere despite the fact that bromine compounds are less abundant than chlorine compounds by a factor of 200. This is due to the fact that bromine is more easily activated, i. e. processed into highly reactive species. Of special importance is the mixed chlorine/bromine reaction pathway given in table 2.7 (McElroy et al., 1986).

---

[4] In the current work, ClO_x is defined as the sum of Cl, ClO, HOCl, OClO, two times Cl_2, and two times Cl_2O_2; it is called “odd chlorine” or “active chlorine” as it contains the rapidly reacting chlorine species.

$$
\begin{array}{llll}
\mathrm{BrO} + \mathrm{ClO} & \longrightarrow & \mathrm{Br} + \mathrm{Cl} + \mathrm{O_2} & \mathrm{(R21)} \\
\mathrm{Br} + \mathrm{O_3} & \longrightarrow & \mathrm{BrO} + \mathrm{O_2} & \mathrm{(R22)} \\
\mathrm{Cl} + \mathrm{O_3} & \longrightarrow & \mathrm{ClO} + \mathrm{O_2} & \mathrm{(R23)} \\
\text{net: } 2\,\mathrm{O_3} & \longrightarrow & 3\,\mathrm{O_2} & \mathrm{(R24)}
\end{array}
$$

Table 2.7: Br reaction cycle

The Ozone Hole

Farman et al. (1985) first detected the Antarctic ozone hole from balloon sounding measurements. It results from halogen-catalysed chemistry (Solomon, 1990). Similarly massive ozone depletion in the Arctic stratosphere is possible but less likely (Brune et al., 1991).

In the years following the discovery of the ozone hole it was concluded that the decrease of stratospheric ozone is a consequence of anthropogenic emissions of chlorofluorocarbons (Molina and Rowland, 1974; Anderson et al., 1991). Chlorofluorocarbons are inert in the troposphere, i. e. they are not removed by chemical reactions with OH radicals or other oxidising constituents. In the stratosphere, however, they are photolysed and act as sources of Cl, ClO, Br, and BrO. $CFCl_3$ and CF_2Cl_2 are the most important stratospheric sources of chlorine. Stratospheric Br atoms and BrO molecules originate from methyl bromide, CH_3Br, from natural and anthropogenic sources, and from other antropogenic halons.

Ozone recovery takes place in late spring and early summer by mixing of polar air with air from lower latitudes following the breakdown of the polar vortex.

Interhemispheric differences in ozone chemistry result from the higher temperatures in the Arctic polar vortex compared to the Antarctic polar vortex. It will be explained in the following section, that polar stratospheric clouds play a crucial role in the chain of processes leading to ozone depletion. Therefore, the less frequent occurrence of the highly temperature sensitive PSCs in the northern polar stratosphere renders Arctic ozone depletion as massive as in the case of the Antarctic ozone hole unlikely. Stronger mixing of the northern polar vortex with outside air further reduces the probability of a persisting severe lack of ozone.

It was mentioned in section 2.1 that the absorption of solar radiation by stratospheric ozone is an important heating mechanism in the stratosphere. Consequently, the decline of ozone in the spring polar stratosphere since the 1970s has led to lower average temperatures there (Randel and Wu, 1999). After the breakdown of the polar vortex, ozone depleted air spreads out and influences the radiative budget even in the mid-latitude stratosphere.

A simulation of the Antarctic ozone hole is presented in chapter 9.

The Role of Polar Stratospheric Clouds

Heterogeneous chemical reactions on the surface of polar stratospheric cloud particles convert the relatively stable chlorine species $ClONO_2$ and HCl in Cl_2

and HOCl, which are easily photolysed. Reactions involving bromine are generally similar to chlorine reactions. However, HBr and $BrNO_3$ are less stable than HCl and $ClONO_2$. In the presence of sunlight, $BrNO_3$ and HBr are easily photolysed so that heterogeneous chemical reactions are of importance for bromine chemistry mainly for nighttime conditions. See table 2.8 (Solomon et al., 1986; Tolbert et al., 1987; Hanson and Ravishankara, 1991; Abbatt and Molina, 1992; Crutzen et al., 1992; Hanson and Ravishankara, 1993)

$$\begin{array}{lcll}
ClONO_2 + HCl & \longrightarrow & HNO_3 + Cl_2 & \text{(R25)} \\
ClONO_2 + H_2O + & \longrightarrow & HNO_3 + HOCl & \text{(R26)} \\
HOCl + HCl & \longrightarrow & Cl_2 + H_2O & \text{(R27)} \\
N_2O_5 + HCl & \longrightarrow & ClNO_2 + HNO_3 & \text{(R28)} \\
N_2O_5 + H_2O & \longrightarrow & 2\,HNO_3 & \text{(R29)} \\
ClONO_2 + HBr & \longrightarrow & HNO_3 + BrCl & \text{(R30)} \\
BrONO_2 + HCl & \longrightarrow & HNO_3 + BrCl & \text{(R31)} \\
HOCl + HBr & \longrightarrow & BrCl + H_2O & \text{(R32)} \\
HOBr + HCl & \longrightarrow & BrCl + H_2O & \text{(R33)} \\
HOBr + HBr & \longrightarrow & Br_2 + H_2O & \text{(R34)} \\
BrONO_2 + H_2O + & \longrightarrow & HNO_3 + HOBr & \text{(R35)}
\end{array}$$

Table 2.8: Heterogeneous reactions on PSCs

Catalytic cycles can be interrupted by conversion of reactive species into more stable "reservoir" compounds: see table 2.9. As the near absence of ozone in the ozone hole favours Cl compared to ClO (see reaction R16), chlorine deactivation in the southern hemisphere leads to HCl (R38), whereas chlorine deactivation in the northern hemisphere rather produces $ClONO_2$ (R39).

$$\begin{array}{lcll}
HO_2 + HO_2 & \longrightarrow & H_2O_2 + O_2 & \text{(R36)} \\
NO_2 + OH & \xrightarrow{M} & HNO_3 & \text{(R37)} \\
Cl + CH_4 & \longrightarrow & HCl + CH_3 & \text{(R38)} \\
ClO + NO_2 & \xrightarrow{M} & ClONO_2 & \text{(R39)} \\
BrO + NO_2 & \xrightarrow{M} & BrNO_3 & \text{(R40)}
\end{array}$$

Table 2.9: Conversion into less reactive reservoir species

One of the sources of NO_2, which is a reactant in the deactivation reactions, is the decomposition of HNO_3 via photolysis or reactions with OH radicals. Denitrification (explained in section 2.3) can thus reduce the availability of NO_2 and, therefore, slow down chlorine deactivation.

2.5 Observations

For measurements of atmospheric constituents in the polar stratosphere, various methods are in use, e. g. in situ measurements with balloons and aeroplanes or remote sensing measurements with LIDAR or from satellites.

Not all types of measurement data are equally suitable in the context of this work. It will be explained in chapter 3 that the data simulated with the computer program ECHAM5/MESSy has a rather coarse resolution (e. g. $1.85° \cdot 1.85°$ in the horizontal and approximately 2 km in the vertical direction). Therefore, a comparison of simulation output with localised measurements is often difficult and sometimes even misleading (von Storch and Zwiers, 1999). Remote sensing instruments on satellites on the other hand can provide data with features similar to the simulation results. They can probe significant portions of the atmosphere and their measurement process normally involves some kind of regional averaging. MIPAS (Michelson Interferometer for Passive Atmospheric Sounding; ESA (2004); http://envisat.esa.int/instruments/mipas) on board of the earth observartion satellite ENVISAT, for example, provides information about trace gases with a horizontal resolution of approximately 250 km × 30 km, a vertical resolution of about 5 km, and covers the whole stratosphere within three days (G. Stiller, pers. comm., 2004). MIPAS data will play an important role for data comparison and model evaluation in chapter 6.

The principle of MIPAS is to measure the infrared emission spectrum of the atmosphere. By comparison with known emission spectra of potential atmospheric constituents, information about their concentration can be derived. MIPAS operated with interruptions from July 2002 to January 2004.

Infrared emission measurements have also been performed in the early 1990s by CLAES (Cryogenic Limb Array Etalon Spectrometer; Roche et al. (1993); http://www.lmsal.com/9120/CLAES/claes_homepage.html) and ISAMS (Improved Stratospheric And Mesospheric Sounder; Taylor et al. (1993); http://-badc.nerc.ac.uk/data/isams), both on the Upper Atmosphere Research Satellite UARS. Compared to MIPAS, however, CLAES and ISAMS datasets had smaller geographic coverage and less spectral resolution.

Another important remote sensing technique for atmospheric research is based on sunlight absorption spectra ("solar occulation"). For polar stratospheric cloud studies, however, it has the major drawback that it is not applicable in the polar night. Therefore, the following satellite instruments could only be used for probing the edge of the polar vortex or its late state in spring: HALOE (Halogen Occultation Experiment; Russell III et al. (1993); http:-//haloedata.larc.nasa.gov), SAGE II (Stratospheric Aerosol and Gas Experiment II; http://www-sage2.larc.nasa.gov), SAGE III (Stratospheric Aerosol and Gas Experiment III; http://www-sage3.larc.nasa.gov), ILAS (Improved Limb Atmospheric Spectrometer; Sasano et al. (1999); http://www-ilas.nies.go.jp), POAM II (Polar Ozone and Aerosol Measurement II; Glaccum et al. (1996); http://wvms.nrl.navy.mil/POAM/poam.html), and POAM III (Polar Ozone and Aerosol Measurement II; Lucke et al. (1999); http://wvms.nrl.navy.mil/-POAM/poam.html).

Unfortunately, satellite instruments cannot measure PSC particle radii and number densities (see Hervig and Deshler (1998) and Foschi and Pagan (2002) for first approaches in that direction) so that these model variables can only be compared with a limited number of balloon or aeroplane measurements.

In chapter 5, a number of in situ measurements of PSC particle types, sizes, and number densities will be cited.

Chapter 3

Model Overview

3.1 Atmospheric Modelling

In the context of this work, a model is a set of algorithms and mathematical equations together with its interpretation as image of atmospheric processes.

Most atmospheric models are too complex to carry out the algorithms or solve the mathematical equations by hand. Therefore, they are implemented as computer code. Processing this code on a computer is called “simulation run” or simply “simulation”.

If a simulation run has been set up to mimic atmospheric processes, differences between simulation results and “the real world” can be caused by several reasons:

Model shortcomings Models are simplified compared to real world processes because the full complexity of atmospheric chemistry and physics is neither understood nor computable.

A discussion of model shortcomings in solid particle radii schemes can be found in section 5.1.

Programming errors Although rarely mentioned in scientific publications, blunders in model implementation do occur (e. g. wrong unit conversions).

Input data errors Uncertainties in input data values, e. g. in temperature fields, can propagate in the model output.

Temperature input uncertainties are discussed in chapter 7, for example.

Numerical errors Most simulation programs of atmospheric processes are written for computer systems that represent real numbers with limited accuracy. Numerical solutions of mathematical equations can thus deviate from the true (often unknown) solutions.

Chapter 4 is devoted to numerical aspects of solid PSC particle sedimentation.

Atmospheric models can generally be classified according to their spatial structure:

Box models If the development of physical quantities in time is calculated for a single point in space, the model is called a box model. With these "zero-dimensional" models even relatively complex processes can be studied with reasonable computational effort.

Box model simulations have been applied for tests of the liquid PSC particle scheme (chapter 8).

1D-models 1-dimensional models can be regarded as linear arrangements of box models which interact with each other. They are suitable, for example, for the investigation of atmospheric processes in vertical columns.

PSC sedimentation is investigated by means of an 1D-model in chapters 4 and 5.

2D-models An example of models with two spatial dimensions is the 2D-model of Brühl and Crutzen (1993) for the simulation of stratospheric chemistry. With height and latitude as resolved dimensions, it aims at deriving trace gas concentration values that can be interpreted as zonal averages.

3D-models To fully capture the spatial depencence of atmospheric processes, models have to resolve latitude, longitude and height. Typically, the relatively complex spatial structure of 3D-models has to be balanced by simplifications in the model physics and chemistry due to limitations of computing resources.

3D-model simulation results can be found in chapter 6 and chapter 9.

Atmospheric models can also be classified as Lagrangian or Eulerian.

Lagrangian models The frame of reference for a Lagrangian model moves according to the wind fields, i. e. along the trajectory of an air parcel. Such models can reproduce adiabatic processes during transport of air parcels through the atmosphere for periods in which exchange with the environment can be neglected. A possible application for this type of model is the analysis of balloon flight measurements where the balloon has been transported by the wind.

Eulerian models The coordinate system of Eulerian models is fixed with respect to the earth.

This work is entirely devoted to Eulerian model studies.

3.2 The GCM ECHAM5

ECHAM5 (Roeckner et al., 2003) is the most recent version in a series of atmospheric general circulation models (GCMs) that originally evolved from the weather forecasting model of the European Centre for Medium Range Weather Forecast.

The Primitive Equations

Calculations of atmospheric dynamics in ECHAM5 are based on the so called primitive equations, which are a simplified version of the full set of equations governing the temporal development of wind fields, pressure and temperature. Their foundations are:

1. Momentum balance for horizontal wind fields
2. Hydrostatic balance, where the vertical pressure gradient force equals the gravitational force
3. The first law of thermodynamics
4. Mass conservation

Despite their name, the primitive equations are far too complex to be solved analytically for real atmospheric situations. ECHAM5 uses the spectral transform method to solve them. The prognostic variables vorticity, divergence, temperature, and logarithm of surface pressure are approximated by finite series of spherical harmonics. The differential equations are then applied to the spherical harmonics and their coefficients.

Advantages of the spectral method include the fact that the spherical harmonics are eigenfunctions of the Laplace operator in spherical coordinates and that some planetary waves can be represented well by low order spherical harmonics.

Model Physics

Apart from the temporal development of wind fields, most processes are calculated in three-dimensional grid-point coordinates rather than via series expansions in spherical harmonics. These grid-point coordinates are based on a Gaussian grid of longitudes, latitudes and vertical levels. Atmospheric processes calculated in grid-point coordinates are summarised as “model physics”.

Spectral representations that use higher order spherical harmonics correspond to close meshed Gaussian grids, whereas series expansions truncated relatively early correspond to coarse meshed latitude/longitude grids. The mapping between spherical and Gaussian representations in ECHAM5 is based on Eliasen et al. (1970) and Machenhauer and Rasmussen (1972).

The PSC submodel is implemented as part of the Gaussian grid “model physics”.

Advection

As a consequence of the wind fields, trace gases are redistributed in the atmosphere. For model applications that involve more than only a few tracers, advection calculation can consume a significant fraction of the total computing time. The standard advection scheme[1] in ECHAM5 was developed by Lin and Rood (1996). It is a flux form semi-Lagrangian scheme, which combines features of Eulerian flux form schemes with the unconditional stability for all Courant numbers typical of semi-Lagrangian schemes. According to van Aalst (2005), the Lin and Rood (1996) advection scheme in ECHAM5 leads to a realistic large-scale transport and to well-defined gradients of amounts-of-substance ratios of tracers to air at the edge of the polar vortex. Descent of long-lived trace gases in the lower part of the polar vortex, however, is underestimated.

Specific aspects of advection schemes are discussed in subsection 4.1.2 and in subsection 6.2.3.

Horizontal Resolution

Simulations presented in later chapters of this thesis use the resolution "T63", which means that spherical harmonics up to zonal and meridional wavenumbers 63 are used in series expansions. The number of longitudes of the corresponding Gaussian grid is 192, the number of latitudes 96, which leads to horizontal mesh sizes of approximately $1.875° \times 1.875°$.

Atmospheric processes that take place on scales smaller than the grid box sizes are notoriously difficult to represent in global models. The effects of these small-scale processes must somehow be linked to the large-scale parameters, hence the term "parameterisation" is used.

Vertical Resolution

The vertical model resolution in ECHAM5 is defined by means of hybrid levels, a combination of terrain following levels near the surface and pressure levels aloft. The pressure at the bottom of a grid box i, $p_{\mathrm{bot}}(i)$, is calculated as

$$p_{\mathrm{bot}}(i) = A_{\mathrm{bot}}(i) + B_{\mathrm{bot}}(i)\, p_0. \tag{3.1}$$

p_0 is the surface pressure, its contribution to the interface pressures is given by the coefficients $B_{\mathrm{bot}}(i)$, $0 \leq B_{\mathrm{bot}}(i) \leq 1$. In practice, the $B_{\mathrm{bot}}(i)$ coefficients are chosen in such a way that the influence of the surface pressure to the grid box interface pressures $p_{\mathrm{bot}}(i)$ decreases with increasing height. For the highest model levels, only the coefficients $A_{\mathrm{bot}}(i)$ contribute to the interface pressures $p_{\mathrm{bot}}(i)$.

The pressures inside the ECHAM5 grid boxes, p_i, are calculated as averages of the upper and lower grid box interface pressures:

$$p_i = \frac{1}{2}\left(p_{\mathrm{bot}}(i) + p_{\mathrm{top}}(i)\right). \tag{3.2}$$

$p_{\mathrm{top}}(i)$ is the pressure at the top of grid box i and equals $p_{\mathrm{bot}}(i-1)$ (levels are counted from the top to the surface in ECHAM5).

---

[1] Alternatively, a semi-lagrangian scheme (Rasch and Williamson, 1990) and SPITFIRE (Split Implementation of Transport Using Flux Integral Representation, Rasch and Lawrence (1998)) are available.

This study uses the 39 level middle atmosphere version of ECHAM5 (sometimes called MA-ECHAM5). The geometric heights of the grid boxes in the polar stratosphere are approximately 2 km to 3 km.

Time Integration

For the calculation of the development of a model variable X in time, time centered differences are used ("leap-frog scheme"):

$$\frac{\partial X(t)}{\partial t} \approx \frac{\Delta X(t)}{\Delta t} = \frac{X(t+\Delta t) - X(t-\Delta t)}{2\Delta t} \tag{3.3}$$

Variable values for even and odd numbered time steps are coupled via an Asselin (1972) time filter.

The model time step, Δt, is 600 s for the horizontal model resolution T63.

3.3 The chemistry-GCM ECHAM5/MESSy

With the advancement of computer hardware, measurement data and modelling experience, increasingly complex atmospheric models are developed. The technical challenges involved in the design, implementation and maintenance of these models require that the computer code is subdivided into manageable pieces like modules, subroutines and functions.

Where different parts of the model are implemented by different modellers, interface standards have to be defined and met to guarantee cooperation of all subprograms.

The polar stratospheric cloud submodel for ECHAM5 has been developed according to the MESSy (Modular Earth Submodel System) standard (Jöckel et al., 2005). Thus it can be coupled to the general circulation model ECHAM5 and to other MESSy submodels (see http://www.messy-interface.org for descriptions of all MESSy submodels).

The combination of the general circulation model ECHAM5 and the MESSy submodels allows simulations of both atmospheric dynamics and chemistry; hence ECHAM5/MESSy constitutes a chemistry-GCM. ECHAM5/MESSy simulation runs presented in this thesis (chapters 6 and 9) are based on the model version 0.9.1. Where reaction rate calculations and the PSC submodel have been modified compared to ECHAM5/MESSy 0.9.1, these updates are included in the ECHAM/MESSy model version 1.0. First applications of previous releases of the chemistry-GCM ECHAM5/MESSy can be found in Traub (2004) and van Aalst (2005).

In the following, the submodels MECCA, CLOUD, and H2O are briefly presented as they are of special importance for PSC simulations.

MECCA

Calculations of polar ozone chemistry require the chemistry submodel MECCA (Module Efficiently Calculating the Chemistry of the Atmosphere; Sander et al.

(2005)), which calculates tendencies of chemical tracers due to chemical reactions. Reaction rate coefficients for gas phase chemical reactions are part of MECCA, reaction rate coefficients for photolytic reactions are provided by the submodel PHOTO and reaction rate coefficients for heterogeneous chemical reactions on polar stratospheric clouds are calculated within the PSC submodel.

The solution of the system of differential equations describing the progress of chemical reactions is based on the "kinetic pre-processor" KPP (Damian et al., 2002).

More information about and an application of MECCA/KPP can be found in chapter 9.

CLOUD

The original ECHAM5 cloud scheme is capable of simulating ice clouds in the polar stratosphere. For the more detailed polar stratospheric cloud studies of this work, however, the respective subroutines are switched off and replaced by the PSC submodel routines in a region of the atmosphere, which is defined as follows:

- The northern border of the southern polar stratosphere is at 55° S.
- The southern border of the northern polar stratosphere is at 45° N (the Arctic vortex is typically less centered around the pole than the Antarctic vortex).
- The upper limit of the modelled PSC region is at 15 hPa.
- The lower limit of the modelled PSC region is between 100 hPa and 180 hPa. Its precise location is calculated each time step for each horizontal column according to the criterion

  $$T_{\mathrm{NAT}} \overset{!}{>} T_{\mathrm{ice}}, \tag{3.4}$$

  i. e. the equilibrium temperature of NAT has to be higher than the equilibrium temperature of ice. Equation (3.4) can be expected to be fulfilled in the dry stratosphere, where T_{ice} is relatively low. In the moister tropopause region, however, T_{ice} becomes higher than T_{NAT}, and the PSC submodel calculations are replaced by the ordinary ECHAM5 cloud scheme.

H2O

If the chemistry submodel MECCA is switched off, ECHAM5/MESSy simulations typically suffer from too low amount-of-substance ratios of H_2O in the stratosphere. This is caused by the absence of a chemical H_2O source: the oxidation of methane (CH_4).

For simulations of polar stratospheric cloud microphysics it can be desirable to neglect the time-consuming chemistry calculation and still have realistic water vapour values in the polar stratosphere.

This can be achieved with the ECHAM5/MESSy submodel H2O (C. Brühl and P. Jöckel, pers. comm., 2004; http://www.mpch-mainz.mpg.de/˜chb/h2o).

It contains a parameterisation of the effect of methane oxidation on stratospheric H_2O. Zonal mean monthly CH_4 concentrations based on HALOE observations are multiplied with average reaction rate coefficients with OH, Cl, and $O(^1D)$ taken from simulations with the chemistry-GCM MA-ECHAM4 (Steil et al., 2003; Saueressig et al., 2001). It is assumed that in every channel one CH_4 molecule yields finally $2\,H_2O$.

Furthermore, the H2O submodel enables the initialisation of stratospheric water vapour with a zonal mean bimonthly climatology derived from HALOE satellite observations.

3.4 Nudging

Overview

Nudging is a data assimilation technique which uses Newtonian relaxation (see equation (3.5) below) to modify the tendencies of prognostic model variables towards observed values.

Newtonian relaxation in ECHAM5 is applied in spectral space. According to Krishnamurti et al. (1991, pp. 67/68) the spectral equations for nudged variables take the following form:

$$\frac{\partial \alpha_l^m}{\partial t} = F_l^m(\alpha, t) + G(\alpha, t) \cdot \left(\alpha_l^{o\,m} - \alpha_l^m\right). \tag{3.5}$$

The influence of nudging, $\alpha_l^{o\,m}(t+\Delta t) - \alpha_l^m(t+\Delta t)$, corresponds to the difference between the unnudged prediction $\alpha_l^{*\,m}$ and the final value α_l^m:

$$\frac{\alpha_l^m(t+\Delta t) - \alpha_l^{*\,m}(t+\Delta t)}{2\Delta t} = G(\alpha, t)\left[\alpha_l^{o\,m}(t+\Delta t) - \alpha_l^m(t+\Delta t)\right]. \tag{3.6}$$

Solving the equation for $\alpha_l^m(t+\Delta t)$ shows that the spectral value is the weighted average of the external value $\alpha_l^{o\,m}$ and the unnudged prediction:

$$\alpha_l^m(t+\Delta t) = \frac{\alpha_l^{*\,m}(t+\Delta t) + 2\Delta t \cdot G(\alpha, t) \cdot \alpha_l^{o\,m}(t+\Delta t)}{1 + 2\Delta t \cdot G(\alpha, t)}. \tag{3.7}$$

Description of symbols:

α_l^m	spectral coefficient of order m and degree l
$\alpha_l^{*\,m}$	predicted value of α_l^m prior to Newtonian relaxation
$\alpha_l^{o\,m}$	future value of α_l^m at which the Newtonian relaxation is aimed
F_l^m	forcing term for variable α_l^m, excluding relaxation
$G(\alpha, t)$	nudging coefficient
t	time
Δt	time step length

The factor 2 in the denominator on the left hand side of equation (3.6) is a convention adopted from Krishnamurti et al. (1991), it could as well be included in the nudging coefficient G.

The nudging method was introduced in the mid-1970s (Kistler, 1973; Anthes, 1974; Hoke and Anthes, 1976). Jeuken et al. (1996) applied nudging in the ECHAM5 predecessor ECHAM3. Their goal was to force the model meteorology towards an observed situation to allow for a comparison of model output with observations. Therefore, ECMWF (European center for Medium-Range Weather Forecasts, http://www.ecmwf.int) analysis data for the time periods of interest was assimilated into ECHAM3.

The implementation of the nudging technique in ECHAM4 and ECHAM5 was performed by Ingo Kirchner (http://www.mad.zmaw.de/nudging and pers. comm.). Guldberg and Kaas (2000) suggested a new set of nudging coefficients. It leads to smaller nudging tendencies, which disturb the balance of model variables less than those in Jeuken et al. (1996) but are still strong enough to "guide" the general circulation model along the ECMWF input data.

An important requirement for the nudging of ECHAM5/MESSy is the interpolation of the ECMWF input data onto the ECHAM5/MESSy model grid. This is done with the preprocessing program INTERA developed by I. Kirchner (pers. comm., 2004).

Full nudging of all spherical harmonics potentially excites spurious small scale waves. This can be avoided by means of a normal mode filter. The normal mode initialisation technique implemented in ECHAM5/MESSy is based on Machenhauer (1977). The idea is to linearise the baroclinic primitive equations so that their normal modes can be determined. Projection of the model equations onto the normal modes yields equations for the normal modes, which can be classified as fast normal modes and slow normal modes. The normal mode expansion coefficients of a certain model state are then modified, mainly by reducing the contribution of fast normal modes. After re-transformation, the model state does not excite high-frequency oscillations any more. A detailed explanation of this method and its background is given in Daley (1991, chapters 6, 9, 10).

Previous applications of ECHAM5/MESSy nudging can be found in Traub (2004) and van Aalst (2005).

Vectorisation of Nudging Routines

The general circulation model ECHAM5 has been designed to run efficiently on scalar processors as well as on vector processors. Vector processors can perform the same operation multiple (e. g. 256) times within one calculation step. To benefit from this capability, a vector processor should always be fed with multiple (e. g. 256) similar instructions at the same time.

Computations for different atmospheric model columns are often similar, especially for grid boxes in the same vertical level. Hence the vectorisation strategy for ECHAM5 is to attribute each grid box within one longitude belt and vertical level to one element of the vector processor. The vector processor then simultaneously performs the calculations for all of these grid boxes.

However, the number of grid boxes within one longitude belt and vertical level (e. g. 192 for the horizontal resolution T63) does not generally equal the number of elements of the vector processor (256 in the example given above).

Therefore, the horizontal latitude-longitude grid in ECHAM5 can be restructured to suit the needs of vector processors. If the number of elements of the vector processor is larger than the number of longitudes in the Gaussian grid, columns of several Gaussian grid longitudes are summarised in pseudo-longitude belts. If the number of elements of the vector processor is smaller than the number of longitudes in the Gaussian grid, columns of a Gaussian grid longitudes are distributed onto several pseudo-longitude belts (A. Rhodin, pers. comm., 2003).

The application of the ECHAM5 vectorisation scheme to the nudging routines was part of this thesis. Thus in ECHAM5/MESSy, nudged simulations can be performed not only on the Gaussian longitude-latitude grid, but also on the restructured grids of pseudo-longitudes and pseudo-latitudes and, therefore, on vector processor systems.

Nudging Coefficients

In the current work, the maximum values of nudging coefficients G ("nudging weights") are adopted from Guldberg and Kaas (2000). The divergence and the vorticity of the horizontal wind fields are nudged (nudging weights G_{div} and G_{vor}) as well as the temperature (G_T) and the logarithm of the surface pressure ($G_{\ln p_0}$). Similar to van Aalst (2005), the lowest three levels and a number of levels from the top are not nudged, with a three level transition zone to the fully nudged levels.

The precluding of nudging near the ground avoids false tendencies due to differences between ECMWF and ECHAM5/MESSy orography, which could disturb the dynamics within the lower model levels. Test runs revealed that nudging in the highest model levels tends to cause numerical difficulties (extremely high wind speeds). Apparently, differences between ECMWF and ECHAM5 model dynamics are larger in this parts of the atmosphere. Hence model levels above the PSC relevant region are not nudged.

The nudging weights used in the nudged simulation runs presented in chapters 6 and 9 are listed in table 3.1. The pressure in the second column is calculated for a surface value of 1013.25 hPa and valid for the middle of the levels. The nudging weights can be interpreted as relaxation rates. In this picture, the e-folding times (i. e. the inverse nudging weights) for surface pressure and temperature are 24 h, 48 h for divergence and 6 h for vorticity.

level i	$\frac{p_i}{\text{hPa}}$	$\frac{G_{\text{div}}}{10^{-5}\,\frac{1}{\text{s}}}$	$\frac{G_{\text{vor}}}{10^{-5}\,\frac{1}{\text{s}}}$	$\frac{G_T}{10^{-5}\,\frac{1}{\text{s}}}$	$\frac{G_{\ln p_0}}{10^{-5}\,\frac{1}{\text{s}}}$
1–15	0.01–9.95	0.0000	0.0000	0.0000	—
16	13.48	0.0723	0.5787	0.1447	—
17	18.09	0.1447	1.1574	0.2894	—
18	24.07	0.2894	2.3148	0.5787	—
19–33	31.77–689.42	0.5787	4.6296	1.1574	—
34	778.48	0.2894	2.3148	0.5787	—
35	857.15	0.1447	1.1574	0.2894	—
36	921.08	0.0723	0.5787	0.1447	—
37–38	967.38–995.65	0.0000	0.0000	0.0000	—
39	1009.34	0.0000	0.0000	0.0000	1.1574

Table 3.1: Nudging weights for the divergence and the vorticity of horizontal wind fields, the temperature, and the logarithm of the surface pressure. The mid-level pressures in the second column relate to a surface pressures of $p_0 = 1013.25\,\text{hPa}$.

Chapter 4

Solid PSC Particle Sedimentation

4.1 Introduction

Section 2.3 briefly explained the importance of PSC sedimentation for microphysical and chemical processes in the polar vortex.

This chapter describes the sedimentation routines in the ECHAM5/MESSy PSC submodel and their performance. A major concern will be the handling of effects of the global model's low grid resolution (i. e. of numerical diffusion).

4.1.1 Literature

A survey of publications regarding solid PSC particle sedimentation showed that details of PSC sedimentation schemes have attracted only little attention in the past:

- In their description of a two-dimensional zonal model of the stratosphere, Fonteyn and Larsen (1996) stress the importance of particle sedimentation in PSC simulations. However, they do not mention how they modelled this process.

- The one-dimensional model of the formation and seasonal evolution of PSCs described in Panegrossi et al. (1996) uses a vertical grid size of 150 m (i. e. a much finer resolution than typically used in ECHAM5/-MESSy). The authors recognise the problem of numerical diffusion, however, they do not take extra measures to reduce it. They argue that the numerical diffusion of a simple sedimentation scheme is somehow counteracted by the uniform fall velocity associated with the model assumption of monodisperse particle radii.

- de Rudder et al. (1996) included detailed microphysical processes leading to PSC formation into a two-dimensional chemical/dynamical model. Solid PSC particle sedimentation is only briefly mentioned.

- Waibel (1997) claims to use a semi-lagrangian transport scheme for PSC particle sedimentation in his denitrification study (although figure 5.1 on page 52 of Waibel (1997) suggests, that this implementation deviates from what is commonly called semi-lagrangian transport). The reasons for and consequences of this choice of algorithm are not discussed.
- The PSC model in the chemistry-GCM MAECHAM4/CHEM calculates size dependent fall velocity for ice particles and mixed ice/NAT particles. The model description in Steil (1999) does not address the choice of the sedimentation scheme.
- The chemistry-transport-model SLIMCAT in the version of Chipperfield (1999b) calculates ice sedimentation with a sedimentation rate appropriate for particles of 10^{-5} m radius and NAT sedimentation as if NAT particles had a radius of 10^{-6} m. Details of the sedimentation algorithm are not mentioned.
- In the documentation of the NASA "Models and Measurements Intercomparison II" (Park et al., 1999) 25 atmospheric models are compared. 13 of them contain polar stratospheric clouds representations, but none of the model descriptions mentions the method for PSC sedimentation calculation (Ko et al., 1999; Jackman et al., 1999; Rosenfield et al., 1999; Zubov et al., 1999; Smyshlyaev et al., 1999; Pitari et al., 1999a; Grewe, 1999; Rodriguez and Rotman, 1999; Douglass and Kawa, 1999; Brasseur and Tie, 1999; Chipperfield, 1999a; Rozanov et al., 1999; Pitari et al., 1999b).
- Considine et al. (2000) stress the influence of the size distribution (several size bins versus monodisperse) on particle fluxes, but not that of the sedimentation scheme.
- The coupled chemistry-climate model UMETRAC uses fixed sedimentation rates of $0.14\ \frac{\mathrm{mm}}{\mathrm{s}}$ for NAT particles and $13\ \frac{\mathrm{mm}}{\mathrm{s}}$ for ice particles (Austin, 2002). The method for sedimentation calculation is not described.
- In their one-dimensional simulation of polar stratospheric cloud particles, Jensen et al. (2002) use the "piecewise parabolic method" (Colella and Woodward, 1984) to calculate sedimentation. However, Jensen et al. (2002) do not explain how they adapted it for their purpose (in Colella and Woodward (1984) the solution for the advection equation is only presented for velocity fields which are constant in space and time). In the light of subsection 4.1.2, it is also noteworthy that Jensen et al. (2002) use "advection in the vertical" as synonym for "sedimentation" – details of the sedimentation algorithm were probably not in the focus of their study.
- Koike et al. (2002) have studied denitrification and renitrification with the chemistry-transport model REPROBUS. Although NAT sedimentation is in the focus of their interest, they do not discuss the influence of the sedimentation scheme on this process.

- Pitari et al. (2002) describe a simulation including stratospheric and tropospheric aerosol components with the three-dimensional global model ULAQ. For sedimentation, NAT and ice particles in polar stratospheric clouds have been divided into nine size bins. The underlying sedimentation algorithm is not explained.

- van den Broek (2004) applies an advection scheme (Russel and Lerner, 1981) for NAT sedimentation calculation. The consequences of this approach are not discussed.

Hence, for the PSC submodel in ECHAM5/MESSy, a well-established technique for the sedimentation calculations was not available.

Several examples for the application of advection schemes for PSC sedimentation have been found in the literature. Therefore, in the following the relation between advection and sedimentation will be investigated in more detail.

4.1.2 Advection Equation and Sedimentation Equation

The numerical problem of tracer redistribution due to sedimentation of tracer containing aerosol particles is related to that of tracer advection. If numerical advection methods were applicable for sedimentation modelling, advantage could be taken of the abundant literature on advection schemes. Therefore, similarities and differences between both problems are clarified first. It will be shown that the treatment of divergent or convergent velocity fields in advection schemes is often inappropriate for sedimentation.

As concrete examples are more vivid than general derivations, the following paragraphs concentrate on the vertical redistribution of H_2O due to the sedimentation of ice. Therefore, number concentrations and related quantities refer either to ice molecules or to air molecules:

$$C_{\mathrm{ice}} = \frac{N_{\mathrm{ice}}}{V} \tag{4.1}$$

where N_{ice} is the number of ice molecules in volume V, or

$$C_{\mathrm{air}} = \frac{N_{\mathrm{air}}}{V} \tag{4.2}$$

where N_{air} is the number of air molecules in volume V. However, all considerations are equally valid for NAT phase HNO_3, the second species affected by the sedimentation calculated in the PSC submodel.

In both physical processes (aerosol particle sedimentation and tracer advection) tracers are neither gained nor lost (mass conservation) and the flux form continuity equation applies:

$$\frac{\partial C_{\mathrm{ice}}}{\partial t} + \nabla \cdot (\vec{u}\, C_{\mathrm{ice}}) = 0. \tag{4.3}$$

In equation (4.3), $\vec{u}$ is the velocity of ice molecules.

For the current purpose, only the vertical dimension, z, is relevant. With w as vertical velocity, equation (4.3) becomes

$$\frac{\partial C_{\text{ice}}}{\partial t} + \frac{\partial \left(w \, C_{\text{ice}} \right)}{\partial z} = 0. \tag{4.4}$$

Using the amount-of-substance ratio of ice to air,

$$x_{\text{ice}} = \frac{C_{\text{ice}}}{C_{\text{air}}} \quad \Leftrightarrow \quad C_{\text{ice}} = C_{\text{air}} \, x_{\text{ice}}, \tag{4.5}$$

the flux form continuity equation becomes

$$\frac{\partial \left(C_{\text{air}} \, x_{\text{ice}} \right)}{\partial t} + \frac{\partial \left(w \, C_{\text{air}} \, x_{\text{ice}} \right)}{\partial z} = 0. \tag{4.6}$$

Application of the chain rule for differentiation leads to

$$\frac{\partial C_{\text{air}}}{\partial t} x_{\text{ice}} + C_{\text{air}} \frac{\partial x_{\text{ice}}}{\partial t} + \frac{\partial \left(w \, C_{\text{air}} \right)}{\partial z} \, x_{\text{ice}} + w \, C_{\text{air}} \frac{\partial x_{\text{ice}}}{\partial z} = 0. \tag{4.7}$$

Now a distinction has to be made whether the vertical velocity w is that of air (w_{air}) or that of falling ice particles (w_{ice}). First $w = w_{\text{air}}$ will be chosen, as in advection problems. In this case, the flux form continuity equation for air

$$\begin{aligned} 0 &= \frac{\partial C_{\text{air}}}{\partial t} + \frac{\partial \left(w_{\text{air}} \, C_{\text{air}} \right)}{\partial z} && (4.8) \\ \Leftrightarrow \quad 0 &= \frac{\partial C_{\text{air}}}{\partial t} x_{\text{ice}} + \frac{\partial \left(w_{\text{air}} \, C_{\text{air}} \right)}{\partial z} x_{\text{ice}} && (4.9) \end{aligned}$$

simplifies equation (4.7):

$$\begin{aligned} 0 &= C_{\text{air}} \frac{\partial x_{\text{ice}}}{\partial t} + w_{\text{air}} \, C_{\text{air}} \frac{\partial x_{\text{ice}}}{\partial z} && (4.10) \\ \Leftrightarrow \quad 0 &= \frac{\partial x_{\text{ice}}}{\partial t} + w_{\text{air}} \frac{\partial x_{\text{ice}}}{\partial z}. && (4.11) \end{aligned}$$

Advection schemes normally solve the flux form continuity equation (4.3) (Bott, 1989a) or its equivalent form (4.6) (Russel and Lerner, 1981; Walcek, 2000). However, equation (4.10) (or its three-dimensional counterpart) can also serve as starting point for numerical solutions of the advection problem (Rood, 1987; Günther, 1995; Brasseur et al., 1999, p. 424). It states that the amount-of-substance ratio of ice to air within an air parcel is unchanged if advection is the only process under consideration.

Going back to (4.7), an equation corresponding to (4.10) can be derived for $w = w_{\text{ice}}$, i. e. for the sedimentation case. Ice particles now move in resting air[1],

$$\frac{\partial C_{\text{air}}}{\partial t} = 0, \tag{4.12}$$

---

[1] In the context of the PSC submodel for ECHAM5/MESSy, air properties are calculated from basic thermodynamic variables by means of the ideal gas equation. Details of the molecular composition of air are not taken into account. Therefore, the (small) amount of ice particles falling from higher grid boxes into lower grid boxes within one model time step does not change C_{air}.

and equation (4.7) becomes

$$\begin{aligned} 0 &= C_{\mathrm{air}} \frac{\partial x_{\mathrm{ice}}}{\partial t} + \frac{\partial \left(w_{\mathrm{ice}} \, C_{\mathrm{air}} \right)}{\partial z} x_{\mathrm{ice}} + w_{\mathrm{ice}} \, C_{\mathrm{air}} \frac{\partial x_{\mathrm{ice}}}{\partial z} && (4.13) \\ &= C_{\mathrm{air}} \frac{\partial x_{\mathrm{ice}}}{\partial t} + \frac{\partial w_{\mathrm{ice}}}{\partial z} C_{\mathrm{air}} x_{\mathrm{ice}} + w_{\mathrm{ice}} \frac{\partial C_{\mathrm{air}}}{\partial z} x_{\mathrm{ice}} + w_{\mathrm{ice}} \, C_{\mathrm{air}} \frac{\partial x_{\mathrm{ice}}}{\partial z}. && (4.14) \end{aligned}$$

A comparison of equations (4.10) and (4.13) shows that for the sedimentation process an additional term $\frac{\partial (w_{\mathrm{ice}} \, C_{\mathrm{air}})}{\partial z} x_{\mathrm{ice}}$, which describes a divergent sedimentation flow, has to be taken into account. In advection problems, divergent flows are balanced by changes in air molecule number concentrations (see continuity equation (4.9)), which cancels out the divergent flow term so that it is not present in equation (4.10).

A simple example that can be used to illustrate this difference between advection and sedimentation is a model grid box that contains air and ice. Let advection or sedimentation out of this grid box be the only processes that affect the amount of ice in it. To remove all ice from the grid box, advection would then also have to remove all air, whereas sedimentation would leave the air unchanged.

The difference between equations (4.10) and (4.13) has been introduced by the simplifications (4.9) versus (4.12); it is not explicitly present in equation (4.3) or equation (4.6). However, several advection schemes based on (4.3) or (4.6) (Russel and Lerner, 1981; Bott, 1989a; Lin and Rood, 1996; Walcek, 2000) introduce it implicitly. They use the advection characteristic that a divergent (or convergent) advective flow is coupled with a change in air molecule number concentration insofar as they apply flow limiters. These flow limiters avoid amount-of-substance ratio buildups or reductions by advection beyond the values of neighbouring grid boxes. Similar effects can be achieved with dissipation mechanisms that smooth profiles of advected quantities wherever velocities converge (Colella and Woodward, 1984).

Advection schemes without flux limiters on the other hand lead to over- and undershoots (including negative amount-of-substance ratios of tracers to air) in areas with strong gradients (Rood, 1987). As solid PSC particle sedimentation regularly includes strong gradients of C_{ice} (e. g. ice in grid box i, no ice in grid box $i+1$), advection schemes which are not flow limited also seem inadequate for sedimentation.

It can thus be concluded that PSC particle sedimentation should be calculated with an algorithm tailor-made for sedimentation problems; advection schemes could only provide an approximate solution for particle sedimentation if it was known in advance that strongly divergent (or convergent) flows will not play an important role.

Estimate of $\frac{\partial (w_{\mathrm{ice}} \, C_{\mathrm{air}})}{\partial z} x_{\mathrm{ice}}$

A sufficient condition (but not necessary in the case of advection schemes based on (4.3) or (4.6)) for the applicability of advection schemes for sedimentation problems is

$$\frac{\partial \left(w_{\mathrm{ice}} \, C_{\mathrm{air}} \right)}{\partial z} x_{\mathrm{ice}} \ll C_{\mathrm{air}} \frac{\partial x_{\mathrm{ice}}}{\partial t} + w_{\mathrm{ice}} \, C_{\mathrm{air}} \frac{\partial x_{\mathrm{ice}}}{\partial z}. \tag{4.15}$$

To demonstrate, that this sufficient condition is indeed sometimes violated in PSC simulations, the relative contribution of the term(s)

$$\frac{\partial\,(w_{\mathrm{ice}}\,C_{\mathrm{air}})}{\partial z}x_{\mathrm{ice}} = \frac{\partial w_{\mathrm{ice}}}{\partial z}C_{\mathrm{air}}\,x_{\mathrm{ice}} + w_{\mathrm{ice}}\frac{\partial C_{\mathrm{air}}}{\partial z}x_{\mathrm{ice}} \tag{4.16}$$

in the sedimentation equation will be estimated. For this estimate, numerical values for the variables and differentials in equation (4.14) are used that could occur with ice PSCs in a chemistry-GCM like ECHAM5/MESSy:

$\partial t \mapsto \Delta t$: model time step, $\Delta t \approx 600\,\mathrm{s}$

$\partial z \mapsto \Delta z$: vertical layer height, $\Delta z \approx 2000\,\mathrm{m}$

x_{ice}: amount-of-substance ratio of ice to air, $x_{\mathrm{ice}} \approx 2 \cdot 10^{-6}\,\frac{\mathrm{mol}}{\mathrm{mol}}$

w_{ice}: ice particle fall velocity, $w_{\mathrm{ice}} \approx \frac{2\,\mathrm{m}}{600\,\mathrm{s}}$

C_{air}: number concentration of air molecules (estimated for an air pressure of 50 hPa and a temperature of 200 K), $C_{\mathrm{air}} \approx 1.8 \cdot 10^{24}\,\frac{1}{\mathrm{m}^3}$

$\partial x_{\mathrm{ice}}$ in $\frac{\partial x_{\mathrm{ice}}}{\partial t} \mapsto \Delta x_{\mathrm{ice}}$: amount-of-substance ratio change per model time step, $\Delta x_{\mathrm{ice}} \approx 10^{-6}\,\frac{\mathrm{mol}}{\mathrm{mol}} \cdot \frac{2\,\mathrm{m}}{2000\,\mathrm{m}} = 10^{-9}\,\frac{\mathrm{mol}}{\mathrm{mol}}$

$\partial x_{\mathrm{ice}}$ in $\frac{\partial x_{\mathrm{ice}}}{\partial z} \mapsto \Delta x_{\mathrm{ice}}$: amount-of-substance ratio deviation between two adjacent vertical layers, $\Delta x_{\mathrm{ice}} \approx 10^{-6}\,\frac{\mathrm{mol}}{\mathrm{mol}}$

$\partial w_{\mathrm{ice}}$ in $\frac{\partial w_{\mathrm{ice}}}{\partial z} \mapsto \Delta w_{\mathrm{ice}}$: sedimentation velocity deviation between two adjacent vertical layers, $\Delta w_{\mathrm{ice}} \approx \frac{1\,\mathrm{m}}{600\,\mathrm{s}}$,

$\partial C_{\mathrm{air}}$ in $\frac{\partial C_{\mathrm{air}}}{\partial z} \mapsto \Delta C_{\mathrm{air}}$: difference in number concentration of air molecules between two adjacent vertical layers (for air pressure, temperature and vertical layer height given above), $\Delta C_{\mathrm{air}} \approx 0.5 \cdot 10^{24}\,\frac{1}{\mathrm{m}^3}$,

These values lead to the conclusion that the four summands in equation (4.14) can be of the same order of magnitude:

$$\begin{aligned} C_{\mathrm{air}}\frac{\partial x_{\mathrm{ice}}}{\partial t} &\approx 1.8 \cdot 10^{24}\,\frac{1}{\mathrm{m}^3} \cdot \frac{10^{-9}}{600}\frac{1}{\mathrm{s}} \\ &= 3.0 \cdot 10^{12}\,\frac{1}{\mathrm{s}\cdot\mathrm{m}^3} \end{aligned} \tag{4.17}$$

$$\begin{aligned} \frac{\partial w_{\mathrm{ice}}}{\partial z}C_{\mathrm{air}}\,x_{\mathrm{ice}} &\approx \frac{\frac{1\,\mathrm{m}}{600\,\mathrm{s}}}{2000\,\mathrm{m}} \cdot 1.8 \cdot 10^{24}\,\frac{1}{\mathrm{m}^3} \cdot 2 \cdot 10^{-6}\,\frac{\mathrm{mol}}{\mathrm{mol}} \\ &= 3.0 \cdot 10^{12}\,\frac{1}{\mathrm{s}\cdot\mathrm{m}^3} \end{aligned} \tag{4.18}$$

$$\begin{aligned} w_{\mathrm{ice}}\frac{\partial C_{\mathrm{air}}}{\partial z}\,x_{\mathrm{ice}} &\approx \frac{2\,\mathrm{m}}{600\,\mathrm{s}} \cdot \frac{0.5 \cdot 10^{24}\,\frac{1}{\mathrm{m}^3}}{2000\,\mathrm{m}} \cdot 2 \cdot 10^{-6}\,\frac{\mathrm{mol}}{\mathrm{mol}} \\ &= 1.6 \cdot 10^{12}\,\frac{1}{\mathrm{s}\cdot\mathrm{m}^3} \end{aligned} \tag{4.19}$$

$$\begin{aligned} w_{\mathrm{ice}}\,C_{\mathrm{air}}\frac{\partial x_{\mathrm{ice}}}{\partial z} &\approx \frac{2\,\mathrm{m}}{600\,\mathrm{s}} \cdot 1.8 \cdot 10^{24}\,\frac{1}{\mathrm{m}^3} \cdot \frac{10^{-6}\,\frac{\mathrm{mol}}{\mathrm{mol}}}{2000\,\mathrm{m}} \\ &= 3.0 \cdot 10^{12}\,\frac{1}{\mathrm{s}\cdot\mathrm{m}^3}. \end{aligned} \tag{4.20}$$

Thus the divergent flow connected with the sedimentation process sometimes cannot be neglected. In general, sedimentation processes should be calculated by means of adequate sedimentation algorithms. If advection schemes are to be applied for sedimentation problems in special cases, it has to be checked carefully whether the treatment of divergent flows is appropriate.

4.1.3 PSC Sedimentation in ECHAM5/MESSy

For the following considerations some particularities of the PSC sedimentation in ECHAM5/MESSy have to be taken into account:

- Pressure is used as vertical coordinate, not geometric height.
- ECHAM5/MESSy can be run in different vertical resolutions The most common one for PSC modelling is currently the 39 level middle atmosphere version, but the PSC sedimentation routines should also work for other vertical resolutions typically used in global models.
- Vertical layers are not generally evenly spaced, neither in geometric height nor in pressure coordinates. Moreover, in the hybrid level system (3.2) layer interface pressures in the lower stratosphere grid box heights are time dependent due to the influence of the varying surface pressure.
- For all currently used combinations of vertical grid structures, model time step and fall velocity, PSC particles never “jump over” a grid box within one model time step, i.e. they fulfill the Courant criterion

$$c := \frac{w_{\text{ice}}}{\frac{\Delta z}{\Delta t}} \overset{!}{<} 1 \tag{4.21}$$

4.2 Solid PSC Particle Sedimentation Schemes

Three solid PSC particle sedimentation schemes are presented in this section.

The simple upwind scheme is one of the most simple ways of implementing PSC particle sedimentation. It is assumed that several of the models mentioned in subsection 4.1.1 use sedimentation methods similar to the simple upwind scheme.

The trapezoid scheme has been developed within this work. Contrary to many advection schemes, it can deal with divergent (or convergent) sedimentation velocity fields.

The Walcek (2000) advection scheme is also applied to sedimentation. Thus the approach of several models cited in subsection 4.1.1, to use advection schemes for sedimentation calculation, can be tested.

4.2.1 Simple Upwind Scheme

The term “simple upwind scheme” is typically used for a certain type of finite difference algorithms that solve the advection equation numerically. The principle of the simple upwind advection scheme can also be applied for sedimentation processes. It will be explained here without explicitly using the sedimentation equation (4.13).

Figure 4.1 shows a vertical profile of amount-of-substance ratios of ice to air with subgrid scale variability. The complex structure is, however, simplified due to the limited grid resolution in ECHAM5/MESSy (see figure 4.2).

For each grid box there is only one single value of x_{ice}, which can be interpreted as a box average. Assuming that the box average value x_{ice} applies to every subvolume of a grid box, the fraction of ice molecules that falls into the next grid box below within one model time step then equals the ratio of one sedimentation step length to the grid box height (which is the Courant number c in equation (4.21); see also figure 4.3).

The amount-of-substance ratio of ice to air in grid box i after a sedimentation step, $x_{\text{ice}}(t+\Delta t, i)$, is calculated in the simple upwind scheme as follows:

$$\begin{aligned} x_{\text{ice}}(t+\Delta t, i) &= x_{\text{ice}}(t,i) \\ &\quad + x_{\text{ice}}(t,i-1)\,\frac{\Delta p_{\text{sed}}(t,i-1)}{p_{\text{bot}}(t,i)-p_{\text{top}}(t,i)} \\ &\quad - x_{\text{ice}}(t,i)\,\frac{\Delta p_{\text{sed}}(t,i)}{p_{\text{bot}}(t,i)-p_{\text{top}}(t,i)} \end{aligned} \tag{4.22}$$

where $\Delta p_{\text{sed}}(t,i-1)$ is the distance-of-fall in pressure units for ice particles in grid box i, $p_{\text{bot}}(t,i)$ is the pressure at the bottom of grid box i, and $p_{\text{top}}(t,i)$ is the pressure at the top of grid box i.

The main step in the derivation of equation (4.22) is the calculation of the amount-of-substance change in box i due to particles sedimenting from box $i-1$:

$$\begin{aligned} \Delta_{i-1}x_{\text{ice}}(t,i) &= \frac{n_{\text{ice}}\left(t,(i-1)_{\text{sed}}\right)}{n_{\text{air}}(t,i)} \\ &= x_{\text{ice}}(t,i-1)\,\frac{n_{\text{air}}\left(t,(i-1)_{\text{sed}}\right)}{n_{\text{air}}(t,i)} && (4.23) \\ &= x_{\text{ice}}(t,i-1)\,\frac{\frac{m_{\text{air}}\left(t,(i-1)_{\text{sed}}\right)}{M_{\text{air}}}}{\frac{m_{\text{air}}(t,i)}{M_{\text{air}}}} && (4.24) \\ &= x_{\text{ice}}(t,i-1)\,\frac{m_{\text{air}}\left(t,(i-1)_{\text{sed}}\right)}{m_{\text{air}}(t,i)} && (4.25) \\ &= x_{\text{ice}}(t,i-1)\,\frac{\frac{A}{g}\Delta p_{\text{sed}}(t,i-1)}{\frac{A}{g}\left(p_{\text{bot}}(t,i)-p_{\text{top}}(t,i)\right)} && (4.26) \\ &= x_{\text{ice}}(t,i-1)\,\frac{\Delta p_{\text{sed}}(t,i-1)}{p_{\text{bot}}(t,i)-p_{\text{top}}(t,i)} && (4.27) \end{aligned}$$

The notation "$(i-1)_{\text{sed}}$" refers to the part of grid box $(i-1)$ from which particles fall into grid box i within one model time step. n_{ice} and n_{air} are amounts-of-substance of ice and air, respectively. m_{air} is the mass of air, M_{air} its molar mass. The horizontal area A in a vertical column has no grid box index i as it is independent of height in ECHAM5/MESSy; the same applies to the acceleration due to gravity, g.

The simple upwind scheme is classified as “zeroth order scheme” as it uses constant x_{ice} values, i. e. zero order polynomials.

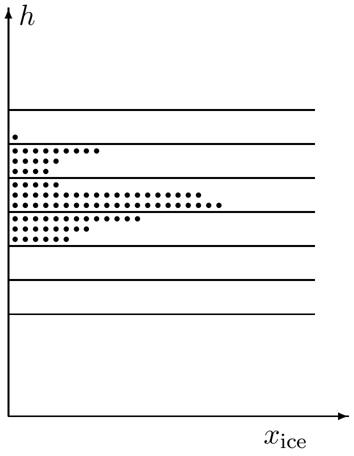

Figure 4.1: *Real vertical ice profiles* vary on height scales smaller than the ECHAM5/MESSy vertical layer heights. The black circles represent ice particles; more circles at a specific height h mean higher amount-of-substance ratios of ice to air. The horizontal lines indicate vertical grid box interfaces.

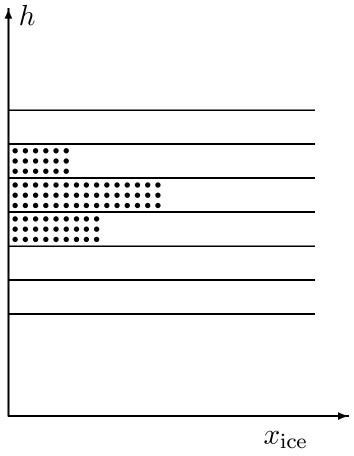

Figure 4.2: *Model vertical ice profiles* approximate real vertical ice profiles by means of a step function, i. e. with one constant value per grid box.

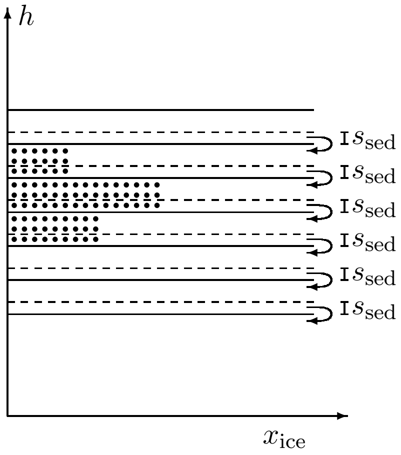

Figure 4.3: *Simple upwind scheme sedimentation* assumes that if particles fall a distance s_{sed}, all particles from the lowermost layer of thickness s_{sed} of a grid box reach the next grid box below. The ice particle content in the lowermost layer is calculated for each grid box using the constant x_{ice} value inside.

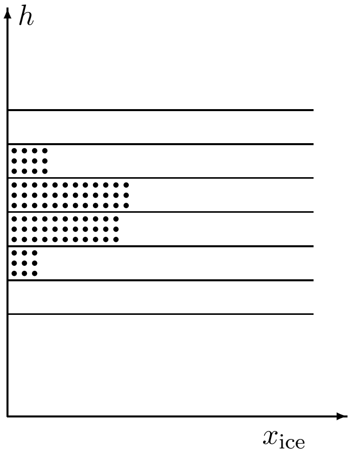

Figure 4.4: *After a sedimentation step* the vertical ice profile is shifted towards lower grid boxes. Changes in the shape of the profile occur as a side effect.

4.2.2 Trapezoid Scheme

A possible improvement of the zeroth order sedimentation scheme described in section 4.2.1 is the use of first order polynomials for the vertical amount-of-substance ratio of ice to air profile. With a first order scheme, the determination of the changes in the x_{ice} profile due to sedimentation is no longer based on the x_{ice} step function shown in figure 4.2. Instead, the amount of ice to move from grid box i downwards into grid box $i+1$ is calculated by means of a straight line approximation for the x_{ice} profile in grid box i.

The modelling of vertical amount-of-substance ratio of ice to air profiles as first order polynomials might not be appropriate for high resolution models as PSCs can have distinct vertical structures on height scales of about 100 m (Hofmann, 1990; Deshler et al., 2003).

In the current context, however, only larger height scales are relevant[2]. Erratic variations in the vertical PSC structure can, therefore, be expected to be smeared out, which results in a continuous x_{ice} profile.

The advantage of a first order vertical PSC ice profile compared to the step function used in the simple upwind scheme becomes apparent by considering a sharp peak in the vertical profile which is located around layer i (see figure 4.5). Straight line approximations for x_{ice} inside the grid boxes can reproduce the feature that in the layer above, $i-1$, more ice molecules are located at the bottom of layer $i-1$ than at the top. Similarly, in layer $i+1$, straight line approximations increase x_{ice} near the top, i. e. near the peak. The step function, on the contrary, does not distinguish between those parts of the layers $i-1$ or $i+1$ which are near the peak and those parts away from the peak. Consequently, in the first order scheme more particles move from the grid box immediately above the peak into the next lower grid box than in the zeroth order simple upwind scheme (compare figures 4.3 and 4.6).

The above arguments for using a first order PSC sedimentation scheme in ECHAM5/MESSy are of qualitative nature only and require support by comparative tests. These tests will be described in section 4.3.

There are several first order approaches for advection problems, e. g. the Walcek scheme discussed in section 4.2.3. However, as shown in subsection 4.1.2, advection schemes are not necessarily suited for sedimentation calculations. Therefore, a first order scheme is developed especially for sedimentation.

The foundation of the first order scheme are the local straight line approximations for the amount-of-substance ratio of ice to air profile. A straight line in the (p, x_{ice})-plane is defined by two points

$$\left(p\left(t, z_1\right), x_{\text{ice}}\left(t, z_1\right)\right)$$

and

$$\left(p\left(t, z_2\right), x_{\text{ice}}\left(t, z_2\right)\right).$$

Its slope is

$$m_{1,2} = \frac{x_{\text{ice}}\left(t, z_2\right) - x_{\text{ice}}\left(t, z_1\right)}{p\left(t, z_2\right) - p\left(t, z_1\right)} \tag{4.28}$$

---

[2] Typical ECHAM5/MESSy grid box interface pressures in the stratosphere are for example 27.45 hPa, 36.10 hPa, 47.10 hPa, 60.97 hPa, 78.35 hPa, 99.60 hPa.

and its intercept is

$$b_{1,2} = x_{\text{ice}}(t, z_1) - \frac{x_{\text{ice}}(t, z_2) - x_{\text{ice}}(t, z_1)}{p(t, z_2) - p(t, z_1)} p(t, z_1) \tag{4.29}$$

The linearly approximated amount-of-substance ratio is, therefore,

$$\begin{aligned} x_{\text{ice}}(t, z) &= \frac{x_{\text{ice}}(t, z_2) - x_{\text{ice}}(t, z_1)}{p(t, z_2) - p(t, z_1)} p(t, z) \\ &\quad + x_{\text{ice}}(t, z_1) - \frac{x_{\text{ice}}(t, z_2) - x_{\text{ice}}(t, z_1)}{p(t, z_2) - p(t, z_1)} p(t, z_1). \end{aligned} \tag{4.30}$$

For the simple upwind scheme, the part of layer i from which ice particles move into the next lower grid box $i + 1$ within one model time step corresponds to a rectangle in the (p, x_{ice})-plane. Using the straight line approximation for $x_{\text{ice}}(t, z)$, this rectangle is replaced by a trapezoid (see figures 4.7 and 4.8).

In mathematical terms, the rectangle in the simple upwind scheme is represented by the product $x_{\text{ice}}(t, i-1)\,\Delta p_{\text{sed}}(t, i-1)$ in equation (4.27). The area of the corresponding trapezoid in the first order scheme is

$$A_{\text{trapezoid}} = \frac{1}{2}\left(x_{\text{ice}}(t, z_1) + x_{\text{ice}}(t, z_2)\right) \Delta p_{\text{sed}}(t, i-1) \tag{4.31}$$

$$\begin{aligned} &= \frac{1}{2}\left(m_{1,2} p(t, z_1) + b_{1,2} + m_{1,2} p(t, z_2) + b_{1,2}\right) \Delta p_{\text{sed}}(t, i-1) \\ &= \left(m_{1,2} \frac{p(t, z_1) + p(t, z_2)}{2} + b_{1,2}\right) \Delta p_{\text{sed}}(t, i-1). \end{aligned} \tag{4.32}$$

i. e. the amount-of-substance ratios $x_{\text{ice}}(t, z_1)$ and $x_{\text{ice}}(t, z_2)$ form the two parallel sides of the trapezoid and $\Delta p_{\text{sed}}(t, i-1)$ its height.

There are several possibilities for choosing the two points which define the straight line approximation. The straight line calculations in Russel and Lerner (1981) and Walcek (2000) are based on the amount-of-substance ratios of tracers to air in the grid boxes i and $i + 1$. Bott (1989a) suggests using $x(t, i)$ and $x(t, i-1)$ as alternative. Generally, there is no optimum choice as each variant of the first order scheme has advantages for some profiles and disadvantages for others. The one selected for ECHAM5/MESSy has performed well in a series of comparing tests. It is characterised as a rather straightforward implementation which refrains from the use of "fudge factors" and treats local extremes even more simply.

Approximation below peak

If the grid box i, from which sedimentation is to be calculated, is located above a peak, the straight line is drawn through the amount-of-substance ratio of ice to air values in the grid boxes i and $i + 1$ (see figure 4.7)

$$(p(t, z_1), x_{\text{ice}}(t, z_1)) = (p(t, i), x_{\text{ice}}(t, i)) \tag{4.33}$$

$$(p(t, z_2), x_{\text{ice}}(t, z_2)) = (p(t, i+1), x_{\text{ice}}(t, i+1)) \tag{4.34}$$

This leads to increased sedimentation compared to the simple upwind scheme.

For steep x_{ice} gradients above a peak, the above equations can lead to trapezoid areas larger than the product $x_{\text{ice}}(t,i) \cdot (p_{\text{bot}}(t,i) - p_{\text{top}}(t,i))$. If these large trapezoid values were used in the sedimentation calculation, more ice than present in grid box i would be moved into grid box $i+1$. To avoid this unphysical behaviour, special precautions ensure that not more ice than available is transported by the sedimentation scheme.

Approximation below peak

For grid boxes i below a peak in the x_{ice} profile, the routines calculate two alternative straight line approximations:

$$\begin{aligned}
(p(t,z_1), x_{\text{ice}}(t,z_1)) &= (p(t,i-1), x_{\text{ice}}(t,i-1)) \qquad (4.35)\\
(p(t,z_2), x_{\text{ice}}(t,z_2)) &= (p(t,i), x_{\text{ice}}(t,i)) \qquad (4.36)
\end{aligned}$$

and

$$\begin{aligned}
(p(t,z_1), x_{\text{ice}}(t,z_1)) &= (p(t,i), x_{\text{ice}}(t,i)) \qquad (4.37)\\
(p(t,z_2), x_{\text{ice}}(t,z_2)) &= (p(t,i+1), x_{\text{ice}}(t,i+1)). \qquad (4.38)
\end{aligned}$$

The sedimentation is then calculated using the smaller trapezoid. Compared to the simple upwind scheme, sedimentation below a peak is reduced (see figure 4.8).

The above choice leads to the use of x_{ice} values from grid box i and $i-1$ if $x_{\text{ice}}(t,i)$ is relatively small compared to $x_{\text{ice}}(t,i-1)$ (see figure 4.9(a)). Those cases are interpreted as a local maximum in the vertical x_{ice} profile which is mainly in grid box $i-1$, but extends slightly into grid box i. Thus it seems appropriate to approximate $x_{\text{ice}}(t,i)$ in such a way that most ice is located in the upper parts of grid box i. For steep x_{ice} gradients, however, the above equations can lead to negative trapezoid areas. In those cases, no ice particle sedimentation takes place.

For $x_{\text{ice}}(t,i)$ values only slightly below $x_{\text{ice}}(t,i-1)$, the vertical x_{ice} profile is interpreted as a peak which has fully arrived in grid box i and extends into grid box $i+1$. The vertical x_{ice} profile near the $i/i+1$ interface is thus best approximated by means of $x_{\text{ice}}(t,i)$ and $x_{\text{ice}}(t,i+1)$ (see figure 4.9(a)).

Treatment of local extremums

For local extremums in the vertical x_{ice} profile, the influence of nearby grid boxes on the ice distribution inside grid box i is less evident. Therefore, if the grid box i under consideration is a local maximum or a local minimum, the vertical x_{ice} profile is not approximated by straight lines. Hence the area which defines the amount of sedimenting is not a trapezoid but the rectangle corresponding to the product $x_{\text{ice}}(t,i-1)\,\Delta p_{\text{sed}}(t,i-1)$, as in the simple upwind scheme (equation (4.27)). See figures 4.10 and 4.11.

Figures

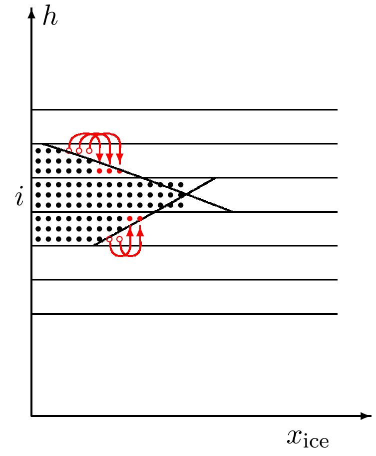

Figure 4.5: In the trapezoid scheme, the constant amount-of-substance ratios of ice to air within each grid box (compare figure 4.2) are replaced by first order approximations

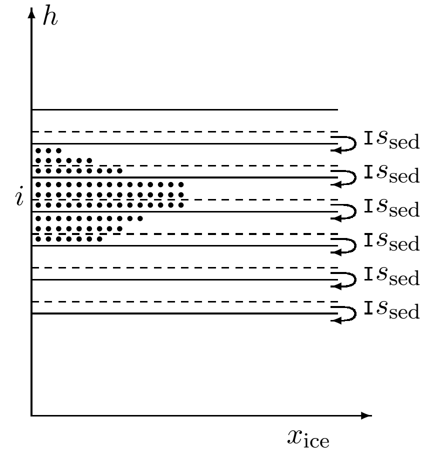

Figure 4.6: A continuous variation of x_{ice} with height leads to increased sedimentation from above a maximum and reduced sedimentation from below a maximum compared to the simple upwind scheme.

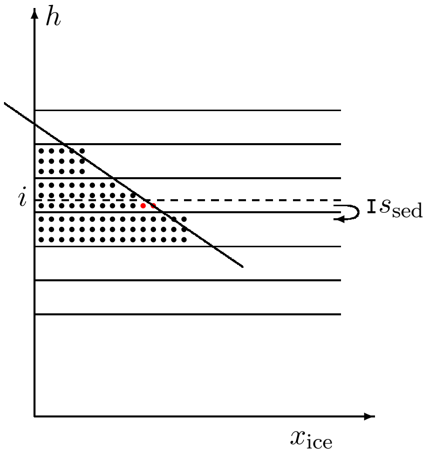

Figure 4.7: The linear approximations above a peak lead to increased particle transport. The red circles indicate ice particles which do sediment in the trapezoid scheme but would not sediment in the simple upwind scheme.

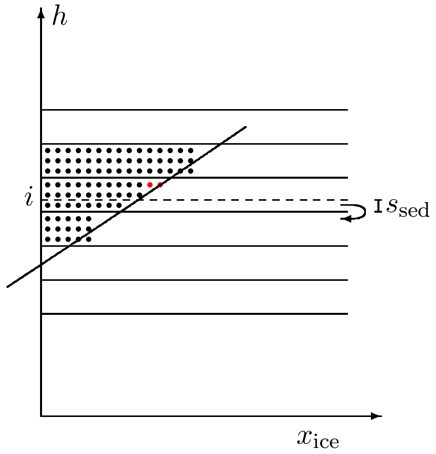

Figure 4.8: Below a peak, linear approximations reduce the amount of transported particles. The red circles indicate ice particles which do not sediment in the trapezoid scheme but would sediment in the simple upwind scheme.

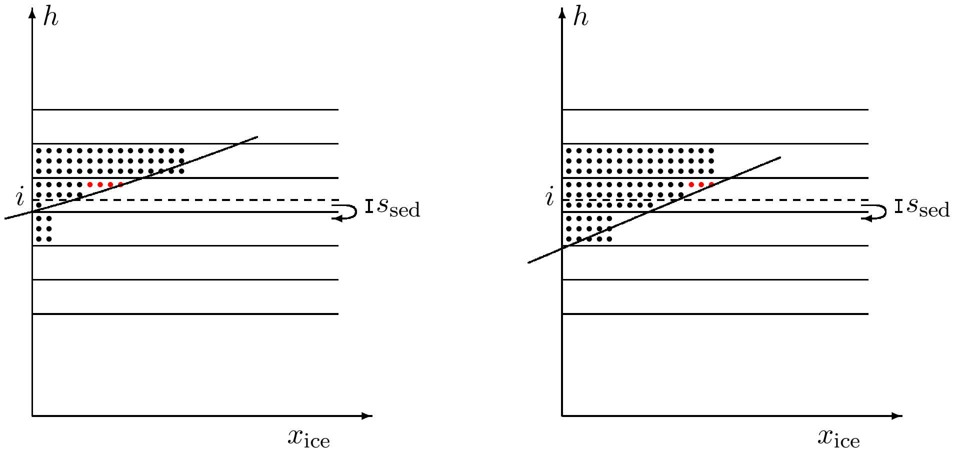

(a) line through box i and above

(b) line through box i and below

Figure 4.9: The linear approximation below a peak is based on the amount of substance ratios of ice to air, x_{ice}, from grid box i and $i-1$ above if $x_{\text{ice}}(i)$ is relatively small compared to $x_{\text{ice}}(i-1)$ (see figure 4.9(a)).
If $x_{\text{ice}}(i)$ is not too much smaller than $x_{\text{ice}}(i-1)$, the linear approximation is based on the x_{ice} values in grid boxes i and $i+1$ (see figure 4.9(b)).

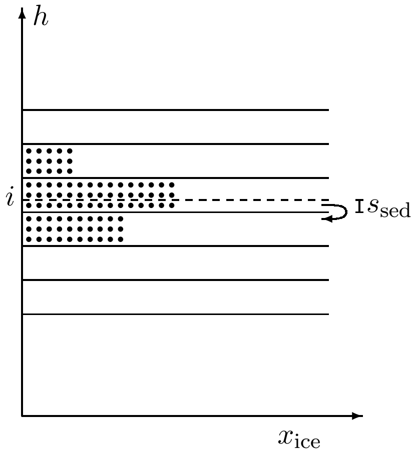

Figure 4.10: No approximation for a local maximum; sedimentation as in the simple upwind scheme.

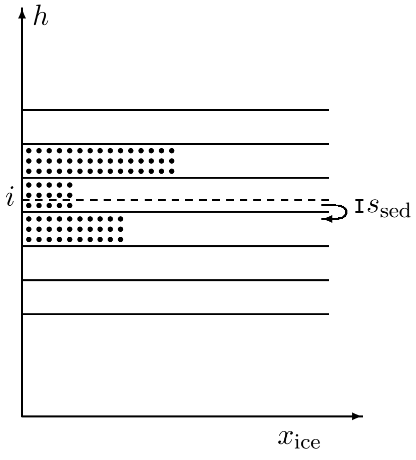

Figure 4.11: No approximation for a local minimum; sedimentation as in the simple upwind scheme.

4.2.3 Walcek Scheme

As explained in depth in subsection 4.1.2, advection schemes treat convergent velocity fields differently than would be appropriate for sedimentation problems. A simple example for a convergent sedimentation velocity field is given by high sedimentation fluxes due to high fall velocities from box $i-1$ into box i in combination with small fluxes due to small $w_{\mathrm{ice}}\,(i)$ for the sedimentation of ice particles from box i into box $i+1$.

Despite the fundamental difference between advection and sedimentation, it cannot be ruled out that an advection scheme could still be of some use for PSC sedimentation in ECHAM5/MESSy. As a consequence of the solid PSC particle model described in later chapters, strong amount-of-substance ratio buildups due to convergent sedimentation velocity fields will not generally occur. In the above example, increasing amount-of-substance ratios of ice to air in grid box i would lead to increased particle radii due to growth processes. As bigger particles have higher sedimentation velocities, growing sedimentation fluxes would counteract the further increase of amount-of-substance ratios ("negative feedback"). Therefore, possible advantages of using an established and well tested advection scheme could outweigh the disadvantage associated with the advection/sedimentation inconsistency.

To test the applicability of an advection scheme for PSC sedimentation in ECHAM5/MESSy, the Walcek (2000) routines will be used. Like the trapezoid scheme, the Walcek scheme is based on first order approximations of amount-of-substance profiles. Compared to other first order advection schemes, e. g. the one published by Bott (1989a,b, 1992), it has the advantage of not being restricted to regular grid spacing.

The advection/sedimentation inconsistency appears in the Walcek algorithm in the form of monotonicity constraints which prevent amount-of-substance ratios to build up due to advection. To simply eliminate the monotonicity constraints is not possible as they are an integral part of the Walcek scheme.

For the current work, the program code given in Walcek (2000) has been modified:

- For sedimentation purposes, only particles moving in one direction (downwards, not upwards) have to be considered.
- Pressure coordinates are used instead of geometric coordinates.
- Contrary to advection, ice sedimentation does not change the air density. Therefore, the different densities of the Walcek algorithm are replaced by one single density (so that equation [2] in Walcek (2000) becomes equation (4.6) above).

4.3 Evaluation

4.3.1 Test Model

As explained in the introduction of this chapter, solid PSC particle sedimentation is of importance as it leads to dehydration and denitrification. However, amount-of-substance ratio of H_2O and HNO_3 to air profiles in the winter polar stratosphere do not depend on sedimentation alone. For example, denitrification can also take place via mixing of non-vortex air into the polar vortex. Furthermore, the influence of sedimentation is superposed by the downward air motion in the polar vortex, i. e. the descending branch of the Brewer-Dobson circulation. Therefore the three sedimentation schemes described above have to be compared in a simplified test model concentrating on sedimentation.

The following tests consider ice sedimentation only, although the sedimentation schemes are applied for NAT as well. The test model uses a single column with vertical layers of 1 km geometric height and ice particles with a uniform sedimentation step per model time step $s_{\mathrm{sed}} = 2.0\,\mathrm{m}$. s_{sed} multiplied by the number of time steps (5000) corresponds to an integer multiple of the model layer height 1 km ($5000 \cdot 2.0\,\mathrm{m} = 10\,\mathrm{km}$). Thus the "true" sedimentation result can easily be calculated by simply shifting the initial ice profile 10 layers downwards. It is desirable to test the sedimentation schemes for air pressures in the range of 10 hPa to 200 hPa. Using a constant temperature of $T = 190.0\,\mathrm{K}$ for the conversion between pressure coordinates and geometric height, the height coordinate ranges from 9 km to 26 km.

Three vertical ice profiles will be used: A sharp peak tests the diffusivity of the sedimentation scheme, a broad peak represents a more realistic PSC occurrence (see e. g. figure 4 in Hofmann et al. (1989)), and a double peak challenges the structure preserving capability.

The runtime of the three sedimentation functions is not examined. For the comparison of three algorithms, runtime measurements can be misleading as they only refer to a specific implementation of the algorithms, specific computer architectures and specific compiler versions. Obviously, neither zeroth order algorithms nor first order algorithms necessarily involve time-consuming computations. Therefore, if one of the three sedimentation routines should ever be a bottleneck in a climate simulation run, only the actual implementation, not the algorithm would have to be changed.

4.3.2 Qualitative Evaluation

Figure 4.12 shows the exact solution for the sedimentation of the three test profiles; figures 4.13–4.15 visualise the results of the three numerical methods. The independent variable, the height h, is represented by the vertical coordinate axis; the horizontal position of the symbols corresponds to the amount-of-substance ratio of ice to air in a vertical layer.

The use of spheres as symbols anticipates the calculation of solid PSC particle surface area densities in the context of heterogeneous chemical reactions, for which spherically shaped particles will be assumed[3]. The velocity-of-fall equation (equation 5.3, subsection 5.1.2) includes a correction for non-sphericity.

For test purposes a uniform w_{ice} in the whole column is desirable since the exact result can then be easily calculated as a reference. Due to the pressure

---

[3] In fact, solid PSC particles are not spheres. However, experimental studies of reaction rates for chemical reactions on PSCs also rely on simple assumptions about the ice surface. Uncertainties in reaction rate calculations are discussed in section 9.2

gradient, a uniform fall velocity in the whole column corresponds to ice particles in lower grid boxes being bigger than those in higher grid boxes, which is illustrated by the height dependence of the sphere sizes.

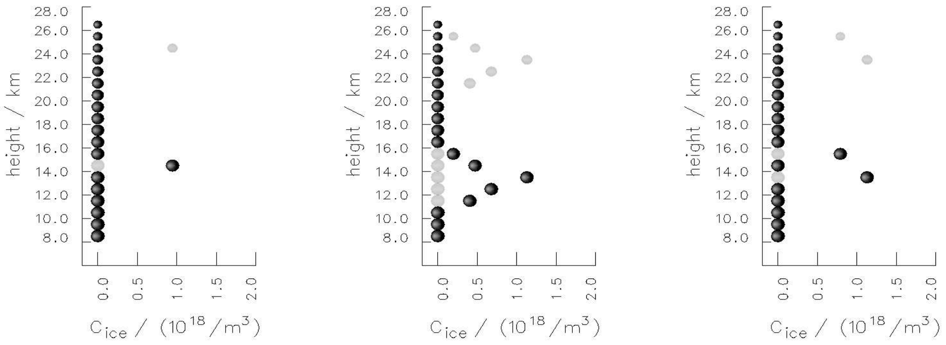

(a) sharp peak (b) broad peak (c) double peak

Figure 4.12: Exact sedimentation results. Grey spheres indicate the initial profiles, black spheres the final profiles.

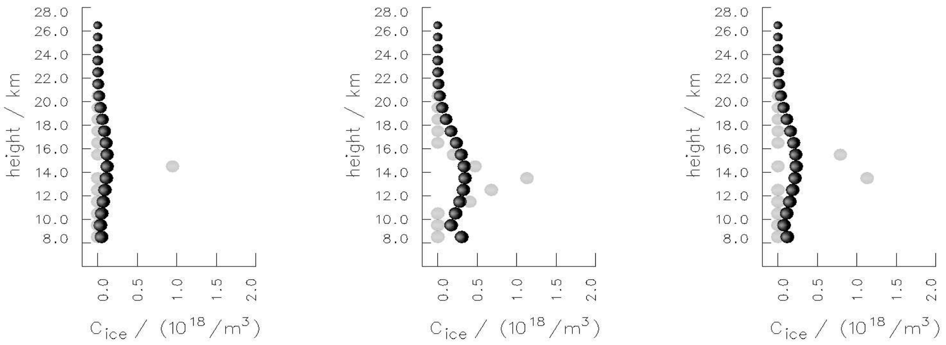

(a) sharp peak (b) broad peak (c) double peak

Figure 4.13: Simple upwind scheme results. Grey spheres indicate the exact, black spheres the numerical solutions.

The zeroth order scheme results show stronger numerical diffusion than the results of the two first order schemes. It converts all three initial distributions into broad peaks. Because it removes a fraction of the ice molecules in a grid box ($\frac{2}{1000}$ for sedimentation steps $s_{\mathrm{sed}} = 2\,\mathrm{m}$ and vertical layer heights of $1\,\mathrm{km}$), an initial ice molecule concentration $C_{\mathrm{ice}} > 0$ is never reduced to zero by sedimentation. On the other hand, if at a time t there are ice molecules in grid box i, a fraction will be in grid box $i+1$ in the following time step $t+\Delta t$. It follows immediately, that within n time steps, some ice molecules are transported as far

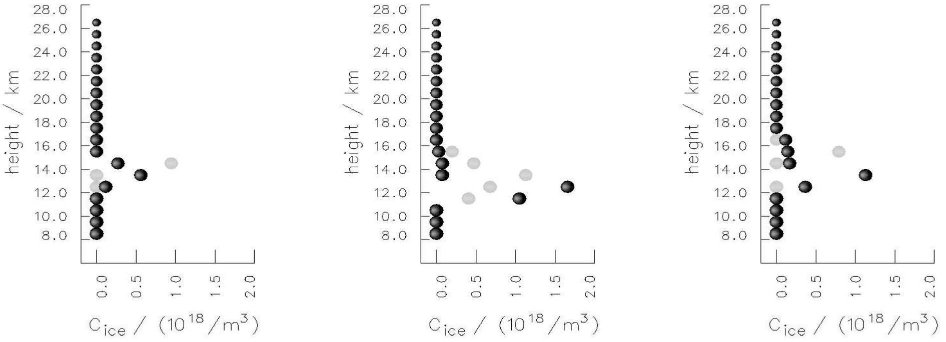

(a) sharp peak (b) broad peak (c) double peak

Figure 4.14: Trapezoid scheme results. Grey spheres indicate the exact, black spheres the numerical solutions.

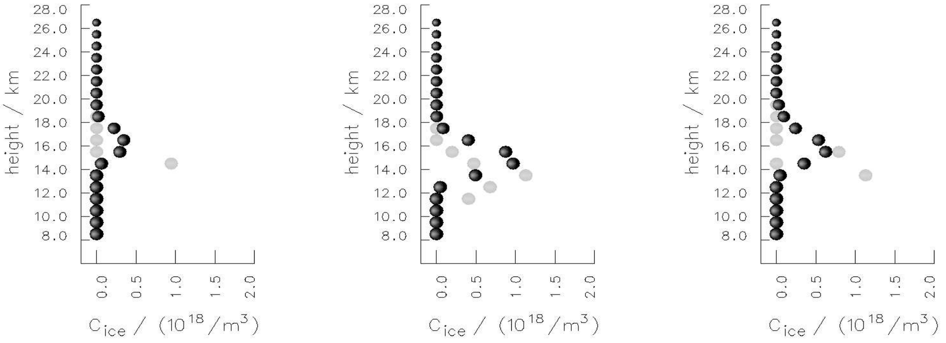

(a) sharp peak (b) broad peak (c) double peak

Figure 4.15: Walcek scheme results. Grey spheres indicate the exact, black spheres the numerical solutions.

as n grid boxes downwards. To summarise, the simple upwind scheme moves some particles much too slow and others much too fast. This characteristic behaviour can cause difficulties in combination with a NAT formation scheme which is triggered by the presence of ice, e. g. Waibel et al. (1999).

The local concentration maximum in the lowermost grid box of the simple upwind scheme results is caused by ice particles being transported too fast in combination with the fact that particles cannot leave the lowermost grid box in the test model. Particles are collected there to allow for mass conservation checks.

For the two first order schemes, it is not obvious which one is to be preferred. Numerical diffusion is slightly stronger for the Walcek scheme; the trapezoid scheme on the other hand increases the broad peak. The effective sedimentation velocity is too small for the Walcek scheme and too large for the trapezoid scheme.

A characteristic difference, which cannot be seen in the plots but from the original data only, is that the ice molecule concentrations are numerically zero above and below the peak for the trapezoid scheme results whereas they are slightly larger than zero above and below the peak in the Walcek scheme results.

It should be kept in mind that the current simple test model uses a non-divergent velocity field (see subsection 4.3.1). Therefore, the situation where the flow limiters of the Walcek advection scheme can be expected to show up in the results, has not been tested here. In chapter 5, the test model will be extended in a way that causes velocity fields to become divergent.

4.3.3 Quantitative Evaluation

The quantitative evaluation uses the six error measures listed in Walcek (2000). Unlike there, number concentrations of ice molecules in air, C_{ice}, will be used instead of amount-of-substance ratios of ice to air, $x_{\text{ice}}(i)$. The concentration based error measures are better suited for variable box sizes and pressures.

In equations (4.39) to (4.44) the index i runs over N grid boxes in a vertical column. The number concentrations $C_{\text{ice}}(i)$ are the ones calculated by the sedimentation scheme under consideration, whereas $C_{\text{ice}}^{\text{ref}}(i)$ is the exact solution, which is used as reference.

Peak Preservation

$$pker = \frac{\max\left\{C_{\text{ice}}^{\text{ref}}(i)\right\} - \max\left\{C_{\text{ice}}(i)\right\}}{\max\left\{C_{\text{ice}}^{\text{ref}}(i)\right\} - \min\left\{C_{\text{ice}}^{\text{ref}}(i)\right\}} \tag{4.39}$$

pker compares the global maximum value of the numerical and the analytical tracer concentration profile. It does not take into account the location of the global maxima. Meaningful results can be expected from *pker* if $\max\left\{C_{\text{ice}}^{\text{ref}}(i)\right\}$ and $\max\left\{C_{\text{ice}}(i)\right\}$ refer to the same feature in the concentration profile.

Mass Conservation

$$mser = 1 - \frac{\sum_i C_{\text{ice}}(i)}{\sum_i C_{\text{ice}}^{\text{ref}}(i)} \tag{4.40}$$

mser controls whether the sedimentation schemes conserve mass. All three sedimentation algorithms under consideration conserve mass by construction. *mser* values other than zero would indicate an error in the algorithm's implementation.

Root-Mean-Square Difference

$$rmser = \frac{\sqrt{\frac{1}{N}\sum_i \left(C_{\text{ice}}(i) - C_{\text{ice}}^{\text{ref}}(i)\right)^2}}{\max\left\{C_{\text{ice}}^{\text{ref}}(i)\right\} - \min\left\{C_{\text{ice}}^{\text{ref}}(i)\right\}} \tag{4.41}$$

Apart from the scale factor in the denominator, *rmser* is the standard deviation of the numerically calculated concentration profile from the exact concentration profile. As usual, the standard deviation weights outliers relatively heavily compared to small and medium deviations.

The *rmser* results have to be interpreted with care if the numerical solution has the same shape as the analytical one though slightly shifted. *rmser* tends to rate those numerical solutions as poor, whereas situations are conceivable where a small error in the effective sedimentation velocity is acceptable as long as the structure of the vertical profile is conserved.

Dispersion

$$dsper = 1 - \frac{\sum_i \left(C_{\text{ice}}(i)\right)^2}{\sum_i \left(C_{\text{ice}}^{\text{ref}}(i)\right)^2} \tag{4.42}$$

The idea of this dispersion test is to measure whether a sharp peak has been broadened in the numerical solution ($dsper > 0$) or whether a broad peak has become too sharp ($dsper < 0$). Note that a well-shaped peak at a wrong location would score well according to *dsper*. Moreover, even a concentration profile $C_{\text{ice}}(i)\left(p_{\text{bot}}(i) - p_{\text{top}}(i)\right)$ totally unrelated to the analytic solution could have $dsper = 0$.

Maximum Absolute Difference

$$m\Delta er = \frac{\max\left|C_{\text{ice}}(i) - C_{\text{ice}}^{\text{ref}}(i)\right|}{\max\left\{C_{\text{ice}}^{\text{ref}}(i)\right\} - \min\left\{C_{\text{ice}}^{\text{ref}}(i)\right\}} \tag{4.43}$$

$m\Delta er$ can be used as complement to *rmser*: Where *rmser* compares the full vertical profiles but rates outliers especially high, $m\Delta er$ only evaluates the maximum deviation. Therefore, if *rmser* and $m\Delta er$ both give high values, the high *rmser* has probably been caused by an outlier.

Minimum Preservation

$$mner = \frac{\min\left\{C_{\text{ice}}(i)\right\} - \min\left\{C_{\text{ice}}^{\text{ref}}(i)\right\}}{\max\left\{C_{\text{ice}}^{\text{ref}}(i)\right\} - \min\left\{C_{\text{ice}}^{\text{ref}}(i)\right\}} \tag{4.44}$$

Analogously to *pker*, *mner* compares the global minimum value of the numerical and the analytical tracer concentration profile. It does not take into account the location of the global minima. Meaningful results can be expected from *mner* if

$\min\left\{C_{\text{ice}}^{\text{ref}}(i)\right\}$ and $\min\left\{C_{\text{ice}}(i)\right\}$ refer to the same feature in the concentration profile.

Sharp Peak Test

The visual impression, that both the Walcek and the trapezoid scheme are less diffusive than the simple upwind scheme is confirmed by the peak preservation test *pker* and by the dispersion test *dsper* (table 4.1). However, the deviations in the effective sedimentation velocity in both first order schemes lead to relatively high *rmser* and $m\Delta er$ values. The root-mean-square difference as well as the maximum absolute difference rate a well-shaped peak at a wrong location as poor. In this test scenario, the mass conservation value and the minimum preservation value have little meaning.

The trapezoid scheme scores better than or equal to the Walcek scheme for all six quantitative measures. Therefore, it seems to be superior for transporting sharp peaks.

measure	**trapezoid**	Walcek	simple upwind
pker	0.407	0.636	0.875
mser	0.000	0.000	0.000
rmser	0.221	0.254	0.216
dsper	0.552	0.710	0.909
$m\Delta er$	0.714	0.935	0.875
mner	0.000000	0.000000	0.000000

Table 4.1: Quantitative measures for the sedimentation of a sharp peak

Broad Peak Test

As the Walcek scheme preserves the height of the broad peak very well, it has the lowest absolute *pker* value (table 4.2). For the trapezoid scheme, the negative *pker* reflects the drawbacks of this sedimentation scheme's ability to preserve sharp peaks: it tends to sharpen broad peaks. The same feature also leads to a negative dispersion measure *dsper*. The *dsper* value for the Walcek scheme on the other hand is very good. Apparently, this scheme is best suited for the treatment of broad peaks. *rmser* and $m\Delta er$ again point out that trapezoid sedimentation is slightly too fast and the Walcek sedimentation is slightly too slow.

Taking into account that the highest grid box was not used for the minimum preservation calculation, the *mner* value larger than zero for the simple upwind scheme means that there is ice in every grid box after the 5000 sedimentation steps. As mentioned before, with the simple upwind scheme it is not possible to completely remove sedimenting particles from a grid box.

measure	trapezoid	**Walcek**	simple upwind
pker	-0.467	0.144	0.696
mser	0.000	0.000	0.000
rmser	0.341	0.283	0.214
dsper	-0.785	0.021	0.643
$m\Delta er$	0.935	0.599	0.696
mner	0.000000	0.000000	0.000008

Table 4.2: Quantitative measures for the sedimentation of a broad peak

Double Peak Test

The above-mentioned strength of the Walcek scheme in preserving broad peak shapes seems to be connected with the weakness that it transforms the double peak structure into a broad peak. This is mainly reflected by the high maximum absolute difference $m\Delta er$ and to a lesser degree by the dispersion measure *dsper* (table 4.3). As the broad peak of the Walcek scheme coincides with the upper peak of the exact solution, *rmser* is surprisingly small. The decrease of the peak height due to the peak broadening is captured by *pker*.

The trapezoid scheme does not conserve the double peak structure either. However, the good representation of the lower peak in combination with small remains of the upper peak in the trapezoid solution leads to results for all six quantitative measures being better than or equal to the ones for the Walcek scheme.

The simple upwind scheme performs worst. Only the root-mean-square error is slightly lower than the one for the Walcek scheme as the outlier in 13.5 km height, which is slightly larger in the Walcek scheme, dominates *rmser*.

measure	**trapezoid**	Walcek	simple upwind
pker	0.003	0.449	0.795
mser	0.000	0.000	0.000
rmser	0.160	0.270	0.245
dsper	0.228	0.544	0.829
$m\Delta er$	0.571	0.959	0.808
mner	0.000000	0.000000	0.000031

Table 4.3: Quantitative measures for the sedimentation of a double peak

4.3.4 Conclusions

Both first order sedimentation schemes perform much better than the zeroth order simple upwind scheme. The above tests did not reveal a clear superiority of either the trapezoid or the Walcek scheme, so that both are included in the PSC submodel; the user can choose the preferred one via a namelist. Whereas quantitative measures for the trapezoid scheme are better for the small peak structure and for the double peak, the Walcek scheme seems to cope better with the relatively important broad peak test case.

As will be explained in chapter 6, in some PSC particle schemes the presence of ice is required for NAT formation, e. g. in Waibel et al. (1999). Therefore, the Walcek scheme's characteristic to leave some ice molecules in the grid boxes above a sedimenting peak and to propagate a few ice particles faster than this main peak requires some attention. According to Panegrossi et al. (1996), this kind of numerical diffusion could compensate the model shortcoming associated with the model assumption of monodisperse particle radii: particles of similar size fall with a uniform velocity whereas real solid PSC particles have different velocities of fall. Hence the Walcek scheme could be more useful in representing real PSC behaviour in a simulation run.

On the other hand, for testing purposes, "compensating errors" are often undesirable: if the validity of the monodisperse particle radii assumption is to be examined in a simulation, its potential drawbacks should not be blurred. For this purpose, the trapezoid scheme might be better suited, as it is stronger in completely avoiding or removing ice molecules in grid boxes apart from a peak in the vertical ice concentration profile.

It should further be noted that the above tests were based on a uniform velocity field. A more complex test situation including velocity divergence will be applied in chapter 5.

The PSC submodel's namelist also allows to use the simple upwind scheme or to avoid solid PSC particle sedimentation altogether, although those features will be needed only in rare occasions.

Chapter 5

Solid PSC Particle Modelling

5.1 Introduction

In chapter 4 the influence of the sedimentation algorithm on solid PSC particle sedimentation was shown. Two first order algorithms were presented as advancement compared to previous, more simple PSC sedimentation schemes. Now that the basic characteristics of the sedimentation schemes are known, their performance in more complex sedimentation problems can be investigated.

This chapter presents the modelling of solid PSC particle sizes and number concentrations in the ECHAM5/MESSy PSC submodel. Tests then demonstrate the combined effects of sedimentation and solid PSC particle schemes.

5.1.1 Literature

Solid PSC Particle Types

In the context of this work, the term “solid PSC particles” includes ice, NAT and ice-NAT mixtures (a more detailed PSC model could also include NAD and SAT (section 2.2). The main differences in the microphysical properties of ice and NAT particles are:

- Ice is thermodynamically stable at temperatures several Kelvin below the NAT equilibrium temperature (Hanson and Mauersberger, 1988; Marti and Mauersberger, 1993).
- The volume density of ice is normally larger than the volume density of NAT, since H_2O is much more abundant than HNO_3 (typical amount-of-substance ratio of H_2O to air: $5\,\frac{\mu\mathrm{mol}}{\mathrm{mol}}$; typical amount-of-substance ratio of HNO_3 to air: $9\,\frac{\mathrm{nmol}}{\mathrm{mol}}$).
- Ice particles reach thermodynamic equilibrium faster (within a few hours at most) than NAT particles (within several days for particles of several micrometer radius) (Peter, 1997).

Despite these differences in numerical values of growth rates and particle sizes, it is assumed that the modelling principles for radii and fall velocities are independent of the particle compositions.

Equilibrium Approach

The “traditional” way of modelling solid PSC particles is to assume thermodynamic equilibrium between the gas phase and the solid phase (Steil, 1999; Ko et al., 1999; Jackman et al., 1999; Zubov et al., 1999; Smyshlyaev et al., 1999; Grewe, 1999; Douglass and Kawa, 1999; Brasseur and Tie, 1999; Chipperfield, 1999b; Rozanov et al., 1999).

This assumption allows the calculation of volume densities for ice and/or NAT. Solid PSC particle number densities, radii and sedimentation velocities are not defined by the thermodynamic equilibrium and have been chosen differently in different models.

Volume densities resulting from the equilibrium approach are valid in the limit of long time scales, i. e. if given enough time, PSC particles grow (or shrink) until thermodynamic equilibrium is reached.

Due to their relatively large growth rate, ice particles can be expected to be described reasonably well with the equilibrium approach. NAT particles can be expected to be near thermodynamic equilibrium when both the actual NAT particle radii and the equilibrium radii derived from particle growth models are relatively small (radius $\lesssim 1\,\mu$m).

If ice/NAT particles exist, the distribution of ice or NAT between the gas phase and the solid phase in equilibrium schemes is entirely defined by the present state of the atmosphere. Hence they are well suited for Eulerian models, where knowledge of the particles’ history is not easily available. In combination with a simple method for particle number density and radius calculations, solid PSC parcticle schemes based on thermodynamic equilibrium between the gas phase and the ice/NAT phase can be implemented in computationally efficient ways.

The equilibrium approach has proven successful in simulations of dehydration, denitrification, and heterogeneous chemical reactions in the Antarctic polar stratosphere.

In the ECHAM5/MESSy PSC submodel, the calculation of ice and NAT volume densities is based on the assumption of thermodynamic equilibrium (details will be given in section 5.2).

It has to be mentioned that equilibrium approaches have been criticised in recent years for shortcomings in the modelling of large NAT particles. These have been measured by Fahey et al. (2001) in the Arctic stratosphere and named “NAT rocks” (mean radius of the large particle mode: $r_\mathrm{s} = 7.3 \cdot 10^{-6}$ m). Fahey et al. (2001) and Carslaw et al. (2002) argue that the growth of larger NAT particles requires too long to be approximated by instantaneous equilibrium. Several attempts have been made since then to reproduce these “NAT rocks” in simulations (Carslaw et al., 2002; Koike et al., 2002; Kleinböhl et al., 2003; van den Broek, 2004).

In the following, two approaches for the detailed modelling of NAT particle sizes will be presented, and the use of equilibrium models in the light of the NAT rock discovery will be discussed.

NAT Particle Growth Kinetics

Whereas the current section 5.1 generally considers both ice and NAT, the issue of growth kinetics is mainly relevant for large NAT particles.

The study of Carslaw et al. (2002) aims at realistic NAT particle radii calculations by taking into account the creation and growth history of each solid PSC particle. Several thousand individual NAT particles were simulated in a three-dimensional Lagrangian transport model.

This approach seems promising for studies that focus on cloud particles. For global climate simulations, however, it consumes too much computing time. And since many aspects of solid PSC particle formation are still not well understood, a more detailed modelling of those uncertain processes does not necessarily lead to more trustworthy results. Furthermore the development of a polar stratospheric cloud submodel for ECHAM5/MESSy is aimed at Eulerian and not at Lagrangian simulations[1].

Van den Broek (2004) addresses the problem of applying the Carslaw et al. (2002) particle growth equations in a global Eulerian model. Several, e. g. 10, NAT particle size classes in each model grid box serve as simplified representation of thousands of NAT particles with individual radii and locations. Particle growth or shrinking processes are modelled as NAT mass redistribution between the size classes within a grid box. For advection, each NAT particle class is treated as a tracer.

Whereas the charm of the Carslaw et al. (2002) approach is the absence of a priori assumptions about NAT particle number concentrations or radii, van den Broek (2004) has to prescribe C_s or r_s as an input value:

> To implement the exact calculation of the NAT properties within a Eulerian model, the advection of another model property, besides mass, would be required, e. g. the NAT number density. This would however result in a double amount of tracers, thereby dramatically decreasing the model efficiency. Furthermore, the separate transport of two quantities that are linked to each other, but are allowed to have different model gradients, will give severe numerical problems during advection. For example, a number density of NAT could exist in a model grid box while no mass of NAT is present. Therefore, we have only included the transport of NAT mass while assumptions are made regarding the particle number density per size bin [C_s] or the radius [r_s].
> (van den Broek, 2004, p. 71)

In simulations over three selected 10-day periods during the Arctic winter 1999/-2000, van den Broek (2004) shows that reasonable agreement with measurements can be achieved if the model input parameters are chosen appropriately.

---

[1] ECHAM5/MESSy includes the submodel ATTILA (Atmospheric Tracer Transport In a LAgrangian model) which allows Lagrangian trajectory studies driven by the ECHAM5/MESSy Eulerian wind fields (Traub, 2004). Detailed cloud simulations based on this tool might be worthwile.

The van den Broek (2004) approach could become the standard way of including NAT particle growth kinetics in a global Eulerian model. However, for present day climate studies there are two drawbacks.[2] Firstly the computational load associated with 10 PSC particle tracers is rather high for simulations where PSCs are not the main area of interest. Secondly, the model results are sensitive to input particle number densities or radii. Since only few measurements of these PSC properties have been performed so far, their correct setting for long term simulations is not at all clear.

If particle number densities are not defined by observations but rather set so that the model output fits measurements, van den Broek (2004) found that a simple equilibrium model, too, can reproduce observed denitrification. Therefore it seems that currently NAT particle size bin models are only superior to more simple equilibrium approaches where observations of particle number densities are available.

Furthermore, Buss (2004) found in his comparison of several NAT nucleation and growth scenarios that particle growth is very sensitive to the HNO_3 load of the surrounding air. Following this argument, a detailed representation of NAT particle sizes can hardly be achieved with amount-of-substance ratios of HNO_3 to air on the coarse grid of a global chemistry-GCM as input for the PSC submodel.

NAT Rocks

Fahey et al. (2001) and Northway et al. (2002) detected relatively large NAT particles ("NAT rocks"; mean radius of the large particle mode: $r_\mathrm{s} = 7.3 \cdot 10^{-6}\,\mathrm{m}$) in the Arctic stratosphere from January to March 2000. These measurements have attracted considerable attention, see e. g. the discussion in Newman et al. (2003).

Large NAT particles cause relatively high sedimentation fluxes leading to efficient denitrification (Fahey et al., 2001).

However, the number of "NAT rock" measurements is very limited. Although Newman et al. (2003) find that some other measurements are "not inconsistent" with Fahey et al. (2001), the frequency of large NAT particle events is unknown. In their simulation of the conditions for large NAT particle formation in the northern winters 1994/1995, 1995/1996, 1996/1997, and 1999/2000, Mann et al. (2003) found no other period as suitable for NAT rock formation as the 1999/2000 winter. Based on indirect evidence, they conclude that NAT rocks might have occurred in the Arctic winters 1988/1989 and 1989/1990. Furthermore, denitrification in the Antarctic winter stratosphere can be explained reasonably well by the sedimentation of mixed ice/NAT particles and without NAT rocks. Therefore, it seems that the capability of a PSC model to reproduce large NAT is relevant in a limited number of cases only.

It is also worth mentioning that deviations between modelled and measured solid PSC particle radii and denitrification effects are not necessarily due to the solid particle scheme. PSC model output depends critically on the input

---

[2] It should be noted that neither of these drawbacks is of fundamental nature. Future progress in computing power and measurement data availability will alleviate them.

values, e. g. on the temperatures. Kleinböhl et al. (2003), for example, conclude that an underestimation of denitrification in early winters in Sinnhuber et al. (2000) suggests that the equilibrium approach might be too simple to describe denitrification. These simulations, however, have been performed on a 5° × 7.5° horizontal grid. It is questionable whether good agreement with observations can be expected from a PSC model at such a coarse resolution.

To summarise, “NAT rocks” seem to be a rather rare phenomenon (Mann et al., 2003). Models that have been tailored to represent them have high computational demands (Carslaw et al., 2002; van den Broek, 2004). Simple equilibrium models that do not explicitly consider large NAT particles, on the other hand, can also reproduce Arctic denitrification reasonably well (van den Broek, 2004). Where PSC models are fed with synoptic input data, deviations between simulated and observed denitrification cannot necessarily be attributed to shortcomings of the particle size scheme.

5.1.2 Calculation of Sedimentation Steps

An important input value for sedimentation calculations is the sedimentation step, i. e. the pressure difference corresponding to the distance-of-fall of an ice particle whithin one model time step, Δp_{sed}.

For the range of one vertical layer, the hydrostatic equation can be used as an analytic expression connecting pressure p and geometric height as a vertical coordinate z:

$$p(z) = p_0 e^{-\frac{M_{\mathrm{air}} g z}{RT}} \tag{5.1}$$

p_0 denotes a reference pressure, M_{air} the molar mass of air, g the acceleration due to gravity, R the universal gas constant, and T the thermodynamic temperature.

Müller and Peter (1992) give an equation for the fall velocity of ice particles of radius r_s:

$$\begin{aligned} w_{\mathrm{ice}}(p) &\approx \frac{v_{\mathrm{s}}}{f_1} C(p) && (5.2) \\ &= \frac{v_{\mathrm{s}}}{f_1}\left(1 + \frac{\alpha_1 T}{p r_s} + \frac{\alpha_2 T}{p r_s} e^{-\frac{p r_s}{\alpha_3 T}}\right) && (5.3) \end{aligned}$$

where

$$v_{\mathrm{s}} \approx \frac{2 g \rho_{\mathrm{ice}} r_s^2}{9 \cdot \left(6.45 \cdot 10^{-8} \frac{\mathrm{kg}}{\mathrm{m \cdot s \cdot K}}\right) \cdot T} \tag{5.4}$$

is the Stokes fall velocity, and the numerical constants

$$\begin{aligned} \alpha_1 &= \frac{f_2}{f_1} \cdot 1.246 \cdot 0.23 \cdot 10^{-4} \, \frac{\mathrm{m \cdot Pa}}{\mathrm{K}} && (5.5) \\ \alpha_2 &= \frac{f_2}{f_1} \cdot 0.42 \cdot 0.23 \cdot 10^{-4} \, \frac{\mathrm{m \cdot Pa}}{\mathrm{K}} && (5.6) \\ \alpha_3 &= \frac{0.23 \cdot 10^{-4}}{0.87} \, \frac{\mathrm{m \cdot Pa}}{\mathrm{K}} && (5.7) \end{aligned}$$

contain correction factors for non-sphericity

$$f_1 = 1.12 \tag{5.8}$$

and

$$f_2 = 0.58248 \tag{5.9}$$

Equation (5.3) and the hydrostatic equation (5.1) lead to a separable differential equation for the pressure change that a falling particle experiences:

$$\begin{aligned}
\frac{dp}{dt} &= \frac{dp}{dz} \cdot \frac{dz}{dt} && (5.10)\\
&= \frac{M_{\mathrm{air}} g}{RT} p \cdot w_{\mathrm{ice}} && (5.11)\\
&= \frac{M_{\mathrm{air}} g}{RT} \frac{v_{\mathrm{s}}}{f_1} \left(p + \frac{\alpha_1 T}{r_s} + \frac{\alpha_2 T}{r_s} e^{-\frac{p r_s}{\alpha_3 T}} \right) && (5.12)
\end{aligned}$$

$$\Rightarrow \int_{p_0}^{p} \frac{dp'}{p' + \frac{\alpha_1 T}{r_s} + \frac{\alpha_2 T}{r_s} e^{-\frac{p' r_s}{\alpha_3 T}}} = \frac{M_{\mathrm{air}} g}{RT} \frac{v_{\mathrm{s}}}{f_1} \int_{t_0}^{t} dt' \tag{5.13}$$

The antiderivative for the argument of the integral on the left hand side of equation (5.13) is not known. Hence the pressure difference corresponding to the distance-of-fall of an ice particle whithin one model time step, Δp_{sed}, can only be calculated approximately. Assuming the time derivative of pressure (i. e. the fall velocity in pressure coordinates) constant, the sedimentation step Δp_{sed} for particles in a grid box with pressure p can be calculated by a first order approximation:

$$\begin{aligned}
\Delta p_{\mathrm{sed}} &\approx \left.\frac{dp}{dt}\right|_t \Delta t && (5.14)\\
&= \left.\left(\frac{dp}{dz} \frac{dz}{dt} \right)\right|_t \Delta t && (5.15)\\
&= -\left.\left(\frac{dp}{dz} w_{\mathrm{ice}} \right)\right|_t \Delta t && (5.16)\\
&= -\left.\left[\frac{d}{dz} \left(p_0 \, e^{-\frac{g\, M_{\mathrm{air}}\, z}{R\, T}} \right) w_{\mathrm{ice}} \right]\right|_t \Delta t && (5.17)\\
&= \left.\left(\frac{g\, M_{\mathrm{air}}}{R T} p_0 \, e^{-\frac{g\, M_{\mathrm{air}}\, z}{R\, T}} w_{\mathrm{ice}} \right)\right|_t \Delta t && (5.18)\\
&= \left.\left(\frac{g\, M_{\mathrm{air}}}{R T} p \, w_{\mathrm{ice}} \right)\right|_t \Delta t && (5.19)
\end{aligned}$$

Note that the time derivative of height, $\frac{dz}{dt}$ is negative.

5.2 Solid PSC Particle Size Scheme

5.2.1 Solid Particle Number Density

The prescribed variable value to be tested is the solid PSC particle number concentration, $C_{\mathrm{s,max}}$. As will be explained in subsection 5.2.2, if the volume density of ice/NAT is low, the actual PSC particle number concentration can become smaller than the prescribed value. Thus $C_{\mathrm{s,max}}$ constitutes an upper limit.

Whereas it is feasible to implement different $C_{\mathrm{s,max}}$ for ice and NAT, the ECHAM5/MESSy PSC submodel uses the same value independent of the composition of the solid phase (ice, NAT, or ice/NAT mixture). Currently, available observational data neither support nor contradict this approach: direct measurements of PSC particle number densities are scarce, and unambiguous particle type classifications are not always possible (see e. g. the discussion of experimental difficulties in Deshler et al. (2003)). Thus the decision of whether to use one particle number density for solid PSC particles or separate ones for ice particles and NAT particles cannot be made based on measurements. Some solid PSC particle nucleation theories (reviewed in chapter 6), however, couple ice and NAT particle formation in such a way that a single $C_{\mathrm{s,max}}$ seems reasonable: NAT forms preferably on preexisting ice particles, and ice deposits rather on solid PSC particles (if available) than on other condensation nuclei.

Observed solid PSC particle number densities are in the range $10^2\,\frac{1}{\mathrm{m}^3} \leq C_{\mathrm{s,max}} \leq 5 \cdot 10^5\,\frac{1}{\mathrm{m}^3}$ (Hofmann et al., 1989; Hofmann and Deshler, 1991; Dye et al., 1992; Voigt et al., 2000; Fahey et al., 2001; Northway et al., 2002; Deshler et al., 2003; Newman et al., 2003; Brooks et al., 2004; Larsen et al., 2004).

Hu et al. (2002) measured ice PSC particle number densities from $4 \cdot 10^6\,\frac{1}{\mathrm{m}^3}$ up to $10^7\,\frac{1}{\mathrm{m}^3}$. These high values are not considered for the current work because they are probably valid for lee wave PSCs only. As mentioned in section 3.2, PSC relevant wave activity takes place on scales that cannot be resolved in current ECHAM5/MESSy simulation runs and the PSC submodel does not aim at modelling wave PSCs. Furthermore, Hu et al. (2002) have not measured PSC particles in situ, but inferred their number concentrations from LIDAR data. Their results depend strongly on the validity of the input assumptions, e. g. that ice particles sizes can be described by a unimodal log-normal distribution.

The experience with other PSC models based on the assumption of thermodynamic equilibrium between solid phase and gas phase and incorporated in three-dimensional models seems to narrow the above given range of reasonable $C_{\mathrm{s,max}}$ values. Waibel et al. (1999) and Koike et al. (2002) found $C_{\mathrm{s,max}} = 5 \cdot 10^3\,\frac{1}{\mathrm{m}^3}$ most suitable for their studies of Arctic denitrification; Considine et al. (2000) use an ice particle number density of $C_{\mathrm{s,max}} = 10^4\,\frac{1}{\mathrm{m}^3}$.

In the following, the effects of choosing $C_{\mathrm{s,max}} = 10^3\,\frac{1}{\mathrm{m}^3}$, $C_{\mathrm{s,max}} = 5 \cdot 10^3\,\frac{1}{\mathrm{m}^3}$, or $C_{\mathrm{s,max}} = 10^4\,\frac{1}{\mathrm{m}^3}$ are compared.

5.2.2 Solid Particle Radii

For the ECHAM5/MESSy PSC submodel an equilibrium approach with one single particle radius value per grid box and time step is used (i. e. a unimodal and monodisperse particle size distribution).

With the exception of Fahey et al. (2001), PSC particle observations are usually in agreement with the assumption of a single solid particle mode. The use of monodisperse sizes, on the other hand, is an approximation; obervations rather suggest a log-normal distribution. As far as sedimentation is concerned, the artificially low diffusivity introduced by the monodisperse fall velocity distribution is probably counteracted by the high diffusivity of transport in the coarse vertical ECHAM5/MESSy grid (chapter 4). As far as the total particle surface area available for chemical reactions is concerned, simulations are currently affected by several large uncertainties (the difficulties involved in the calculation of reaction rates for heterogeneous chemical reactions on PSCs are discussed in section 9.2). As long as these persist, the calculation of heterogeneous chemical reactions would not become significantly more accurate by the explicit consideration of PSC particle size distributions. Moreover, the consideration of solid PSC particle mode parameters would introduce new uncertainties in the model, since solid PSC particle measurements by optical particle counters are affected with relatively large experimental errors.

If ice or NAT is present in a grid box, the solid phase volume density $\frac{V_\mathrm{s}}{V}$ is calculated so that the solid phase vapour pressure and the gas phase partial pressure are equal. The vapour pressure over ice is calculate according to Marti and Mauersberger (1993), the vapour pressure over NAT with the empirical equation given in Hanson and Mauersberger (1988). The Kelvin effect of increased vapour pressure over small particles can be neglected for the minimum particle radius defined at the end of this subsection (e. g. Larsen (2000, figure 3.1)).

The ice/NAT is then distributed evenly on a prescribed number of solid particles per volume, $C_\mathrm{s,max}$, which leads to the particle radius

$$r_\mathrm{s} = \sqrt[3]{\frac{3\,V_\mathrm{s}}{4\,\pi\,V\,C_\mathrm{s,max}}}. \tag{5.20}$$

For very small ice/NAT volume densities $\frac{V_\mathrm{s}}{V} \to 0$, equation (5.20) leads to $r_\mathrm{s} \to 0$. Since extremely small radii are unrealistic and a potential source of numerical problems, a lower limit $r_\mathrm{s,min}$ is introduced. Where r_s according to (5.20) would be smaller than $r_\mathrm{s,min}$, r_s is set to the minimum value $r_\mathrm{s,min}$ and the solid PSC particle number density

$$C_\mathrm{s} = \frac{4\,\pi\,V_\mathrm{s}\,r_\mathrm{s,min}^3}{3\,V} \tag{5.21}$$

is used instead of $C_\mathrm{s,max}$. Thus the minimum solid PSC particle radius $r_\mathrm{s,min}$ is the second prescribed model parameter.

Hofmann and Deshler (1991) present several bimodal fits to measured particle size distributions. According to these graphs, the minimum radius for the solid particle mode is around $r_\mathrm{s,min} = 2.0 \cdot 10^{-7}\,\mathrm{m}$. Similarly, Brooks et al. (2004) measured two distinct PSC particle modes. Their minimum radius for the large particle mode is roughly $r_\mathrm{s,min} = 10^{-7}\,\mathrm{m}$.

The above-mentioned detailed NAT simulation by Carslaw et al. (2002) used $r_\mathrm{s,min} = 2.0 \cdot 10^{-7}\,\mathrm{m}$. Mann et al. (2003) used the same model for a more extended study with $r_\mathrm{s,min} = 10^{-7}\,\mathrm{m}$. Here, $r_\mathrm{s,min} = 10^{-7}\,\mathrm{m}$ will be used.

5.3 Evaluation

5.3.1 Test Model

The focus of the current chapter is to investigate the influence of the solid PSC particles' radii on sedimentation. For this purpose a test model similar to the one described in chapter 4 is set up. It allows to concentrate on the interplay of the above examined sedimentation schemes and the particle radius calculation. Other processes influencing solid PSC particles (e. g. evaporation, condensation, advection) do not occur in this scenario.

The test model uses the same vertical grid structure as in chapter 4, i. e. vertical layers of 1 km height. Again, for the calculation of sedimentation velocities, a constant temperature $T = 190\,\mathrm{K}$ is applied.

Results based on the broad peak initial distribution (compare page 45) are presented in detail. Tests with the small peak and the double peak have been performed as well. As in chapter 4, only ice sedimentation is illustrated in figures 5.1 to 5.3. However, NAT sedimentation has been investigated, too.

An important feature of the test model is that it conserves the total mass of sedimenting solid particles. If effects of the grid structure were absent, mass conservation in combination with the constant solid PSC particle number density would lead to constant particle radii. Note that the assumption of constant ice particle number densities is part of the solid PSC particle schemes, which are tested here, and not part of the test scenario. Therefore, it is in accordance with the test model to allow non-constant particle number densities for the calculation of an exact reference solution.

The fact that a reference solution can be calculated is an important advantage of the simple test model. This reference final profile is a numerical solution of equation (5.13) and can be interpreted as Lagrangian transport calculation, as opposed to the sedimentation in the Eulerian grid, which is to be tested here. Although the reference solution has been calculated numerically, not analytically, it will sometimes be called "exact" for simplicity.

5.3.2 Qualitative Evaluation

Broad Peak Initial Profile

The sedimentation is calculated for 720 time steps of 600 s, i. e. for 5 days.

Results are shown in figures 5.1 to 5.3. The positions of the spheres in theses figures represent the amount-of-substance ratio of ice to air depending on the height. The spheres' sizes illustrates the solid particle radii calculated via equation (5.20). Exact solutions are light grey; spheres of final profiles are coloured depending on their fall velocity, which is given by equation (5.3). Note that the spheres indicating the exact solution are not restricted to grid positions.

Before the results of the sedimentation schemes can be discussed, first the deformation of the broad peak initial profile during the transport process has to be explained: as a consequence of the particle size scheme (section 5.2), vertical layers with higher number concentrations of ice molecules, C_{ice}, contain larger

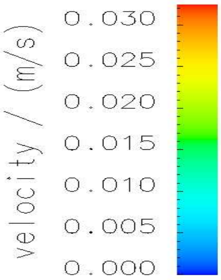

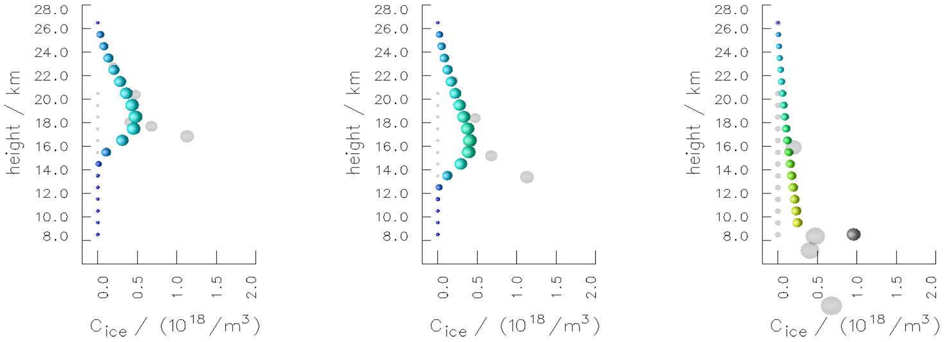

(a) $C_{\mathrm{s,max}} = 10^4 \, \frac{1}{\mathrm{m}^3}$ (b) $C_{\mathrm{s,max}} = 5 \cdot 10^3 \, \frac{1}{\mathrm{m}^3}$ (c) $C_{\mathrm{s,max}} = 10^3 \, \frac{1}{\mathrm{m}^3}$

Figure 5.1: Particle size effects for simple upwind sedimentation. Light grey spheres indicate the exact reference solution, coloured spheres the one calculated with the simple upwind scheme.

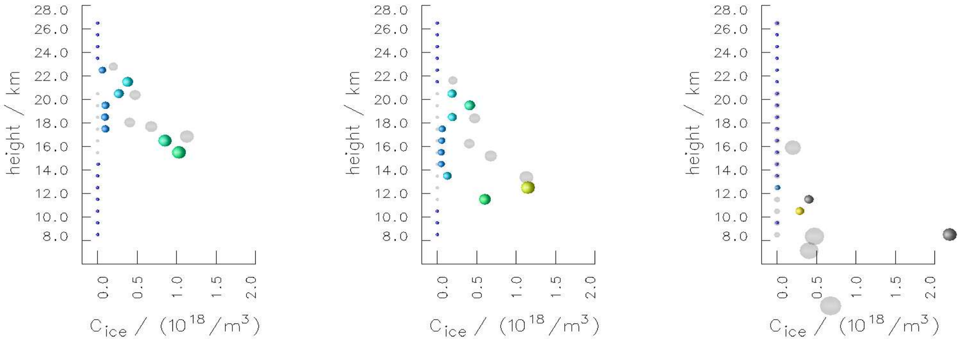

(a) $C_{\mathrm{s,max}} = 10^4 \, \frac{1}{\mathrm{m}^3}$ (b) $C_{\mathrm{s,max}} = 5 \cdot 10^3 \, \frac{1}{\mathrm{m}^3}$ (c) $C_{\mathrm{s,max}} = 10^3 \, \frac{1}{\mathrm{m}^3}$

Figure 5.2: Particle size effects for trapezoid sedimentation. Light grey spheres indicate the exact reference solution, coloured spheres the one calculated with the trapezoid scheme.

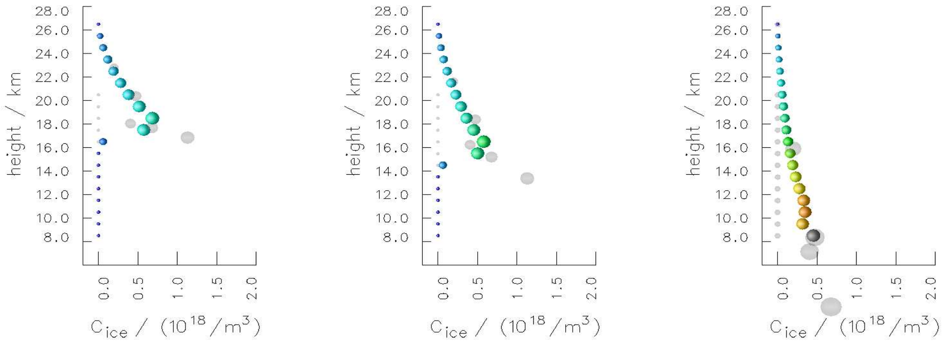

(a) $C_{\mathrm{s,max}} = 10^4 \, \frac{1}{\mathrm{m}^3}$ (b) $C_{\mathrm{s,max}} = 5 \cdot 10^3 \, \frac{1}{\mathrm{m}^3}$ (c) $C_{\mathrm{s,max}} = 10^3 \, \frac{1}{\mathrm{m}^3}$

Figure 5.3: Particle size effects for Walcek sedimentation. Light grey spheres indicate the exact reference solution, coloured spheres the one calculated with the Walcek scheme.

ice particles. If pressure effects can be neglected, larger ice particles have higher fall velocities, so that the "summit" of the broad peak inital profile started with a higher sedimentation velocity than the "tails". Since the ice particles' radii are conserved in the reference sedimentation process, the initially faster particles maintain a higher fall velocity and can even "overtake" slower ones. Given the discussion in subsection 4.1.2, it is of great interest how the three sedimentation schemes can deal with the convergent velocities below the "summit" of the broad peak and the divergent velocities above it.

Sedimentation results calculated by means of the simple upwind scheme are shown in figure 5.1. A slight steepening of the profiles for $C_{\mathrm{s,max}} = 10^4 \, \frac{1}{\mathrm{m}^3}$ and $C_{\mathrm{s,max}} = 5 \cdot 10^3 \, \frac{1}{\mathrm{m}^3}$ can be attributed to the above-mentioned properties of the velocity field, as it did not occur in the tests of chapter 4, which used uniform velocity fields. However, the simple upwind scheme does not reproduce the separation of the reference peak into two peaks for $C_{\mathrm{s,max}} = 5 \cdot 10^3 \, \frac{1}{\mathrm{m}^3}$. Furthermore, the high numerical diffusion of the simple upwind scheme broadens and flattens the vertical profile.

For the lowest ice particle number density $C_{\mathrm{s,max}} = 10^3 \, \frac{1}{\mathrm{m}^3}$, which corresponds to the largest particle radii, the simple upwind scheme as well as the other two sedimentation schemes transport most of the particles into the lowest grid box, where the ice mass is collected in the test model. This behaviour is in accordance with the exact solution; however, it will be concluded below that this effective sedimentation velocity is too high for PSC sedimentation.

Trapezoid scheme results are illustrated in figure 5.2. The most noticeable feature is this scheme's capability to reproduce the separation of the initial broad peak into two peaks. Thus the effort to find an algorithm that can deal with divergent velocity fields has been successful. However, for $C_{\mathrm{s,max}} = 5 \cdot 10^3 \, \frac{1}{\mathrm{m}^3}$ the movement of the faster peak is too fast in the trapezoid scheme result compared to the exact solution. If the trapezoid method is to be used to calculate PSC sedimentation, the ice particle number density $C_{\mathrm{s,max}} = 10^4\,\frac{1}{\mathrm{m}^3}$ should be used.

The Walcek advection scheme on the other hand includes flux limiters inconsistent with divergent velocity fields (subsection 4.2.3). Therefore, in figure 5.3 the splitting up of the broad peak cannot be reproduced. Like the simple upwind scheme, the Walcek scheme only calculates a steepening of the initial profile.

Quantitative Evaluation?

In chapter 4 the qualitative comparison of the three sedimentation schemes is supported by means of six quantitative performance measures. An application of these quantitative measures to the mixed sedimentation/particle size test of the current chapter is possible, but less helpful.

Whereas in the figures 5.1, 5.2, and 5.3 the spheres corresponding to the exact solution have been positioned independent of the vertical grid, the application of the qualitative measures requires the redistribution of the transported ice into the vertical grid structure.

Depending on the final position of a sphere of the exact solution in relation to the grid, ice particles which started in the same vertical layer end up in one single vertical layer or in two different vertical layers. In the first case, the initial peak hight, i. e. the number concentration of ice molecules, is preserved, in the latter case the peak hight is reduced.

This has important consequences for the comparison with the sedimentation scheme results. In figure 5.2(b), for example, it can be seen that the trapezoid scheme preserves the maximum grid height rather well. If the maximum peak of the exact solution would now be reduced by distribution into two vertical layers, the trapezoid scheme maximum C_{ice} would misleadingly seem to be too high.

The final position of exactly sedimented ice particles and thus their redistribution over the vertical grid depends on the duration of the sedimentation test. Therefore, in the current test model the quantitative measure results strongly depend on the total simulation time and were felt to give little insight into the sedimentation schemes' performances. Hence they are not listed here.

Small Peak and Double Peak Initial Profile

For the small peak profile the initial velocity field is not divergent; for the double peak initial profile the divergence is small. Therefore, results of combined sedimentation scheme/solid particle size scheme tests are rather similar to the pure sedimentation scheme test results presented in chapter 4.

The small peak distribution is best preserved by the trapezoid scheme, whereas the Walcek and the simple upwind scheme are more affected by numerical diffusion. None of the three sedimentation schemes can preserve the double peak structure satisfyingly.

For $C_{\mathrm{s,max}} = 5 \cdot 10^e\,\frac{1}{\mathrm{m}^3}$ the trapezoid scheme transports particles too fast, so that this method is probably better used with the setting $C_{\mathrm{s,max}} = 10^4\,\frac{1}{\mathrm{m}^3}$. The effective sedimentation velocity of the Walcek scheme and the sedimentation scheme is less well defined due to the broadening of the initial structure.

Tests with NAT

In the discussion of subsection 5.1.1 it was mentioned that equilibrium schemes with simplified particle size calculations cannot be expected to reproduce effective denitrification due to large NAT particles.

To test this for the solid PSC particle size model in this work, the test model of subsection 5.3.1 has been modified for simulations of pure NAT sedimentation. To account for the lower amount-of-substance ratios of HNO_3 compared to H_2O, the molecule number concentrations in the initial profiles have been reduced by factors of 500 to 1000 compared to the initial vertical distributions of ice molecules shown in figure 4.12. Furthermore, for the calculation of NAT particle radii, now the mass density of NAT ($\rho_{\mathrm{NAT}} = 1620\,\frac{\mathrm{kg}}{\mathrm{m}^3}$, Drdla et al. (1993)) has been used instead of the mass density of ice.

The results of these NAT tests are as expected: the NAT test scenario lead to much smaller particle radii with typical values between $0.5\,\mu$m and $1\,\mu$m. As a consequence, sedimentation velocities are too small for efficient denitrification. Hence strong denitrification can only be achieved by sedimentation of mixed ice/NAT particles.

Observational data

The above discussion of the figures 5.1, 5.2, and 5.3 has mainly concentrated on the comparison of the sedimentation schemes' results with the exact reference profiles. Now the experience with the performance of the sedimentation schemes in the test model has to be transferred to more realistic atmospheric situations.

The physical quantities of interest in this chapter are the radii of solid PSC particles and their velocities of fall. Unfortunately, measurements for these two PSC particle properties are scarce.

Early measurements of size distributions were restricted to radii less than $2\cdot10^{-6}$ m (Hofmann et al., 1989). This instrument limitation has been overcome in later observations (Hofmann and Deshler, 1991; Dye et al., 1992; Adriani et al., 1995; Fahey et al., 2001; Northway et al., 2002; Deshler et al., 2003; Brooks et al., 2004; Larsen et al., 2004). See Newman et al. (2003) for a summary. However, each of these airborne in situ measurements refers to specific PSC events only, and given the rather large variability of their results they probably do not provide comprehensive statistics. Hence they only mark a range of typical radii ($10^{-6}\,\mathrm{m} \lesssim r_{\mathrm{s}} \lesssim 10^{-5}\,\mathrm{m}$). The radii simulated in the test model are consistent with this measured radius range for all three solid particle number density values.

PSC particle radii derived from LIDAR measurements of wave PSCs (Hu et al., 2002) are not considered here, as the ECHAM5/MESSy PSC submodel is mainly developed for the simulation of synoptic PSCs.

For solid PSC particle sedimentation velocities there are even less comparative data available, as there are no direct measurements of this quantity.

Indirect information can be gained from the resulting denitrification effect. Tabazadeh et al. (2000) conclude that PSC particles over Antarctica fell about 4 km in 5 to 8 days in June 1992. These conclusion refers to a meteorological situation where solid PSC particles can be expected to be smaller than typical ice particles in Antarcic winters before the onset of dehydration. Therefore it seems reasonable that the sedimentation velocity derived in Tabazadeh et al. (2000) is smaller than the peak maximum movement in figures 5.1(a), 5.1(b), 5.2(a), 5.2(b), 5.3(a), and 5.3(b).

Sedimentation for the number density $C_{\mathrm{s,max}} = 10^3\,\frac{1}{\mathrm{m}^3}$, however, is probably much too strong. It was mentioned in section 2.3 that the denitrified and dehydrated vertical column in the Antarctic polar stratosphere in early spring is typically of the order of 10 km. If the solid PSC particle number density in the ECHAM5/MESSy PSC submodel was set to $C_{\mathrm{s,max}} = 10^3\,\frac{1}{\mathrm{m}^3}$, this degree of dehydration could already be reached within 5 days.

Fortunately, this uncertainty about the best choice of solid PSC particle number densities and, as a consequence, radii and sedimentation velocities might not necessarily result in large uncertainties in modelled denitrification. In their detailed denitrification study, Jensen et al. (2002) find that HNO_3 depletion depends only moderately sensitive on cloud particle number densities in the intervall $10^3\,\frac{1}{\mathrm{m}^3} \lesssim C_{\mathrm{s,max}} \lesssim 10^4\,\frac{1}{\mathrm{m}^3}$.

5.3.3 Conclusions

From the discussion in section 5.1 it can be concluded that a thermodynamic equilibrium approach with monodisperse but variable particle sizes is adequate for the solid PSC particle calculation in ECHAM5/MESSy.

This solid PSC particle model is computationally efficient and suitable for Eulerian models. If the prescribed parameters $C_{\mathrm{s,max}}$ (maximum solid particle number density) and $r_{\mathrm{s,min}}$ are set to values within the observed ranges for solid PSC particle number densities and minimum radii, the resulting solid PSC particle radii as well as dehydration and denitrification effects also agree reasonably well with observations.

The trapezoid sedimentation is superior to the simple upwind scheme due to its lower numerical diffusion and more suitable for divergent (or convergent) velocity fields than the Walcek advection algorithm. If the trapezoid scheme is used for sedimentation calculation, the particle number density $C_{\mathrm{s,max}} = 10^4\,\frac{1}{\mathrm{m}^3}$ can be recommended.

A known shortcoming of the solid PSC particle size modelling approach for ECHAM5/MESSy is its inability to simulate NAT rocks. This deficiency seems acceptable for a global chemistry-climate model since NAT rocks are probably a rather rare phenomenon.

However, the argumentation in sections 5.1 and 5.2 strongly depends on the facts that the synoptic input data for the PSC submodel introduces large uncertainties into the modelling of PSCs and that synoptic observations of PSC particle number densities and radii hardly exist. Given these large uncertainties, reasonable results of denitrification, dehydration, and surface area densities (for heterogeneous chemistry) can be achieved with a relatively simple model.

Due to improvements in model resolution, observational data and knowledge about PSC microphysics, future PSC modellers may choose to move on to more sophisticated solid PSC particle size schemes, especially for case studies in which PSCs play a central role.

Chapter 6

PSC Simulations and Evaluation

6.1 Introduction

The modelling of solid PSC particle radii and number densities has been discussed extensively in the previous chapter. The present chapter addresses the question of how solid PSC particles come into existence. First a review of literature on PSC formation will be given in subsection 6.1.1. Section 6.2 explains how different PSC particle formation approaches have been incorporated in the ECHAM5/MESSy PSC submodel. Section 6.3 is dedicated to simulations and observations of PSC occurrence, i.e. the combined effects of PSC particle formation, growth (chapter 5), and sedimentation (chapter 4).

6.1.1 Literature

Relevant PSC Particle Types

It has already been explained that ice[1] and NAT are the dominant forms of the solid PSC phase (section 2.2); the relevance of other particle types is unclear. If the PSC effects like denitrification and heterogeneous chemical processing are in the focus of interest, it seems to be sufficient to model ice and NAT only.

As NAD grows much more slowly than NAT (Jensen et al., 2002), NAD can be expected to be of little importance in the presence of NAT particles. NAD occurrence in the absence of NAT, on the other hand, seems not to be a widespread phenomenon; in the homogeneous freezing scenarios discussed in Drdla and Browell (2004) and also in the study of Salcedo et al. (2001), NAD appears mainly as a transition state for NAT formation. Furthermore, “pure NAD” causes by far less denitrification than NAT particles (Jensen et al., 2002). In addition, given the very limited knowledge about reaction rates for heterogeneous chemical reactions on NAD (Sander et al., 2003), currently modelling of

---

[1] In this thesis, “ice” always refers to solid phase H_2O, possibly with some impurities like H_2SO_4 or HNO_3 molecules. Crystalline hydrates like sulphuric acid tetrahydrate and nitric acid trihydrate are not regarded as ice.

polar chemistry cannot be expected to be improved by considering NAD/NAT differences.

Similar arguments apply to SAT: according to Fortin et al. (2003), SAT probably plays only a minor role in PSC formation. Moreover, if it was included in a PSC model, it would introduce rather large uncertainties, so that any model improvement would be fortuitous. Consequently, the PSC submodel for ECHAM5/MESSy considers only ice and NAT as solid PSC particle components.

The detailed representation of NAD and SAT, of course, is relevant for model studies that focus on PSCs themselves rather than on the PSC effects. Examples can be found in Tabazadeh et al. (2001) or Carslaw et al. (2002), where NAD plays an important role, and in the PSC model of Larsen (2000), which also considers SAT. Note that these detailed PSC studies, in turn, are the basis for PSC effect studies within a climate context.

Ice Formation

Whereas the processes leading to NAT particle formation are still unclear (see discussion below), the freezing of ice particles from liquid aerosol particles seems rather straightforward.

It is widely accepted that ice particle nucleation in the polar stratosphere requires a supercooling ΔT_{ice} of a few K below the ice frost point (Fortin et al., 2003). Alternatively, the ice formation barrier can be expressed in terms of a supersaturation: whereas in thermodynamic equilibrium the water vapour pressure over ice equals the partial pressure of H_2O in air, for initialising ice particle nucleation the H_2O partial pressure has to exceed the temperature dependent equilibrium water vapour pressure over ice by a factor of $S_{\mathrm{H_2O}}$.

Based on experimental data from Bertram et al. (1996) and classical nucleation theory, Tabazadeh et al. (1997) found that a supersaturation $S_{\mathrm{H_2O}} = 1.35$ or correspondingly a supercooling of 2 K leads to ice PSC particles (these numbers are cited here as approximate values; in fact, Tabazadeh et al. (1997) present a functional dependence of ΔT_{ice} and $S_{\mathrm{H_2O}}$ on the ice frost point temperature).

Koop et al. (1998) applied the same theoretical framework to their experimental data and found a higher ice particle nucleation barrier. As supersaturation necessary for ice PSC particle formation they give $S_{\mathrm{H_2O}} = 1.65$, which corresponds to a supercooling $\Delta T_{\mathrm{ice}} = 3\,\mathrm{K}$.

Further suggestions for parameterising ice particle formation can be found in descriptions of other PSC models. Considine et al. (2000) use a $S_{\mathrm{H_2O}} = 1.4$ as critical value; Larsen (2000, 2002) uses a supersaturation ratio of $S_{\mathrm{H_2O}} \approx 1.62$ (average value for the relevant temperature range) as particle formation requirement.

The theoretical considerations in Koop et al. (2000) explain the $S_{\mathrm{H_2O}}$ uncertainty at least partially: the required supersaturation depends on the radius of the freezing aerosol droplets and on the duration of the freezing process. For example, to freeze about two thirds of liquid aerosol particles of radius $r_{\mathrm{SSA}} = 10^{-7}\,\mathrm{m}$ within one minute, a supersaturation of $S_{\mathrm{H_2O}} = 1.67$ is required. Lower supersaturation limits can be justified if more time is allowed for ice particle nucleation, e. g. the ECHAM5/MESSy model time step length ($\Delta t = 10\,\mathrm{min}$ for the simulation runs presented in this thesis).

Fortin et al. (2003) show that the presence of SAT reduces the supersaturation/supercooling required for ice formation. However, they also conclude that background sulfate aerosols often remain liquid down to very low temperatures. It seems that SAT particles do not play a major role as ice particle nuclei and hence do not influence the supercooling or supersaturation threshold for ice formation.

NAT formation on ice

For the formation of polar stratospheric cloud particles composed of nitric acid trihydrate (NAT), several pathways are discussed in the literature.

Based on their experiments with supercooled $H_2SO_4/HNO_3/H_2O$ solutions, Koop et al. (1995) first suggested that ice PSCs might provide suitable nuclei for NAT formation. Homogeneous NAT formation and heterogeneous freezing on various types of dust particles was ruled out by their experiments.

An extended and refined set of experiments (Koop et al., 1997) confirmed that homogeneous nucleation of STS is not a relevant pathway for NAT formation at temperatures above the ice frost point. Only for H_2SO_4 mass fractions as low as $10^{-4}\,\frac{\mathrm{kg}}{\mathrm{kg}}$, nucleation rates for homogeneous nucleation are sufficiently high to explain observed NAT occurrences. Heterogeneous NAT nucleation on ice, however, was again found to be an effective process for NAT freezing.

Whereas Koop et al. (1995) and Koop et al. (1997) investigated bulk solutions, Anthony et al. (1997) made laboratory experiments with free-floating aerosols with compositions and sizes representative of stratospheric particles. These led to similar conclusions: in the temperature range from 188 K to 195 K, no homogeneous freezing was observed within the experiments of several hours duration.

Based on the findings of Koop et al. (1995, 1997), Waibel et al. (1999) performed a model study of denitrification in the Arctic winter 1994/1995. They showed that a NAT formation mechanism where nitric acid trihydrate does not nucleate homogeneously but only on preexisting ice or NAT particles is a reasonable parameterisation for a synoptic scale model.

In his study of several approaches for NAT particle modelling, Buss (2004) confirmes that the “NAT on ice” formation mechanism performs at least not worse than others. This conclusion is based on comparisons with airborne measurements for the Arctic winter 1999/2000.

Homogeneous NAT nucleation

Although it is widely accepted that NAT can form on ice, there is some evidence that other nucleation mechanisms are also relevant.

Tabazadeh et al. (2000) used Lagrangian trajectory studies to show that in the Antarctic winter 1992 denitrification occurred in air parcels that had not encountered temperatures below the ice frost point before. Thus NAT must have been formed via pathways other than exposure to ice surfaces. Since the air parcels that finally experienced denitrification due to NAT sedimentation did encounter temperatures below the NAT equilibrium temperature for several days, Tabazadeh et al. (2000) conclude that NAT particles can nucleate homogeneously within this period of time, even if nucleation rates are rather small. They suggest to include denitrification in large-scale models by creating NAT particles after 7 days below the NAT equilibrium temperature.

Experimental results of Salcedo et al. (2001) support this idea. Salcedo et al. (2001) investigated homogeneous freezing of NAT from H_2O/HNO_3 and found that NAT can come to existence either via heterogeneous nucleation on ice or via homogeneous nucleation if temperatures remain between the NAT equilibrium temperature and the ice frost point for more than one day.

Unfortunately the 7-day-criterion cannot easily be applied in Eulerian models like ECHAM5/MESSy, where temperatures are known for fixed grid points but not for moving air parcels.

Furthermore, the analysis of four years of POAM satellite data by Steele et al. (2002) casts doubt on the NAT nucleation scheme suggested by Tabazadeh et al. (2000). A depencence of PSC sightings on the time that the respective air parcels previously spent below the NAT condensation temperature was not found. And the experimental findings of Salcedo et al. (2001) are probably of limited relevance in the polar stratosphere, as they do not apply to solutions containing H_2SO_4. As mentioned above, Koop et al. (1997) found that H_2SO_4 mass fractions as low as $10^{-4}\,\frac{\mathrm{kg}}{\mathrm{kg}}$ prevent homogeneous nucleation of aqueous solutions.

NAT Nucleation Parameterised as Homogeneous

The Tabazadeh et al. (2000) argument against heterogeneous NAT nucleation on ice as the dominant pathway for NAT formation strongly depends on the evaluation of National Center for Environmental Prediction (NCEP) temperature fields.

Similarly, Drdla et al. (2003) use UK Meteorological Office synoptic temperature, reaching the conclusion that only a NAT freezing process above the ice frost point can explain the observed denitrification in the 1999/2000 Arctic winter. The same applies to Drdla and Browell (2004), who argue that this additional NAT formation pathway at $T \approx T_{\mathrm{NAT}} - 3\mathrm{K}$ is heterogeneous nucleation on a hitherto unknown substratum.

However, Fueglistaler et al. (2003) and Buss (2004) demonstrate that small scale temperature fluctuations caused by atmospheric wave activity are not resolved in synoptic temperature fields. The short term existence of ice particles in local temperature minima cannot be ruled out whenever synoptic analysis temperatures are slightly above T_{ice}. In accordance with the possibility of small scale ice clouds that triggered NAT formation, some observations of minor dehydration coincide with the denitrification events in Tabazadeh et al. (2000).

Therefore, despite the results of Tabazadeh et al. (2000), Drdla et al. (2003), and Drdla and Browell (2004), the evidence against heterogeneous nucleation of NAT on ice as only relevant pathway for the formation of NAT PSCs is not yet conclusive.

The dispute on NAT formation cannot be resolved at the current state of knowledge about polar stratospheric clouds. Luckily, modelling PSC particle occurrence in a chemistry-GCM is possible without consideration of all microphysical details. In summary, the above cited studies indicate that global models should allow NAT to form at $T_{\mathrm{NAT}} \geq T > T_{\mathrm{ice}}$. Consequently, a parameterisation that couples NAT formation technically to the NAT equilibrium temperature can be implemented independently of whether NAT nucleation is a homogeneous or a heterogeneous process.

For example, Steil (1999) allowed NAT to form at temperatures 3 K below the NAT equilibrium temperature, while Steil et al. (2003) modelled NAT formation immediately at T_{NAT}, without any nucleation barrier in their PSC model for MA-ECHAM4.

Freezing Belt

Tabazadeh et al. (2001) investigated the precise temperature requirements for homogeneous NAT nucleation in the Antarctic winter 1992 and in the Arctic winters 1994/1995 and 1999/2000.

They claim that nucleation rates for homogeneous NAT (or NAD) nucleation are sufficiently high to explain observed NAT particle number densities within a temperature range of approximately 2 K (the "freezing belt"). However, Knopf et al. (2002) argue that the nucleation rate estimates of Tabazadeh et al. (2001), based on linear extrapolations of laboratory data, are erroneous. Based on their own nucleation rate calculations, Knopf et al. (2002) conclude that homogeneous nucleation of NAT from STS alone would not lead to the observed polar denitrification.

Furthermore, especially for the Arctic polar stratosphere with its strong wave activity, it is highly unlikely that temperatures in the environment of a liquid aerosol droplet stay whithin a small interval around approximately 190 K for several days. The temperature averaging effect of large grid boxes in a global model could be misleading in this respect.

Surface Nucleation

Tabazadeh et al. (2002) introduce the idea of surface nucleation (also called "pseudo-heterogeneous nucleation") of supercooled ternary solutions. They suggest that homogeneous nucleation of NAT from liquid aerosols is not a volume dependent process but rather a function of the aerosol particle's surface area.

In that case, the findings of Koop et al. (1995, 1997), which made homogeneous nucleation seem unlikely, would not be applicable, as they are based on experiments with bulk solutions, where surface effects play a much smaller role than in small aerosol droplets.

The surface nucleation approach was included in a thorough comparison of different theories for homogeneous NAT nucleation by Drdla and Browell (2004). Like the other homogeneous nucleation approaches, it was not capable of explaining observed PSCs in the 1999–2000 Arctic winter.

6.2 Solid PSC Particle Formation Schemes

This section first explains how ice PSCs come to existence according to the ECHAM5/MESSy PSC submodel (subsection 6.2.1), then three alternative NAT formation schemes are presented (subsections 6.2.2, 6.2.3, and 6.2.4), and finally the coexistence of NAT and STS in the model is discussed (subsection 6.2.5).

6.2.1 Ice Formation

For the current work, a supersaturation criterion for ice formation of $S_{\mathrm{H_2O}} = 1.5$ is applied; this choice is in the middle of the range of supersaturation thresholds found in the above discussed literature. Water vapour pressure over ice is calculated according to Marti and Mauersberger (1993).

If NAT is present in a grid box, ice can form without supersaturation, i. e. at $S_{\mathrm{H_2O}} = 1$. Thus the choice of a NAT formation scheme has some feedback on ice formation. Note that SAT as possible nucleation site for ice has not been considered.

6.2.2 NAT on Ice

Following the literature survey, heterogeneous NAT nucleation on ice is implemented in the PSC submodel for ECHAM5/MESSy.

For each grid box in the polar stratosphere the information of whether solid PSC particles are present is saved each model time step. In the following model time step, ice and NAT can form without barrier if solid phase PSCs already existed in the previous time step. Otherwise, NAT cannot come to existence and ice formation requires a supersaturation of $S_{\mathrm{H_2O}} = 1.5$ as mentioned above.

If ice exists, solid PSC particles consist of an ice/NAT mixture. If temperatures increase above the ice frost point but remain below the NAT equilibrium temperature, solid PSC particles are pure NAT. On further temperature increase, NAT evaporates immediately, without the requirement of subsaturation.

6.2.3 Advection Influence

The heterogeneous NAT formation process described in the subsection 6.2.2 depends on the presence of solid PSC particles in a certain grid box in the previous time step. However, ice and NAT transport processes are not taken into account, i. e. the formation barriers for ice or NAT cannot be circumvented by ice or NAT which comes into a grid box via advection or sedimentation.

Whether transported ice and NAT should be considered in solid PSC particle formation modelling is disputable. On the one hand, there is no physical difference between ice (NAT) that has been formed in a grid box and ice (NAT) that has been transported into it. On the other hand, for typical Courant numbers of much less than one, transported ice (NAT) occupies only a small portion of a grid box and may be neglected.

Moreover, ice and especially NAT advection suffers from the general difficulties of advection schemes in dealing with strong gradients in the distribution of tracers. Amount-of-substance ratios of ice (NAT) to air often have relatively high values in grid boxes with low temperatures whereas neigbouring grid boxes with higher temperatures contain no ice (NAT) at all.

Solid PSC particle formation influenced by transport processes has been implemented as alternative to the “NAT on ice” scheme described in subsection 6.1.1.

6.2.4 Temperature Barrier

As was explained in subsection 6.1.1, several studies indicate that global scale models should consider homogeneous NAT nucleation above the ice formation threshold as pathway for NAT formation.

In the PSC submodel for ECHAM5/MESSy, this process can be switched on via the namelist, in addition to NAT nucleation on ice. It has to be stressed that this “temperature barrier” scheme is a parameterisation. No statement is made about whether the additional NAT formation pathway accounts for homogeneous NAT nucleation, surface nucleation, heterogeneous NAT nucleation on particles other than ice, or heterogeneous nucleation on ice which formed in sub-synoptic temperature minima.

If desired, the submodel user can define a temperature criterion as nucleation barrier. For example, NAT nucleation in the absence of ice can be allowed for temperatures $T \approx T_{\mathrm{NAT}} - 3\,\mathrm{K}$.

6.2.5 NAT versus STS

The equilibrium based determination of solid PSC particle radii as described in chapter 5 concentrates on the distribution of HNO_3 between the gas phase and the NAT phase. However, liquid aerosol particles can also take up large amounts of HNO_3. Therefore, the available HNO_3 has to be distributed into three phases.

Simultaneous measurements of both NAT and STS coexisting in polar stratospheric clouds have been performed by Brooks et al. (2004). Unfortunately, these kinds of observations are sporadic and do not give a complete picture of the HNO_3 distribution in the NAT/STS/gas system. Hence the HNO_3 distribution scheme for the ECHAM5/MESSy PSC submodel is based on theoretical considerations.

Waibel (1997) compares HNO_3 vapour pressures over NAT (Hanson and Mauersberger, 1988) and STS (Carslaw et al., 1995b) in the relevant temperature range. He concludes that the HNO_3 uptake in NAT dominates over the HNO_3 uptake in liquid aerosols because of the larger HNO_3 vapour pressure over STS.

As solid particle modelling in the current work is based on the thermodynamic equilibrium approach, it seems consistent to follow the argumentation of Waibel (1997). Hence in each model time step the formation of NAT is calculated taking all HNO_3 molecules into account. Afterwards, only non-NAT HNO_3 is partitioned between liquid aerosol particles and gas phase.

Laboratory results of Koop et al. (1997) support this approach insofar as they indicate that NAT formation (on ice surfaces) preferably takes place from HNO_3 rich solutions. Therefore, if atmospheric conditions allow NAT nucleation, liquid aerosol particles can be expected not to contain large amounts of HNO_3 because otherwise they would turn into NAT.

Compared to kinetic models where HNO_3 is slowly released from liquid aerosols during NAT growth, the above mechanism, where HNO_3 is quickly and completely available for NAT formation, probably overestimates NAT compared to STS. According to Borrmann et al. (1997) and Del Negro et al. (1997), reaction rates are larger for chlorine activation on STS than for chlorine activation on NAT. However, this does not necessarily lead to an underestimation of chlorine activation because even the slower reactions on NAT are probably fast enough to enable a nearly complete chlorine activation.

6.3 Evaluation

6.3.1 Test Model

The modelling of PSC particle formation and evaporation is tested in simulations of an Antarctic winter.

As it is highly uncertain how NAT formation is best incorporated in chemistry-GCMs (subsection 6.1.1), all three NAT schemes listed in section 6.2 ("NAT on ice", "advection influence", "temperature barrier") are applied in simulation runs under similar conditions. Thus the performance of the three schemes can be compared. For the "temperature barrier scheme" (subsection 6.2.4) the threshold for NAT formation is set to $T_{\mathrm{NAT}} - 3\,\mathrm{K}$.

Subsequently, these three simulation runs are repeated with a modified temperature: (only) within the PSC submodel, all calculations use temperatures that are 4 K higher than the respective ECHAM5/MESSy temperatures. This sensitivity study is motivated by the analysis of ECHAM5/MESSy temperatures in chapter 7, which leads to the conclusion that the model temperatures in the Antarctic polar stratosphere are too low by several degrees.

All six simulation runs use a horizontal resolution of $1.85^\circ \times 1.85^\circ$ (T63) and the vertical resolution of the 39 level middle atmosphere version of ECHAM4 (section 3.2). By means of nudging (section 3.4), the ECHAM5/MESSy model meteorology reproduces the Antarctic winter 2003. The simulation starts at 1 May 2003 and ends at 31 October 2003.

The PSC relevant variables are stored with an output intervall of 8 h (relating to simulated time, not to computing time).

H_2O is initialised with bimonthly and zonal mean climatological values derived from HALOE measurements (C. Brühl, pers. comm., 2004). HNO_3 is initialised with ECHAM4 model output from a KODYACS project simulation run (Dameris, 2004; Hassler et al., 2004; Steil et al., 2004; Steinbrecht et al., 2004). The HNO_3 distribution of 1 May 1998 from the transient 40-year KODYACS run was chosen because it is rather typical, i. e. free from extraordinary features, and because the simulated QBO (quasi-biennial oscillation) phase for this data set corresponds to the QBO phase of 1 May 2003 (C. Brühl, pers. comm., 2004).

To save computing time, no chemical reactions are calculated in the six simulation runs described above. Stratospheric H_2O and HNO_3 are only affected by advection, by phase transitions, and by sedimentation of solid PSC particles. An exeption is the H_2O production via photolysis of CH_4. Here the H2O submodel models the chemical source for stratospheric H_2O based on climatological CH_4 values (section 3.3).

One of the simulations ("NAT on ice" scheme, no temperature shift) is repeated with full stratospheric chemistry. Thus the model shortcoming associated with the absence of chemical reactions in the other six simulation runs can be estimated (more information about stratospheric chemistry can be found in section 2.4 and chapter 9; the list of simulated chemical reactions is given in appendix C).

6.3.2 Measurement data

In the introductory section 2.5 and in the evaluation of modelled PSC radii (section 5.3) it was mentioned that the evaluation of PSC submodels is hampered by a lack of long-term observations. Several attempts have been made to relieve this problem as far as PSC occurrence is concerned.

Poole and Pitts (1994) produced a PSC occurrence dataset from 1978 to 1989 based on SAM II satellite measurements. However, SAM II is a solar occultation experiment and cannot observe PSCs in the polar night. Furthermore, the Poole and Pitts (1994) dataset does not distinguish different PSC types.

Foschi and Pagan (2002) suggest a method to calculate an ice PSC climatology from advanced very high resolution radiometer (AVHRR) data. AVHRR is an operational weather sensor on board of the TIROS-N/NOAA series of polar-orbiting satellites. The idea seems very promising as AVHRR instruments do not depend on the presence of sunlight and have been operational since 1981.

Currently, the probably best long-term PSC occurrence database is the one presented in Fromm et al. (2003). It contains combined analysis results of data from the satellite instruments SAM II, SAGE II, POAM II and POAM III and reaches back to the year 1978. However, none of the four measuring instruments can probe the polar night so that many important PSC episodes are excluded from observations.

The evaluation of simulation results in this work is based on a comparison with PSC occurrence data derived from MIPAS infrared spectra (Höpfner et al. (2004) and pers. comm., 2004, 2005). The MIPAS analysis data set consists of 110832 observations from 14 May 2003 to 04 October 2003. For the current purpose, those 55731 observations were extracted that fall within the area where the ECHAM5/MESSy PSC submodel is active: south of 55° S and from 180 hPa to 15 hPa (section 3.3). Within these ranges, the analysis of MIPAS infrared spectra revealed the presence of ice 3146 times, 7652 times NAT, 12903 times STS, and 32030 times the absence of polar stratospheric clouds.

The outstanding advantage and value of this MIPAS analysis is that it is not limited to sunlight conditions. To our knowledge, it is currently the most comprehensive observational data set of PSC occurrence in an Antarctic winter.

The presence of polar stratospheric clouds can be detected in MIPAS infrared spectra if the volume density of PSC particles exceeds $0.3 \cdot 10^{-12}\,\frac{\mathrm{m}^3}{\mathrm{m}^3}$ to $0.4 \cdot 10^{-12}\,\frac{\mathrm{m}^3}{\mathrm{m}^3}$ (M. Höpfner, pers. comm., 2004). The classification of polar stratospheric cloud particles as STS, NAT, or ice is reliable for ice. Mixed NAT/STS clouds are interpreted as NAT or STS, depending on the dominant aerosol particle type; large NAT particles (radii from $2\,\mu$m to $3\,\mu$m), however, can sometimes be confused with STS. (M. Höpfner, pers. comm., 2005).

6.3.3 Qualitative Evaluation

A first impression of the simulation results can be gained from a visual comparison of plotted MIPAS analysis and simulation data. For this purpose, MIPAS measurements taken within 24 h are to be compared to a single simulation data output event.

The data to be shown has been chosen according to the following criteria:

1. To limit the number of figures, not more than four are shown for each simulation run.
2. To gain an overview over the whole Antarctic winter, days from four different months are selected.
3. Simulation results from different model levels are to be visualised; MIPAS analysis data for the corresponding pressure ranges is given for comparison.
4. Dates and levels are chosen for which a relatively large number of MIPAS measurements is available.
5. The selection should contain atmospheric situations that are simulated well by certain NAT formation schemes and others which reveal difficulties.

The following dates and levels fullfilled these criteria:

- 22 May 2003, model level 20, pressure range 36.10 hPa to 47.10 hPa
- 19 June 2003, model level 24, pressure range 99.92 hPa to 126.54 hPa
- 1 August 2003, model level 23, pressure range 78.35 hPa to 99.92 hPa
- 3 October 2003, model level 22, pressure range 60.97 hPa to 78.35 hPa

In the figures based on simulation results, PSCs are shown if the volume density of PSC particles within a grid box exceeds $0.3 \cdot 10^{-12}\,\frac{\mathrm{m}^3}{\mathrm{m}^3}$.

The colour code for figures 6.1 to 6.4 is:

white no data available

yellow no PSC particles

green STS particles

red NAT particles

blue ice particles

Note that ice particles might also contain some NAT. Furthermore, as explained in subsection 6.2.5, the PSC model allows STS to coexist with NAT and/or ice. However, the HNO_3 is first assigned to NAT according to the thermodynamic equilibrium condition, and for STS only the "rest" is available. Therefore liquid aerosol droplets are unlikely to grow to large sizes in the presence of NAT. In the simulation runs under consideration, STS volume densities exceeded $0.3 \cdot 10^{-12}\,\frac{\mathrm{m}^3}{\mathrm{m}^3}$ in the presence of NAT or ice only in very rare events so that extra colours for "NAT + STS" or "ice + STS" are dispensable.

NAT on ice

Figure 6.1 presents results for the NAT formation scheme "NAT on ice" (subsection 6.2.2).

Figures 6.1(a), 6.1(d), 6.1(g), and 6.1(j) in the left column show MIPAS analysis results. The middle column, i. e. figures 6.1(b), 6.1(e), 6.1(h), and 6.1(k), give simulation data based on the unmodified ECHAM5/MESSy temperatures. If the PSC microphysics is calculated with temperatures that are 4 K higher than those of ECHAM5/MESSy, PSCs occur as shown in figures 6.1(c), 6.1(f), 6.1(i), and 6.1(l) (right column).

For the meteorological situation of 22 May 2003 (figures 6.1(a), 6.1(b), and 6.1(c), i. e. first row), the simulation with unmodified temperatures (figure 6.1(b)) calculated STS occurrence similar to that observed by MIPAS. In the simulation with increased PSC submodel internal temperatures, temperatures at 40 hPa for 22 May 2003 are too high for STS (figure 6.1(c)).

Correspondingly, for 19 June 2003 PSC microphysics with unmodified ECHAM5/MESSy temperatures (figure 6.1(e)) leads to better agreement with MIPAS (figure 6.1(d)) than PSC microphysics based on shifted temperatures (figure 6.1(f)).

At 1 August 2003, both simulation runs (figures 6.1(h) and 6.1(i)) underestimate NAT occurrence. This discrepancy is not limited to the "NAT on ice" scheme as the two alternative NAT formation schemes do not lead to sufficient NAT either at 1 August 2003 (figures 6.2(h), 6.2(i), 6.3(h), and 6.3(h)). An inspection of the HNO_3 and H_2O values in the corresponding region reveals that these are very low ($x_{\mathrm{HNO_3}} < 1\,\frac{\mathrm{nmol}}{\mathrm{mol}}$, $x_{\mathrm{H_2O}} \approx 1\,\frac{\mu\mathrm{mol}}{\mathrm{mol}}$). Therefore, the simulation overestimates denitrification and dehydration at 1 August 2003 in the pressure range from 78.35 hPa to 99.92 hPa. From the thorough evaluation in chapters 4 and 5 it is known that the solid PSC particle sedimentation scheme and the solid PSC particle size scheme model realistic denitrification and dehydration but depend strongly on input variable values. ECHAM5/MESSy temperatures that are too low by more than 4 K before 1 August 2003 would lead to an overestimation of solid PSC particle occurrence and sizes and, therefore, to an

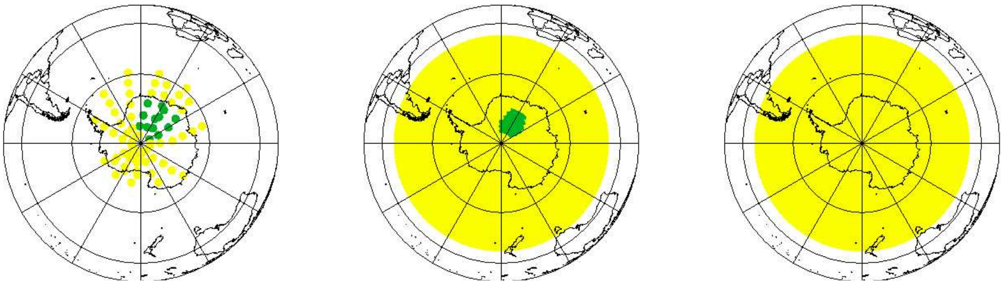

(a) 22 May, 40 hPa

(b) 22 May, 40 hPa

(c) 22 May, 40 hPa

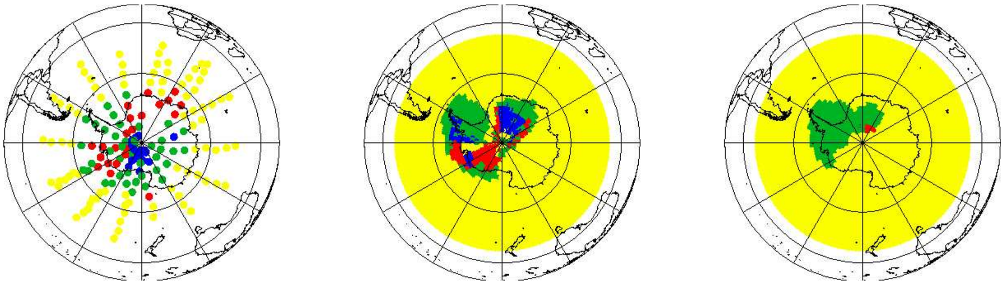

(d) 19 June, 110 hPa

(e) 19 June, 110 hPa

(f) 19 June, 110 hPa

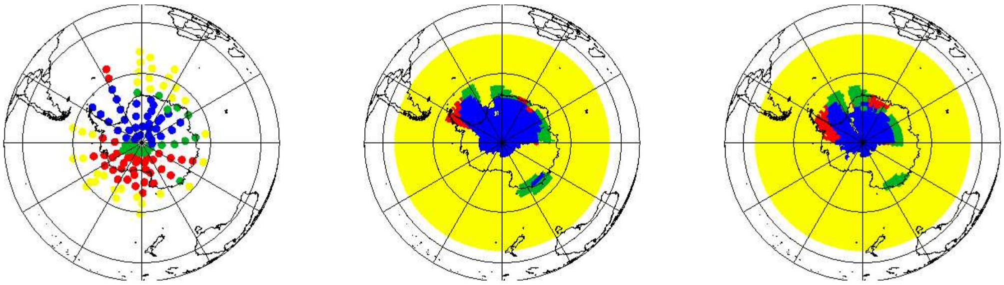

(g) 1 August, 90 hPa

(h) 1 August, 90 hPa

(i) 1 August, 90 hPa

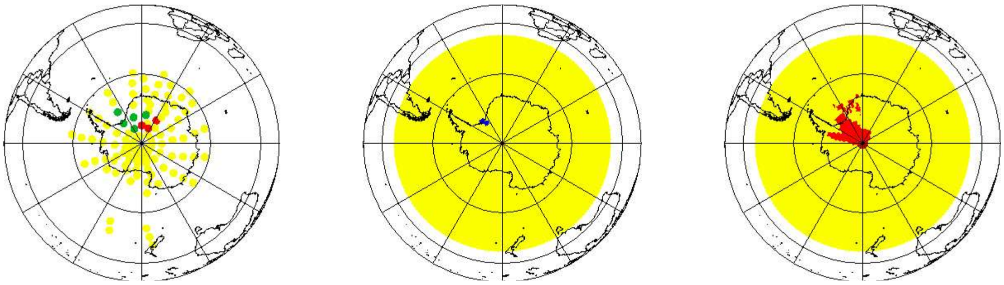

(j) 3 October, 70 hPa

(k) 3 October, 70 hPa

(l) 3 October, 70 hPa

Figure 6.1: Left: MIPAS analysis; middle: “NAT on ice” simulation; right: “NAT on ice, +4 K” simulation; colours: blue – ice, red – NAT, green – STS, yellow – no PSCs

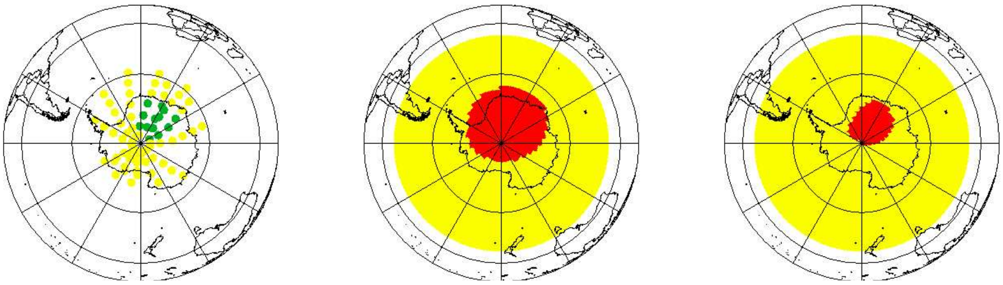

(a) 22 May, 40 hPa (b) 22 May, 40 hPa (c) 22 May, 40 hPa

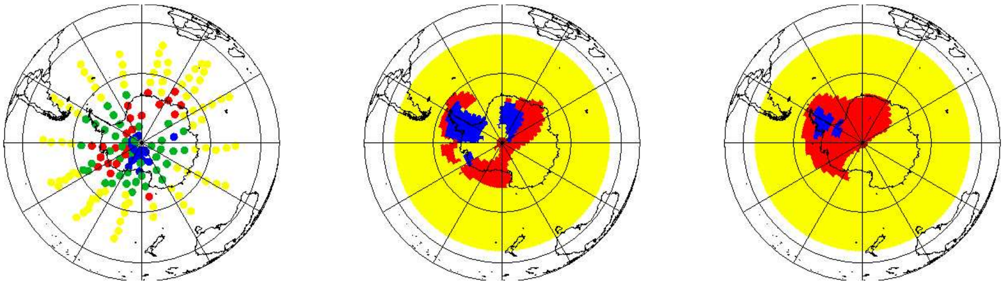

(d) 19 June, 110 hPa (e) 19 June, 110 hPa (f) 19 June, 110 hPa

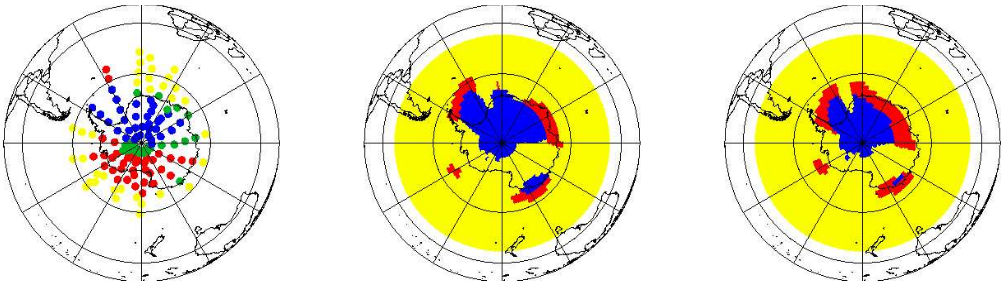

(g) 1 August, 90 hPa (h) 1 August, 90 hPa (i) 1 August, 90 hPa

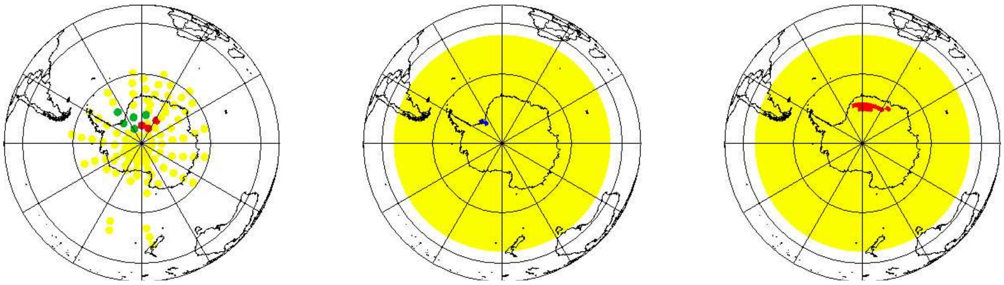

(j) 3 October, 70 hPa (k) 3 October, 70 hPa (l) 3 October, 70 hPa

Figure 6.2: Left: MIPAS analysis; middle: "Advection Influence" simulation; right: "Advection Influence, +4 K"; blue – ice, red – NAT, green – STS, yellow – no PSCs

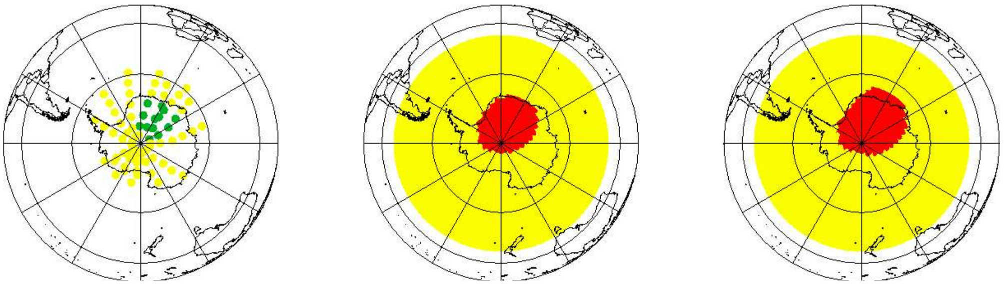

(a) 22 May, 40 hPa (b) 22 May, 40 hPa (c) 22 May, 40 hPa

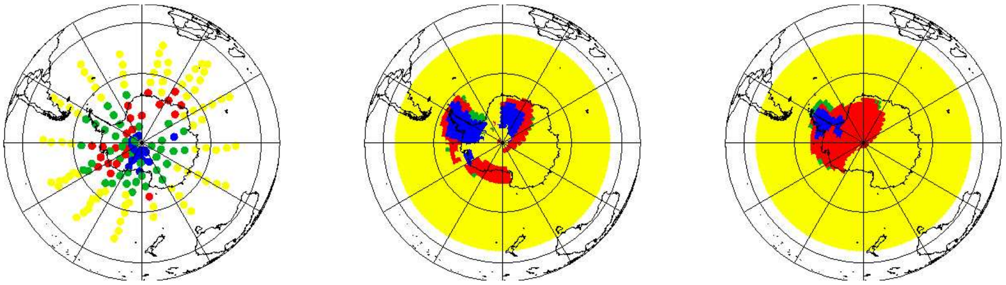

(d) 19 June, 110 hPa (e) 19 June, 110 hPa (f) 19 June, 110 hPa

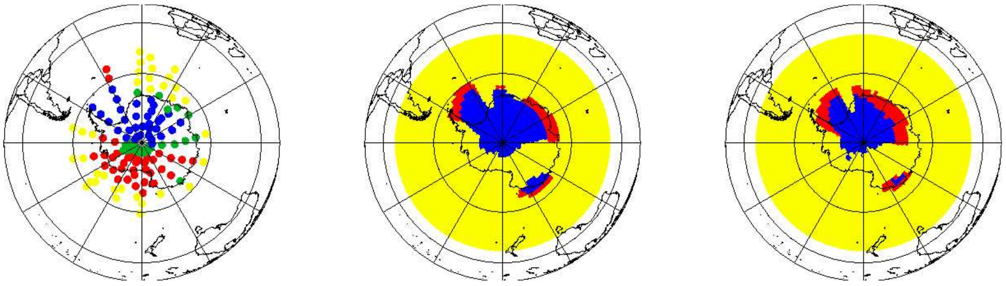

(g) 1 August, 90 hPa (h) 1 August, 90 hPa (i) 1 August, 90 hPa

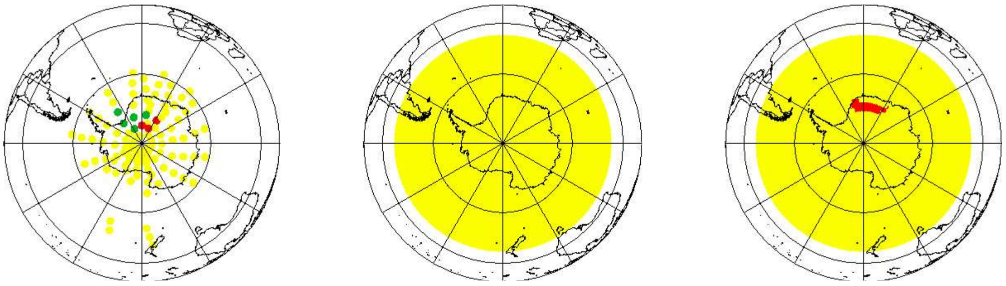

(j) 3 October, 70 hPa (k) 3 October, 70 hPa (l) 3 October, 70 hPa

Figure 6.3: Left: MIPAS analysis; middle: "temp. barrier" simulation; right: "temp. barrier, +4 K"; colours: blue – ice, red – NAT, green – STS, yellow – no PSCs

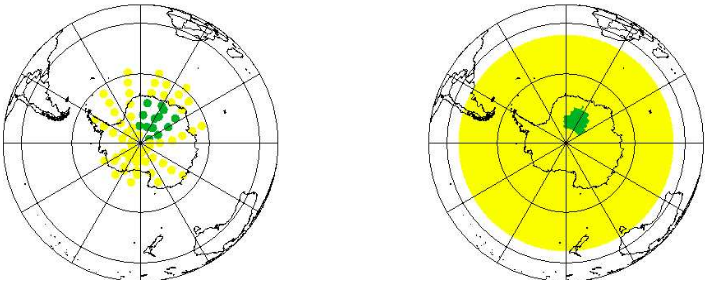

(a) 22 May, 40 hPa

(b) 22 May, 40 hPa

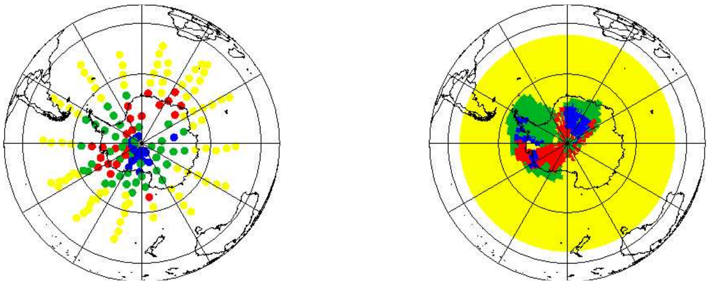

(c) 19 June, 110 hPa

(d) 19 June, 110 hPa

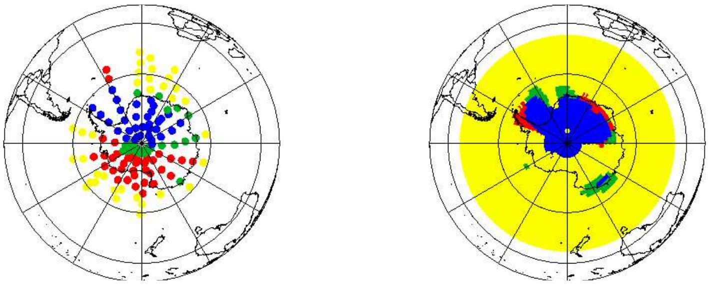

(e) 1 August, 90 hPa

(f) 1 August, 90 hPa

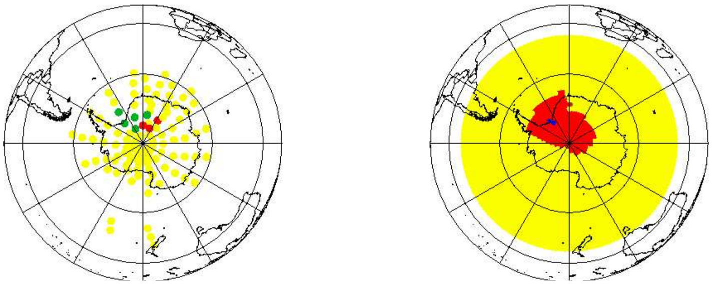

(g) 3 October, 70 hPa

(h) 3 October, 70 hPa

Figure 6.4: Left: MIPAS analysis; middle: "NAT on ice" simulation with full stratospheric chemistry

overestimation of sedimentation. This could cause the low HNO_3 and H_2O values in the pressure range from 78.35 hPa to 99.92 hPa. In chapter 7 it will be demonstrated that this kind of model temperature deviation is conceivable.

Note that the use of more diffusive sedimentation schemes “simple upwind” and “Walcek” (chapter 4) leads to higher amount-of-substance ratios of HNO_3 and H_2O to air in the situation under discussion. However, it is arguable whether this is a model improvement or rather an undesirable side-effect covering up temperature errors.

For 3 October 2003, the simulation run with unmodified ECHAM5/MESSy temperatures (figure 6.1(k)) does not show NAT or STS formation as observed by MIPAS, although temperatures must have been low enough: figure 6.1(l) demonstrates that even $T + 4\,\mathrm{K}$ was cold enough for NAT. Therefore, the lack of NAT in figure 6.1(k) is a consequence of low amount-of-substance ratios of HNO_3 to air.

A comparison of figure 6.1(k) with figure 6.4(h) reveals that amount-of-substance ratios of HNO_3 to air must have been higher in the simulation with full stratospheric chemistry. This can be explained by the absence of chemical HNO_3 sources, mainly $N_2O_5 + H_2O \longrightarrow 2\,HNO_3$, in the simulations without chemical reactions. In the polar night, these HNO_3 sources are not counteracted by the photolytic decay of nitric acid so that chemistry leads to a net HNO_3 production in the polar winter stratosphere.

The presence of NAT at 3 October 2003 in the simulation with upwards shifted temperatures (figure 6.1(l)) indicates that denitrification throughout the polar night is significantly reduced by the 4 K temperature shift. The above-mentioned figures 6.1(e) and 6.1(f) support this statement: without temperature shift, solid PSC particles are widespread at 19 June 2003, with temperature shift there is mostly STS, which is not affected by sedimentation in the ECHAM5/MESSy PSC submodel.

Advection Influence

Figure 6.2 shows results from a simulation run that takes advection effects into account as described in subsection 6.2.3.

Although it seems reasonable to consider the advection of ice and NAT for the formation of further solid PSC particles, the visual inspection demonstrates that this NAT formation scheme is inferior to the “NAT on ice” scheme. In figure 6.2(b) NAT occurs already over a large area, whereas the corresponding figure 6.1(b) shows limited STS occurrence as measured by MIPAS (see figure 6.1(a)). Apparently, the presence of ice has triggered NAT formation in the days before 22 May 2005. In the “NAT on ice” scheme (figure 6.1(b)), this effect was limited to a small region, in accordance to MIPAS observations, whereas it quickly spread to neighbouring grid boxes in the “advection influence” scheme (figure 6.2(b)).

Also at 19 June 2003 and 1 August 2003, solid PSC particles are more widespread in figure 6.2 than in figure 6.1.

As a consequence, no STS appears in the simulation results. It seems that the effectively lowered formation barrier for NAT in the “Advection Influence” scheme compared to the “NAT on ice” scheme is ill suited for STS simulation, if the order of PSC particle formation gives solid PSC particles preference over STS.

The simulation run with shifted temperatures (figures 6.2(d), 6.2(f), 6.2(i), and 6.2(l)) is not fundamentally different from the one based on unmodified ECHAM5/MESSy temperatures (figures 6.2(b), 6.2(e), 6.2(g), and 6.2(k)). Generally, ice PSCs are less widespread. NAT occurrence is reduced in the early winter; the resulting decreased denitrification allows some additional NAT occurrence later on.

Temperature Barrier

Figure 6.3 presents results with the third NAT formation scheme, where NAT is allowed to nucleate on preexisting ice or 3 K below the NAT equilibrium temperature (subsection 6.2.4).

Recalling that the most restrictive NAT formation scheme, “NAT on ice”, leads to solid PSC particle occurrence roughly comparable to the MIPAS analysis data (figure 6.1), an overestimation of solid PSC particle formation can be expected from additionally allowing homogeneous NAT nucleation.

This effect is clearly present at 22 May 2003 (figures 6.3(a), 6.3(b), and 6.3(c)). The rare presence of STS, too, fits in this picture: as in the “advection influence” results (figure 6.2), widespread NAT formation depletes the air of HNO_3 and thus prevents liquid aerosol particles from absorbing large amounts of HNO_3.

The simulated PSC occurrence for 3 October 2003 (figures 6.3(k) and 6.3(l)) is also comparable to the one in the “advection influence” runs (figures 6.2(k) and 6.2(l)). For the simulation with unmodified ECHAM5/MESSy temperatures, the overestimation of solid PSC particle formation and, consequently the overestimation of denitrification prevents STS or NAT from forming at 70 hPa (figure 6.3(k)). In the simulation with elevated temperatures, NAT formation is still possible (figure 6.3(l)) but fits the MIPAS observation (figure 6.3(j)) less than in the “NAT on ice” scheme results (figure 6.1(l)).

6.3.4 Quantitative Evaluation

In the above subsection, insight into the properties and capabilities of the different NAT formation schemes was gained by a qualitative comparison of selected simulation and MIPAS analysis data.

However, both the simulation and the MIPAS analysis data set are too large to be completely considered by visual inspection. Furthermore, for an unambiguous judgement about the superiority of one of the simulation settings a quantitative measure is most suitable.

Therefore, a method for the quantitative comparison of the full MIPAS analysis set and the simulation data is developed, applied, and discussed in this subsection.

Data Comparison Method

As a first approach, agreements between results of a simulation run and MIPAS analysis data are counted according to the following procedure:

1. Each of the MIPAS observation events is attributed to the simulation data output event which is nearest in time. As simulation data is available on intervalls of 8 h, the maximum time difference between an MIPAS observation and the corresponding simulation data is 4 h.
2. A model level is attributed to each of the MIPAS data points so that the pressure of the MIPAS data point is in between the upper and the lower interface pressures of the model level.
3. The simulation grid point with the horizontal coordinates closest to the horizontal coordinates of the MIPAS data point is identified.
4. For each MIPAS observation it is checked whether simulated PSC occurrence at the thus defined "nearest" simulation data point agrees with the MIPAS analysis. This is done for three volume densities as PSC detection threshold in the simulation data: $0.2 \cdot 10^{-12}\,\frac{\mathrm{m}^3}{\mathrm{m}^3}$, $0.3 \cdot 10^{-12}\,\frac{\mathrm{m}^3}{\mathrm{m}^3}$, and $0.35 \cdot 10^{-12}\,\frac{\mathrm{m}^3}{\mathrm{m}^3}$.
5. The number of matches between MIPAS analysis and the "nearest" simulation data point is counted and divided by the number of MIPAS analysis data points. This quotient will be referred to as M_{nxt}.

Number 4 in this procedure description requires some explanation. In subsection 6.3.2 a volume density range of $0.3 \cdot 10^{-12}\,\frac{\mathrm{m}^3}{\mathrm{m}^3}$ to $0.4 \cdot 10^{-12}\,\frac{\mathrm{m}^3}{\mathrm{m}^3}$ was mentioned as lower limit of PSC detection by MIPAS. Therefore, the simulation data was first evaluated with threshold values of $0.3 \cdot 10^{-12}\,\frac{\mathrm{m}^3}{\mathrm{m}^3}$, $0.35 \cdot 10^{-12}\,\frac{\mathrm{m}^3}{\mathrm{m}^3}$, and $0.4 \cdot 10^{-12}\,\frac{\mathrm{m}^3}{\mathrm{m}^3}$. The results for $0.4 \cdot 10^{-12}\,\frac{\mathrm{m}^3}{\mathrm{m}^3}$ are not listed in the following because they are nearly identical with the results for $0.35 \cdot 10^{-12}\,\frac{\mathrm{m}^3}{\mathrm{m}^3}$. The use of an additional, lower threshold value of $0.2 \cdot 10^{-12}\,\frac{\mathrm{m}^3}{\mathrm{m}^3}$ is motivated by the fact that for $0.3 \cdot 10^{-12}\,\frac{\mathrm{m}^3}{\mathrm{m}^3}$ and $0.35 \cdot 10^{-12}\,\frac{\mathrm{m}^3}{\mathrm{m}^3}$ simulated STS and NAT occurrence is systematically too low.

The spatial assignement of MIPAS observations to simulation grid points in the above developed quantitative measure M_{nxt}, however, is hampered by some uncertainties. Due to the limited resolution, MIPAS measurements average over an area of about 30 km width, 300 km length, and 3 km height (M. Höpfner, pers. comm., 2005). On the model side, the spatial resolution is defined by the horizontal and vertical grid; a model variable value defined at a grid point is interpreted as grid box average. Thus MIPAS and ECHAM5/MESSy average over different regions.

Comparing the MIPAS analysis data with the nearest data point in the simulation grid might not always be the only reasonable choice. Where the MIPAS measurement region overlaps rather similarly with two, three, or even more ECHAM5/MESSy grid boxes, the simulation grid point second, third, ...

nearest to the coordinates of a MIPAS analysis data point could be suitable as well.

A second relative agreement measure, $M_{1.5}$, rates MIPAS analysis/simulation comparisons as a match if one of the nearest simulated value matches the MIPAS analysis. The precise definition of "one of the nearest" is as follows. Let d_{min} be the distance between a MIPAS analysis data point and the nearest ECHAM5/MESSy grid box center. For the $M_{1.5}$ measure, the MIPAS analysis data point will then be compared with all simulated data points within a distance of $1.5 \cdot d_{\mathrm{min}}$. In the vertical, this comparison is limited to the model layers $i-1$, i, and $i+1$, where i is the vertical level index of the grid box nearest to the MIPAS observation.

M_{nxt} and $M_{1.5}$ aim at measuring the relative agreement between the complete MIPAS analysis data set and all corresponding simulation data points. A third, a fourth, and a fifth relative agreement measure, M_{STS}, M_{NAT}, and M_{ice}, probe the PSC model performance especially for simulating STS, NAT, and ice, respectively.

For M_{STS}, the number of matches is counted where both the MIPAS analysis and the nearest simulation data point suggest the presence of STS (matches of this type are called "yes both" in the column heading of table 6.2). This number is divided by itself plus the number of MIPAS STS events without simulated STS ("no sim." in table 6.2) plus the number of simulated STS events where MIPAS observations are available but do not reveal the presence of STS ("no obs." in table 6.2)

$$M_{\mathrm{STS}} = \frac{\text{number ``yes both''}}{\text{number ``yes both''} + \text{number ``no sim.''} + \text{number ``no obs.''}} \tag{6.1}$$

M_{NAT} and M_{ice} are defined analogously.

Results

The results of the data comparison are listed in tables 6.1 to 6.4. Important aspects of the results are also summarised in the following.

Table 6.1 (relative agreement measures):

- According to the relative agreement mesures M_{nxt} and $M_{1.5}$, the solid PSC particle formation scheme "NAT on ice, +4 K" is best.
- The relative agreement between simulated and observed PSC particle occurrence is generally rather low (from 0.000 to 0.272) for the particle type measures M_{STS}, M_{NAT}, and M_{ice}.
- Simulated ice occurrence fits the MIPAS analysis better than simulated NAT or STS ($0.220 \leq M_{\mathrm{ice}} \leq 0.272$ versus $0.000 \leq M_{\mathrm{STS}} \leq 0.192$ or $0.025 \leq M_{\mathrm{NAT}} \leq 0.119$).

Table 6.2 (agreement/disagreement numbers for STS):

- The volume density threshold considerably affects the results. Simulated liquid aerosol volume densities often seem to be below the lower limit of

Table 6.1: Relative agreement measure results for six simulation setups and three voume densities. See section 6.3 for definitions of the relative agreement measures and subsection 6.3.1 for explanations of the simulation runs.

	M_{nxt}	$M_{1.5}$	M_{STS}	M_{NAT}	M_{ice}
volume density $= 0.2 \cdot 10^{-12} \frac{\mathrm{m}^3}{\mathrm{m}^3}$					
NAT on ice	0.641	0.716	0.185	0.111	0.269
advection infl.	0.611	0.692	0.100	0.062	0.231
temp. barrier	0.621	0.700	0.105	0.054	0.226
NAT on ice, +4 K	0.651	0.739	0.192	0.054	0.221
advection infl., +4 K	0.640	0.719	0.080	0.119	0.272
temp. barrier, +4 K	0.641	0.716	0.085	0.111	0.269
volume density $= 0.3 \cdot 10^{-12} \frac{\mathrm{m}^3}{\mathrm{m}^3}$					
NAT on ice	0.636	0.700	0.135	0.031	0.220
advection infl.	0.588	0.643	0.000	0.048	0.231
temp. barrier	0.598	0.652	0.006	0.041	0.227
NAT on ice, +4 K	0.635	0.697	0.140	0.038	0.221
advection infl., +4 K	0.616	0.656	0.000	0.090	0.272
temp. barrier, +4 K	0.618	0.657	0.009	0.080	0.270
volume density $= 0.35 \cdot 10^{-12} \frac{\mathrm{m}^3}{\mathrm{m}^3}$					
NAT on ice	0.633	0.689	0.123	0.025	0.220
advection infl.	0.589	0.629	0.000	0.043	0.232
temp. barrier	0.598	0.637	0.003	0.036	0.227
NAT on ice, +4 K	0.632	0.690	0.132	0.032	0.221
advection infl., +4 K	0.614	0.650	0.000	0.081	0.272
temp. barrier, +4 K	0.615	0.647	0.004	0.071	0.270

Table 6.2: Agreement/disagreement between MIPAS analysis and simulations for STS. "yes both" counts matches between observations and simulation values in minimum distance d_{min}. "yes 1.5" counts observations where a simulation value within $1.5\,d_{\text{min}}$ matches (vertically, search for matching simulation value is limited to ±1 model level). "no obs." counts observations other than STS where nearest simulated PSC occurrence is STS. "no sim." counts STS observations where the nearest simlation values is not STS.

	yes 1.5	yes both	no obs.	no sim.
volume density $= 0.2 \cdot 10^{-12}\,\frac{\text{m}^3}{\text{m}^3}$				
NAT on ice	5511	2952	2415	9951
advection infl.	3389	1426	1379	11477
temp. barrier	3523	1505	1480	11398
NAT on ice, +4 K	6124	2967	2538	9936
advection infl., +4 K	2946	1114	1109	11789
temp. barrier, +4 K	3135	1201	1186	11702
volume density $= 0.3 \cdot 10^{-12}\,\frac{\text{m}^3}{\text{m}^3}$				
NAT on ice	3828	1880	1070	11023
advection infl.	758	2	2	12901
temp. barrier	1002	84	82	12819
NAT on ice, +4 K	4106	2020	1505	10883
advection infl., +4 K	192	2	2	12901
temp. barrier, +4 K	440	113	53	12790
volume density $= 0.35 \cdot 10^{-12}\,\frac{\text{m}^3}{\text{m}^3}$				
NAT on ice	3349	1705	934	11198
advection infl.	1	0	0	12903
temp. barrier	221	34	36	12869
NAT on ice, +4 K	3838	1887	1398	11016
advection infl., +4 K	1	0	0	12903
temp. barrier, +4 K	154	50	30	12853

Table 6.3: Agreement/disagreement between MIPAS analysis and simulations for NAT. “yes both” counts matches between observations and simulation values in minimum distance d_{min}. “yes 1.5” counts observations where a simulation value within $1.5\,d_{\text{min}}$ matches (vertically, search for matching simulation value is limited to ±1 model level). “no obs.” counts observations other than NAT where nearest simulated PSC occurrence is NAT. “no sim.” counts NAT observations where the nearest simlation values is not NAT.

	yes 1.5	yes both	no obs.	no sim.
volume density $= 0.2 \cdot 10^{-12} \frac{\text{m}^3}{\text{m}^3}$				
NAT on ice	897	382	840	7270
advection infl.	1414	775	4764	6877
temp. barrier	1206	609	3547	7043
NAT on ice, +4 K	1144	472	1084	7180
advection infl., +4 K	2835	1622	6000	6030
temp. barrier, +4 K	2415	1381	4799	6271
volume density $= 0.3 \cdot 10^{-12} \frac{\text{m}^3}{\text{m}^3}$				
NAT on ice	623	254	650	7398
advection infl.	1041	564	4015	7088
temp. barrier	906	435	3031	7217
NAT on ice, +4 K	814	316	773	7336
advection infl., +4 K	2037	1106	4679	6546
temp. barrier, +4 K	1770	923	3815	6729
volume density $= 0.35 \cdot 10^{-12} \frac{\text{m}^3}{\text{m}^3}$				
NAT on ice	516	206	570	7446
advection infl.	915	492	3734	7160
temp. barrier	794	382	2853	7270
NAT on ice, +4 K	701	265	708	7387
advection infl., +4 K	1837	973	4309	6679
temp. barrier, +4 K	1513	792	3524	6860

Table 6.4: Agreement/disagreement between MIPAS analysis and simulations for ice. "yes both" counts matches between observations and simulation values in minimum distance d_{min}. "yes 1.5" counts observations where a simulation value within $1.5\,d_{\mathrm{min}}$ matches (vertically, search for matching simulation value is limited to ±1 model level). "no obs." counts observations other than ice where nearest simulated PSC occurrence is ice. "no sim." counts ice observations where the nearest simlation values is not ice.

	yes 1.5	yes both	no obs.	no sim.
volume density $= 0.2 \cdot 10^{-12}\,\frac{\mathrm{m}^3}{\mathrm{m}^3}$				
NAT on ice	2251	2251	7102	895
advection infl.	2902	2662	8386	484
temp. barrier	2887	2574	8235	572
NAT on ice, +4 K	2001	1453	3429	1693
advection infl., +4 K	2511	2063	4450	1083
temp. barrier, +4 K	2471	2002	4289	1144
volume density $= 0.3 \cdot 10^{-12}\,\frac{\mathrm{m}^3}{\mathrm{m}^3}$				
NAT on ice	2696	2251	7080	895
advection infl.	2902	2661	8360	485
temp. barrier	2887	2573	8210	573
NAT on ice, +4 K	2001	1453	3420	1693
advection infl., +4 K	2511	2063	4438	1083
temp. barrier, +4 K	2471	2002	4275	1144
volume density $= 0.35 \cdot 10^{-12}\,\frac{\mathrm{m}^3}{\mathrm{m}^3}$				
NAT on ice	2696	2251	7075	895
advection infl.	2902	2661	8347	485
temp. barrier	2887	2573	8202	573
NAT on ice, +4 K	2001	1453	3417	1693
advection infl., +4 K	2510	2062	4430	1084
temp. barrier, +4 K	2471	1999	4270	1147

what can be detected in MIPAS spectra ($0.3 \cdot 10^{-12}\,\frac{\mathrm{m}^3}{\mathrm{m}^3}$ to $0.4 \cdot 10^{-12}\,\frac{\mathrm{m}^3}{\mathrm{m}^3}$). This could at least partially be caused by an underestimation of amount-of-substance ratios of $\mathrm{HNO_3}$ to air in the simulation. A comparison of zonally averaged MIPAS $x_{\mathrm{HNO_3}}$ measurements for 17 March 2003 (M. Höpfner, pers. comm., 2005) and corresponding simulation results indicate a low bias of $1\,\frac{\mathrm{nmol}}{\mathrm{mol}}$ to $3\,\frac{\mathrm{nmol}}{\mathrm{mol}}$ in the simulations.

- In the simulation runs there is far too little STS.
- The last statement is still valid even if spatial uncertainty is taken into account (first column of the table, named “yes / 1.5”).

Table 6.3 (agreement/disagreement numbers for NAT):

- The influence of the NAT particle volume density threshold on the results is evident but less than the corresponding influence of the volume density threshold on the STS results (compare table 6.2). It seems that NAT, if it exists, reaches larger volume densities more easily.
- For all six simulation runs and independently of the volume density threshold, mismatches between simulation results and MIPAS analysis are more often caused by a lack of simulated NAT than by a lack of observed NAT.
- From the simulation/MIPAS analysis mismatches it can be seen that the “NAT on ice” scheme calculates most often no NAT where NAT is present in the MIPAS analysis data, whereas the “advection influence” scheme calculates relatively often NAT where none is observed. This confirms the qualitative evaluation results that the “NAT on ice” scheme is the most restrictive one and the “Advection Influence” scheme leads to NAT formation most easily.

Table 6.4 (agreement/disagreement numbers for ice):

- For ice, the volume density threshold is only of marginal importance. Ice particles, if present at all, easily exceed volume densities of $0.4 \cdot 10^{-12}\,\frac{\mathrm{m}^3}{\mathrm{m}^3}$.
- Contrary to STS and NAT, ice is more often simulated than observed, as can be seen from the relatively high numbers of “no obs.” type mismatches.
- Allowing matches within 1.5 times the minimum difference between a MIPAS measurement and the nearest grid box has less effect for ice than for STS and NAT. This corresponds to the previous remark that ice is simulated too often rather than not often enough.

Weaknesses of the Data Comparison Method

Whereas MIPAS measures continuously, simulation results are known as snapshots with 8 h data gaps in between. Therefore, the comparison is based on PSC occurrence simulation/analysis results with times differing up to 4 h.

The most straightforward cure for this problem would be to write out simulation data more often. However, each of the six simulation runs without chemistry calculation already produces 50 GByte of data. A further increase in data volume would sooner or later be limited by available storage space. Even future hardware development will probably not abolish this restriction because it is accompanied by a growing output data volume of increasingly complex and detailed chemistry-GCM simulations.

For studies that aim at a comparison between simulation data and a specific observation data set, data output could be restricted to the times and locations, where observation data is available. Unfortunately, ECHAM5/MESSy currently does not allow that kind of data output.

To estimate the influence of the time gap on the results with the currently available means, the relative agreement measures have been recalculated with MIPAS analysis data points restricted to time intervals of $\pm 1\,\mathrm{h}$ around the simulation data output.

The results are slightly different from, but not systematically better than the ones listed in table 6.1. Hence the time gap between the MIPAS analysis and the simulation data does not seem to influence the comparison result strongly.

A more in-depth evaluation of PSC occurrence simulation would be possible if the MIPAS PSC occurrence data were accompanied by measurements of temperatures, amount-of-substance ratios of H_2O to air and amount-of-substance ratios of HNO_3 to air. Currently, detailed measurements of T, $x_{\mathrm{H_2O}}$, and $x_{\mathrm{HNO_3}}$ are not available. Hopefully, further analysis of MIPAS infrared spectra will close this gap at least partially. However, remote sensing measurements in the presence of polar stratospheric clouds tend to be difficult and affected with relatively large measurement errors.

Further potential for improvement of the data comparison method may be seen in selecting special subsets of the MIPAS analysis data. A general recommendation cannot be given here, as the optimum choice depends on the question to be investigated. For an overall benchmarking of the different PSC submodel setups, i. e. for the relative agreement measures M_{nxt} and $M_{1.5}$, it seems reasonable to use the whole data set; examples for special subsets are the ones used for calculating M_{STS}, M_{NAT}, and M_{ice}.

Model Limitations and Shortcomings

A fundamental shortcoming of global models is the limited spatial resolution (section 3.2). In comparisons with MIPAS data the averaging effect of the coarse ECHAM5/MESSy grid somehow corresponds to an averaging effect of the MIPAS horizontal and vertical resolution. However, where MIPAS averages over the results of microphysical processes, i. e. the aerosol content of the polar stratosphere, ECHAM5/MESSy averages the input values for the PSC submodel, i. e. the temperatures. For non-linear processes like ice formation below a temperature threshold, both averaging procedures can lead to different results. If temperatures in one half of an atmospheric region are much above the ice formation temperature and slightly below in the other half, the MIPAS observation for the whole atmospheric region is “some ice present”. The

PSC submodel, however, on getting input temperatures averaged over the same atmospheric region, simulates no ice.

The vertical distribution of HNO_3 and H_2O throughout the winter strongly depends on solid PSC particle sedimentation. For this reason, the sedimentation scheme and the solid PSC particle size scheme have been evaluated before PSC particle formation. From chapters 4 and 5 it is concluded that the simulation of sedimentation works well. However, the issue of denitrification and dehydration would make the simulation of PSC occurrence difficult even with the best possible representation of sedimentation in the model: any error in the simulated particle formation potentially causes errors in the HNO_3 and H_2O distribution later on and thus more errors in solid PSC particle occurrence.

The impact of the neglect of chemical reactions in six of the simulation runs can be estimated from the comparison of the "NAT on ice" simulation run without chemistry with the seventh simulation run, which included full stratospheric chemistry. The relative agreement measures for both are listed in table 6.5.

Table 6.5: Relative agreement measures from simulations excluding and including stratospheric chemistry.

	M_{nxt}	$M_{1.5}$	M_{STS}	M_{NAT}	M_{ice}
volume density $= 0.2 \cdot 10^{-12} \frac{\text{m}^3}{\text{m}^3}$					
NAT on ice	0.641	0.716	0.185	0.111	0.269
NAT on ice, with chemistry	0.573	0.689	0.147	0.091	0.150
volume density $= 0.3 \cdot 10^{-12} \frac{\text{m}^3}{\text{m}^3}$					
NAT on ice	0.636	0.700	0.135	0.031	0.220
NAT on ice, with chemistry	0.562	0.659	0.091	0.060	0.150
volume density $= 0.35 \cdot 10^{-12} \frac{\text{m}^3}{\text{m}^3}$					
NAT on ice	0.633	0.689	0.123	0.025	0.220
NAT on ice, with chemistry	0.564	0.649	0.084	0.050	0.150

According to the figures in table 6.5, the overall performance of the simulation is worse with chemistry than without, mainly due to lower agreement for ice. The noticeable difference in ice simulation can be attributed to the use of the H2O submodel in the simulation runs without full stratospheric chemistry versus the explicit calculation of all chemical reactions affecting H_2O (subsection 6.3.1). Whereas the H2O submodel introduces methane as photochemical source for stratospheric H_2O, it does not include photolytic decay of H_2O in the mesosphere. In combination with the downward motion in the polar vortex, water vapour in the PSC relevant region is thus slightly higher than in simulations with full chemistry calculation. A detailed inspection of the agreement/disagreement numbers for NAT and STS reveals that taking chemical HNO_3 sources and sinks into account leads to more NAT. STS occurrence, however, is still underestimated, even if stratospheric chemistry is considered in the simulation. This can partially be explained by the STS/NAT coexistence scheme described in subsection 6.2.5, which prefers NAT formation over STS. Another possible explanation for a lack of STS in all simulations and a lack of NAT in most of them are errors in the HNO_3 initialisation. First MIPAS HNO_3 retrievals for May 2003 (M. Höpfner, pers. comm., 2005) indicate that the simulations underestimate x_{HNO_3} in the polar stratosphere by $1\,\frac{\mathrm{nmol}}{\mathrm{mol}}$ to $3\,\frac{\mathrm{nmol}}{\mathrm{mol}}$.

Furthermore, deviations between ECHAM5/MESSy temperatures, nudged towards ECMWF data, and real temperatures in the 2003 Antarctic winter polar stratosphere could have a strong influence on the highly temperature dependent formation of PSC particles. Probably ECHAM5/MESSy temperatures are too low by several degrees (chapter 7). Therefore, the three NAT formation setups have been compared in simulation runs where the input temperatures for the PSC submodel were shifted by $+4\,\mathrm{K}$. It can be seen from table 6.1 that simulated PSC occurrence based on these modified temperatures agrees slightly better with the MIPAS analysis data.

Analysis Data Errors

The uncertainty in the MIPAS geolocation is relatively small ($\ll 50\,\mathrm{km}$ in the horizontal and $\approx 0.5\,\mathrm{km}$ in the vertical; M. Höpfner, pers. comm., 2005) and hence no relevant error source for the current comparison.

It was mentioned in subsection 6.2.5 that the analysis prodecure is not entirely reliable as far as the distinction between STS and NAT is concerned. The dataset used for the current work contains no information about the reliability of certain data points. For some tests, however, a preliminary MIPAS analysis data set was used where some data points where marked as “probably NAT, but possibly STS” or “probably STS, but possibly NAT”. Additional relative agreement measures that took these uncertainties into account led to different numerical values, but the general features of the results were not affected.

The investigation of simulation results revealed that the number of simulated PSCs considerably depends on the volume density threshold. With more knowledge about the MIPAS PSC detection characteristics some improvement of the comparison would be feasible. However, a precise definition of the lower limit for PSC detection in the MIPAS analysis is hard give. It depends, amongst others, on particle sizes, cloud cover in the troposphere, and on temperatures of the tropospheric clouds or of the surface (M. Höpfner, pers. comm., 2005)

6.3.5 Conclusions

With the new MIPAS analysis data set made available by M. Höpfner observed PSC occurrence in an Antarctic winter is known with unprecedented spatial and temporal coverage. Thus for the first time simulated PSC occurrence in the polar winter stratosphere including the polar night can be evaluated based on a comprehensive data set instead of anecdotal evidence only. This new model evaluation opportunity was used to investigate the highly disputed problem of NAT formation modelling. According to the overall relative agreement measure

$M_{1.5}$ the NAT formation scheme “NAT on ice” performs best.

Nevertheless, the general agreement between simulated and observed PSC events is rather low for all simulation setups. Some possibilities for improving the simulations, MIPAS analysis, and the comparison procedure have been identified. However, it has been argued that these modifications cannot be expected to lead to a high degree of agreement between the simulations and the MIPAS analysis. Rather it seems that the limited model resolution and uncertainties in the amount-of-substance ratios of H_2O and HNO_3 to air pose a fundamental restriction to the capability to reproduce individual PSC observations in space and time.

Both error sources are present not only in ECHAM5/MESSy simulations but in all global models and also in small scale models that rely on input from large scale models. Therefore, the question arises how the conclusion of an overwhelming influence of model resolution and H_2O/HNO_3 uncertainties on simulated PSC occurrence relates to previous simulation results. Since previous results have not been compared to an observational data set as extensive as the MIPAS analysis data set used here, a definite answer cannot be given.

It should be noted that the above-mentioned uncertainties can explain at least partially the difficulties involved in the search for relevant NAT formation pathways (subsection 6.1.1). Similarly, simulation/observation disagreements that have been attributed to solid PSC particle size schemes could as well have been caused by model resolution and tracer distribution issues (subsection 5.1.1).

Previous success in simulations of polar ozone destructions might have been achieved despite significant deficiencies in the simulated spatial and temporal PSC distribution. In table 6.6, monthly binned relative PSC sighting frequencies are compared for the MIPAS analysis data set and the different simulation setups. According to these figures, all simulations reproduce the order of magnitude of MIPAS PSC sighting in the winter months where heterogeneous chemical reations on PSC particles are most relevant. As long as there are sufficient polar stratospheric clouds for nearly complete chlorine (and bromine) activation, polar ozone chemistry might be rather insensitive to details of the PSC occurrence. It is even conceivable that the best results in the simulation of the ozone hole do not coincide with the best simulated PSC occurrence. The overestimation of PSCs in September in the simulation with stratospheric chemistry, for example, enhances the important process of chlorine activation.

To summarise, this study highlights fundamental limitations of global scale models to reproduce individual PSC events. General features of PSC ocurrence (e. g. first and last PSC events in an Antarctic winter, PSC sighting probability), on the other hand, can be simulated well with the ECHAM5/MESSy PSC submodel.

Table 6.6: Relative PSC sighting frequency (number of PSC events divided by number of observations) for the Antarctic winter 2003. PSC particle types are not distinguished. For comparability, the simulation data are only evaluated at MIPAS observation events. The volume density threshold $0.2 \cdot 10^{-12} \frac{\mathrm{m}^3}{\mathrm{m}^3}$ is applied for simulated PSC events.

	May	June	July	August	Sept.	Oct.
MIPAS analysis	0.08	0.43	0.37	0.23	0.03	0.01
NAT on ice	0.05	0.39	0.33	0.20	0.02	0.01
advection infl.	0.22	0.48	0.36	0.21	0.03	0.01
temp. barrier	0.12	0.44	0.35	0.20	0.02	0.01
NAT on ice, +4 K	0.00	0.20	0.30	0.17	0.03	0.04
advection infl., +4 K	0.05	0.37	0.31	0.18	0.03	0.01
temp. barrier, +4 K	0.01	0.32	0.29	0.16	0.03	0.01
NAT on ice, with chemistry	0.00	0.48	0.42	0.33	0.23	0.05

Chapter 7

Notes on Model Temperatures

Introduction

Temperatures in the polar winter stratosphere are often near the threshold of PSC particle formation. Therefore, the PSC submodel output strongly depends on the temperature input from ECHAM5/MESSy. This chapter briefly summarises some features of temperatures in nudged[1] ECHAM5/MESSy simulations.

ECHAM5/MESSy Temperatures versus ECMWF Temperatures

ECHAM5/MESSy simulation runs in this work are nudged towards divergence, vorticity, temperature, and surface pressure data from the ECMWF (European Centre for Medium-Range Weather Forecasts, http://www.ecmwf.int) operational weather forecast model. The ECMWF data is interpolated by the program INTERA (I. Kirchner, pers. comm., 2004) to fit the ECHAM5/MESSy spatial and temporal resolution. During the simulation run, the ECHAM5/-MESSy simulated meteorology is relaxed towards the interpolated ECMWF data so that the resulting ECHAM5/MESSy wind fields and temperatures generally follow the ECMWF meteorology but are allowed to deviate in details.

Figure 7.1 gives an impression of the differences between ECMWF and ECHAM5/MESSy temperatures in a simulation of the southern hemisphere winter 2003. From May to September 2003 the temperature difference averaged over this part of the southern polar stratosphere where the PSC submodel is active (section 3.3) fluctuates around 1 K with the ECHAM5/MESSy model being colder (black line in figure 7.1). Maximum and minimum temperature difference (red and blue lines, respectively) in the southern polar stratosphere vary more strongly than the mean value. However, after a short initialisation period and before October, they are confined to a relatively narrow temperature band of about ±2 K around the mean difference. It seems that the ECMWF weather forecast model and the chemistry-GCM ECHAM5/MESSy simulate

---

[1] Background information about the data assimilation technique "nudging" can be found in section 3.4; results of nudged ECHAM5/MESSy simulations are shown in sections 6.3 and 9.4.

the relatively stable and regular meteorological situation in and around the southern polar vortex rather similarly.

In the middle of October, large temperature deviations occur. This is due to the fact that the polar vortex shows signs of a breakdown in the first half of October in ECHAM5/MESSy[2], whereas it was still stable in the ECMWF model at that time. Peaks in the maximum and minimum temperature deviations alternate with intermediate periods where the nudging manages to stabilise the ECHAM5/MESSy polar vortex.

In the light of the PSC occurrence simulation of chapter 6 the main conclusion from figure 7.1 is that ECHAM5/MESSy has a low bias of approximately 1 K compared to the ECMWF operational model data in the nudged simulation of the southern hemisphere winter 2003.

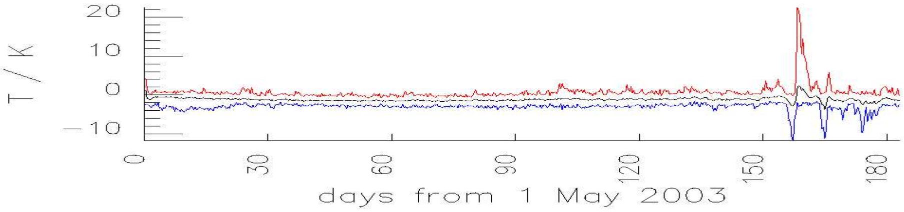

Figure 7.1: Comparison of ECMWF and ECHAM5/MESSy temperatures in the southern polar stratosphere. Black line: average temperature difference "ECHAM5/MESSy–ECMWF"; red: maximum temperature difference; blue: minimum temperature difference

Meteorological Analysis Temperatures

After gaining an impression of the differences between the ECHAM5/MESSy temperatures and the nudging input temperatures, the question arises of how accurate the nudging input temperatures are.

As far as the southern hemisphere winter 2003 is concerned, a comparison of ECMWF operational model temperatures with about 100 balloon based measurements in the time from 18 May 2003 to 30 June 2003 reveals a cold bias of the ECMWF temperatures of 1 K to 4 K (M. Höpfner, pers. comm., 2004). In the case of the two Arctic winters 1999/2000 and 2000/2001, Buss (2004) found a warm bias of 1 K to 6 K in the ECMWF operational weather forecast model temperatures compared to radiosondes and aircraft observations, especially for temperatures near the ice frost point.

However, nudging input data cannot only be gained from the ECMWF operational weather forecast model. The INTERA interpolation program can also

---

[2] It seems to be a general feature of the ECHAM5/MESSy model version 0.9.1 to simulate relatively unstable polar vortices in early October (C. Brühl pers. comm., 2005). Possible causes are under investigation. They include the use of climatological ozone values (Fortuin and Kelder, 1998) for the calculation of radiative heating and the gravity wave parameterisation (Manzini et al., 1997).

process the ECMWF reanalysis data sets "ERA15" and "ERA40", which contain synoptic meteorological information for the periods 1979–1993 and 1957–2001, respectively. It is also conceivable to nudge ECHAM5/MESSy with other meteorological analysis data sets.

Manney et al. (2003) compare several temperature data sets for the Arctic winters 1995/1996 and 1999/2000. They generally found agreement within a few K in the Arctic polar stratosphere. Therefore, an uncertainty of a few K can be expected for temperatures in meteorological analysis data sets. Note that for temperatures near the PSC formation threshold even these rather small deviations lead to differences in the total PSC covered area of 25 % (Manney et al., 2003). A similar conclusion about the uncertainty in synoptic temperature data sets was drawn by Randel et al. (2004), who have compared several temperature climatologies.

Lee Wave Effects on Temperatures

From the review of literature on PSC particle formation in subsection 6.1.1 it can be seen that details of the PSC occurrence in northern hemisphere winters have attracted much attention in recent years. In this context it has to be mentioned that simulations of Arctic PSC events with global models are especially affected by temperature errors which arise from the low grid resolution: in the Arctic, temperature fluctuations in the lee waves of mountain ranges are important for PSC formation. Buss (2004) shows that a horizontal resolution of 0.125°, i. e. much higher than typically used in global chemistry-GCMs, is required to resolve the PSC relevant wave activity. [3]

Conclusions

In the polar stratosphere of the southern hemisphere winter 2003, the ECMWF operational model simulates temperatures which are a few K lower than those determined in balloon based measurements; in addition, the nudged ECHAM5/-MESSy simulation has a cold bias compared to the ECMWF data set of about 1 K on the average. Both effects combined motivated the simulations with a +4 K temperature shift in chapter 6.

Furthermore, the above quoted temperature uncertainties in synoptic temperature datasets support the line of argument of chapters 5 (Solid PSC Particle Modelling) and 6 (PSC Simulations and Evaluation), in which it is pointed out that errors in input variable values for PSC models propagate into the output. Since the temperature in current synoptic data sets has errors of a few K, PSC simulations based on these data can be expected to reproduce general features of PSC observations but not necessarily individual PSC events.

---

[3] Dörnbrack et al. (2001) and Dörnbrack and Leutbecher (2001) suggested a parameterisation for lee wave effects. Based on a climatology of mountain waves, conditions for PSC formation could be modified in the model for those grid boxes where temperatures are known to fluctuate strongly on a sub-synoptic scale.

Chapter 8

Liquid PSC Particle Scheme

Whereas chapters 4 and 5 deal with solid PSC particles, the simulations of PSC occurrence (chapter 6) and of PSC chemistry (chapter 9) also include liquid PSC particles. This chapter documents the liquid PSC particle scheme in the ECHAM5/MESSy PSC submodel. Within the current work, previously existing program components have been modified. Both the origin of the previous liquid aerosol model and the program improvements are described here.

8.1 Introduction

Liquid sulfate aerosol (abbreviated SSA – stratospheric sulfate aerosol) is ubiquitously present in the stratosphere. In the extreme cold of the polar winter stratosphere, these SSA particles can take up relatively large amounts of HNO_3 and become ternary $H_2O/H_2SO_4/HNO_3$ solutions (STS – supercooled ternary solutions; section 2.2).

In an extensive study based on theoretical considerations and laboratory work, Carslaw et al. (1995a) have investigated the properties of SSA and STS. Carslaw et al. (1995a) developed a predictive thermodynamic model for the water and dissolved acid activities in aqueous solutions of HNO_3, H_2SO_4, and HCl. It is based on the calculation of the excess Gibbs energy per amount-of-substance of the solution. The contribution of long-range and short-range ion-ion interactions to the excess Gibbs energy are considered in summations over all pairs, triples, and quadruples of ions. Equations for other quantities describing the liquid solution can then be derived from the excess Gibbs energy. Different types of data (partial pressure measurements, activities, enthalpies, heat capacities, and hydrate solubilities) can thus be related to the basic model equations and contribute to the determination of interaction parameters. An alternative SSA/STS model by Tabazadeh et al. (1994) is mainly based upon the partial pressure data available for stratospheric temperatures and predicts HNO_3 uptake of liquid aerosol particles at slightly lower temperatures (1 K to 2 K; Carslaw et al. (1997)).

However, the calculation of liquid aerosol particles according to Carslaw et al. (1995a) or Tabazadeh et al. (1994) is too complicated for typical PSC simulations. Therefore, Carslaw et al. (1995b) have developed a parameterisation that approximately reproduces the results of the Carslaw et al. (1995a) model by means of more simple formulas. This parameterisation is implemented in the Mainz Photochemical Box Model for the simulation of PSC microphysics and stratospheric chemistry (Crutzen et al., 1992; Müller, 1994; Grooß, 1996; Meilinger, 2000).

The validity of the Carslaw et al. (1995b) parameterisation is limited to a certain range of input variable values, e. g. to temperatures $185\,\mathrm{K} \leq T \leq 240\,\mathrm{K}$. This validity range covers most of the PSC relevant situations and does not impose severe restrictions for box model studies (e. g. with the Mainz Photochemical Box Model), where temperatures and other input variable values are controllable by the user. In chemistry-GCMs, however, atmospheric variables are calculated interactively within the model. In principle, the chemistry-GCM also reproduces more rare atmospheric situations (e. g. polar stratospheric temperatures below 180 K). Moreover, since a chemistry-GCM is not a perfect representation of the real atmosphere, unrealistic variable values may also occur in simulations. Hence in the liquid particle scheme for the ECHAM5/MESSy PSC submodel precautions had to be taken for input variable values outside the limits of the Carslaw et al. (1995b) parameterisation. Otherwise unreasonable results like negative molalities and even program crashes would occur.

The calculation of SSA and STS in the current work is based on program code from the Mainz Photochemical Box Model. The modifications that have been performed to account for ECHAM5/MESSy variable values outside the range of the Carslaw et al. (1995b) parameterisation are listed in subsection 8.2.1. Similarly, the program routines for the calculation of Henry coefficients (based on Luo et al. (1995) and Huthwelker et al. (1995)) and mass fractions in the Mainz Photochemical Box Model had to be revised (subsections 8.2.2 to 8.2.6) before they could be included in the ECHAM5/MESSy PSC submodel.

8.2 Liquid Aerosol Properties

8.2.1 HNO_3, H_2SO_4 molalities

The following quantities are calculated according to Carslaw et al. (1995b):

$b_{H_2SO_4}$	molality of H_2SO_4 in a binary solution of H_2SO_4 in water (SSA)
b_{HNO_3}	molality of HNO_3 in a binary solution of HNO_3 in water (SSA)
$b_{H_2SO_4\,(\mathrm{tern.})}$	molality of H_2SO_4 in a ternary solution of HNO_3 and H_2SO_4 in water (STS)
$b_{HNO_3\,(\mathrm{tern.})}$	molality of HNO_3 in a ternary solution of HNO_3 and H_2SO_4 in water (STS)
π_{HNO_3}	HNO_3 partitioning, i. e. the fraction $\frac{N_{HNO_3\,(g)}}{N_{HNO_3\,(g)}+N_{HNO_3\,(l)}}$ of HNO_3 molecules remaining in the gas phase, where $N_{HNO_3\,(g)}$ is the number of HNO_3 molecules in the gas phase and $N_{HNO_3\,(l)}$ the number of HNO_3 molecules in the liquid phase

Limitation of T

The validity of the Carslaw et al. (1995b) parameterisation is limited to

$$185\,\mathrm{K} \leq T \leq 240\,\mathrm{K}. \tag{8.1}$$

If the ECHAM5/MESSy temperature is below the lower limit, $T = 185\,\mathrm{K}$ is used for the calculation of $b_{\mathrm{H_2SO_4}}$, $b_{\mathrm{HNO_3}}$, $b_{\mathrm{H_2SO_4\,(tern.)}}$, $b_{\mathrm{HNO_3\,(tern.)}}$, and $\pi_{\mathrm{HNO_3}}$ in the PSC submodel. Note that for temperatures below $T = 185\,\mathrm{K}$ most H_2O and HNO_3 molecules are in the solid phase. Therefore, the error in the liquid aerosol scheme caused by the temperature substitution can be expected to be of little importance.

Similarly temperatures above 240 K are replaced by $T = 240\,\mathrm{K}$ for the calculation of $b_{\mathrm{H_2SO_4}}$ in the PSC submodel. Temperatures in the Junge layer of stratospheric sulfate aerosols are typically below 240 K so that the simulation of realistic atmospheric situations is not affected.

As in the Mainz Photochemical Box Model, the calculations of $b_{\mathrm{HNO_3}}$, $b_{\mathrm{H_2SO_4\,(tern.)}}$, $b_{\mathrm{HNO_3\,(tern.)}}$, and $\pi_{\mathrm{HNO_3}}$ are simplified for temperatures $T > 215\,\mathrm{K}$. The HNO_3 content of liquid aerosols can then be neglected so that

$$\begin{aligned} b_{\mathrm{HNO_3}} &= 0\,\frac{\mathrm{mol}}{\mathrm{kg}} && (8.2)\\ b_{\mathrm{H_2SO_4\,(tern.)}} &= b_{\mathrm{H_2SO_4}} && (8.3)\\ b_{\mathrm{HNO_3\,(tern.)}} &= 0\,\frac{\mathrm{mol}}{\mathrm{kg}} && (8.4)\\ \pi_{\mathrm{HNO_3}} &= 1. && (8.5) \end{aligned}$$

Limitation of $p_{\mathrm{H_2O\,(gl)}}$

$p_{\mathrm{H_2O\,(gl)}}$ is the water vapour pressure for the theoretical situation that no H_2O molecule is in the liquid phase[1]. If it exceeds the validity range given in Carslaw et al. (1995b),

$$0.002\,\mathrm{Pa} \leq p_{\mathrm{H_2O\,(gl)}} \leq 0.2\,\mathrm{Pa}, \tag{8.6}$$

calculations of $b_{\mathrm{H_2SO_4}}$, $b_{\mathrm{HNO_3}}$, $b_{\mathrm{H_2SO_4\,(tern.)}}$, $b_{\mathrm{HNO_3\,(tern.)}}$, and $\pi_{\mathrm{HNO_3}}$ in the PSC submodel are based on the respective limiting values, i. e. on 0.002 Pa for $p_{\mathrm{H_2O\,(gl)}} < 0.002\,\mathrm{Pa}$ and on 0.2 Pa for $p_{\mathrm{H_2O\,(gl)}} > 0.2\,\mathrm{Pa}$. Whereas the upper limit is relatively high for polar stratospheric water vapour pressures, the lower limit has been reached indeed in simulation runs, e. g. if most of the H_2O molecules were in the solid phase. Certain problems that can occur if the liquid particle scheme thus overestimates the available water vapour are dealt with in subsection 8.2.6.

---

[1] The solid phase is not considered here. In the ECHAM5/MESSy PSC submodel only those molecules are available for the liquid particle scheme which have not already been distributed into ice or NAT; more details are given in subsection 6.2.5.

Limitation of x_{HNO_3}

The amount-of-substance ratio of HNO_3 to air, x_{HNO_3}, has to be below 20 $\frac{\mathrm{nmol}}{\mathrm{mol}}$ for the Carslaw et al. (1995b) parameterisation to be applicable. This upper limit could be exceeded in the polar stratosphere. Santee et al. (1999) found amount-of-substance ratios of HNO_3 to air up to 14 $\frac{\mathrm{nmol}}{\mathrm{mol}}$ in UARS/MLS (Upper Atmosphere Research Satellite/Microwave Limb Sounder) observations. Given the vertical resolution of 6 km for the HNO_3 retrieval, local x_{HNO_3} values higher than 20 $\frac{\mathrm{nmol}}{\mathrm{mol}}$ are conceivable. If it happens in a simulation run, the liquid PSC particle scheme uses $x_{\mathrm{HNO}_3} = 20\,\frac{\mathrm{nmol}}{\mathrm{mol}}$ for the calculation of $b_{\mathrm{H_2SO_4\,(tern.)}}$, $b_{\mathrm{HNO_3\,(tern.)}}$, and π_{HNO_3}. This might lead to an underestimation of HNO_3 uptake in special atmospheric situations.

Moreover, it was necessary to also introduce a lower limit for x_{HNO_3}. On rare occasions ECHAM5/MESSy components other than the PSC submodel lead to zero or even slightly negative amount-of-substance ratios of HNO_3. The liquid particle scheme then uses a minimum value ϵ, which depends on the numerical precision of the simulation and is given by the Fortran 95 function "epsilon".

Limitation of $x_{\mathrm{H_2SO_4}}$

For the calculation of $b_{\mathrm{H_2SO_4\,(tern.)}}$ in the Carslaw et al. (1995b) parameterisation, the amount-of-substance ratio of $\mathrm{H_2SO_4}$ to air has to be in the range

$$0.1\,\frac{\mathrm{nmol}}{\mathrm{mol}} \leq x_{\mathrm{H_2SO_4}} \leq 100\,\frac{\mathrm{nmol}}{\mathrm{mol}}. \tag{8.7}$$

$x_{\mathrm{H_2SO_4}}$ outside this range should occur only on rare occasions. If so, the liquid PSC particle uses the respective limiting value instead.

Division by zero

In the Carslaw et al. (1995b) parameterisation, a division by zero occurs in the calculation of b_{HNO_3} for the temperature $T = 211.9101933\,\mathrm{K}$. The reason is that in solving a quadratic equation the special case that the coefficient of the quadratic term is zero has not been considered (Carslaw et al., 1995b, equations (9) and (10)). In the ECHAM5/MESSy PSC submodel, this degenerate case of the quadratic equation is considered and hence the division by zero avoided.

8.2.2 HCl, HBr effective Henry coefficients

The calculation of the effective Henry coefficients of HCl and HBr uses vapour pressure relations from Luo et al. (1995). In addition it is assumed that the mass fractions of HCl and HBr in stratospheric aerosol particles are negligible, and that approximately all $\mathrm{H_2SO_4}$ molecules are in the liquid phase (Carslaw et al., 1997). The validity range of the parameterisation in Luo et al. (1995) is

$$185\,\mathrm{K} < T < 235\,\mathrm{K}. \tag{8.8}$$

In the liquid PSC particle scheme, temperatures below or above these limits are replaced by $T = 185\,\mathrm{K}$ or $T = 235\,\mathrm{K}$. The latter case does not normally occur in the Junge layer of stratospheric sulfate aerosols. Temperatures below $T = 185\,\mathrm{K}$ are observed as well as simulated in the Antarctic polar night stratosphere. If the HCl and HBr effective Henry coefficients vary strongly for those cases, an extension of the Luo et al. (1995) parameterisation would be desirable.

8.2.3 HOCl, HOBr effective Henry coefficients

HOCl effective Henry coefficients are calculated according to Huthwelker et al. (1995). Due to a lack of better HOBr data, a suggestion by Hanson and Ravishankara (1995) is used to relate the HOBr effective Henry coefficient to the one for HOCl. The parameterisation given in Huthwelker et al. (1995) is reliable only where HNO_3 is a minor component of the liquid aerosol droplets. If HNO_3 becomes the dominant solute, the authors recommend to use their formula with $b_{\mathrm{HN0_3}}$ instead of $b_{\mathrm{H_2SO_4}}$ as input parameter. The present work uses this recommendation whereas the Mainz Photochemical Box Model code used the sum $b_{\mathrm{HN0_3}} + b_{\mathrm{H_2SO_4}}$.

8.2.4 HNO_3, H_2SO_4 mass fractions

The mass fractions $w_{\mathrm{HN0_3}}$ and $w_{\mathrm{H_2SO_4}}$ are calculated from the respective molalities with the approximation that masses of species other than H_2O, HNO_3, and H_2SO_4 are negligible in stratospheric liquid aerosol particles.

8.2.5 HCl, HBr, HOCl, HOBr mass fractions

The mass fractions of HCl, HBr, HOCl, and HOBr in stratospheric liquid aerosol particles are calculated from their respective effective Henry coefficients. These calculations use the approximation that only H_2O, HNO_3, and H_2SO_4 contribute to the aerosol mass. Moreover, H_2SO_4 is assumed to be entirely in the liquid phase.

8.2.6 Liquid phase H_2O, HNO_3, HCl, HBr, HOCl, HOBr

The liquid phase composition parameterisation of Carslaw et al. (1995b), Luo et al. (1995), and Huthwelker et al. (1995) relates the liquid phase content of trace gases to variables other than the respective trace gas amount-of-substance ratio.

For example, the molality of binary H_2O/HNO_3 solutions, $b_{\mathrm{HN0_3}}$, is calculated from temperature, pressure, and the total amount-of-substance ratio of water to air; it is not a function of $x_{\mathrm{HNO_3}}$. As a consequence, the parameterisation can calculate relatively high HNO_3 molalities even if HNO_3 is absent.

In the ECHAM5/MESSy PSC submodel, it is explicitly avoided that more H_2O, HNO_3, HCl, HBr, HOCl, or HOBr than available is distributed into the liquid phase.

8.3 Conclusions

The ECHAM5/MESSy PSC submodel calculates liquid PSC particle properties according to Carslaw et al. (1995b), Luo et al. (1995), and Huthwelker et al. (1995). If input values for the liquid particle scheme exceed the scope of the parameterisations of Carslaw et al. (1995b) and Luo et al. (1995), the nearest values still within the definition range of the parameterisation are used instead.

Where atmospheric conditions unsuitable for the Carslaw et al. (1995b) and Luo et al. (1995) formulas can occur naturally, future research will hopefully lead to extended SSA and STS parameterisations.

However, even then input values outside the parameterisation range would have to be considered during the development of a liquid PSC particle scheme because extreme values can always occur due to shortcomings of other model components in a chemistry-GCM. In those cases, a PSC submodel should react in a controlled and documented way.

Chapter 9

PSC Chemistry and Ozone Depletion

The purpose of this chapter is threefold :

- The limitation of reaction rate coefficients for heterogeneous chemical reactions on polar stratospheric clouds is explained (in section 9.2). In this context, some aspects of chemistry simulations with the ECHAM5/-MESSy chemistry submodel MECCA are mentioned (section 9.1).
- The ECHAM5/MESSy tracer family concept is documented (in section 9.3).
- The functionality of the PSC submodel within ECHAM5/MESSy is demonstrated by means of an “ozone hole” simulation (in section 9.4).

The tracer family concept and the reaction rate coefficient limiters are examples of program improvements that have been developed in the course of this work. These are prerequisites for successful PSC chemistry simulations. Finally, results of the Antarctic stratospheric chemistry simulation are compared with MIPAS observations.

9.1 Chemical Reaction Calculation

Elemental chemical reactions of the type

$$\mathrm{A} + \mathrm{B} \longrightarrow \mathrm{C} + \mathrm{D}$$

lead to first order ordinary differential equations for the concentration of the reacting species A, B, C, and D:

$$\frac{dc_{\mathrm{A}}}{dt} = \frac{dc_{\mathrm{B}}}{dt} = -k^{\mathrm{II}}\, c_{\mathrm{A}}\, c_{\mathrm{B}} \qquad (9.1)$$

$$\frac{dc_{\mathrm{C}}}{dt} = \frac{dc_{\mathrm{D}}}{dt} = +k^{\mathrm{II}}\, c_{\mathrm{A}}\, c_{\mathrm{B}} \qquad (9.2)$$

The reaction rate coefficient k^{II} is a positive quantity. It is independent of the concentrations of the reacting species, but typically dependent on the environmental conditions, e. g. the temperature. The superscript “II” marks the reaction as being of second order, i. e. the time derivative is a function of two concentrations.

Hence a set of interdependent chemical reactions like the one listed in section C.1 leads to a set of interdependent ordinary differential equations. The solutions of this set of differential equations are the time dependent concentrations of all reacting tracers.

For the numerical solution of sets of ordinary differential equations, a number of standard methods is available. The ECHAM5/MESSy chemistry submodel MECCA (Sander et al., 2005) uses the "kinetic preprocessor" (KPP) (Damian et al., 2002) to automatically generate computer code for the solution of a user defined set of chemical reactions. MECCA/KPP allows to choose from several solvers for the solution of sets of ordinary differential equations: the Rosenbrock method of 2nd order, the Rosenbrock method of 3rd order, and the Radau method. A number of tests revealed that basically all three solvers are capable of calculating stratospheric chemistry.

The choice of the time step for the chemistry calculation is of high importance. As mentioned in section 3.2, the ECHAM5/MESSy time step Δt is defined by the model meteorology, i. e. it is suitable for the solution of the primitive equations by means of the spectral method. For the simulation of chemical reactions, however, smaller time steps are required; otherwise numerical errors occur (e. g. negative amount-of-substance ratios of tracers to air). Therefore, the ECHAM5/MESSy model time step Δt must be subdivided for the chemistry calculation. On the other hand, smaller time steps are associated with increased computing time, so that chemistry time steps must not be chosen too small either.

Note that the sets of differential equations describing atmospheric chemistry are affected by "stiffness", i. e. the simultaneous presence of equations for fast and for slow processes: a set of slow chemical reactions can be simulated efficiently with relatively large time steps; a set of fast chemical reactions requires small time steps, but quickly leads to the final state, where the calculation can be stopped; mixed sets of slow and fast chemical reactions combine drawbacks of both situations and require small time steps as well as long simulation times.

In principle, the solvers can choose the ideal time step lengths automatically. This option has proven useful for reference simulations. However, the automatic time step method as implemented in the KPP based code calculates solutions with a higher accurracy than required for typical stratospheric chemistry applications. Therefore, user defined fixed time steps seem to be a better choice. The following chemistry time steps have been determined for stable, reasonably accurate and efficient calculations of stratospheric gas phase chemistry with the 2nd order Rosenbrock solver (B. Steil and C. Brühl, pers. comm., 2004; in MECCA, this time step setting is named "ros2-log10"):

$$\begin{array}{rrrrr} 0.0005 \cdot \Delta t, & 0.0015 \cdot \Delta t, & 0.005 \cdot \Delta t, & 0.02 \cdot \Delta t, & 0.06 \cdot \Delta t \\ 0.1 \cdot \Delta t, & 0.15 \cdot \Delta t, & 0.1875 \cdot \Delta t, & 0.23775 \cdot \Delta t, & 0.23775 \cdot \Delta t \end{array}$$

Thus each ECHAM5/MESSy model time step Δt is subdivided into 10 chemistry time steps. The first chemistry time steps within an ECHAM5/MESSy model time step are relatively short, whereas later ones are longer. This corresponds to the fact that the rate of change of tracer concentrations is typically higher in the beginning of a chemical process and converges towards a steady state later on.

Chemical reactions on PSCs tend to be fast compared to gas phase reactions. Therefore, combining stratospheric gas phase chemistry with heterogeneous reactions on PSCs can increase the "stiffness" of the corresponding sets of differential equations. These could possibly still be solved by means of a solver with automatic time step choice. However, to avoid longer computation times it was highly desirable to include PSC chemistry in such a way that still the stratospheric gas phase solver setup could be used (i. e. 2nd order Rosenbrock scheme with 10 chemistry time steps per ECHAM5/MESSy time step). The increase of the stiffness of stratospheric chemistry equations in the presence of PSCs could be avoided by means of the reaction rate coefficient limitation described in the following section.

9.2 Reaction Rate Coefficient Limitation

Introduction

The heterogeneous chemical reactions on/in polar stratospheric cloud particles are of the type

$$\mathrm{A} + \mathrm{B} \longrightarrow \mathrm{C} + \mathrm{D}.$$

Despite the fact that these PSC reactions take place at the surface of, or even in, aerosol particles, they ultimately affect the gas phase. Hence in the context of reaction rate calculations, concentrations are gas phase concentrations. The effect of uptake or sticking characteristics of different trace gases on the reaction rates is included in the reaction rate coefficients.

The ECHAM5/MESSy PSC submodel calculates the second order reaction rate coefficients k^{II} for the reactions listed in section C.3 and passes them on to the ECHAM5/MESSy chemistry submodel MECCA. These k^{II} values must be limited by a maximum value $k^{\mathrm{II}}_{\mathrm{max}}$ for two reasons:

1. The reaction rate coefficient limitation reduces the reaction velocity for relatively fast PSC reactions and thus the stiffness of the stratospheric chemistry differential equation set.

2. The formulas for the calculation of second order reaction rate coefficients for PSC reactions are associated with difficulties and can lead to unreasonably large results.

If $k^{\mathrm{II}}_{\mathrm{max}}$ is set to $10^{-19}\,\frac{\mathrm{m}^3}{\mathrm{s}}$, stratospheric chemistry including PSC reactions can be simulated by means of the 2nd order Rosenbrock scheme with 10 chemistry time steps described in the previous section (C. Kurz, pers. comm., 2004). The less restrictive $k^{\mathrm{II}}_{\mathrm{max}} = 10^{-16}\,\frac{\mathrm{m}^3}{\mathrm{s}}$ is sufficient, if additionally the tracer family scheme (section 9.3) is used to reduce numerical problems associated with tracer advection (C. Brühl, pers. comm., 2004).

Effects of Reaction Rate Coefficient Limitation

The PSC reaction R26,

$$\mathrm{ClONO_2 + H_2O \rightarrow HOCl + HNO_3},$$

will serve as an example to discuss the effect of the reaction rate coefficient limitation.

Similar to equations (9.1) and (9.2), the time dependence of the $\mathrm{ClONO_2}$ concentration due to reaction R26 is

$$\frac{dc_{\mathrm{ClONO_2}}}{dt} = -k^{\mathrm{II}}\, c_{\mathrm{H_2O}}\, c_{\mathrm{ClONO_2}}. \tag{9.3}$$

With $k^{\mathrm{II}} = k^{\mathrm{II}}_{\mathrm{max}} = 10^{-19}\,\frac{\mathrm{m^3}}{\mathrm{s}}$ and $c_{\mathrm{H_2O}} = 10^{19}\,\frac{1}{\mathrm{m^3}}$ (rough estimate for polar stratospheric winter conditions) it follows, that $\mathrm{ClONO_2}$ decays exponentially with an e-folding time of 1 s. For the less restrictive $k^{\mathrm{II}}_{\mathrm{max}} = 10^{-16}\,\frac{\mathrm{m^3}}{\mathrm{s}}$, $\mathrm{ClONO_2}$ decays to a fraction of $\frac{1}{\mathrm{e}}$ of its initial concentration within about 0.001 s.

With either maximum value for the second order reaction rate coefficient, reaction R26 is still capable of consuming $\mathrm{ClONO_2}$ to a large degree within an ECHAM5/MESSy model time step (e. g. 10 min for the horizontal resolution T63).

The $\mathrm{ClONO_2}$ decay via reaction R26 is not counteracted by a fast chemical reaction in the backward direction, i. e. $\mathrm{ClONO_2}$ formation from HOCl and $\mathrm{HNO_3}$. Therefore, the limitation of the second order reaction rate coefficients for heterogeneous chemical reactions on PSC does not disturb a delicate dynamical balance.

Similar arguments apply to the other HCl, HBr, $\mathrm{ClONO_2}$, $\mathrm{BrONO_2}$, and $\mathrm{N_2O_5}$ loss reactions listed in section C.3. Even taking into account the lower reactant concentrations for some of them, the reactions on PSCs can lead to a large degree of chlorine activation, bromine activation, and $\mathrm{N_2O_5}$ decay within less than a day for second order reaction rate coefficients $k^{\mathrm{II}} = k^{\mathrm{II}}_{\mathrm{max}}$, where $k^{\mathrm{II}}_{\mathrm{max}}$ is in the above-mentioned range.

First Order PSC Reactions

First order reaction rate coefficients (symbol: k^{I}) correspond to processes of the type

$$\mathrm{X} \longrightarrow \mathrm{Y},$$

whose temporal development is described by the differential equation

$$\frac{dc_{\mathrm{X}}}{dt} = -k^{\mathrm{I}}\, c_{\mathrm{X}} \tag{9.4}$$

The label "first order" expresses that $\frac{dc_{\mathrm{X}}}{dt}$ depends on exactly one concentration.

The calculation of heterogeneous chemical reactions in the ECHAM5/MESSy PSC submodel is based on parts of the "Mainz Photochemical Box Model" (Crutzen et al., 1992; Müller, 1994; Grooß, 1996; Meilinger, 2000). In the Mainz

Photochemical Box model, heterogeneous reaction rate coefficients for reactions on solid PSC particles are calculated by means of a numerical value equation [1] given in Turco et al. (1989):

$$\frac{k^{\mathrm{I}}}{\frac{1}{\mathrm{s}}} = \frac{\gamma\, 4.56 \cdot 10^4 \sqrt{\frac{\frac{T}{\mathrm{K}}}{\frac{M_{\mathrm{X}}}{\frac{\mathrm{g}}{\mathrm{mol}}}}} \left(\frac{r_{\mathrm{particle}}}{\mathrm{cm}}\right)^2 \frac{C_{\mathrm{X}}}{\frac{1}{\mathrm{cm}^3}} \frac{C_{\mathrm{particle}}}{\frac{1}{\mathrm{cm}^3}}}{1 + 3.3 \cdot 10^4 \frac{\gamma \frac{r_{\mathrm{particle}}}{\mathrm{cm}} \frac{p}{\mathrm{hPa}}}{\frac{T}{\mathrm{K}}}} \tag{9.5}$$

Definitions:

k^{I}: pseudo[2] first order reaction rate coefficient for tracer X

γ: reactive uptake coefficient, also called "reaction probability"

$$\gamma = \frac{\text{number of molecules reacting on collision with particle surface}}{\text{number of collisions with particle surface}} \tag{9.6}$$

T: thermodynamic temperature

M_{X}: molar mass of tracer X

r_{particle}: radius of PSC particle

C_{X}: number concentration of molecules of tracer X

C_{particle}: number concentration of PSC particles

p: pressure

Reaction rate coefficients for chemical reactions on/in liquid PSC particles depend on the aerosol composition. For details see e. g. Carslaw (1994).

The result of equation (9.5) and also of the formulas for chemical reactions on/in liquid particles are pseudo first order reaction rate coefficients k^{I}. The description of chemical reactions on aerosols as first order reactions is common practice (Ammann et al., 2003). Formulas for pseudo first order reaction rate coefficients like equation (9.5) depend on the probability that a molecule of type X impinges on an aerosol surface and also on properties of the chemical reaction under consideration. It is assumed that a reaction partner for molecule X is always available on the aerosol surface.

Currently neither a comprehensive theory nor sufficient experimental data for an entirely satisfying calculation of second order reaction rate coefficients for heterogeneous chemical reactions on PSCs are available.

---

[1] The notation of the numerical values of physical quantities is explained in section B.3.

[2] The adjective "pseudo" refers to the fact that a first order reaction rate coefficient is used here to describe a chemical process which would be formally described by a second order reaction rate coefficient. The relation between first order and second order reaction rate coefficients is explained in more detail in the following subsection "Second Order PSC Reactions".

Second Order PSC Reactions

Despite the fact that PSC reactions are often modelled as first order reactions, they are in fact of the type "A + B $\longrightarrow$ C + D" and described by the differential equations (9.1) and (9.2); see section C.3 for the list of reactions simulated by the ECHAM5/MESSy PSC submodel.

The approximation of second order reactions as first order reactions can be justified if one of the reactants has much larger concentrations than the other. The reaction R26 for example,

$$\mathrm{ClONO_2} + \mathrm{H_2O} \rightarrow \mathrm{HOCl} + \mathrm{HNO_3},$$

consumes the same amount of $ClONO_2$ molecules and H_2O molecules. Since the amount-of-substance ratio of H_2O to air is three orders of magnitude larger than the amount-of-substance ratio of $ClONO_2$ to air, the effect of reaction R26 on the atmospheric water vapour is relatively small (typical values for the polar winter stratosphere: $x_{\mathrm{H_2O}} = 5\,\frac{\mu\mathrm{mol}}{\mathrm{mol}}$ and $x_{\mathrm{ClONO_2}} = 2\,\frac{\mathrm{nmol}}{\mathrm{mol}}$).

The prerequisite that one of the reactants is present in high concentrations is consistent with the derivation of equation (9.5), where one of the reactants is assumed to be always available for reactions on the aerosol particle surface.

For the ECHAM5/MESSy chemistry submodel MECCA, however, second order reaction rate coefficients are required as input from the PSC submodel. For a reaction "A + B $\longrightarrow$ C + D", the relation between the second order reaction rate coefficient and pseudo first order reaction rate coefficients is as follows:

$$\frac{dc_\mathrm{A}}{dt} = -\underbrace{k^\mathrm{II}\,c_\mathrm{A}}_{k^\mathrm{I}_\mathrm{A}}\,c_\mathrm{B} = -\underbrace{k^\mathrm{II}\,c_\mathrm{B}}_{k^\mathrm{I}_\mathrm{B}}\,c_\mathrm{A} \tag{9.7}$$

This shows that two pseudo first order reaction rate coefficients k^I_A and k^I_B can be formed as product of the second order reaction rate coefficient k^II and one of the concentrations c_A or c_B.

As the H_2O concentration is much higher than the $ClONO_2$ concentration, the pseudo first order reaction rate coefficient for reaction R26 is interpreted as product of the second order reaction rate coefficient k^II and the H_2O concentration $c_{\mathrm{H_2O}}$:

$$\frac{dc_{\mathrm{ClONO_2}}}{dt} = -k^\mathrm{I}_{\mathrm{H_2O}}\,c_{\mathrm{ClONO_2}} = -\left(k^\mathrm{II}\,c_{\mathrm{H_2O}}\right)\,c_{\mathrm{ClONO_2}}. \tag{9.8}$$

Therefore the second order reaction rate coefficient k^II can be calculated from the pseudo first order reaction rate coefficient $k^\mathrm{I}_{\mathrm{H_2O}}$ as follows:

$$k^\mathrm{II} = \frac{k^\mathrm{I}_{\mathrm{H_2O}}}{c_{\mathrm{H_2O}}}. \tag{9.9}$$

The traditional usage of pseudo first order reaction rate coefficients for PSC chemistry assumes that one of the reactants is available in excess and its concentration is included in the reaction rate coefficient. However, PSC chemistry can violate this condition. $ClONO_2$ and HCl, for example, can have similar concentrations in the Arctic winter stratosphere (Müller et al., 1994) and are both reactants in PSC reaction R25:

$$\mathrm{ClONO_2 + HCl \rightarrow Cl_2 + HNO_3},$$

For reaction R25, the pseudo first order reaction rate coefficient $k^{\mathrm{I}}_{\mathrm{HCl}}$ is calculated by equation (9.5) and the second order reaction rate coefficient is, therefore, calculated via division by c_{HCl}.

In situations where HCl is no longer in excess, the application of equation (9.5), which assumes a $\mathrm{ClONO_2}$ decay which is independent of the HCl concentration, becomes dubious. The limitation of second order reaction rate coefficients relieves this problem. Whilst unmodified second order reaction rate coefficients can become very high for low HCl concentrations,

$$k^{\mathrm{II}} = \frac{k^{\mathrm{I}}_{\mathrm{HCl}}}{c_{\mathrm{HCl}}}, \tag{9.10}$$

second order reaction rate coefficients in the ECHAM5/MESSy PSC submodel are set to $k^{\mathrm{II}}_{\mathrm{max}}$ in those cases. It follows then from the differential equation

$$\frac{dc_{\mathrm{ClONO_2}}}{dt} = -\left(k^{\mathrm{II}}_{\mathrm{max}}\, c_{\mathrm{HCl}}\right) c_{\mathrm{ClONO_2}} \tag{9.11}$$

that small HCl concentrations lead to small $\mathrm{ClONO_2}$ decay, as would be expected from chemical reactions with low reactant concentrations.

Uncertainties in the Reaction Rate Calculation

It has been shown above that the limitation of reaction rate coefficients for PSC chemistry can be expected to lead to qualitatively reasonable results. However, the question arises to which degree quantitative agreement can be achieved between simulations and real atmospheric processes in the polar stratosphere. In this context, the following uncertainties should be considered:

- Only synoptic values are known for atmospheric variables like temperature in a global chemistry-GCM. Due to the non-linear dependence of reaction rates on temperatures, spatially averaged temperatures cannot be expected to lead to correct average tracer concentrations (Murphy and Ravishankara, 1994; Edouard et al., 1996; Borrmann et al., 1997; Carslaw et al., 1998).

- Simulated PSC occurrence and observed PSC occurrence differ considerably (chapter 6).

- For heterogeneous reaction rate calculations, knowledge of the available surface area is required. Both laboratory experiments (with Knudsen cells or flow tube reactors) and simulations use simple macroscopic estimates for the ice and NAT surfaces. Depending on its roughness, the microscopic ice/NAT surface can be much larger.

- For several reactions on certain types of PSC particles listed in section C.3, no laboratory data is available for the reactive uptake coefficients γ. Therefore, the calculation of the corresponding reaction rate coefficients has to rely on estimated γ values.
- The derivation of equation (9.5) for the calculation of pseudo first order reaction rates is of heuristic nature and uses several approximations (Ammann et al., 2003). For example it is assumed that the surface concentration of reactants is controlled by reactive processes and not by adsorption/desorption (Turco et al., 1989). The use of more sophisticated reaction rate coefficient calculations would require knowledge of details of the reaction process (e. g. laboratory data on the adsorption characteristics of various trace gases on PSC particle surfaces), which is currently not available.

Given these large uncertainties, more than a qualitatively reasonable behaviour cannot be expected from a PSC chemistry scheme. In the ECHAM5/MESSy PSC submodel, heterogeneous chemical processing in agreement with expectations has been achieved in a simple and computationally efficient way by limiting the second order reaction rate coefficients.

9.3 Tracer Families

As a preparation for simulations of atmospheric chemistry, a tracer familiy scheme has been developed for ECHAM5/MESSy[3].

Traditional versus ECHAM5/MESSy Tracer Families

Tracer families are a well-established approach for reducing the stiffness of chemical reaction sets (Wayne, 2000, pp. 147/148). If fast chemical reactions lead to an approximate chemical equilibrium among a set of tracers (the "tracer family") A_1, A_2, ..., A_n, these chemical reactions need not be explicitly calculated. Their effect can be approximated by setting the concentration ratios within the tracer family constant:

$$\frac{c_{\mathrm{A}_i}}{c_{\mathrm{A}_j}} = \text{const.} \quad \forall \ i,j \ \in \ \{1,2,\ldots,n\} \tag{9.12}$$

As a side effect, the tracer family can be regarded as a single tracer for the advection calculation.

The ECHAM5/MESSy tracer family concept is more general insofar as conversions between the single tracer mode and the family mode are possible at any time during a model time step. Thus modelled atmospheric processes (including, but not limited to chemistry and advection) can affect the whole family as well as single tracers.

---

[3] The algorithm described in this section has been designed within this thesis. The integration of the tracer family scheme in ECHAM5/MESSy was accomplished by P. Jöckel. A. Kerkweg has contributed with helpful suggestions.

In the stratospheric chemistry simulation presented in section 9.4, the tracer family scheme has been applied exclusively to avoid strong spatial gradients in the concentrations of advected species. Thus numerical difficulties with the advection of highly inhomogeneously distributed tracers are relieved.

Definitions

- The standard way of representing tracers in ECHAM5/MESSy will be called “single tracer mode”. The alternative tracer representation introduced in the ECHAM5/MESSy tracer family scheme will be called “family tracer mode”.
- x_i is the amount-of-substance ratio of tracer i to air in the single tracer mode. Chemical, microphysical, and meteorological processes simulated by ECHAM5/MESSy lead to changes of x_i: Δx_i. The difference quotient $\left(\frac{\Delta x_i}{\Delta t}\right)$ is called tracer tendency. For each tracer in ECHAM5/MESSy, there is also a tracer tendency as a corresponding model variable.
- In tracer family mode, not the ordinary amount-of-substance ratios of tracers to air but fractions of tracers in their respective families are stored in the tracer variables and tracer tendency variables. For those cases, the variable symbols ξ_i and ξ'_i will be used in this description (ξ'_i is an updated version of ξ_i, see below for details).
- x_{family} represents the tracer family; $\left(\frac{\Delta x_{\text{family}}}{\Delta t}\right)$ is a tendency for the tracer family.
- The variables κ_i are scaling factors that can be applied during the collection of tracers into families. If all κ_i are 1.0, the tracer family concept conserves the number of molecules. For other choices of κ_i, other quantities are conserved. For example, if all tracers in a tracer family were scaled with their molecular weights, the family concept would conserve mass. If all tracers in a tracer family were scaled with the number of chlorine atoms per molecule, the family concept would conserve the number of chlorine atoms.

Algorithm Description

First the standard conversions between single tracer mode and family tracer mode are explained. The first and the last conversion within a model time step require special treatment and are explained in the end.

1 *Before single tracer mode to family tracer mode conversion*: In the single tracer mode the variable x_i contains the amount-of-substance ratio of tracer i to air from the beginning of the time step (i. e. from after the first conversion into single tracer mode). The variable $\left(\frac{\Delta x_i}{\Delta t}\right)$ is the tracer tendency of all processes that have had an effect on tracer i so far within the current time step. x_{family} and $\left(\frac{\Delta x_{\text{family}}}{\Delta t}\right)$ are zero.

2a *Single tracer mode to family tracer mode conversion*: x_{family} and $\left(\frac{\Delta x_{\text{family}}}{\Delta t}\right)$ are weighted sums of single tracer variables.

$$x_{\text{family}} = \sum_{i \,\in\, \text{family}} x_i \cdot \kappa_i \tag{9.13}$$

$$\left(\frac{\Delta x_{\text{family}}}{\Delta t}\right) = \sum_{i \,\in\, \text{family}} \left(\frac{\Delta x_i}{\Delta t}\right) \cdot \kappa_i \tag{9.14}$$

2b *Single tracer mode to family tracer mode conversion*: ξ_i and ξ_i' are weighted fractions of the single tracers in the tracer family. ξ_i' is an up-to-date version of ξ_i.

$$\xi_i = \frac{x_i \cdot \kappa_i}{x_{\text{family}}} \tag{9.15}$$

$$\xi_i' = \frac{\left(x_i + \left(\frac{\Delta x_i}{\Delta t}\right) \cdot \Delta t\right) \cdot \kappa_i}{x_{\text{family}} + \left(\frac{\Delta x_{\text{family}}}{\Delta t}\right) \cdot \Delta t} \tag{9.16}$$

3 Processes affecting the tracer family now change $\left(\frac{\Delta x_{\text{family}}}{\Delta t}\right)$.

4a *Family tracer mode to single tracer mode conversion*: Amount-of-substance ratios x_i are reconstructed.

$$x_i = \frac{x_{\text{family}} \cdot \xi_i}{\kappa_i} \tag{9.17}$$

4b *Family tracer mode to single tracer mode conversion*: $\left(\frac{\Delta x_i}{\Delta t}\right)$ is now calculated from the difference between the product of the up-to-date amount-of-substance ratio of the tracer family to air, $\left(x_{\text{family}} + \left(\frac{\Delta x_{\text{family}}}{\Delta t}\right) \cdot \Delta t\right)$, with the up-to-date tracer fraction, $\frac{\xi_i'}{\kappa_i}$, and the old amount-of-substance ratio x_i:

$$\left(\frac{\Delta x_i}{\Delta t}\right) = \frac{\left(x_{\text{family}} + \left(\frac{\Delta x_{\text{family}}}{\Delta t}\right) \cdot \Delta t\right) \cdot \frac{\xi_i'}{\kappa_i} - x_i}{\Delta t} \tag{9.18}$$

5 *End of model time step (special case)*: The single tracer variables are converted to family mode as normal (equations 9.13 and 9.14). However, the calculation of ξ_i and ξ_i' is different now. Remember that in family mode the tracer fractions ξ_i' do not contain tracer tendencies. ECHAM5/-MESSy, however, still treats these variables as tracer tendencies and adds them (multiplied with the model time step) to the amount-of-substance ratios of tracers to air at the end of the time step. Special measures ensure that the family mechanism is not disturbed at the end of the model time step: the up-to-date-fractions are now stored in the tracer variables

$$\xi_i = \frac{\left(x_i + \left(\frac{\Delta x_i}{\Delta t}\right) \cdot \Delta t\right) \cdot \kappa_i}{x_{\text{family}} + \left(\frac{\Delta x_{\text{family}}}{\Delta t}\right) \cdot \Delta t} \tag{9.19}$$

whereas the variables ξ_i' are set to zero.

6 *Beginning of model time step (special case)*: At the beginning of the model time step ξ_i contains tracer fractions from the end of the last model time step, ξ_i' is zero, x_{family} contains the amount-of-substance ratio of the tracer family to air updated by the leapfrog mechanism and $\left(\frac{\Delta x_{\text{family}}}{\Delta t}\right)$ is the advection tendency for the tracer family. After copying the tracer fractions from the end of the last model time step into ξ_i', $\xi_i' = \xi_i$, an ordinary transformation from family tracer mode to single tracer mode can be performed (equations 9.17 and 9.18).

Application to Stratospheric Chemistry

The use of tracer families for reactive chlorine, bromine, and nitrogen compounds is required for calculations of stratospheric chemistry with the standard advection scheme (see section 3.2) and the chemistry solver settings described in section 9.1. The following family definitions are recommended (C. Brühl, pers. comm., 2004):

ClO_x Cl, ClO, HOCl, OClO, Cl_2 ($\kappa_{\text{Cl}} = 2$), Cl_2O_2 ($\kappa_{\text{Cl}_2\text{O}_2} = 2$)

BrO_x Br, BrO, HOBr, BrCl, Br_2 ($\kappa_{\text{Br}_2} = 2$)

NO_x N, NO, NO_2, NO_3, N_2O_5 ($\kappa_{\text{N}_2\text{O}_5} = 2$)

As indicated in brackets, weighting factors for the active chlorine family ClO_x are set in such a way that the number of chlorine atoms is conserved in the transformations between single tracer mode and family tracer mode. Correspondingly, the number of bromine atoms is conserved for the active bromine family and the number of nitrogen atoms for the active nitrogen family NO_x.

9.4 Polar Stratospheric Chemistry Simulations

9.4.1 Simulations

In the following subsections, results from two simulation runs are presented and compared with observations. The first of the two simulation runs has already been described in subsection 6.3.1. It included all chemical reactions listed in appendix C. The second simulation run is largely similar, however, heterogeneous chemical reactions on polar stratospheric particles are excluded. Thus the comparison of both simulation runs illustrates the effect of PSC chemistry. The nudging technique (section 3.4) is applied in both simulations to reproduce the meteorology of the Antarctic winter 2003.

Initial trace gas distributions for the start of both simulation runs (1 May 2003) have been adopted from a previous ECHAM5/MESSy simulation (C. Brühl, pers. comm., 2005).

9.4.2 MIPAS Data

For late July 2003 and late October 2003, MIPAS observations of trace gas distributions were available for comparison. A brief introduction to the MIPAS instrument on board of ENVISAT is given in section 2.5. General information about the MIPAS data retrieval can be found in Stiller et al. (2003), von Clarmann et al. (2003a), and von Clarmann et al. (2003b). Specific information about the HNO_3 and H_2O analysis is presented in Stiller et al. (2005) and Milz et al. (2005), respectively. The ozone retrieval is explained in further detail in Lopez-Puertas et al. (2005).

The MIPAS analysis data described in these references has a vertical resolution of 1 km. For the current purpose, ECHAM5/MESSy simulation data from single vertical model levels are illustrated together with MIPAS analysis data points that fall within this vertical level. As the ECHAM5/MESSy vertical resolution for the current work is $\gtrsim 2\,\mathrm{km}$, sometimes two MIPAS analysis data values are available for a single horizontal location. In those cases, the average of these two values is used.

9.4.3 Denitrification and Dehydration

Figure 9.1 compares MIPAS observations and simulation results (from the simulation run with PSC chemistry) for gas phase HNO_3 in three vertical levels. Both MIPAS analysis and the simulation show negligible amount-of-substance ratios of HNO_3 to air inside the polar vortex due to denitrification. Simulated amount-of-substance ratios of HNO_3 to air outside the polar vortex are too low. This is consistent with the findings of section 6.3 and can be attributed to the initialisation at 1 May 2003.

Simulated $x_{\mathrm{H_2O}}$ values (figure 9.2) agree well with MIPAS observations outside the polar vortex. Inside the polar vortex, simulated dehydration seems to be too strong. This can partially be attributed to a cold bias of a few K in the simulation (chapter 7). However, it is also conceivable that the solid PSC particle size scheme overestimates PSC particle sizes and, therefore, sedimentation velocities. As described in chapter 5, the modelling of PSC particle sizes is associated with relatively large uncertainties since there are only few measurements for model evaluation.

A comparison of the simulation results with climatological HNO_3 and H_2O data from Nedoluha et al. (2003), Steil et al. (2003), Manzini et al. (2003), and Santee et al. (2004) confirm these findings: the simulation reproduces denitrification inside the polar vortex and $x_{\mathrm{H_2O}}$ outside the polar vortex well, whereas $x_{\mathrm{HNO_3}}$ outside the polar vortex is underestimated and dehydration probably too strong.

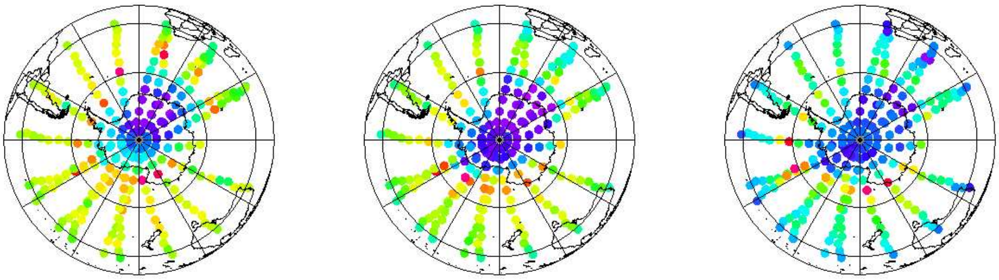

(a) $p = 42\,\mathrm{hPa}$ (b) $p = 54\,\mathrm{hPa}$ (c) $p = 70\,\mathrm{hPa}$

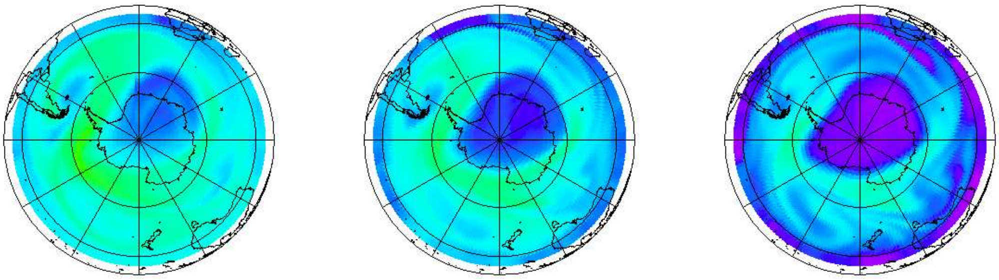

(d) $p = 42\,\mathrm{hPa}$ (e) $p = 54\,\mathrm{hPa}$ (f) $p = 70\,\mathrm{hPa}$

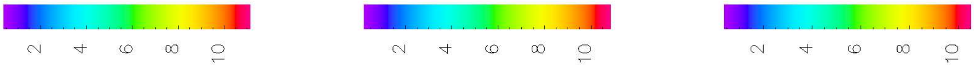

(g) $\frac{x_{\mathrm{HNO_3}}}{\frac{\mathrm{nmol}}{\mathrm{mol}}}$ at $42\,\mathrm{hPa}$ (h) $\frac{x_{\mathrm{HNO_3}}}{\frac{\mathrm{nmol}}{\mathrm{mol}}}$ at $54\,\mathrm{hPa}$ (i) $\frac{x_{\mathrm{HNO_3}}}{\frac{\mathrm{nmol}}{\mathrm{mol}}}$ at $70\,\mathrm{hPa}$

Figure 9.1: Amount-of-substance ratios of HNO_3 to air for 21 October 2003. First row: MIPAS observations; second row: simulation including PSC chemistry.

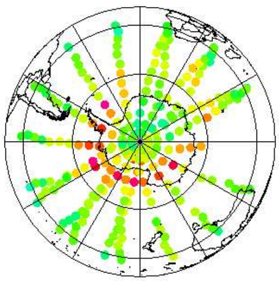

(a) $p = 42\,\mathrm{hPa}$ (b) $p = 54\,\mathrm{hPa}$ (c) $p = 70\,\mathrm{hPa}$

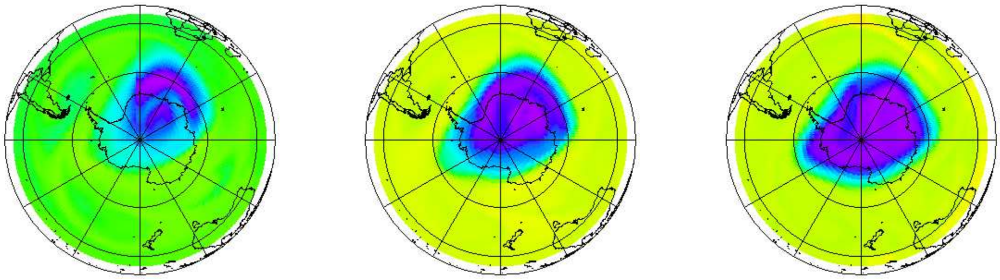

(d) $p = 42\,\mathrm{hPa}$ (e) $p = 54\,\mathrm{hPa}$ (f) $p = 70\,\mathrm{hPa}$

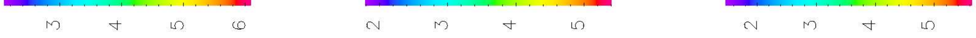

(g) $\frac{x_{\mathrm{H_2O}}}{\frac{\mu\mathrm{mol}}{\mathrm{mol}}}$ at $42\,\mathrm{hPa}$ (h) $\frac{x_{\mathrm{H_2O}}}{\frac{\mu\mathrm{mol}}{\mathrm{mol}}}$ at $54\,\mathrm{hPa}$ (i) $\frac{x_{\mathrm{H_2O}}}{\frac{\mu\mathrm{mol}}{\mathrm{mol}}}$ at $70\,\mathrm{hPa}$

Figure 9.2: Amount-of-substance ratios of H_2O to air for 21 October 2003. First row: MIPAS observations; second row: simulation including PSC chemistry.

9.4.4 Chlorine Activation

The figures 9.3, 9.4, and 9.5 demonstrate chlorine activation due to PSCs. Figures 9.3(a), 9.4(a), and 9.5(a) correspond to the simulation run with PSC chemistry, figures 9.3(b), 9.4(b), and 9.5(b) are based on results from the simulation without PSC chemistry. The principles of chlorine activation have been explained in section 2.4. Briefly, in the presence of PSC particles, the reservoir species $\mathrm{ClONO_2}$ and HCl are converted into active chlorine species, which are summarised as ClO_x.

As can be seen from the comparison of figure 9.3(a) with figure 9.3(b), ClO_x in the polar vortex is present in relevant amounts only as a result of PSC chemistry. The most prominent feature of figure 9.4(a) is the so called "chlorine nitrate collar". At the edge of the polar vortex, ClO from inside the vortex mixes with $\mathrm{NO_2}$ from outside the polar vortex and forms $\mathrm{ClONO_2}$. The high amount-of-substance ratios of HCl in figure 9.5(b) are a consequence of downward transport inside the polar vortex during the winter. Thus a realistic modelling of this process is a prerequisite for the chlorine activation shown in figure 9.3(a).

At the time of writing, no suitable MIPAS observation for early October were available. The amount-of-substance ratios of chlorine species to air are thus compared with results of the chemistry-GCM MA-ECHAM4/CHEM as well as with measurements of the UARS satellite instruments HALOE and MLS (Steil et al., 2003; Manzini et al., 2003; Santee et al., 2003). The results of the ECHAM5/MESSy simulation including PSC chemistry are in reasonable agreement with these climatological values. However, maximum values for the sum of inorganic chlorine species in the simulation ($\approx 2.5\,\frac{\mathrm{nmol}}{\mathrm{mol}}$) are rather low compared to observations ($\gtrsim 2.8\,\frac{\mathrm{nmol}}{\mathrm{mol}}$). This discrepancy is probably caused by an underestimation of downward transport in the polar vortex in ECHAM5/-MESSy (C. Brühl and B. Steil, pers. comm., 2005).

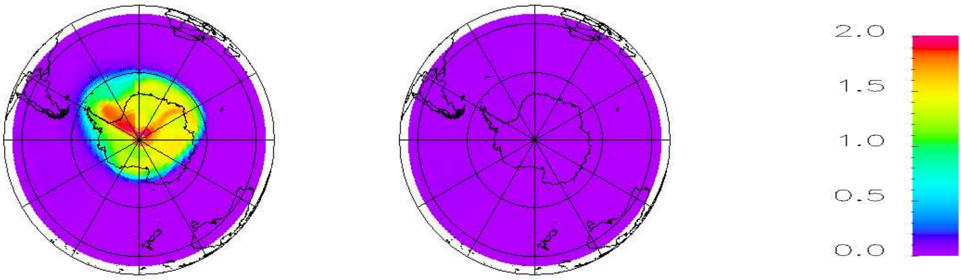

(a) Simulation with PSC chemistry

(b) Simulation without PSC chemistry

(c) $\frac{x_{\mathrm{ClO}_x}}{\frac{\mathrm{nmol}}{\mathrm{mol}}}$

Figure 9.3: Amount-of-substance ratios of ClO_x to air in $\frac{\mathrm{nmol}}{\mathrm{mol}}$ for 1 October 2003 at 54 hPa.

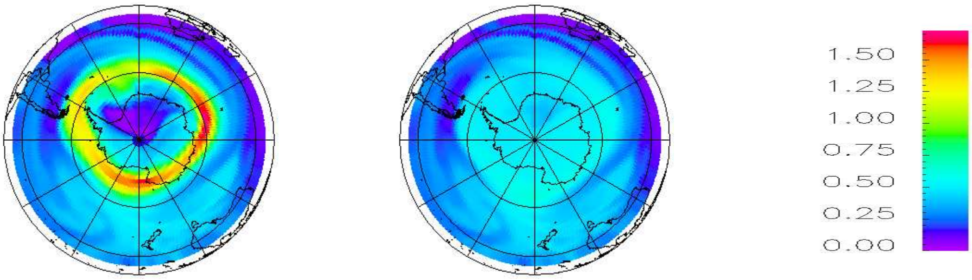

(a) Simulation with PSC chemistry

(b) Simulation without PSC chemistry

(c) $\frac{x_{\mathrm{ClONO_2}}}{\frac{\mathrm{nmol}}{\mathrm{mol}}}$

Figure 9.4: Amount-of-substance ratios of $\mathrm{ClONO_2}$ to air in $\frac{\mathrm{nmol}}{\mathrm{mol}}$ for 1 October 2003 at 54 hPa.

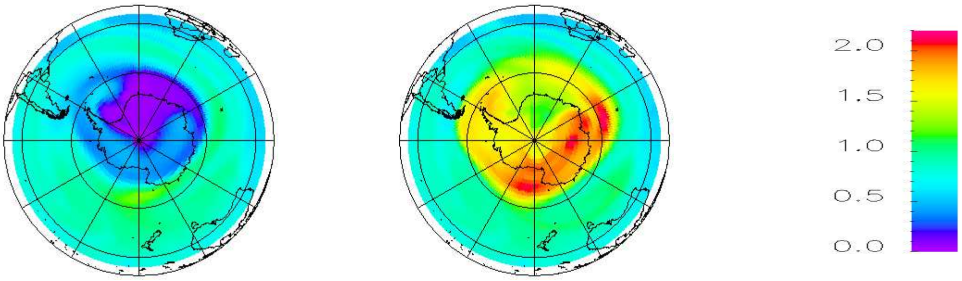

(a) Simulation with PSC chemistry

(b) Simulation without PSC chemistry

(c) $\frac{x_{\mathrm{HCl}}}{\frac{\mathrm{nmol}}{\mathrm{mol}}}$

Figure 9.5: Amount-of-substance ratios of HCl to air in $\frac{\mathrm{nmol}}{\mathrm{mol}}$ for 1 October 2003 at 54 hPa.

9.4.5 Bromine Activation

The figures 9.6, 9.7, and 9.8 demonstrate bromine activation due to PSCs. Figures 9.6(a), 9.7(a), and 9.8(a) correspond to the simulation run with PSC chemistry, figures 9.6(b), 9.7(b), and 9.8(b) are based on results from the simulation without PSC chemistry.

In contrast to active chlorine (ClO_x), active bromine species (summarised as BrO_x) are not only formed in heterogeneous reactions on PSC particles but also by gas phase photochemical reactions. Thus BrO_x is not only present in the polar vortex in the simulation run including PSC chemistry (figure 9.6(a)) but to some degree also on the whole sunlit hemisphere in both figures 9.6(a) and 9.6(b) (the simulated BrO_x values correspond to 15:50 UTC).

The comparison of figures 9.7 and 9.8 reveals that inactive bromine is present as BrNO_3 rather than in form of HBr. The higher HBr values in the simulation run with PSC chemistry (figure 9.8(a)) compared to the simulation run without PSC chemistry (figure 9.8(b)) are an indirect effect of the heterogeneous chemical reactions listed in table 2.8 and in section C.3: both HBr and BrNO_3 are converted into active bromine BrO_x. The ratio of x_{HBr} to x_{BrNO_3} produced from BrO_x in de-activation reactions then depends on the environmental conditions (e. g. the abundances of ozone and methane).

Observational data for the comparison with simulation results for bromine species is scarce. In view of the discussions in WMO (2003), the peak x_{BrO_x} values in the simulation with PSC chemistry are probably too low ($x_{\mathrm{BrO}_x} \approx 14\,\frac{\mathrm{pmol}}{\mathrm{mol}}$ instead of $x_{\mathrm{BrO}_x} \approx 20\,\frac{\mathrm{pmol}}{\mathrm{mol}}$). Since this low bias of roughly 25 % corresponds to an underestimation of the total bromine load of the stratosphere in the data set used for initialisation, it is not interpreted as indication for errors in the simulation of stratospheric chemistry. The underestimation of total stratospheric bromine load in the previous simulation run from which the inital data was derived can be explained partially by the neglect of short-lived source gases for anorganic bromine, e. g. bromoform (CHBr_3).

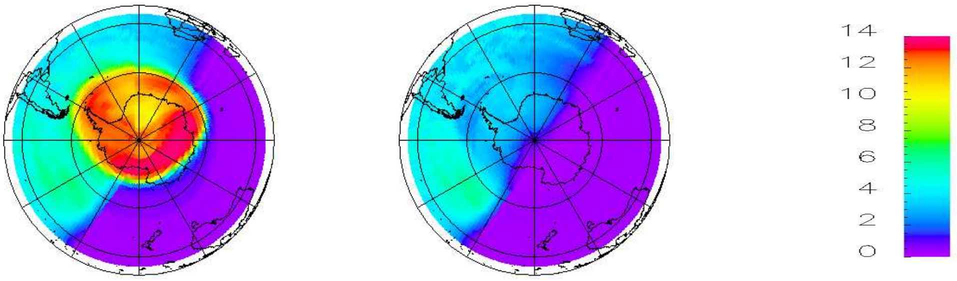

(a) Simulation with PSC chemistry

(b) Simulation without PSC chemistry

(c) $\frac{x_{\mathrm{BrO}_x}}{\frac{\mathrm{pmol}}{\mathrm{mol}}}$

Figure 9.6: Amount-of-substance ratios of BrO_x to air in $\frac{\mathrm{pmol}}{\mathrm{mol}}$ for 1 October 2003 at 54 hPa.

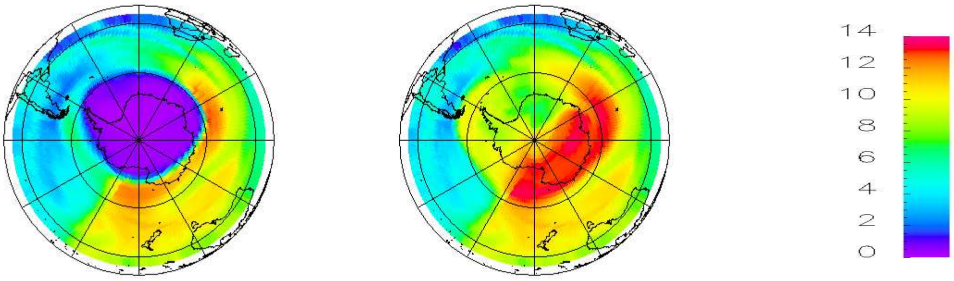

(a) Simulation with PSC chemistry

(b) Simulation without PSC chemistry

(c) $\frac{x_{\mathrm{BrNO_3}}}{\frac{\mathrm{pmol}}{\mathrm{mol}}}$

Figure 9.7: Amount-of-substance ratios of $\mathrm{BrNO_3}$ to air in $\frac{\mathrm{pmol}}{\mathrm{mol}}$ for 1 October 2003 at 54 hPa.

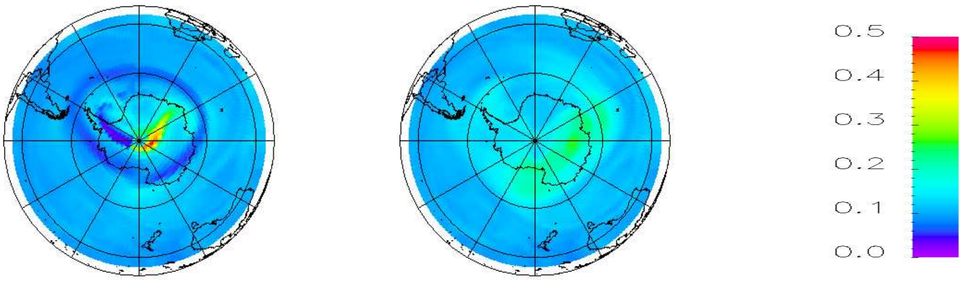

(a) Simulation with PSC chemistry

(b) Simulation without PSC chemistry

(c) $\frac{x_{\mathrm{HBr}}}{\frac{\mathrm{pmol}}{\mathrm{mol}}}$

Figure 9.8: Amount-of-substance ratios of HBr to air in $\frac{\mathrm{pmol}}{\mathrm{mol}}$ for 1 October 2003 at 54 hPa.

9.4.6 Ozone Hole

The overview of PSC chemistry is finalised with a presentation of the ozone hole in figure 9.9. Figures 9.9(a), 9.9(b), and 9.9(c) (i. e. the first row) show MIPAS analysis data. Figures 9.9(d), 9.9(e), and 9.9(f) (the second row) are based on the simulation run with PSC chemistry; figures 9.9(g), 9.9(h), and 9.9(i) demonstrate that the ozone hole does not appear in the simulation run without PSC chemistry.

Important features of the ozone hole are reproduced well in the simulation with PSC chemistry. The minimum ozone values in the polar vortex, however, are too high (ca. $1 \, \frac{\mu\text{mol}}{\text{mol}}$ instead of near zero). This is consistent with the findings of subsections 9.4.4 and 9.4.5 that both the total inorganic chlorine and reactive bromine are underestimated in the simulation.

Another possible explanation for too high ozone values in the late October polar vortex has been given in chapter 7: in the ECHAM5/MESSy simulation run the polar vortex has been too unstable in the middle of October; this could have led to some inflow of air from outside the polar vortex. However, this would have also increased the amount-of-substance ratios of HNO_3 and H_2O to air inside the polar vortex, which is inconsistent with the strong denitrification and dehydration shown in subsection 9.4.3.

Except for the bias in simulated ozone depletion, it is concluded that both the MIPAS analysis and the ECHAM5/MESSy simulation results are in reasonable agreement with HALOE observations and MA-ECHAM4/CHEM simulation results (Brühl et al., 1996; Steil et al., 2003; Manzini et al., 2003).

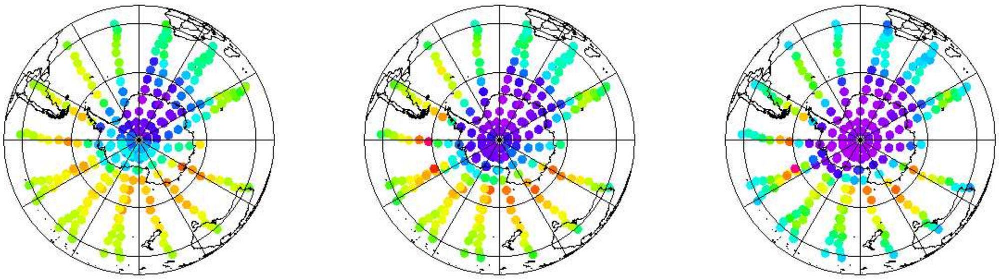

(a) $p = 42\,\mathrm{hPa}$ (b) $p = 54\,\mathrm{hPa}$ (c) $p = 70\,\mathrm{hPa}$

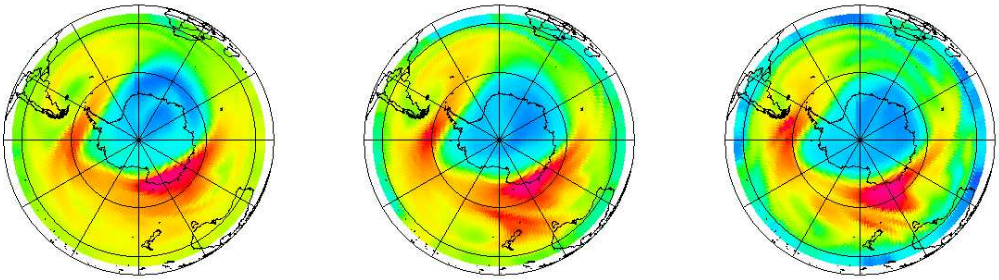

(d) $p = 42\,\mathrm{hPa}$ (e) $p = 54\,\mathrm{hPa}$ (f) $p = 70\,\mathrm{hPa}$

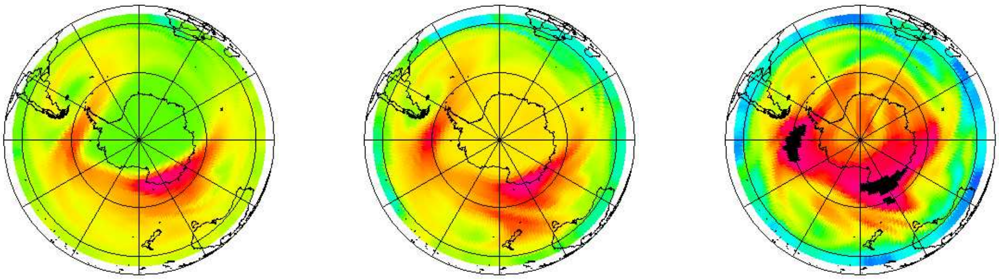

(g) $p = 42\,\mathrm{hPa}$ (h) $p = 54\,\mathrm{hPa}$ (i) $p = 70\,\mathrm{hPa}$

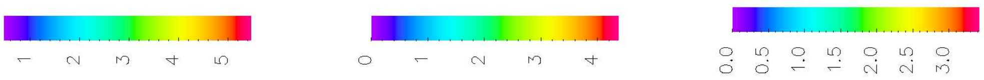

(j) $\frac{x_{\mathrm{O}_3}}{\frac{\mu\mathrm{mol}}{\mathrm{mol}}}$ at 42 hPa (k) $\frac{x_{\mathrm{O}_3}}{\frac{\mu\mathrm{mol}}{\mathrm{mol}}}$ at 54 hPa (l) $\frac{x_{\mathrm{O}_3}}{\frac{\mu\mathrm{mol}}{\mathrm{mol}}}$ at 70 hPa

Figure 9.9: Amount-of-substance ratio of ozone to air for 21 October 2003. First row: MIPAS observations; second row: simulation including PSC chemistry; third row: simulation without PSC chemistry.

Chapter 10

Summary and Outlook

A PSC submodel for the chemistry-GCM ECHAM5/MESSy has been developed and implemented. PSC particle microphysics and sedimentation as well as heterogeneous chemical reactions on PSC particles can thus be simulated with ECHAM5/MESSy.

Solid PSC particle sedimentation

For solid PSC particle sedimentation, the need for a thorough revision of previously used algorithms has been elucidated. A sedimentation scheme based on first order approximations of vertical amount-of-substance ratio profiles has been developed to address certain inconsistencies in PSC sedimentation schemes that rely on advection routines. This PSC particle sedimentation method has been compared with a more simple alternative and an advection scheme. It is concluded that the new first order sedimentation scheme is most suitable for solid PSC particle sedimentation in ECHAM5/MESSy. (Chapter 4)

Solid PSC Particle Modelling

For the determination of solid PSC particle sizes, an efficient algorithm has been adapted. It is based on the assumption of thermodynamic equilibrium between the gas phase and the solid phase. Particles are modelled as spherical and monodisperse within each ECHAM5/MESSy grid box. Combined sedimentation and solid PSC particle size tests document that the PSC submodel produces particle number densities and radii within the observed range. (Chapter 5)

PSC Simulations and Evaluation

The formation of solid PSC particles, especially of NAT, is highly disputed in the stratospheric research community. Two particle formation schemes in accordance with the most widespread approaches have been identified and implemented. The modelling approach that NAT forms only on preexisting ice or NAT has been shown to be superior to the temperature barrier method, where NAT can form 3 K below the NAT equilibrium temperature. Furthermore, it has been tested whether advected ice and NAT should be allowed to bypass the formation thresholds for ice and NAT. A comparative study reveals that it is preferable not to take advected ice and NAT into account in the particle formation scheme. (Chapter 6)

Liquid PSC particle scheme

To the extent possible, existing program code has been adapted for use in the ECHAM5/MESSy PSC submodel. An example for technical improvements of previously existing program routines are modifications of the liquid particle scheme. Parameterisations for the calculation of the composition of stratospheric sulfate aerosols and stratospheric ternary solutions have been made applicable to chemistry-GCM simulations (Chapter 8).

PSC particle occurrence

The solid PSC particle microphysics and sedimentation schemes combined with the liquid PSC particle model allow simulations of PSC occurrence. Due to the sparse measurement data, previously the evaluation of simulated PSC occurrence was often restricted to anecdotal or indirect evidence. For this work, new observational data was available. In chapter 6 a model evaluation method is suggested and applied, which compares ECHAM5/MESSy PSC simulations with about 56000 MIPAS observations during the Antarctic winter 2003. It reveals limited agreement between details of the simulated PSC occurrence and MIPAS analysis data. The discrepancies found can be ascribed to the use of synoptic ECHAM5/MESSy model variables as input for the PSC submodel and to uncertainties in the H_2O and HNO_3 distribution. The overall simulated relative PSC occurrence frequency, which is more relevant for simulations of polar ozone depletion, matches observations well.

Heterogeneous chemical reactions on PSCs

In chapter 1, the link between polar stratospheric clouds and ozone depletion has been emphasised. Therefore, the PSC submodel development is finalised with a simulation of atmospheric chemistry in the Antarctic spring stratosphere. The simulated trace gas distributions are compared with MIPAS measurements and with results from the chemistry-climate model MAECHAM4/CHEM. Considering the uncertainties and simplifications involved, the model can succesfully reproduce ozone hole conditions. Furthermore, a technique for reducing the stiffness of the differential equations for the calculation of stratospheric chemistry and a new tracer family concept are presented. (Chapter 9)

Outlook

The development of the ECHAM5/MESSy PSC submodel has been finished, resulting in a state-of-the-art modelling system, and for the near future its use within climate simulations of the stratosphere will be in the foreground.

The growth of our knowledge about PSCs continues, of course. Therefore, in a few years time some fine tuning, e. g. of reaction rate coefficients and parameters determining particle formation, will seem appropriate.

With improving computational facilities and ECHAM5/MESSy spatial resolution, the desire for more detailed PSC modelling will likely arise. In this context, the sedimentation scheme and the solid PSC particle size scheme will probably be candidates for revision.

Currently, however, it seems that the simulation of polar stratospheric chemistry can best be improved not by modifying the PSC submodel but by concentrating on other aspects of ECHAM5/MESSy: shortcomings of the advection scheme and of the representation of upward propagating gravity waves are examples of unresolved issues.

Further possibilities for future ECHAM5/MESSy development related to the PSC submodel are Lagrangian studies based on the ATTILA submodel (Traub, 2004) and the extension of heterogeneous chemistry calculations to cirrus clouds in the tropopause region. The latter suggestion is inspired by the fact that predecessors of the chemistry routines in the ECHAM5/MESSy PSC submodel have been applied to tropopause cirrus clouds by Meilinger (2000) and Meilinger et al. (2001).

Appendix A

Abbreviations and Acronyms

ATTILA Atmospheric Tracer Transport In a LAgrangian model

AVHRR Advanced Very High Resolution Radiometer

BrO_x the sum of Br, BrO, HOBr, BrCl, and two times Br_2; it is called "odd bromine" or "active bromine" as it contains the rapidly reacting bromine species

CCM Chemistry-Climate Model

CLAES Cryogenic Limb Array Etalon Spectrometer (measuring instrument on UARS)

ClO_x the sum of Cl, ClO, HOCl, OClO, two times Cl_2, and two times Cl_2O_2; it is called "odd chlorine" or "active chlorine" as it contains the rapidly reacting chlorine species

ECHAM name of a general circulation model which is based on an ECMWF weather forecast model and which was developed in Hamburg; the abbreviation ECHAM is composed of "ECMWF" and "Hamburg"

ECMWF European Centre for Medium-Range Weather Forecasts

ENVISAT European ENVIronmental SATellite

ERA-15 ECMWF global reanalysis data set for the period 1979–1993

ERA-40 ECMWF global reanalysis data set for the period 1957–2001

ESA European Space Agency

GCM General Circulation Model

HALOE Halogen Occultation Experiment (measuring instrument on UARS)

HO_x the sum of H, OH, and HO_2; called "odd hydrogen" or "active hydrogen" as it contains the rapidly reacting hydrogen species

ILAS Improved Limb Atmospheric Spectrometer

IPCC Intergovernmental Panel on Climate Change

ISAMS Improved Stratospheric and Mesospheric Sounder (measuring instrument on UARS)

IUPAC International Union of Pure and Applied Chemistry

KODYACS KOpplung von DYnamik und Atmosphärischer Chemie in der Stratosphäre (coupling of dynamics and atmospheric chemistry in the stratosphere)

LIDAR LIght Detection And Ranging

MA-ECHAM middle atmosphere version of ECHAM

MA-ECHAM/CHEM middle atmosphere version of ECHAM plus model components for the calculation of atmospheric chemistry

MECCA Module Efficiently Calculating the Chemistry of the Atmosphere

MESSy Modular Earth Submodel System

MLS Microwave Limb Sounder (measuring instrument on UARS)

MIPAS Michelson Interferometer for Passive Atmospheric Sounding

NAD Nitric Acid Dihydrate

NAT Nitric acid Trihydrate

NO_x the sum of N, NO, NO_2, NO_3, and two times N_2O_5; it is called “odd nitrogen family” or “active nitrogen” as it contains the rapidly reacting nitrogen species

POAM Polar Ozone and Aerosol Measurement

QBO Quasi-Biennial Oscillation

PSC Polar Stratospheric Cloud

SAGE Stratospheric Aerosol and Gas Experiment

SAM II Stratospheric Aerosol Measurement II

SAT Sulphuric Acid Tetrahydrate

SSA Stratospheric Sulfate Aerosol

STS Supercooled Ternary Solution

UARS Upper Atmosphere Research Satellite

UTC Universal Time Coordinates

Appendix B

Symbols, Constants, Notation, and Units

B.1 Symbols and Constants

$\left(\frac{\Delta x_{\mathrm{family}}}{\Delta t}\right)$: tendency of a tracer family

$\left(\frac{\Delta x_i}{\Delta t}\right)$: tendency of tracer i

α_1: numerical constant in Stokes fall velocity equation

α_2: numerical constant in Stokes fall velocity equation

α_3: numerical constant in Stokes fall velocity equation

α_l^m: spectral coefficient of order m and degree l

$\alpha_l^{*\,m}$: predicted value of α_l^m prior to Newtonian relaxation

$\alpha_l^{o\,m}$: future value of α_l^m at which the Newtonian relaxation is aimed

ΔC_{air}: difference in number concentration of air molecules between two adjacent vertical layers

$\Delta_{i-1} x_{\mathrm{ice}}$: change of amount-of-substance ratio of ice due to particles sedimenting from grid box $i-1$

Δp_{sed}: sedimentation step s_{sed} in pressure units

ΔT_{ice}: supercooling required for ice formation

Δt: model time step

Δx_i: change of amount-of-substance ratio of tracer i

Δx_{ice}: amount-of-substance ratio of ice to air change per model time step or amount-of-substance ratio of ice to air deviation between two adjacent vertical layers

Δw_{ice}: sedimentation velocity deviation between two adjacent vertical layers

Δz: vertical layer height

γ: reactive uptake coefficient; also called "reaction probability"

γ_{ice}: reactive uptake coefficient for chemical reactions on ice

γ_{NAT}: reactive uptake coefficient for chemical reactions on NAT

γ_{STS}: reactive uptake coefficient for chemical reactions on STS

κ_i scaling factor for the amount-of-substance ratio of tracer i in conversions between the single tracer mode and the family tracer mode

$\partial C_{\mathrm{air}}$: numerator of partial derivative; approximated by ΔC_{air}

∂t: denominator of partial derivative; approximated by Δt

$\partial x_{\mathrm{ice}}$: numerator of partial derivative; approximated by Δx_{ice}

$\partial w_{\mathrm{ice}}$: numerator of partial derivative; approximated by Δw_{ice}

∂z: denominator of partial derivative; approximated by Δz

$\pi_{\mathrm{HNO_3}}$: HNO_3 partitioning, i. e. the fraction $\frac{N_{\mathrm{HNO_3\,(g)}}}{N_{\mathrm{HNO_3\,(g)}}+N_{\mathrm{HNO_3\,(l)}}}$ of HNO_3 molecules remaining in the gas phase, where $N_{\mathrm{HNO_3\,(g)}}$ is the number of HNO_3 molecules in the gas phase and $N_{\mathrm{HNO_3\,(l)}}$ the number of HNO_3 molecules in the liquid phase

ρ_{ice}: mass density of ice; the value $\rho_{\mathrm{ice}} = 980\,\frac{\mathrm{kg}}{\mathrm{m^3}}$ is taken from Waibel (1997, page 104), however, some ECHAM5 routines use $\rho_{\mathrm{ice}} = 910\,\frac{\mathrm{kg}}{\mathrm{m^3}}$

ρ_{NAT}: mass density of NAT; $\rho_{\mathrm{NAT}} = 1620\,\frac{\mathrm{kg}}{\mathrm{m^3}}$ (Drdla et al., 1993)

ξ_i: fraction of tracer i in its tracer family

ξ_i': updated version of ξ_i

A: horizontal area of a model grid box

A_{bot}: coefficient for vertical hybrid pressure coordinate (constant contribution)

$A_{\mathrm{trapezoid}}$: area of a trapezoid (auxiliary variable in the trapezoid sedimentation scheme)

B_{bot}: coefficient for vertical hybrid pressure coordinate (surface pressure dependent contribution)

$b_{1,2}$: intercept of straight line through points 1 and 2

$b_{\mathrm{H_2SO_4}}$: molality of H_2SO_4 in a binary solution of H_2SO_4 in water (SSA)

$b_{\mathrm{H_2SO_4\,(tern.)}}$: molality of H_2SO_4 in a ternary solution of HNO_3 and H_2SO_4 in water (STS)

$b_{\mathrm{HNO_3}}$: molality of HNO_3 in a binary solution of HNO_3 in water (SSA)

$b_{\mathrm{HNO_3\,(tern.)}}$: molality of HNO_3 in a ternary solution of HNO_3 and H_2SO_4 in water (STS)

C_{air}: number density of air molecules

C_{ice}: number density of ice molecules

$C_{\mathrm{ice}}^{\mathrm{ref}}$: exact solution for number density of ice molecules after sedimentation, used as reference

C_{particle}: number concentration of PSC particles

C_{s}: particle number density of solid PSC particles

$C_{\mathrm{s,max}}$: maximum particle number density of solid PSC particles

C_{X}: number concentration of molecules of tracer X

c: Courant number

c_{A}: concentration of molecular species A

c_{A_i}: concentration of molecular species A_i

c_{A_j}: concentration of molecular species A_j

c_{B}: concentration of molecular species B

c_{C}: concentration of molecular species C

$c_{\mathrm{ClONO_2}}$: concentration of $ClONO_2$

c_{D}: concentration of molecular species D

$c_{\mathrm{H_2O}}$: concentration of H_2O

c_{X}: concentration of molecular species X

d_{min}: distance between a MIPAS analysis data point and the nearest ECHAM5/MESSy grid box center

$dsper$: dispersion; a performance figure for sedimentation schemes

F_l^m: forcing term for variable α_l^m, excluding relaxation

f_1: correction factor for non-sphericity in Stokes fall velocity

f_2: correction factor for non-sphericity in Stokes fall velocity

G: nudging coefficient

G_{div}: nudging coefficient for divergence

$G_{\ln p_0}$: nudging coefficient for the logarithm of the surface pressure

G_{T}: nudging coefficient for temperature

G_{vor}: nudging coefficient for vorticity

g: acceleration due to gravity, $g = 9.80665\,\frac{\mathrm{m}}{\mathrm{s}^2}$

h: geometric height

i: index of grid box; index of vertical model layer; index of tracer in a tracer family

j: index of tracer in a tracer family

k^{I}: first order reaction rate coefficient

$k^{\mathrm{I}}_{\mathrm{A}}$: first order reaction rate coefficient formed as product of a second order reaction rate coefficient and the concentration of molecular species A

$k^{\mathrm{I}}_{\mathrm{B}}$: first order reaction rate coefficient formed as product of a second order reaction rate coefficient and the concentration of molecular species B

$k^{\mathrm{I}}_{\mathrm{H_2O}}$: first order reaction rate coefficient formed as product of a second order reaction rate coefficient and the concentration of H_2O

$k^{\mathrm{I}}_{\mathrm{HCl}}$: first order reaction rate coefficient formed as product of a second order reaction rate coefficient and the concentration of HCl

k^{II}: second order reaction rate coefficient

$k^{\mathrm{II}}_{\mathrm{max}}$: upper limit for second order reaction rate coefficient

$k^{\mathrm{II}}_{\mathrm{min}}$: lower limit for second order reaction rate coefficient

$M_{1.5}$: quantitative measure for relative agreement between simulated and observed PSC occurrence, based on comparison of measured with simulated data points within a certain distance

M_{air}: molar mass of dry air, $M_{\mathrm{air}} = 28.970\,\frac{\mathrm{g}}{\mathrm{mol}}$

M_{ice}: quantitative measure for relative agreement between simulated and observed PSC occurrence, takes only ice PSCs into account

M_{NAT}: quantitative measure for relative agreement between simulated and observed PSC occurrence, takes only NAT PSCs into account

M_{nxt}: quantitative measure for relative agreement between simulated and observed PSC occurrence, based on comparison of measured with next simulated data point

M_{STS}: quantitative measure for relative agreement between simulated and observed PSC occurrence, takes only STS PSCs into account

M_{X}: molar mass of tracer X

$m_{1,2}$: slope of straight line through points 1 and 2

m_{air}: mass of air molecules

$m\Delta er$: maximum absolute difference; a performance figure for sedimentation schemes

$mner$: minimum preservation; a performance figure for sedimentation schemes

$mser$: mass conservation; a performance figure for sedimentation schemes

N: for calculation of $rmser$: number of grid boxes in vertical column

N_{air}: number of air molecules

N_{ice}: number of ice molecules

$N_{\mathrm{HNO_3\,(g)}}$: number of HNO_3 molecules in the gas phase

$N_{\mathrm{HNO_3\,(l)}}$: number of HNO_3 molecules in the liquid phase

n_{air}: amount-of-substance of air molecules

p: pressure

$p\,(z)$: pressure as function of geometric height

p_0: surface pressure

p_{bot}: pressure at the bottom of a grid box

$p_{\mathrm{H_2O}}$: water vapour partial pressure

$p_{\mathrm{H_2O\,(gl)}}$: water vapour partial pressure for the theoretical situation that no H_2O molecule is in the liquid phase

p_i: pressure in grid box i

$pker$: peak preservation; a performance figure for sedimentation schemes

p_{top}: pressure at the top of a grid box

R: universal gas constant, $R = 8.314\,\frac{\mathrm{J}}{\mathrm{mol\,K}}$

$rmser$: root-mean-square difference; a performance figure for sedimentation schemes

r_{particle}: radius of PSC particle

r_{SSA}: radius of stratospheric sulfate aerosol particles

r_{s}: radius of solid PSC particles

$r_{\mathrm{s,min}}$: minimum radius of solid PSC particles

$S_{\mathrm{H_2O}}$: supersaturation required for ice formation

s: distance

s_{sed}: sedimentation step, i. e. the distance that falling particles travel within one model time step

T: thermodynamic temperature

T_{NAT}: NAT equilibrium temperature, i. e. temperature for coexistence of gaseous HNO_3, gaseous H_2O, and solid nitric acid trihydrate

T_{ice}: ice equilibriume temperature, i. e. temperature for coexistence of gaseous H_2O and water ice

t: time

$\vec{u}$: three-dimensional velocity vector

V: volume

V_{s}: total volume of solid PSC particles

v: velocity

v_s: Stokes fall velocity

w: vertical velocity

w_{air}: vertical velocity of air

w_{ice}: vertical sedimentation velocity of ice

w_{sed}: sedimentation velocity

X: arbitrary model variable

x: amount-of-substance ratio (*not* amount-of-substance fraction and *not* first coordinate in a Cartesian coordinate system)

$x_{\mathrm{BrNO_3}}$: amount-of-substance ratio of $BrNO_3$ to air

x_{BrO_x}: amount-of-substance ratio of BrO_x to air

x_{ClO_x}: amount-of-substance ratio of ClO_x to air

$x_{\mathrm{ClONO_2}}$: amount-of-substance ratio of $ClONO_2$ to air

x_{family}: amount-of-substance ratio of the tracer representing a tracer family to air

$x_{\mathrm{H_2O}}$: amount-of-substance ratio of H_2O to air

$x_{\mathrm{H_2SO_4}}$: amount-of-substance ratio of H_2SO_4 to air

x_{HBr}: amount-of-substance ratio of HBr to air

x_{HCl}: amount-of-substance ratio of HCl to air

$x_{\mathrm{HNO_3}}$: amount-of-substance ratio of HNO_3 to air

x_i: amount-of-substance ratio of tracer i to air

x_{ice}: amount-of-substance ratio of ice to air

$x_{\mathrm{O_3}}$: amount-of-substance ratio of O_3 to air

z: geometric height coordinate

B.2 Notation

Throughout the text, abbreviations and symbols are defined when they are used for their first time. They are also listed with brief explanations in appendices A and B, respectively. The latter also contains some comments regarding the labeling of graph legends and table columns.

The physical quantity that is used to express the atmospheric content of trace substances ("tracers"), however, is discussed more extensively below. Although this quantity is pivotal in atmospheric chemistry, its usage is afflicted with some complications.

Mixing Ratios

In atmospheric chemistry, the tracer content of air is often described via the "mixing ratio", which is defined by IUPAC as follows (McNaught and Wilkinson, 1997)

> **mixing ratio**
> In meteorology, the dimensionless ratio of the mass of a substance (such as water vapour) in an air parcel to the mass of the remaining substances in the air parcel. For trace substances, this is approximated by the ratio of the mass of the substance to the mass of air. However, in the case of water vapour the mass of dry air is used. In atmospheric chemistry, mixing ratios (molecular, molar, by volume, as well as by weight) are used to describe relative concentrations of atmospheric trace gases and impurities.

Several difficulties involved in this definition and the use of the term "mixing ratio" are:

1. McNaught and Wilkinson (1997) do not give an established symbol for the physical quantity mixing ratio (as there is none).

2. The mixing ratio is dimensionless, which increases the ambiguity of mixing ratio symbols. Using "parts per billion" as unit does not alleviate this problem as the meaning of the numeral "billion" is also mistakable (10^9 in American English, 10^{12} in traditional British English).

3. It is not obvious whether a mixing ratio of a tracer X has in its denominator the mass of "air including water and X" or "air including X but without water" or "air including water but without X" or "air without water and X".

4. For scientific work related to both, meteorology and air chemistry, "mixing ratio" could mean a ratio of masses, amounts of substance, volumes, or weights. Air chemistry usage further complicates the situation by calling ratios of two amounts of substance "volume mixing ratios". Although for ideal gases the ratio of two amounts of substance is equivalent to the ratio of two volumes, a terminology which is not restricted to this special physical model of matter would be preferable.

Following Taylor (1995), this thesis never uses the term "mixing ratio" to describe the content of tracers in the atmosphere but rather *amount-of-substance fraction* or *amount-of-substance ratio.* "Amount-of-substance fraction of X in air" means the amount-of-substance of X divided by the amount-of-substance of air including X; "amount-of-substance ratio of X to air" means the amount-of-substance of X divded by the amount-of-substance of air without X.

Whether tracer variables in the general circulation model ECHAM5/MESSy are actually amount-of-substance fractions or amount-of-substance ratios is debatable. Whereas most ECHAM5/MESSy users rather think of amount-of-substance fractions, the calculation of the amount-of-substance of air for the denominator of tracer variables is in fact based on the ideal gas equation

$$n_{\mathrm{air}} = \frac{pV}{RT}. \tag{B.1}$$

where n_{air} is the amount-of-substance of air, p the air pressure, V the volume, R the universal gas constant, and T the thermodynamic temperature.

Therefore, the denominator of the tracer variables for a tracer X does not directly depend on the amount-of-substance of tracer X. Hence ECHAM5/-MESSy tracer variables are rather amount-of-substance ratios than amount-of-substance fractions.

For amount-of-substance ratios Taylor (1995) recommends the symbol r. Contradictory to that recommendation, the symbol x is be used in this thesis, as r is needed for particle radii. In this thesis, x is never used as symbol for the first coordinate in a Cartesian coordinate system.

For ECHAM5/MESSy, amount-of-substance ratios always refer to dry air, not to air including water. This means in particular that changes in the water content of air do not directly affect amount-of-substance ratios of other atmospheric constituents.

The fraction $\frac{\mathrm{mol}}{\mathrm{mol}}$ (sometimes with SI decimal prefixes: $\frac{\mu\mathrm{mol}}{\mathrm{mol}}$, $\frac{\mathrm{nmol}}{\mathrm{mol}}$) is used as unit for amount-of-substance ratios (Taylor, 1995).

B.3 Quantities and Numerical Values

Follwing recommendations in Taylor (1995, chap. 7), graph legends or headings of table columns are labeled as

$\frac{p}{\mathrm{hPa}}, \frac{T}{\mathrm{K}}, \frac{V}{\mathrm{m}^3}, \ldots$

This notation is based on the fact that the value of a quantity A is the product of its numerical value $\{A\}$ and its unit $[A]$:

$$A = \{A\}[A] \tag{B.2}$$

Therefore, the numerical value $\{A\}$ can be written as value A divided by unit $[A]$:

$$\{A\} = \frac{A}{[A]}. \tag{B.3}$$

Using the quotient of value and unit for a graph legend stresses the fact that a graph visualises *numerical values* of physical quantities, but not the values including their units.

The distinction between a value and a numerical value is emphasised here as it is of special importance in programming context. Whereas a quantity equation like

$$v = \frac{s}{t} \tag{B.4}$$

is valid independently of the units used to express the quantities involved, the following program code is not:

```
ELEMENTAL FUNCTION velocity(distance, time)
  REAL, INTENT(in) :: distance, time
  REAL :: velocity

  velocity = distance/time

END FUNCTION velocity
```

Results of the FORTRAN 95 function velocity can differ if the numerical values of the input parameters change due to the use of different units. In fact, the function velocity implements a numerical value equation, not a quantity equation.

Trivial as the distinction of physical quantities and their numerical values may seem, sloppiness in this respect causes numerous programming errors in practice.

Appendix C

Reaction Rate Coefficients

C.1 Gas Phase Reactions

Gas phase reaction rate coefficients are calculated within the ECHAM5/MESSy chemistry submodel MECCA (Sander et al., 2005). The following table is based on output of the xmecca skript by Rolf Sander and Astrid Kerkweg

#	Reaction	Reaction Rate Coefficient
G1000	$O_2 + O(^1D) \rightarrow O(^3P) + O_2$	`3.2E-11*EXP(70/temp)`
G1001	$O_2 + O(^3P) \rightarrow O_3$	`6.E-34*cair *((temp/300.)**(-2.4))`
G1002	$O_3 + O(^1D) \rightarrow 2\ O_2$	`1.2E-10`
G1003	$O_3 + O(^3P) \rightarrow 2\ O_2$	`8.E-12*EXP(-2060/temp)`
G2100	$H + O_2 \rightarrow HO_2$	`k_3rd(temp,cair,5.7E-32, 1.6,7.5E-11,0,0.6)`
G2101	$H + O_3 \rightarrow OH$	`1.4E-10*EXP(-470/temp)`
G2102	$H_2 + O(^1D) \rightarrow H + OH$	`1.1E-10`
G2103	$OH + O(^3P) \rightarrow H$	`2.2E-11*EXP(120/temp)`
G2104	$OH + O_3 \rightarrow HO_2$	`1.7E-12*EXP(-940/temp)`
G2105	$OH + H_2 \rightarrow H_2O + H$	`5.5E-12*EXP(-2000/temp)`
G2106	$HO_2 + O(^3P) \rightarrow OH$	`3.E-11*EXP(200/temp)`
G2107	$HO_2 + O_3 \rightarrow OH$	`1.E-14*EXP(-490/temp)`
G2108a	$HO_2 + H \rightarrow 2\ OH$	`0.69*8.1E-11`
G2108b	$HO_2 + H \rightarrow H_2$	`0.29*8.1E-11`
G2108c	$HO_2 + H \rightarrow O(^3P) + H_2O$	`0.02*8.1E-11`
G2109	$HO_2 + OH \rightarrow H_2O$	`4.8E-11*EXP(250/temp)`
G2110	$HO_2 + HO_2 \rightarrow H_2O_2$	`k_HO2_HO2`
G2111	$H_2O + O(^1D) \rightarrow 2\ OH$	`2.2E-10`
G2112	$H_2O_2 + OH \rightarrow H_2O + HO_2$	`2.9E-12*EXP(-160/temp)`
G3100	$N + O_2 \rightarrow NO + O(^3P)$	`1.5E-11*EXP(-3600/temp)`
G3101	$N_2 + O(^1D) \rightarrow O(^3P) + N_2$	`1.8E-11*EXP(110/temp)`
G3102a	$N_2O + O(^1D) \rightarrow 2\ NO$	`6.7E-11`
G3102b	$N_2O + O(^1D) \rightarrow N_2 + O_2$	`4.9E-11`
G3103	$NO + O_3 \rightarrow NO_2 + O_2$	`3.E-12*EXP(-1500/temp)`
G3104	$NO + N \rightarrow O(^3P) + N_2$	`2.1E-11*EXP(100/temp)`

#	Reaction	Reaction Rate Coefficient
G3105	$NO_2 + O(^3P) \rightarrow NO + O_2$	`5.6E-12*EXP(180/temp)`
G3106	$NO_2 + O_3 \rightarrow NO_3 + O_2$	`1.2E-13*EXP(-2450/temp)`
G3107	$NO_2 + N \rightarrow N_2O + O(^3P)$	`5.8E-12*EXP(220/temp)`
G3108	$NO_3 + NO \rightarrow 2\ NO_2$	`1.5E-11*EXP(170/temp)`
G3109	$NO_3 + NO_2 \rightarrow N_2O_5$	`k_NO3_NO2`
G3110	$N_2O_5 \rightarrow NO_2 + NO_3$	`k_NO3_NO2/(3.E-27*EXP(10990/temp))`
G3201	$NO + HO_2 \rightarrow NO_2 + OH$	`3.5E-12*EXP(250/temp)`
G3202	$NO_2 + OH \rightarrow HNO_3$	`k_3rd(temp,cair,2.E-30,3,2.5E-11,0,0.6)`
G3203	$NO_2 + HO_2 \rightarrow HNO_4$	`k_NO2_HO2`
G3206	$HNO_3 + OH \rightarrow H_2O + NO_3$	`k_HNO3_OH`
G3207	$HNO_4 \rightarrow NO_2 + HO_2$	`k_NO2_HO2/(2.1E-27*EXP(10900/temp))`
G3208	$HNO_4 + OH \rightarrow NO_2 + H_2O$	`1.3E-12*EXP(380/temp)`
G4100	$CH_4 + O(^1D) \rightarrow 0.75\ CH_3O_2 + 0.75\ OH + 0.25\ HCHO + 0.4\ H + 0.05\ H_2$	`1.5E-10`
G4101	$CH_4 + OH \rightarrow CH_3O_2 + H_2O$	`1.85E-20*EXP(2.82*log(temp)-987/temp)`
G4103a	$CH_3O_2 + HO_2 \rightarrow CH_3OOH$	`4.1E-13*EXP(750/temp)/(1+1/497.7*EXP(1160/temp))`
G4103b	$CH_3O_2 + HO_2 \rightarrow HCHO + H_2O + O_2$	`4.1E-13*EXP(750/temp)/(1+497.7*EXP(-1160/temp))`
G4104	$CH_3O_2 + NO \rightarrow HCHO + NO_2 + HO_2$	`2.8E-12*EXP(300/temp)`
G4106a	$CH_3O_2 + CH_3O_2 \rightarrow 2\ HCHO + 2\ HO_2$	`9.5E-14*EXP(390/temp)/(1+1/26.2*EXP(1130/temp))`
G4106b	$CH_3O_2 + CH_3O_2 \rightarrow HCHO + CH_3OH$	`9.5E-14*EXP(390/temp)/(1+26.2*EXP(-1130/temp))`
G4107	$CH_3OOH + OH \rightarrow 0.7\ CH_3O_2 + 0.3\ HCHO + 0.3\ OH + H_2O$	`k_CH3OOH_OH`
G4108	$HCHO + OH \rightarrow CO + H_2O + HO_2$	`9.52E-18 * EXP(log(temp) * 2.03 + 636/temp)`
G4110	$CO + OH \rightarrow H + CO2$	`1.57E-13 + cair*3.54E-33`
G6100	$Cl + O_3 \rightarrow ClO$	`2.3E-11*EXP(-200/temp)`
G6101	$ClO + O(^3P) \rightarrow Cl$	`3.E-11*EXP(70/temp)`
G6102	$ClO + ClO \rightarrow Cl_2O_2$	`k_ClO_ClO`
G6103	$Cl_2O_2 \rightarrow ClO + ClO$	`k_ClO_ClO/(1.27E-27*EXP(8744/temp))`
G6200	$Cl + H_2 \rightarrow HCl + H$	`3.7E-11*EXP(-2300/temp)`
G6201a	$Cl + HO_2 \rightarrow HCl$	`1.8E-11*EXP(170/temp)`

#	Reaction	Reaction Rate Coefficient
G6201b	$Cl + HO_2 \rightarrow ClO + OH$	`4.1E-11*EXP(-450/temp)`
G6202	$Cl + H_2O_2 \rightarrow HCl + HO_2$	`1.1E-11*EXP(-980/temp)`
G6203a	$ClO + OH \rightarrow Cl + HO_2$	`7.4E-12*EXP(270/temp)`
G6203b	$ClO + OH \rightarrow HCl$	`6.E-13*EXP(230/temp)`
G6204	$ClO + HO_2 \rightarrow HOCl$	`2.7E-12*EXP(220/temp)`
G6205	$HCl + OH \rightarrow Cl + H_2O$	`2.6E-12*EXP(-350/temp)`
G6206	$HOCl + OH \rightarrow ClO + H_2O$	`3.E-12*EXP(-500/temp)`
G6300	$ClO + NO \rightarrow NO_2 + Cl$	`6.4E-12*EXP(290/temp)`
G6301	$ClO + NO_2 \rightarrow ClONO_2$	`k_3rd(temp, cair, 1.8E-31, 3.4, 1.5E-11, 1.9, 0.6)`
G6303	$ClONO_2 + O(^3P) \rightarrow ClO + NO_3$	`2.9E-12*EXP(-800/temp)`
G6304	$ClONO_2 + Cl \rightarrow Cl_2 + NO_3$	`6.5E-12*EXP(135/temp)`
G6400	$Cl + CH_4 \rightarrow HCl + CH_3O_2$	`9.6E-12*EXP(-1360/temp)`
G6401	$Cl + HCHO \rightarrow HCl + CO + HO_2$	`8.1E-11*EXP(-30/temp)`
G6402	$Cl + CH_3OOH \rightarrow CH_3O_2 + HCl$	`5.7E-11`
G6403	$ClO + CH_3O_2 \rightarrow HO_2 + Cl + HCHO$	`3.3E-12*EXP(-115/temp)`
G6404	$CCl_4 + O(^1D) \rightarrow ClO + 3\ Cl$	`3.3E-10`
G6405	$CH_3Cl + O(^1D) \rightarrow OH + Cl$	`1.65E-10`
G6406	$CH_3Cl + OH \rightarrow H_2O + Cl$	`2.4E-12*EXP(-1250/temp)`
G6407	$CH_3CCl_3 + O(^1D) \rightarrow OH + 3\ Cl$	`3.E-10`
G6408	$CH_3CCl_3 + OH \rightarrow H_2O + 3\ Cl$	`1.6E-12*EXP(-1520/temp)`
G6500	$CF_2Cl_2 + O(^1D) \rightarrow ClO + Cl$	`1.4E-10`
G6501	$CFCl_3 + O(^1D) \rightarrow ClO + 2\ Cl$	`2.3E-10`
G7100	$Br + O_3 \rightarrow BrO$	`1.7E-11*EXP(-800/temp)`
G7101	$BrO + O(^3P) \rightarrow Br + O_2$	`1.9E-11*EXP(230/temp)`
G7102a	$BrO + BrO \rightarrow Br + Br$	`2.4E-12*EXP(40/temp)`
G7102b	$BrO + BrO \rightarrow Br_2$	`2.8E-14*EXP(869/temp)`
G7200	$Br + HO_2 \rightarrow HBr$	`1.5E-11*EXP(-600/temp)`
G7201	$BrO + HO_2 \rightarrow HOBr$	`3.4E-12*EXP(540/temp)`
G7202	$HBr + OH \rightarrow Br + H_2O$	`1.1E-11`
G7203	$HOBr + O(^3P) \rightarrow OH + BrO$	`1.2E-10*EXP(-430/temp)`
G7301	$BrO + NO \rightarrow Br + NO_2$	`8.8E-12*EXP(260/temp)`
G7302	$BrO + NO_2 \rightarrow BrONO_2$	`k_BrO_NO2`
G7400	$Br + HCHO \rightarrow HBr + CO + HO_2$	`1.7E-11*EXP(-800/temp)`
G7403	$CH_3Br + OH \rightarrow H_2O + Br$	`2.35E-12*EXP(-1300/temp)`
G7603a	$BrO + ClO \rightarrow Br + OClO$	`9.5E-13*EXP(550/temp)`
G7603b	$BrO + ClO \rightarrow Br + Cl$	`2.3E-12*EXP(260/temp)`
G7603c	$BrO + ClO \rightarrow BrCl$	`4.1E-13*EXP(290/temp)`

Reaction rates have been taken from Sander et al. (2003) if not explicitly stated otherwise in the following notes.

Notes:

G1002 path leading to 2 $O(^3P)$ + O_2 neglected

G2108 branching ratio from Hack et al., see note B5 of Sander et al. (2003)

G2110 The reaction rate coefficient is: `k_HO2_HO2 = (1.5E-12 * EXP(19 / temp) + 1.7E-33 * EXP(1000 / temp) * zcon) * (1.0 + 1.4E-21 * EXP(2200 / temp) * C(KPP_H2O))`. The value for the first part (which is independent of pressure) is from Christensen et al. (2002), the water term from Kircher and Sander (1984)

G3109 The reaction rate coefficient is: `k_NO3_NO2 = k_3rd(temp, zcon, 2.E-30, 4.4, 1.4E-12, 0.7, 0.6)`.

G3110 The reaction rate coefficient is defined as backward reaction divided by equilibrium constant.

G3206 The reaction rate coefficient is: `k_HNO3_OH = 2.4E-14 * EXP(460 / temp) + 1 / ((1 / 6.5E-34 * EXP(1335 / temp) * zcon) + (1 / 2.7E-17 * EXP(2199 / temp)))`

G3207 The reaction rate coefficient is defined as backward reaction divided by equilibrium constant.

G4101 from Atkinson (2003)

G4103 product distribution is from Elrod et al. (2001)

G4107 The reaction rate coefficient is: `k_CH3OOH_OH = 3.8E-12 * EXP(200 / temp)`

G4108 from Sivakumaran et al. (2003)

G4109 same temperature dependence assumed as for CH_3CHO+NO_3

G4110 from McCabe et al. (2001)

G4201 product distribution is from von Kuhlmann (2001) (see also Neeb et al. (1998))

G4206 Reaction rate coefficient calculated by von Kuhlmann (pers. comm. 2004) using self reactions of CH_3OO and C_2H_5OO from Sander et al. (2003) and geometric mean as suggested by Madronich and Calvert (1990) and Kirchner and Stockwell (1996). The product distribution (branching = 0.5 / 0.25 / 0.25) is calculated by von Kuhlmann (pers. comm. 2004) based on Villenave and Lesclaux (1996) and Tyndall et al. (2001).

G4207 same value as for G4107: CH_3OOH + OH assumed

G4213 The reaction rate coefficient is: `k_PA_NO2 = k_3rd(temp, zcon, 8.5E-29, 6.5, 1.1E-11, 1.0, 0.6)`.

G4216 `1.0E-11` from Atkinson et al. (1999), temperature dependence from Kirchner and Stockwell (1996)

G4218 same value as for G4107: CH_3OOH+OH assumed

G4219 according to Pöschl et al. (2000), the same value as for CH_3CHO+OH can be assumed

G4220 50% of the upper limit given by Sander et al. (2003), as suggested by von Kuhlmann (2001)

G4221 The reaction rate coefficient is: `k_PAN_M = k_PA_NO2 / 9.E-29 * EXP( -14000 / temp)`, i.e. the rate coefficient is defined as backward reaction divided by equilibrium constant.

G4301 product distribution is for terminal olefin carbons from Zaveri and Peters (1999)

G4304 The reaction rate coefficient is: `k_PrO2_HO2 = 1.9E-13 * EXP(1300 / temp)`. Value for generic RO_2 + HO_2 reaction from Atkinson (1997) is used.

G4305 The reaction rate coefficient is: `k_PrO2_NO = 2.7E-12*EXP(360/temp)`

G4306 The reaction rate coefficient is: `k_PrO2_CH3O2 = 9.46E-14 * EXP(431 / temp)`. The product distribution is fromvon Kuhlmann (2001).

G4307 same value as for G4107: CH_3OOH+OH assumed

G4309 products are from von Kuhlmann (2001)

G4315 same value as for G4107: CH_3OOH+OH assumed

G4319 same value as for PAN assumed

G4401 same value as for propyl group assumed (`k_PrO2_CH3O2`)

G4402 same value as for propyl group assumed (`k_PrO2_HO2`)

G4403 same value as for propyl group assumed (`k_PrO2_NO`)

G4404 same value as for G4107: CH_3OOH+OH assumed

G4409 The factor 0.25 was recommended by Uli Poeschl (pers. comm. 2004).

G4414 same value as for propyl group assumed (`k_PrO2_HO2`)

G4415 same value as for propyl group assumed (`k_PrO2_NO`)

G4416 same value as for G4107: CH_3OOH+OH assumed

G4417 value for $C_4H_9ONO_2$ used here

G4503 same temperature dependence assumed as for other RO_2+HO_2 reactions

G4504 Yield of 12 % $RONO_2$ assumed as suggested in Table 2 of Sprengnether et al. (2002).

G6103 The reaction rate coefficient is defined as backward reaction divided by equilibrium constant.

G6204 At low temperatures, there may be a minor reaction channel leading to O_3+HCl. See Finkbeiner et al. (1995) for details. It is neglected here.

G6405 average of reactions with CH_3Br and CH_3F (B. Steil, pers. comm., see also note A15 in Sander et al. (2003)).

G6407 extrapolated from reactions with CH_3CF_3, CH_3CClF_2, and CH_3CCl_2F (B. Steil, pers. comm., see also note A15 in Sander et al. (2003)).

G7302 Reaction rate coefficient: `k_BrO_NO2 = k_3rd(temp, zcon, 5.2E-31, 3.2, 6.9E-12, 2.9, 0.6)`

G7303 The reaction rate coefficient is defined as backward reaction (Sander et al., 2003) divided by equilibrium constant (Orlando and Tyndall, 1996).

C.2 Photolytic Reactions

#	Reaction	Reference
J1000	$O_2 + h\nu \rightarrow O(^3P) + O(^3P)$	Koppers and Murtagh (1996), DeMore et al. (1997)
J1001a	$O_3 + h\nu \rightarrow O(^1D)$	Molina and Molina (1986), Talukdar et al. (1998)
J1001b	$O_3 + h\nu \rightarrow O(^3P)$	Molina and Molina (1986), Talukdar et al. (1998)
J2100	$H_2O + h\nu \rightarrow H + OH$	DeMore et al. (1997)
J2101	$H_2O_2 + h\nu \rightarrow 2\ OH$	DeMore et al. (1997)
J3100	$N_2O + h\nu \rightarrow O(^1D)$	DeMore et al. (1997)
J3101	$NO_2 + h\nu \rightarrow NO + O(^3P)$	DeMore et al. (1997), G. Moortgart, priv. comm.
J3102	$NO + h\nu \rightarrow N + O(^3P)$	Allen and Frederick (1982)
J3103a	$NO_3 + h\nu \rightarrow NO_2 + O(^3P)$	DeMore et al. (1997)
J3103b	$NO_3 + h\nu \rightarrow NO$	DeMore et al. (1997)
J3104	$N_2O_5 + h\nu \rightarrow NO_2 + NO_3$	DeMore et al. (1997)
J3201	$HNO_3 + h\nu \rightarrow NO_2 + OH$	DeMore et al. (1997)
J3202	$HNO_4 + h\nu \rightarrow$ $0.667\ NO_2 + 0.667\ HO_2$ $+ 0.333\ NO_3 + 0.333\ OH$	DeMore et al. (1997)
J4100	$CH_3OOH + h\nu \rightarrow$ $HCHO + OH + HO_2$	DeMore et al. (1997)
J4101a	$HCHO + h\nu \rightarrow H_2 + CO$	DeMore et al. (1997)
J4101b	$HCHO + h\nu \rightarrow H + COH$	DeMore et al. (1997)
J4102	$CO2 + h\nu \rightarrow CO + O(^3P)$	Shemansky (1972)
J6000	$Cl_2 + h\nu \rightarrow Cl + Cl$	DeMore et al. (1997)
J6100	$Cl_2O_2 + h\nu \rightarrow 2\ Cl$	DeMore et al. (1997)
J6101	$OClO + h\nu \rightarrow ClO + O(^3P)$	Wahner et al. (1987)
J6200	$HCl + h\nu \rightarrow Cl + H$	DeMore et al. (1997)
J6201	$HOCl + h\nu \rightarrow OH + Cl$	DeMore et al. (1997)
J6301	$ClONO_2 + h\nu \rightarrow Cl + NO_3$	DeMore et al. (1997)
J6400	$CH_3Cl + h\nu \rightarrow Cl + CH_3O_2$	DeMore et al. (1997)
J6401	$CCl_4 + h\nu \rightarrow 4\ Cl$	DeMore et al. (1997)
J6402	$CH_3CCl_3 + h\nu \rightarrow 3\ Cl$	DeMore et al. (1997)
J6500	$CFCl_3 + h\nu \rightarrow 3\ Cl$	DeMore et al. (1997)
J6501	$CF_2Cl_2 + h\nu \rightarrow 2\ Cl$	DeMore et al. (1997)
J7000	$Br_2 + h\nu \rightarrow Br + Br$	Hubinger and Nee (1995)
J7200	$HOBr + h\nu \rightarrow Br + OH$	DeMore et al. (1997)
J7300	$BrNO_2 + h\nu \rightarrow Br + NO_2$	Scheffler et al. (1997)
J7301	$BrONO_2 + h\nu \rightarrow Br + NO_3$	DeMore et al. (1997)
J7400	$CH_3Br + h\nu \rightarrow Br + CH_3O_2$	DeMore et al. (1997)
J7500	$CF_3Br + h\nu \rightarrow Br$	DeMore et al. (1997)
J7600	$BrCl + h\nu \rightarrow Br + Cl$	DeMore et al. (1997)
J7601	$CF_2ClBr + h\nu \rightarrow Br + Cl$	DeMore et al. (1997)

Photolysis rate coefficients are calculated by the ECHAM5/MESSy photolysis submodel PHOTO (see http://www.mpch-mainz.mpg.de/˜chb/messy/photo/). They are passed on to the ECHAM5/MESSy chemistry submodel MECCA via the MESSy interface.

Notes:

- Several of the above reactions are not balanced as far as the number of O and N atoms is concerned. Chemical oxygen and nitrogen tendencies can be neglected because they are generally very small compared to the overall abundance of these two main constituents of the earth's atmosphere.
- Fluorine is generally not considered in the current stratospheric chemistry setup. Therefore, chlorofluorocarbons and halons act only as chlorine and bromine source in the photolytic reactions, but not as fluorine source.
- As a further approximation, oxidised carbon products are neglected for those photolytic reactions that do not contribute significantly to the overall carbon budget.

C.3 Heterogeneous Reactions on PSC Particles

#	Reaction	PSC types
R25	$ClONO_2 + HCl \rightarrow Cl_2 + HNO_3$	ice, NAT, STS
R26	$ClONO_2 + H_2O \rightarrow HOCl + HNO_3$	ice, NAT, STS
R27	$HOCl + HCl \rightarrow Cl_2 + H_2O$	ice, NAT, STS
R28	$N_2O_5 + HCl \rightarrow ClNO_2 + HNO_3$	ice, NAT
R29	$N_2O_5 + H_2O \rightarrow HNO_3 + HNO_3$	ice, NAT, STS
R30	$ClONO_2 + HBr \rightarrow BrCl + HNO_3$	ice, NAT
R31	$BrONO_2 + HCl \rightarrow BrCl + HNO_3$	ice, NAT
R32	$HOCl + HBr \rightarrow BrCl + H_2O$	ice, NAT, STS
R33	$HOBr + HCl \rightarrow BrCl + H_2O$	ice, NAT, STS
R34	$HOBr + HBr \rightarrow Br_2 + H_2O$	ice, NAT, STS
R35	$BrONO_2 + H_2O \rightarrow HOBr + HNO_3$	ice, NAT, STS

Notes:

R25 $\gamma_{\rm ice} = 0.3$ (Sander et al., 2003); $\gamma_{\rm NAT} = 0.2$ (Sander et al., 2003); $\gamma_{\rm STS}$ is composition dependent (Carslaw, 1994)

R26 $\gamma_{\rm ice} = 0.3$ (Sander et al., 2003); $\gamma_{\rm NAT} = 0.004$ (Sander et al., 2003); $\gamma_{\rm STS}$ is composition dependent (Carslaw, 1994)

R27 $\gamma_{\rm ice} = 0.2$ (Sander et al., 2003); $\gamma_{\rm NAT} = 0.1$ (Sander et al., 2003); $\gamma_{\rm STS}$ is composition dependent (Carslaw, 1994)

R28 $\gamma_{\rm ice} = 0.03$ (Sander et al., 2003); $\gamma_{\rm NAT} = 0.003$ (Sander et al., 2003)

R29 $\gamma_{\rm ice} = 0.02$ (Sander et al., 2003); $\gamma_{\rm NAT} = 0.0004$ (Sander et al., 2003); $\gamma_{\rm STS}$ is composition dependent (Carslaw, 1994)

R30 $\gamma_{\rm ice} = 0.3$ (Sander et al., 2003); $\gamma_{\rm NAT} = 0.3$ (Sander et al., 2003)

R31 $\gamma_{\rm ice} = 0.3$ (estimate by K. Carslaw); $\gamma_{\rm NAT} = 0.3$ (estimate by K. Carslaw)

R32 $\gamma_{\rm ice} = 0.3$ (estimate by K. Carslaw); $\gamma_{\rm NAT} = 0.3$ (estimate by K. Carslaw); $\gamma_{\rm STS}$ is composition dependent (Carslaw, 1994)

R33 $\gamma_{\rm ice} = 0.3$ (Sander et al., 2003); $\gamma_{\rm NAT} = 0.1$ (estimate by K. Carslaw); $\gamma_{\rm STS}$ is composition dependent (Carslaw, 1994)

R34 $\gamma_{\rm ice} = 0.1$ (Sander et al., 2003); $\gamma_{\rm NAT} = 0.1$ (estimate by K. Carslaw); $\gamma_{\rm STS}$ is composition dependent (Carslaw, 1994)

R35 $\gamma_{\rm ice} = 0.3$ (Sander et al., 2003); $\gamma_{\rm NAT} = 0.001$ (estimate by K. Carslaw); $\gamma_{\rm STS}$ is composition dependent (Carslaw, 1994)

Appendix D

PSC Submodel Namelist

The PSC submodel as described in this thesis is part of ECHAM5/MESSy version 1.0. Its mode of operation is set via the namelists CTRL and CPL. To facilitate future use of the PSC submodel, the namelist variables are briefly documented in this appendix.

Namelist Variable Types

Namelist variables in the PSC submodel namelist are of the Fortran 95 variable types `LOGICAL`, `REAL(dp)`, and `INTEGER(i4)`. The kind type parameters `dp` and `i4` for the variable types `REAL(dp)` and `INTEGER(i4)` are defined by the functions `SELECTED_REAL_KIND` and `SELECTED_INT_KIND`:

```
INTEGER, PARAMETER :: dp = SELECTED_REAL_KIND(12,307)
INTEGER, PARAMETER :: i4 = SELECTED_INT_KIND(9)
```

Namelist CTRL

LAdvectIceNat: variable of type `LOGICAL`; default value: `.false.`
`LAdvectIceNat` is a switch which determines whether ice or NAT transported into a grid box bypasses the supersaturation requirement for ice formation and the supercooling requirement for NAT formation.

The modelling approach of advection influence on solid PSC particle formation is described in subsection 6.2.3 and evaluated in section 6.3.

LHomNucNAT: variable of type `LOGICAL`; default value: `.false.`
`LHomNucNAT` is a switch which determines whether NAT formation below a certain temperature threshold is allowed in addition to NAT formation on ice.

The modelling approach of NAT formation below a certain temperature threshold is described in subsection 6.2.4 and evaluated in section 6.3.

NatFormThreshold: variable of type `REAL(dp)`; default value: `-3.0_dp`
`NatFormThreshold` is the numerical value of the temperature in K relative

to the NAT equilibrium temperature T_{NAT} below which NAT can form in the case of `LHomNucNAT` = `.true.`

The modelling approach of NAT formation below a certain temperature threshold is described in subsection 6.2.4 and evaluated in section 6.3.

minKhet: variable of type `REAL(dp)`; default value: `0.0_dp`
`minKhet` $= \frac{k^{\mathrm{II}}_{\mathrm{min}}}{\frac{\mathrm{cm}^3}{s}}$ is the numerical value of the lower limit for the second order reaction rate coefficient.

In this thesis, only the trivial choice (i. e. zero) for `minKhet` has been applied.

maxKhet: variable of type `REAL(dp)`; default value: `1.0e-13_dp`
`maxKhet` $= \frac{k^{\mathrm{II}}_{\mathrm{max}}}{\frac{\mathrm{cm}^3}{s}}$ is the numerical value of the upper limit for the second order reaction rate coefficient.

The concept of limiting the second order reaction rate coefficients for heterogeneous chemical reactions on PSC particles is discussed in section 9.2.

SupSatIce: variable of type `REAL(dp)`; default value: `1.5_dp`
`SupSatIce` $= S_{\mathrm{H_2O}}$ is the supersaturation required for ice formation.

$S_{\mathrm{H_2O}}$ is discussed in chapter 6, especially in subsection 6.2.1.

r_min: variable of type `REAL(dp)`; default value: `1.0e-7_dp`
`r_min` $= \frac{r_{\mathrm{s,min}}}{\mathrm{m}}$ is the numerical value of the minimum radius of solid PSC particles.

$r_{\mathrm{s,min}}$ is discussed in chapter 5, especially in subsection 5.2.2.

N_solid_max: variable of type `REAL(dp)`; default value: `0.01e6_dp`
`N_solid_max` $= \frac{C_{\mathrm{s,max}}}{\frac{1}{\mathrm{m}^3}}$ is the numerical value of the maximum solid PSC particle number concentration.

$C_{\mathrm{s,max}}$ is discussed in chapter 5, especially in subsection 5.2.1.

SedScheme: variable of type `INTEGER(i4)`; default value: `3`
`SedScheme` defines the sedimentation scheme to be used:

1	simple upwind scheme
2	Walcek (2000) scheme
3	trapezoid scheme
other integer value	no sedimentation

The sedimentation schemes are discussed in chapter 4.

Namelist CPL

LCalcChem: variable of type `LOGICAL`; default value: `.true.`
`LCalcChem` is a switch which determines whether the PSC submodel calculates reaction rate coefficients for heterogeneous chemical reactions on

PSC particles. If LCalcChem is set `.false.`, the PSC submodel only simulates PSC microphysics and sedimentation.

Chapter 9.4 presents results of two otherwise similar simulation runs that differ in the setting of `LCalcChem`.

TempShift: variable of type `REAL(dp)`; default value: `0.0_dp`

`TempShift` is the numerical value of an internal temperature shift in the PSC submodel in K.

This temperature shift is discussed in chapter 6 (especially in section 6.3) and in chapter 7.

Bibliography

Abbatt, J. P. D. and Molina, M. J.: The heterogeneous reaction of HOCl + HCl $\rightarrow$ Cl_2 + H_2O on ice and nitric-acid trihydrate – reaction probabilities and stratospheric implications, Geophysical Research Letters, 19, 461–464, 1992.

Adriani, A., Deshler, T., Di Donfrancesco, G., and Gobbi, G. P.: Polar stratospheric clouds and volcanic aerosol during spring 1992 over McMurdo Station, Antarctica: Lidar and particle counter comparisons, Journal of Geophysical Research, 100, 25 877–25 897, 1995.

Allen, M. and Frederick, J. E.: Effective photo-dissociation cross-sections for molecular-oxygen and nitric-oxide in the Schumann-Runge bands, Journal of the Atmospheric Sciences, 39, 2066–2075, 1982.

Ammann, M., Pöschl, U., and Rudich, Y.: Effects of reversible adsorption and Langmuir-Hinshelwood surface reactions on gas uptake by atmospheric particles, Physical Chemistry Chemical Physics, 5, 351–356, doi: 10.1039/b208708a, 2003.

Anderson, J. G., Toohey, D. W., and Brune, W. H.: Free radicals within the Antarctic vortex: The role of CFCs in the Antarctic ozone loss, Science, 251, 39–46, 1991.

Andrews, D. G., Holton, J. R., and Leovy, C. B.: Middle Atmosphere Dynamics, Academic Press, San Diego, 1987.

Anthes, R. A.: Data Assimilation and Initialization of Hurricane Prediction Models, Journal of Atmospheric Sciences, 31, 702–719, 1974.

Anthony, S. E., Onasch, T. B., Tisdale, R. T., Disselkamp, R. S., and Tolbert, M. A.: Laboratory studies of ternary H_2SO_4/HNO_3H_2O particles: Implications for polar stratospheric cloud formation, Journal of Geophysical Research, 102, 10 777–10 784, 1997.

Arnold, F.: Stratospheric aerosol increases and ozone destruction – implications from mass-spectrometer measurements, Berichte der Bunsen-Gesellschaft für physikalische Chemie, 96, 339–350, 1992.

Asselin, R.: Frequency filter for time integrations, Monthly Weather Review, 100, 487–490, 1972.

Atkinson, R.: Gas-phase tropospheric chemistry of volatile organic compounds: 1. Alkanes and alkenes, Journal of Physical and Chemical Reference Data, 26, 215–290, 1997.

Atkinson, R.: Kinetics of the gas-phase reactions of OH radicals with alkanes and cycloalkanes, Atmospheric Chemistry and Physics, 3, 2233–2307, 2003.

Atkinson, R., Baulch, D. L., Cox, R. A., Hampson, Jr., R. F., Kerr, J. A., Rossi, M. J., and Troe, J.: Summary of evaluated kinetic and photochemical data for atmospheric chemistry: Web version August 1999, http://www.-iupac-kinetic.ch.cam.ac.uk/, 1999.

Austin, J.: A three-dimensional coupled chemistry-climte model simulation of past stratospheric trends, Journal of the Atmospheric Sciences, 59, 218–232, 2002.

Bertram, A. K., Patterson, D. D., and Sloan, J. J.: Mechanisms and temperatures for the freezing of sulfuric acid aerosols measured by FTIR extinction spectroscopy, Journal of Physical Chemistry, 100, 2376–2383, 1996.

Biermann, U. M., Presper, T., Koop, T., Mößinger, J., Crutzen, P. J., and Peter, T.: The unsuitability of meteoritic and other nuclei for polar stratospheric cloud freezing, Geophysical Research Letters, 23, 1693–1696, 1996.

Borrmann, S., Solomon, S., Dye, J. E., Baumgardner, D., Kelly, K. K., and Chan, K. R.: Heterogeneous reactions on stratospheric background aerosols, volcanic sulfuric acid droplets, and type I polar stratospheric clouds: Effects of temperature fluctuations and differences in particle phase, Journal of Geophysical Research, 102, 3639–3648, 1997.

Bott, A.: A Positive Definite Advection Scheme Obtained by Nonlinear Renormalization of the Advective Fluxes, Monthly Weather Review, 117, 1006–1015, 1989a.

Bott, A.: Reply, Monthly Weather Review, 117, 2633–2636, 1989b.

Bott, A.: Monotone Flux Limitation in the Area-preserving Flux-form Advection Algorithm, Monthly Weather Review, 120, 1992.

Brasseur, G. and Tie, X. X.: NCAR-3D, in: Models and Measurement Intercomparison II, edited by Park, J. H., Ko, M. K. W., Jackman, C. H., Plumb, R. A., Kaye, J. A., and Sage, K. H., pp. 31–37, National Aeronautics and Space Administration, Langley Research Center, Hampton, Virginia, 1999.

Brasseur, G. P., Orlando, J. J., and Tyndall, G. S., eds.: Atmospheric Chemistry and Global Change, Oxford University Press, Oxford, 1999.

Brewer, A. W.: Evidence for a world circulation provided by the measurements of helium and water vapor distribution in the stratosphere, Quarterly Journal of the Royal Meteorological Society, 75, 351–363, 1949.

Brooks, S. D., Toon, O. B., Tolbert, M. A., Baumgardner, D., Gandrud, B. W., Browell, E. V., Flentje, H., and Wilson, J. C.: Polar stratospheric clouds during SOLVE/THESEO: Comparison of lidar observations with in situ measurements, Journal of Geophysical Research, 109, doi: 10.1029/2003JD003463, 2004.

Brühl, C. and Crutzen, P. J.: MPIC Two-Dimensional Model, in: The Atmospheric Effects of Stratospheric Aircraft: Report of the 1992 Models and Measurements Workshop, edited by Prather, M. J. and Remsberg, E. E., vol. I of *NASA Reference Publication*, p. 126, NASA, Washington, D. C., 1993.

Brühl, C., Drayson, S. R., III, J. M. R., Crutzen, P. J., McInerney, J. M., Purcell, P. N., Claude, H., Gernandt, H., McGee, T. J., McDermid, I. S., and Gunson, M. R.: Halogen Occultation Experiment ozone channel validation, Journal of Geophysical Research, 101, 10 217–10 240, 1996.

Brune, W. H., Anderson, J. G., Toohey, D. W., Fahey, D. W., Kawa, S. R., Jones, R. L., McKenna, D. S., and Poole, L. R.: The potential for ozone depletion in the Arctic stratosphere, Science, 252, 1260–1266, 1991.

Buss, S.: Dynamical aspects of polar stratospheric cloud formation, denitrification and ozone loss, Ph.D. thesis, Swiss Federal Institute of Technology Zürich, 2004.

Carslaw, K. S.: The Properties of Aqueous Stratospheric Aerosols and the Depletion of Ozone, Ph.D. thesis, University of East Anglia, 1994.

Carslaw, K. S., Luo, B. P., Clegg, S. L., Peter, T., Brimblecombe, P., and Crutzen, P. J.: Stratospheric aerosol growth and HNO_3 gase phase depletion from coupled HNO_3 and water vapour uptake by liquid particles, Geophysical Research Letters, 21, 2479–2482, 1994.

Carslaw, K. S., Clegg, S. L., and Brimblecombe, P.: A Thermodynamic Model of the System $HCl–HNO_3–H_2SO_4–H_2O$, Including Solubilities of HBr, from <200 to 328 K, Journal of Phyical Chemistry, 99, 11 557–11 574, 1995a.

Carslaw, K. S., Luo, B., and Peter, T.: An analytic expression for the composition of aqueous $HNO_3–H_2SO_4$ stratospheric aerosols including gas phase removal of HNO_3, Geophysical Research Letters, 22, 1877–1880, 1995b.

Carslaw, K. S., Peter, T., and Clegg, S. L.: Modeling the composition of liquid stratospheric aerosols, Reviews of Geophysics, 35, 125–154, 1997.

Carslaw, K. S., Wirth, M., Tsias, A., Luo, B. P., Dörnbrack, A., Leutbecher, M., Volkert, H., Renger, W., Bacmeister, J. T., Reimer, E., and Peter, T.: Increased stratospheric ozone depletion due to mountain-induced atmospheric waves, Nature, 291, 675–678, 1998.

Carslaw, K. S., Kettleborough, J. A., Northway, M. J., Davies, S., Gao, R.-S., Fahey, D. W., Baumgardner, D. G., Chipperfield, M. P., and Kleinböhl, A.: A vortex-scale simulation of the growth and sedimentation of large nitric acid hydrate particles, Journal of Geophysical Research, 107, 8300, doi: 10.1029/2001JD000467, 2002.

Chapman, S.: On ozone and atomic oxygen in the upper atmosphere, Philosophical Magazine, 10, 369, 1930.

Chipperfield, M.: SLIMCAT 3-D Chemical Transport Model, in: Models and Measurement Intercomparison II, edited by Park, J. H., Ko, M. K. W., Jackman, C. H., Plumb, R. A., Kaye, J. A., and Sage, K. H., pp. 31–37, National Aeronautics and Space Administration, Langley Research Center, Hampton, Virginia, 1999a.

Chipperfield, M. P.: Multiannual simulations with a three-dimensional chemical transport model, Journal of Geophysical Research, 104, 1781–1805, 1999b.

Christensen, L. E., Okumura, M., Sander, S. P., Salawitch, R. J., Toon, G. C., Sen, B., Blavier, J.-F., and Jucks, K. W.: Kinetics of $HO_2 + HO_2 \rightarrow H_2O_2 + O_2$: Implications for stratospheric H_2O_2, Geophysical Research Letters, 29, doi: 10.1029/2001GL014525, 2002.

Colella, P. and Woodward, P. R.: The Piecewise Parabolic Method for Gas-Dynamical Simulations, Journal of Computational Physics, 54, 174–201, 1984.

Considine, D. B., Douglass, A. R., Connell, P. S., Kinnison, D. E., and Rotman, D. A.: A polar stratospheric cloud parameterization for the global modeling initiative three-dimensional model and its response to stratospheric aircraft, Journal of Geophysical Research, 105, 3955–3973, 2000.

Crutzen, P. J.: The influence of nitrogen oxide on the atmospheric ozone content, Quarterly Journal of the Royal Meteorological Society, 96, 320–325, 1970.

Crutzen, P. J. and Arnold, F.: Nitric acid cloud formation in the cold Antarctic stratosphere: a major cause for the springtime "ozone hole", Nature, 324, 651–655, 1986.

Crutzen, P. J., Müller, R., Brühl, C., and Peter, T.: On the potential importance of the gas-phase reaction $CH_3O_2 + ClO \rightarrow ClOO + CH_3O$ and the heterogeneous reaction $HOCl + HCl \rightarrow H_2O + Cl_2$ in ozone hole chemistry, Geophysical Research Letters, 19, 1113–1116, 1992.

Daley, R.: Atmospheric Data Analysis, Cambridge University Press, Cambridge, 1991.

Dameris, M.: KODYACS – Coupling of dynamics and atmospheric chemistry in the stratosphere, Project report, http://www.pa.op.dlr.de/kodyacs, 2004.

Damian, V., Sandu, A., Damian, M., Potra, F., and Carmichael, G. R.: The kinetic preprozessor KPP – a software environment for solving chemical kinetics, Computers and Chemical Engineering, 26, 1567–1579, 2002.

de Rudder, A., Larsen, N., Tie, X., Brasseur, G. P., and Granier, C.: Model study of polar stratospheric clouds and their effect on stratospheric ozone, Journal of Geophysical Research, 101, 12 567–12 574, 1996.

Del Negro, L. A., Fahey, D. W., Donnelly, S. G., Gao, R. S., Keim, E. R., Wamsley, R. C., Woodbridge, E. L., Dye, J. E., Baumgardner, D., Gandrud, B. W., Wilson, J. C., Jonsson, H. H., Loewenstein, M., Podolske, J. R., Webster, C. R., May, R. D., Worsnop, D. R., Tabazadeh, A., Tolbert, M. A., Kelly, K. K., and Chan, K. R.: Evaluating the role of NAT, NAD, and liquid $H_2SO_4/H_2O/HNO_3$ solutions in Antarctic polar stratospheric cloud aerosol: Observations and implications, Journal of Geophysical Research, 102, 13 255–13 282, 1997.

DeMore, W. B., Sander, S. P., Golden, D. M., Hampson, R. F., Kurylo, M. J., Howard, C. J., Ravishankara, A. R., Kolb, C. E., and Molina, M. J.: Chemical Kinetics and Photochemical Data for Use in Stratospheric Modeling, Evaluation Number 12, NASA, Jet Propulsion Laboratory, Pasadena, California, http://jpldataeval.jpl.nasa.gov, 1997.

Deshler, T., Larsen, N., Weissner, C., Schreiner, J., Mauersberger, K., Cairo, F., Adriani, A., Donfrancesco, G. D., Ovarlez, J., Ovarlez, H., Blum, U., Fricke, K. H., and Dörnbrack, A.: Large nitric acid particles at the top of an Arctic stratospheric cloud, Journal of Geophysical Research, 108, 4517, doi: 10.1029/2003JD003479, 2003.

Dobson, G. M. B.: Origin and distribution of the polyatomic molecules in the atmosphere, Proceedings of the Royal Society London, pp. 187–193, 1956.

Dörnbrack, A. and Leutbecher, M.: Relevance of mountain waves for the formation of polar stratospheric clouds over Scandinavia: A 20 year climatology, Journal of Geophysical Research, 106, 1583–1593, 2001.

Dörnbrack, A., Leutbecher, M., Reichardt, J., Behrendt, A., Müller, K.-P., and Baumgarten, G.: Relevance of mountain wave cooling for the formation of polar stratospheric clouds over Scandinavia: Mesoscale dynamics and observations for January 1997, Journal of Geophysical Research, 106, 1569–1581, 2001.

Douglass, A. R. and Kawa, S. R.: GSFC 3D Chemistry and Transport Model, in: Models and Measurement Intercomparison II, edited by Park, J. H., Ko, M. K. W., Jackman, C. H., Plumb, R. A., Kaye, J. A., and Sage, K. H., pp. 31–37, National Aeronautics and Space Administration, Langley Research Center, Hampton, Virginia, 1999.

Drdla, K. and Browell, E. V.: Microphysical modeling of the 1999–2000 Arctic winter: 3. Impact of homogeneous freezing on polar stratospheric clouds, Journal of Geophysical Research, 109, doi: 10.1029/2003JD004352, 2004.

Drdla, K., Turco, R. P., and Elliott, S.: Heterogeneous chemistry on Antarctic polar stratospheric clouds – a microphysical estimate of the extent of chemical processing, Journal of Geophysical Research, 98, 8965–8981, 1993.

Drdla, K., Tabazadeh, A., Turco, R. P., Jacobson, M. Z., Dye, J. E., Twohy, C., and Baumgardner, D.: Analysis of the physical state of one Arctic polar stratospheric cloud based on observations, Geophysical Research Letters, 21, 2475–2478, 1994.

Drdla, K., Schoeberl, M. R., and Browell, E. V.: Microphysical modeling of the 1999–2000 Arctic winter: 1. Polar stratospheric clouds, denitrification, and dehydration, Journal of Geophysical Research, 108, 8312, doi: 10.1029/2001JD000782, 2003.

Dye, J. E., Baumgardner, D., Gandrud, B. W., Kawa, S. R., Kelly, K. K., Loewenstein, M., Ferry, G. V., Chan, K. R., and Gary, B. L.: Particle size distribution in Arctic polar stratospheric clouds, growth and freezing of sulfuric acid droplets, and implications for cloud formation, Journal of Geophysical Research, 97, 8015–8034, 1992.

Edouard, S., Legras, B., Lefevre, F., and Eymard, R.: The effect of small-scale inhomogeneities on ozone depletion in the Arctic, Nature, 384, 444–447, 1996.

Eliasen, E., Machenhauer, B., and Rasmussen, E.: On a numerical method for integration of the hydrodynamical equation with a spectral representation of the horizontal fields, Institut of Theoretical Meteorology, University of Copenhagen, 1970.

Elrod, M. J., Ranschaert, D. L., and Schneider, N. J.: Direct kinetics study of the temperature dependence of the CH_2O branching channel for the CH_3O_2 + HO_2 reaction, International Journal of Chemical Kinetics, 33, 363–376, 2001.

ESA: MIPAS Product Handbook, European Space Agency, 1.2 edn., 2004.

Fahey, D. W., Gao, R. S., Carslaw, K. S., Kettleborough, J., Popp, P. J., Northway, M. J., Holecek, J. C., Ciciora, S. C., McLaughlin, R. J., Thompson, T. L., Winkler, R. H., Baumgardner, D. G., Gandrud, B., Wennberg, P. O., Dhaniyala, S., McKinney, K., Peter, T., Salawitch, R. J., Bui, T. P., Elkins, J. W., Webster, C. R., Atlas, E. L., Jost, H., Wilson, J. C., Herman, R. L., Kleinböhl, A., and von König, M.: The Detection of Large HNO_3-Containing Particles in the Winter Arctic Stratosphere, Science, 291, 1026–1030, 2001.

Farman, J. C., Gardiner, B. G., and Shanklin, J. D.: Large losses of total ozone in Antarctica reveal seasonal ClO_x/NO_x interaction, Nature, 315, 207–210, 1985.

Finkbeiner, M., Crowley, J. N., Horie, O., Müller, R., Moortgat, G. K., and Crutzen, P. J.: Reaction between HO_2 and ClO: Product formation between 210 and 300 K, Journal of Physical Chemistry, 99, 16 264–16 275, 1995.

Fonteyn, D. and Larsen, N.: Detailed PSC formation in a two-dimensional chemical transport model of the stratosphere, Annales Geophysicae – Atmospheres Hydrospheres and Space Sciences, 14, 315–328, 1996.

Fortin, T. J., Drdla, K., Iraci, L. T., and Tolbert, M. A.: Ice condensation on sulfuric acid tetrahydrate: Implications for polar stratospheric ice clouds, Atmospheric Chemistry and Physics, 3, 987–997, www.atmos-chem-phys.-org/acp/3/987/, 2003.

Fortuin, J. P. F. and Kelder, H.: An ozone climatology based on ozonesonde and satellite measurements, Journal of Geophysical Research, 103, 31 709–31 724, 1998.

Foschi, P. G. and Pagan, K. L.: Toward a polar stratospheric cloud climatology using advanced very high resolution radiometer thermal infrared data, Canadian Journal for Remote Sensing, 28, 187–195, 2002.

Fromm, M., Alfred, J., and Pitts, M.: A unified, long-term, high-latitude stratospheric aerosol and cloud database using SAM II, SAGE II, and POAM II/III data: Algorithm description, database definition, and climatology, Journal of Geophysical Research, 108, 4366, doi: 10.1029/2002JD002772, 2003.

Fueglistaler, S., Buss, S., Luo, B. P., Wernli, H., Flentje, H., Hostetler, C. A., Poole, L. R., Carslaw, K. S., and Peter, T.: Detailed modeling of mountain wave PSCs, Atmospheric Chemistry and Physics, 3, 697–712, www.atmos-chem-phys.org/acp/3/697/, 2003.

Glaccum, W., Lucke, R., Bevilacqua, R. M., Shettle, E. P., Hornstein, J. S., Chen, D. T., Lumpe, J. D., Krigman, S. S., Debrestian, D. J., Fromm, M. D., Dalaudier, F., Chassefiere, E., Deniel, C., Randall, C. E., Rusch, D. W., Olivero, J. J., Brogniez, C., Lenoble, J., and Kremer, R.: The Polar Ozone and Aerosol Measurement (POAM II) Instrument, Journal of Geophysical Research, 101, 14 479–14 488, 1996.

Grewe, V.: ECHAM3/CHEM, in: Models and Measurement Intercomparison II, edited by Park, J. H., Ko, M. K. W., Jackman, C. H., Plumb, R. A., Kaye, J. A., and Sage, K. H., pp. 31–37, National Aeronautics and Space Administration, Langley Research Center, Hampton, Virginia, 1999.

Grooß, J.-U.: Modelling of Stratospheric Chemistry based on HALOE/UARS Satellite Data, Ph.D. thesis, Universität Mainz, 1996.

Guldberg, A. and Kaas, E.: Danish Meteorological Institute Contribution to the Final Report, in: Project On Tendency Evaluations Using New Techniques to Improve Atmospheric Long-term Simulations(POTENTIALS) – Final Report, edited by Kaas, E., Danish Meteorological Institute (DMI), Copenhagen, Denmark, 2000.

Günther, G.: Die numerische Simulation von Transportprozessen in der mittleren Atmosphäre, Ph.D. thesis, Universität zu Köln, Institut für Geophysik und Meteorologie, 1995.

Hanson, D. and Mauersberger, K.: Laboratory studies of the nitric acid trihydrate: implications ofor the south polar stratosphere, Geophysical Research Letters, 15, 855–858, 1988.

Hanson, D. R. and Ravishankara, A. R.: The reaction probabilities of $ClONO_2$ and N_2O_5 on polar stratospheric cloud materials, Journal of Geophysical Research, 96, 5081–5090, 1991.

Hanson, D. R. and Ravishankara, A. R.: The reaction of $ClONO_2$ with HCl on NAT, NAD, and frozen sulfuric acid and hydrolysis of N_2O_5 and $ClONO_2$ on frozen sulfuric acid, Journal of Geophysical Research, 96, 22 931–22 936, 1993.

Hanson, D. R. and Ravishankara, A. R.: Heterogeneous chemistry of Bromine species in sulfuric acid under stratospheric conditions, Geophysical Research Letters, 22, 385–388, 1995.

Hassler, B., Steinbrecht, W., Winkler, P., Dameris, M., Matthes, S., Schnadt, C., Brühl, C., and Steil, B.: Comparison of observed stratospheric ozone and temperature time series with chemistry-climate model simulations, in: Proceedings of the XX Quadrennial Ozone Symposium, Kos, Greece, edited by Zerefos, C. S., p. 757f, University of Athens, 2004.

Hervig, M. E. and Deshler, T.: Stratospheric aerosol surface area and volume inferred from HALOE, CLAES, and ILAS measurements, Journal of Geophysical Research, 103, 25 345–25 352, 1998.

Hofmann, D. J.: Stratospheric cloud micro-layers and small-scale temperature variations in the Arctic in 1989, Geophysical Research Letters, 17, 369–372, 1990.

Hofmann, D. J. and Deshler, T.: Stratospheric cloud observations during formation of the antarctic ozone hole, Journal of Geophysical Research, 96, 2897–2912, 1991.

Hofmann, D. J., Rosen, J. M., Harder, J. W., and Hereford, J. V.: Balloon-Borne Measurements of Aerosol, Condensation Nuclei, and Cloud Particles in the Stratosphere at McMurdo Station, Antarctica, During the Spring of 1987, Journal of Geophysical Research, 94, 11 253–11 269, 1989.

Hoke, J. E. and Anthes, R. A.: The initialization of Numerical models by a Dynamic-Initialization Technique, Monthly Weather Review, 104, 1551–1556, 1976.

Holton, J. R.: An Introduction to Dynamic Meteorology, Academic Press, San Diego, 3rd edn., 1992.

Höpfner, M., von Clarmann, T., Fischer, H., Glatthor, N., Grabowski, U., Kellmann, S., Kiefer, M., Linden, A., Mengistu Tsidu, G., Milz, M., Steck, T., Stiller, G. P., Wang, D.-Y., Massoli, P., Cairo, F., and Adriani, A.: Determination of PSC properties from MIPAS/ENVISAT limb emission measurements during the Antarctic winter 2003, in: Proceedings of the XX Quadrennial Ozone Symposium, Kos, Greece, edited by Zerefos, C. S., p. 974f, University of Athens, 2004.

Hu, R.-M., Carslaw, K. S., Hostetler, C., Poole, L. R., Luo, B., Peter, T., Füeglistaler, S., McGee, T. J., and Burris, J. F.: Microphysical properties of wave polar stratospheric clouds retrieved from lidar measurements during SOLVE/THESEO 2000, Journal of Geophysical Research, 107, 8294, doi: 10.1029/2001JD001125, 2002.

Hubinger, S. and Nee, J. B.: Absorption-spectra of CL-2, Br-2 and BrCl between 190-nm and 600-nm, Journal of Photochemistry and Photobiology A – Chemistry, 86, 1–7, 1995.

Huthwelker, T., Peter, T., Luo, B. P., Clegg, S. L., Carslaw, K. S., and Brimblecombe, P.: Solubility of HOCl in Water and Aqueous H_2SO_4 to Stratospheric Temperatures, Journal of Atmospheric Chemistry, 21, 81–95, 1995.

Iraci, L. T., Fortin, T. J., and Tolber, M. A.: Dissolution of sulfuric acid tetrahydrate at low temperatures and subsequent growth of nitric acid trihydrate, Journal of Geophysical Research, 103, 8491–8498, 1998.

Jackman, C. H., Considine, D. B., and Fleming, E. L.: GSFC 2D Model Description, in: Models and Measurement Intercomparison II, edited by Park, J. H., Ko, M. K. W., Jackman, C. H., Plumb, R. A., Kaye, J. A., and Sage, K. H., pp. 31–37, National Aeronautics and Space Administration, Langley Research Center, Hampton, Virginia, 1999.

Jensen, E. J., Toon, O. B., Tabazadeh, A., and Drdla, K.: Impact of polar stratospheric cloud particle composition, number density, and lifetime on denitrification, Journal of Geophysical Research, 107, 8284, doi: 10.1029/2001JD000440, 2002.

Jeuken, A. B. M., Siegmund, P. C., Heijboer, L. C., Feichter, J., and Bengtsson, L.: On the potential of assimilating meteorological analyses in a global climate model for the purpose of model validation, Journal of Geophysical Research, 101, 16 939–16 950, 1996.

Jöckel, P., Sander, R., Kerkweg, A., Tost, H., and Lelieveld, J.: Technical Note: The Modular Earth Submodel System (MESSy) - a new approach towards Earth System Modeling, Atmospheric Chemistry and Physics, 5, 433–444, 2005.

Junge, C. E., Chagnon, C. W., and Manson, J. E.: Stratospheric Aerosols, Journal of Meteorology, 18, 81–108, 1961.

Kircher, C. C. and Sander, S. P.: Kinetics and mechanism of HO_2 and DO_2 disproportionations, Journal of Physical Chemistry, 88, 2082–2091, 1984.

Kirchner, F. and Stockwell, W. R.: Effect of peroxy radical reactions on the predicted concentrations of ozone, nitrogenous compounds, and radicals, Journal of Geophysical Research, 101D, 21 007–21 022, 1996.

Kistler, R. E.: A study of data assimilation techniques in an autobarotropic, primitive equation channel model, Master's thesis, The Pennsylvania State University, 1973.

Kleinböhl, A., Bremer, H., von König, M., Küllmann, H., Künzi, K. F., Goede, A. P. H., Browell, E. V., Grant, W. B., Toon, G. C., Blumenstock, T., Galle, B., Sinnhuber, B.-M., and Davies, S.: Vortexwide denitrification of the Arctic polar stratosphere in winter 1999/2000 determined by remote observations, Journal of Geophysical Research, 108, 8305, doi: 10.1029/2001JD001042, 2003.

Knopf, D. A., Koop, T., Luo, B. P., Weers, U. G., and Peter, T.: Homogeneous nucleation of NAD and NAT in liquid stratospheric aerosols: insufficient to explain denitrification, Atmospheric Chemistry and Physics, 2, 207–214, www.atmos-chem-phys.org/acp/2/207/, 2002.

Ko, M., Weisenstein, D., Scott, C. J., Shia, R.-L., Rodriguez, J., and Sze, N. D.: Description of the AER 2-D Photochemical Transport Model, in: Models and Measurement Intercomparison II, edited by Park, J. H., Ko, M. K. W., Jackman, C. H., Plumb, R. A., Kaye, J. A., and Sage, K. H., pp. 31–37, National Aeronautics and Space Administration, Langley Research Center, Hampton, Virginia, 1999.

Koike, M., Kondo, Y., Takegawa, N., Lefevre, F., Ikeda, H., Irie, H., Hunton, H. D. E., Viggiano, A. A., Miller, T. M., Ballenthin, J. O., Sachse, G. W., Anderson, B. E., Avery, M., and Masui, Y.: Redistribution of reactive nitrogen in the Arctic lower stratosphere in the 1999/2000 winter, Journal of Geophysical Research, 107, 8275, doi: 10.1029/2001JD001089, 2002.

Koop, T. and Carslaw, K. S.: Melting of $H_2SO_4 \cdot 4H_2O$ particles upon cooling: Implications for polar stratospheric clouds, Science, 272, 1638–1641, 1996.

Koop, T., Biermann, U. M., Raber, W., Luo, B. P., Crutzen, P. J., and Peter, T.: Do stratospheric aerosol droplets freeze above the ice frost point, Geophysical Research Letters, 22, 917–920, 1995.

Koop, T., Luo, B., Biermann, U. M., Crutzen, P. J., and Peter, T.: Freezing of $HNO_3/H_2SO_4/H_2O$ Solutions at Stratospheric Temperatures: Nucleation Statistics and Experiments, Journal for Physical Chemistry A, 101, 1117–1133, 1997.

Koop, T., Ng, H. P., Molina, L. T., and Molina, M. J.: A New Optical Technique to Study Aerosol Phase Transitions: The Nucleation of Ice from H_2SO_4 Aerosols, Journal of Physical Chemistry A, 102, 8924–8931, 1998.

Koop, T., Luo, B., Tsias, A., and Peter, T.: Water activity as the determinant for homogeneous ice nucleation in aqueous solutions, Nature, 406, 611–614, 2000.

Koppers, G. A. A. and Murtagh, D. P.: Model studies of the influence of O-2 photodissociation parameterizations in the Schumann-Runge bands on ozone related photolysis in the upper atmosphere, Annales Geophysicae – Atmospheres Hydrospheres and Space Sciences, 14, 68–79, 1996.

Krishnamurti, T. N., Xue, J., Bedi, H. S., Ingles, K., and Oosterhof, D.: Physical initialization for numerical weather prediction over the tropics, Tellus, 43AB, 53–81, 1991.

Larsen, N.: Polar Stratospheric Clouds – Microphysical and optical models, Danish Meteorological Institute (DMI), Copenhagen, Denmark, 2000.

Larsen, N.: Polar Stratospheric Clouds – Microphysical and optical models, Addendum, Danish Meteorological Institute (DMI), Copenhagen, Denmark, 2002.

Larsen, N., Knudsen, B. M., Svendsen, S. H., Deshler, T., Rosen, J. M., Kivi, R., Weisser, C., Schreiner, J., Mauersberger, K., Cairo, F., Ovarlez, J., Oelhaf, H., and Spang, R.: Formation of solid particles in synoptic-scale Arctic PSCs in early winter 2002/2003, Atmospheric Chemistry and Physics, 4, 2001–2013, www.atmos-chem-phys.org/acp/4/2001, 2004.

Lin, S. J. and Rood, R. B.: Multidimensional flux form semi-Lagrangian transport, Monthly Weather Review, 124, 2046–2068, 1996.

Lopez-Puertas, M., Funke, B., Gil-Lopez, S., von Clarmann, T., Stiller, G. P., Kellmann, S., Fischer, H., and Jackman, C. H.: Observation of NO_x Enhancement and Ozone Depletion in the Northern and Southern Hemisphere After the October-November 2003 Solar Proton Events, Journal of Geophysical Research, submitted February 2005, revised April 2005, 2005.

Lucke, R. L., Korwan, D. R., Bevilacqua, R. M., Hornstein, J. S., Shettle, E. P., Chen, D. T., Daehler, M., Lumpe, J. D., Fromm, M. D., Debrestian, D., Neff, B., Squire, M., König-Langlo, G., and Davies, J.: The Polar Ozone and Aerosol Measurement (POAM) III instrument and early validation results, Journal of Geophysical Research, 104, 18 785–18 800, 1999.

Luo, B., Carslaw, K., and ans S. Clegg, T. P.: Vapour pressures of H_2SO_4/-HNO_3/HCl/HBr/H_2O solutions to low stratospheric temperatures, Geophysical Research Letters, 22, 247–250, 1995.

Machenhauer, B.: On tht Dynamics of Gravity Oscillations in a Shallow Water Model, with Applications to Normal Mode Initialization, Beiträge zur Physik der Atmosphäre, 50, 253–271, 1977.

Machenhauer, B. and Rasmussen, E.: On the integration of the spectral hydrodynamical equations by a transform method, Institut of Theoretical Meteorology, University of Copenhagen, 1972.

Madronich, S. and Calvert, J. G.: Permutation reactions of organic peroxy radicals in the troposphere, Journal of Geophysical Research, 95D, 5697–5715, 1990.

Mann, G. W., Davies, S., Carslaw, K. S., and Chipperfield, M. P.: Factors controlling Arctic denitrification in cold winters of the 1990s, Atmospheric Chemistry and Physics, 3, 403–416, 2003.

Manney, G. L., Sabutis, J. L., Pawson, S., Santee, M. L., Naujokat, B., Swinbank, R., Gelman, M. E., and Ebisuzaki, W.: Lower stratospheric temperature differences between meteorological analyses in two cold Arctic winters and their impact on polar processing studies, Journal of Geophysical Research, 108, 8328, doi: 10.1029/2001JD001149, 2003.

Manzini, E., McFarlane, N. A., and McLandress, C.: Impact of the Doppler spread parameterization on the simulation of the middle atmosphere circulation using the MA/ECHAM4 general circulation model, Journal of Geophysical Research, 102, 25 751–25 762, 1997.

Manzini, E., Steil, B., Brühl, C., Giorgetta, M. A., and Krüger, K.: A new interactive chemistry-climate model: 2. Sensitivity of the middle atmosphere to ozone depletion and increase in greenhouse gases and implications for recent stratospheric cooling, Journal of Geophysical Research, 108, 4429, doi: 10.1029/2002JD002977, 2003.

Marti, J. and Mauersberger, K.: Temperatures between 170 and 250 K, Geophysical Research Letters, 20, 363–366, 1993.

McCabe, D. C., Gierczak, T., Talukdar, R. K., and Ravishankara, A. R.: Kinetics of the reaction OH + CO under atmospheric conditions, Geophysical Research Letters, 28, 3135–3138, 2001.

McCormick, M. P., Steele, H. M., Hamill, P., Chu, W. P., and Swissler, T. J.: Polar Stratospheric Cloud Sightings by SAM II, Journal of the Atmospheric Sciences, 39, 1387–1397, 1982.

McElroy, M. B., Salawitch, R. J., Wolfsy, S. C., and Logan, J. A.: Reductions of Antarctic ozone due to synergistic interactions of chlorine and bromine, Nature, 321, 759–762, 1986.

McNaught, A. D. and Wilkinson, A.: Compendium of Chemical Terminology, no. ISBN 0865426848 in The Gold Book, Blackwell Science, second edition, online version edn., 1997.

Meilinger, S. K.: Heterogeneous Chemistry in the Tropopause Region: Impact of Aircraft Emissions, Ph.D. thesis, Swiss Federal Institute of Technology (ETH), Zürich, 2000.

Meilinger, S. K., Kärcher, B., von Kuhlmann, R., and Peter, T.: On the Impact of Heterogeneous Chemistry on Ozone in the Tropopause Region, Geophysical Research Letters, 28, 515–518, 2001.

Milz, M., von Clarmann, T., Fischer, H., Glatthor, N., Grabowski, U., Höpfner, M., Kellmann, S., Kiefer, M., Linden, A., Mengistu Tsidu, G., Steck, T., Stiller, G. P., Funke, B., and Lopez-Puertas, M.: Water vapour distributions measured with MIPAS/ENVISAT, Journal of Geophysical Research, submitted March 2005, 2005.

Molina, L. T. and Molina, M. J.: Absolute absorption cross-section of ozone in the 185-nm to 350-nm wavelength range, Journal of Geophysical Research, 91, 14 501–14 508, 1986.

Molina, L. T. and Molina, M. J.: Production of Cl_2O_2 from the Self-Reaction of the ClO Radical, The Journal of Physical Chemistry, 91, 433–436, 1987.

Molina, M. J. and Rowland, F. S.: Stratospheric sink for chlorofluoromethanes: Chlorine atome catalysed destruction of ozone, Nature, 249, 810–812, 1974.

Molina, M. J., Zhang, R., Wooldridge, P. J., McMahon, J. R., Kim, J. E., Chang, H., and Beyer, K. D.: Physical Chemistry of the $H_2SO_4/HNO_3/H_2O$ System: Implications for Polar Stratospheric Clouds, Science, 261, 1418–1423, 1993.

Müller, R.: Die Chemie des Ozons in der polaren Stratosphäre, Ph.D. thesis, Freie Universität Berlin, 1994.

Müller, R. and Peter, T.: The Numerical Modelling of the Sedimentation of Polar Stratospheric Clouds, Berichte der Bunsengesellschaft für Physikalische Chemie, 96, 1992.

Müller, R., Peter, T., Crutzen, P. J., Oelhaf, H., Adrian, G. P., v. Clarmann, T., Wegner, A., Schmidt, U., and Lary, D.: Chlorine chemistry and the potential for ozone depletion in the arctic stratospher in the winter of 1991/92, Geophysical Research Letters, 21, 1427–1430, 1994.

Murphy, D. M. and Ravishankara, A. R.: Temperature averages and rates of stratospheric reactions, Geophysical Research Letters, 21, 2471–2474, 1994.

Nedoluha, G. E., Bevilaqua, R. M., Fromm, M. D., Hoppel, K. W., and Allen, D. R.: POAM measurements of PSCs and water vapor in the 2002 Antarctic vortex, Geophysical Research Letters, 30, 1796, doi: 10.1029/2003GL017577, 2003.

Neeb, P., Horie, O., and Moortgat, G. K.: The ethene-ozone reaction in the gas phase, Journal of Physical Chemistry A, 102, 6778–6785, 1998.

Newman, P. A., Pyle, J. A., Austin, J., Braathen, G. O., Canziani, P. O., Carslaw, K. S., de F. Foster, P. M., Godin-Beekmann, S., Knudsen, B. M., Kreher, K., Nakane, H., Pawson, S., Ramaswamy, V., Rex, M., Salawitch, R. J., Shindell, D. T., Tabazadeh, A., and Toohey, D. W.: Scientific Assessment of Ozone Depletion: 2002, Global Ozone Research and Monitoring Project—Report No. 47, chap. 3, World Meteorological Organization, Geneva, 2003.

Northway, M. J., Gao, R. S., Popp, P. J., Holecek, J. C., Fahey, D. W., Carslaw, K. S., Tolbert, M. A., Lait, L. R., Dhaniyala, S., Flagan, R. C., Wennberg, P. O., Mahoney, M. J., Herman, R. L., Toon, G. C., and Bui, T. P.: An analysis of large HNO_3-containing particles sampled in the Arctic stratosphere during the winter of 1999/2000, Journal of Geophysical Research, 107, 8298, doi: 10.1029/2001JD001079, 2002.

Orlando, J. J. and Tyndall, G. S.: Rate coefficients for the thermal decomposition of $BrONO_2$ and the heat of formation of $BrONO_2$, Journal of Physical Chemistry, 100, 19 398–19 405, 1996.

Panegrossi, G., Fua, D., and Fiocco, G.: A 1-D model of the formation and evolution of Polar Stratospheric Clouds, Journal of Atmospheric Chemistry, 23, 5–35, 1996.

Park, J. H., Ko, M. K. W., Jackman, C. H., Plumb, R. A., Kaye, J. A., and Sage, K. H., eds.: Models and Measurement Intercomparison II, National Aeronautics and Space Administration, Langley Research Center, Hampton, Virginia, 1999.

Peter, T.: Microphysics and heterogeneous chemistry of polar stratospheric clouds, Annual Review of Physical Chemistry, 48, 785–822, 1997.

Pitari, G., Grassi, B., and Ricciardulli, L.: UNIVAQ-2D Photochemical Transport Model, in: Models and Measurement Intercomparison II, edited by Park, J. H., Ko, M. K. W., Jackman, C. H., Plumb, R. A., Kaye, J. A., and Sage, K. H., pp. 31–37, National Aeronautics and Space Administration, Langley Research Center, Hampton, Virginia, 1999a.

Pitari, G., Grassi, B., and Visconti, G.: UNIVAQ-3D Photochemical Transport Model, in: Models and Measurement Intercomparison II, edited by Park, J. H., Ko, M. K. W., Jackman, C. H., Plumb, R. A., Kaye, J. A., and Sage, K. H., pp. 31–37, National Aeronautics and Space Administration, Langley Research Center, Hampton, Virginia, 1999b.

Pitari, G., Mancini, E., Rizi, V., and Shindell, D. T.: Impact of future climate and emission changes on stratospheric aerosols and ozone, Journal of the Atmospheric Sciences, 59, 414–440, 2002.

Poole, L. R. and McCormick, M. P.: Polar stratospheric clouds and the antarctic ozone hole, Journal of Geophysical Research, 93, 8423–8430, 1988.

Poole, L. R. and Pitts, M. C.: Polar stratospheric cloud climatology based on Stratospheric Aerosol Measurement II observation from 1978 to 1989, Journal of Geophysical Research, 99, 13 083–13 089, 1994.

Pöschl, U., von Kuhlmann, R., Poisson, N., and Crutzen, P. J.: Development and intercomparison of condensed isoprene oxidation mechanisms for global atmospheric modeling, Journal of Atmospheric Chemistry, 37, 29–52, 2000.

Randel, W., Udelhofen, P., Fleming, E., Geller, M., Gelman, M., Hamilton, K., Karoly, D., Ortland, D., Pawson, S., Swinbank, R., Wu, F., Baldwin, M., Chanin, M.-L., Keckhut, P., Labitzke, K., Remsberg, E., Simmons, A., and Wu, D.: The SPARC Intercomparison of Middle-Atmosphere Climatologies, Journal of Climate, 17, 986–1003, 2004.

Randel, W. J. and Wu, F.: Cooling of the Arctic and Antarctic polar stratospheres due to ozone depletion, Journal of Climate, 12, 1467–1479, 1999.

Rasch, P. J. and Lawrence, M.: Recent Development in Transport Methods at NCAR, in: MPI Workshop on Conservative Transport Schemes, edited by Machenhauer, B., Report No. 265, pp. 65–75, Max-Planck-Institut für Meteorologie, Hamburg, 1998.

Rasch, P. J. and Williamson, D. L.: Computational aspects of moisture transport in global models of the atmosphere, Quarterly Journal of the Royal Meteorological Society, 116, 1071–1090, 1990.

Roche, A. E., Kumer, J. B., Mergenthaler, J. L., Ely, G. A., Uplinger, W. G., Potter, J. F., James, T. C., and Sterritt, L. W.: The Cryogenic Limb Array Etalon Spectrometer CLAES on UARS: Experiment Description and Performance, Journal of Geophysical Research, 98, 10 763–10 775, 1993.

Rodriguez, J. and Rotman, D.: NASA Global Modeling Initiative (GMI) Assessment Model, in: Models and Measurement Intercomparison II, edited by Park, J. H., Ko, M. K. W., Jackman, C. H., Plumb, R. A., Kaye, J. A., and Sage, K. H., pp. 31–37, National Aeronautics and Space Administration, Langley Research Center, Hampton, Virginia, 1999.

Roeckner, E., Bäuml, G., Bonaventura, L., Brokopf, R., Esch, M., Giorgetta, M., Hagemann, S., Kirchner, I., Kornblueh, L., Manzini, E., Rhodin, A., Schlese, U., Schulzweida, U., and Tompkins, A.: The atmospheric general circulation model ECHAM5. PART I: Model description, Tech. Rep. 349, Max Planck Institute for Meteorology, Hamburg, 127 pp., 2003.

Rood, B. R.: Numerical advection algorithms and their role in atmospheric transport and chemistry, Review of Geophysics, 25, 71–100, 1987.

Rosenfield, J. E., Considine, D. B., and Bacmeister, J. T.: GSFC-INT 2D Model Description, in: Models and Measurement Intercomparison II, edited by Park, J. H., Ko, M. K. W., Jackman, C. H., Plumb, R. A., Kaye, J. A., and Sage, K. H., pp. 31–37, National Aeronautics and Space Administration, Langley Research Center, Hampton, Virginia, 1999.

Rozanov, E. V., Schlesinger, M. E., Yang, F., and Andronova, N.: UIUC-3D Model, in: Models and Measurement Intercomparison II, edited by Park, J. H., Ko, M. K. W., Jackman, C. H., Plumb, R. A., Kaye, J. A., and Sage, K. H., pp. 31–37, National Aeronautics and Space Administration, Langley Research Center, Hampton, Virginia, 1999.

Russel, G. L. and Lerner, J. A.: A New Finite-Differencing Scheme for the Tracer Transport Equation, Journal of Applied Meteorology, 20, 1483–1498, 1981.

Russell III, J. M., Gordley, L. L., Park, J. H., Drayson, S. R., Cicerone, D. H. R. J., Tuck, A. F., Frederick, J. E., Harries, J. E., and Crutzen, P.: The Halogen Occultation Experiment, Journal of Geophysical Research, 98, 10 777–10 797, 1993.

Salcedo, D., Molina, L. T., and Molina, M. J.: Homogeneous Freezing of Concentrated Aqueous Nitric Acid Solutions at Polar Stratospheric Temperatures, Journal of Physical Chemistry A, 105, 1433–1439, 2001.

Sander, R., Kerkweg, A., Jöckel, P., and Lelieveld, J.: Technical Note: The new comprehensive atmospheric chemistry module MECCA, Atmospheric Chemistry and Physics, 5, 445–450, 2005.

Sander, S. P., Friedl, R. R., Ravishankara, A. R., Golden, D. M., Kolb, C. E., Kurylo, M. J., Huie, R. E., Orkin, V. L., Molina, M. J., Moortgat, G. K., and Finlayson-Pitts, B. J.: Chemical Kinetics and Photochemical Data for Use in Atmospheric Studies – Evaluation 14, NASA, Jet Propulsion Laboratory, Pasadena, California, http://jpldataeval.jpl.nasa.gov, 2003.

Santee, M. L., Manney, G. L., Froidevaux, L., Read, W. G., and Waters, J. W.: Six years of UARS Microwave Limb Sounder HNO_3 observations: Seasonal, interhemispheric, and interannual variations in the lower stratosphere, Journal of Geophysical Research, 104, 8225–8246, 1999.

Santee, M. L., Manney, G. L., Waters, J. W., and Livesey, N. J.: Variations and climatology of ClO in the polar lower stratosphere from UARS Microwave Limb Sounder measurements, Journal of Geophysical Research, 108, 4454, doi: 10.1029/2002JD003335, 2003.

Santee, M. L., Manney, G. L., Livesey, N. J., and Read, W. G.: Three-dimensional structure and evolution of stratospheric HNO_3 based on UARS Microwave Limb Sounder measurements, Journal of Geophysical Research, 109, doi: 10.1029/2004JD004578, 2004.

Sasano, Y., Suzuki, M., Yokota, T., and Kanzawa, H.: Improved Limb Atmospheric Spectrometer (ILAS) for stratospheric ozone layer measurements by solar occultation technique, Geophysical Research Letters, 26, 197–200, 1999.

Saueressig, G., Crowley, J. N., Bergamaschi, P., Brühl, C., Brenninkmeijer, C. A. M., and Fischer, H.: Carbon 13 and D kinetic isotope effects in the reaction of CH4 with $O(^1D)$ and OH: New laboratory measurements and their implications for the isotopic composition of stratospheric methane, Journal of Geophysical Research, 106, 23 127–23 138, 2001.

Scheffler, D., Grothe, H., Willner, H., Frenzel, A., and Zetzsch, C.: Properties of pure nitryl bromide. Thermal behavior, UV/Vs and FTIR spectra, and photoisomerization to trans-BrONO in an argon matrix, Inorganic Chemistry, 36, 335–338, 1997.

Schreiner, J., Voigt, C., Kohlmann, A., Arnold, F., Mauersberger, K., and Larsen, N.: Chemical Analysis of Polar Stratospheric Cloud Particles, Science, 283, 968–970, doi: 10.1126/science.283.5404.968, 1999.

Shemansky, D. E.: CO2 extinction coefficient 1700–3000 A, Journal of Chemical Physics, 56, 1582, 1972.

Sinnhuber, B.-M., Chipperfield, M. P., Davies, S., Burrows, J. P., Eichmann, K.-U., Weber, M., von der Gathen, P., Guirlet, M., Cahill, G. A., Lee, A. M., and Pyle, J. A.: Large loss of total ozone during the Arctic winter of 1999/2000, Geophysical Research Letters, 27, 3473–3476, 2000.

Sivakumaran, V., Hölscher, D., Dillon, T. J., and Crowley, J. N.: Reaction between OH and HCHO: temperature dependent rate coefficients (202-399 K) and product pathways (298 K), Physical Chemistry Chemical Physics, 5, 4821–4827, 2003.

Smyshlyaev, S. P., Dvortsov, V. L., Yudin, V. A., and Geller, M. A.: SUNY-SPb 2D Model Description, in: Models and Measurement Intercomparison II, edited by Park, J. H., Ko, M. K. W., Jackman, C. H., Plumb, R. A., Kaye, J. A., and Sage, K. H., pp. 31–37, National Aeronautics and Space Administration, Langley Research Center, Hampton, Virginia, 1999.

Solomon, S.: Progress towards a quantitative understanding of Antarctic ozone depletion, Nature, 347, 347–354, 1990.

Solomon, S., Garcia, R. R., Rowland, F. S., and Wuebbles, D. J.: On the depletion of Antarctic ozone, Nature, 321, 755–758, 1986.

Sprengnether, M., Demerjian, K. L., Donahue, N. M., and Anderson, J.: Product analysis of the OH oxidation of isoprene and 1,3-butadiene in the presence of NO, Journal of Geophysical Research, 107D, doi: 10.1029/2001JD000716, 2002.

Steele, H. M., Hamill, P., McCormick, M. P., and Swissler, T. J.: The Formation of Polar Stratospheric Clouds, Journal of the Atmospheric Sciences, 40, 2055–2067, 1983.

Steele, H. M., Lumpe, J. D., Bevilacqua, R. M., Hoppel, K. W., and Turco, R. P.: Role of temperature history in polar stratospheric cloud sightings, Journal of Geophysical Research, 107, 4618, doi: 10.1029/2001JD001261, 2002.

Steil, B.: Modellierung der Chemie der globalen Strato- and Troposphäre mit einem dreidimensionalen Zirkulationsmodell, Ph.D. thesis, Universität Hamburg, 1999.

Steil, B., Brühl, C., Manzini, A., Crutzen, P. J., Lelieveld, J., Rasch, P. J., Roeckner, E., and Krüger, K.: A new interactive chemistry-climate model: 1. Present-day climatology and interannual variability of the middle atmosphere using the model and 9 years of HALOE/UARS data, Journal of Geophysical Research, 108, 4290, doi: 10.1029/2002JD002971, 2003.

Steil, B., Brühl, C., Giorgetta, M., Manzini, E., Grewe, V., and Mager, F.: The impact of CFCs, greenhouse gases, solar cycle, QBO, ENSO and major volcanoes on stratospheric ozone; transient simulation with the middle atmosphere coupled chemistry climate model ECHAM for the last 40 years, in:

Proceedings of the XX Quadrennial Ozone Symposium, Kos, Greece, edited by Zerefos, C. S., p. 832f, University of Athens, 2004.

Steinbrecht, W., Hassler, B., Winkler, P., Dameris, M., Matthes, S., Schnadt, C., Brühl, C., and Steil, B.: Comparison of observed stratospheric ozone and temperature time series with chemistry-climate model simulations, in: Proceedings of the XX Quadrennial Ozone Symposium, Kos, Greece, edited by Zerefos, C. S., p. 793f, University of Athens, 2004.

Stiller, G. P., von Clarmann, T., Chidiezie Chineke, T., Fischer, H., Funke, B., Gil-Lopez, S., Glatthor, N., Grabowski, U., Höpfner, M., Kellmann, S., Kiefer, M., Linden, A., Lopez-Puertas, M., Mengistu Tsidu, G., Milz, M., and Steck, T.: Early IMK MIPAS/ENVISAT results, in: Remote Sensing of Clouds and the Atmosphere VII, Proceedings of SPIE, edited by Schäfer, K. and Lado Bordowsky, O., vol. 4882, pp. 184–193, 2003.

Stiller, G. P., Mengistu Tsidu, G., von Clarmann, T., Glatthor, N., Höpfner, M., Kellmann, S., Linden, A., Ruhnke, R., Fischer, H., Lopez-Puertas, M., Funke, B., and Gil-Lopez, S.: An extraordinary high HNO_3 second maximum in the Antarctic mid-winter upper stratosphere 2003, Journal of Geophysical Research, submitted March 2005, 2005.

Tabazadeh, A., Turco, R., and Jacobson, M.: A model for studying the composition and chemical effects of stratospheric aerosols, Journal of Geophysical Research, 99, 12 897–12 914, 1994.

Tabazadeh, A., Jensen, E. J., and Toon, O. B.: A model description for cirrus cloud nucleation from homogeneous freezing of sulfate aerosols, Journal of Geophysical Research, 102, 23 845–23 850, 1997.

Tabazadeh, A., Santee, M. L., Danilin, M. Y., Pumphrey, H. C., Newman, P. A., Hamill, P. J., and Mergenthaler, J. L.: Quantifying Denitrification and Its Effect on Ozone Recovery, Science, 288, 1407–1411, 2000.

Tabazadeh, A., Jensen, E. J., Toon, O. B., Drdla, K., and Schoeberl, M. R.: Role of the Stratospheric Polar Freezing Belt in Denitrification, Science, 291, 2591–2594, 2001.

Tabazadeh, A., Djikaev, Y. S., Hamill, P., and Reiss, H.: Laboratory Evidence for Surface Nucleation of Solid Polar Stratospheric Cloud Particles, Journal of Physical Chemistry A, 106, 10 238–10 246, 2002.

Talukdar, R. K., Longfellow, C. A., Gilles, M. K., and Ravishankara, A. R.: Quantum yields of O(D-1) in the photolysis of ozone between 289 and 329 nm as a function of temperature, Geophysical Research Letters, 25, 143–146, 1998.

Taylor, B. N.: Guide for the Use of the International System of Units (SI), NIST Special Publication 811, United States Department of Commerce, National Institute of Standards and Technology (NIST), 1995.

Taylor, F. W., Rodgers, C. D., Whitney, J. G., Werrett, S. T., Barnett, J. J., Peskett, G. D., Venters, P., Ballard, J., Palmer, C. W. P., Knight, R. J., Morris, P., Nightingale, T., and Dudhia, A.: Remote-Sensing of Atmospheric Structure and Composition by Pressure Modulator Radiometry from Space – the ISAMS Experiment on UARS, Journal of Geophysical Research, 98, 10 799–10 814, 1993.

Tolbert, M. A., Rossi, M. J., Malhotra, R., and Golden, D. M.: Reaction of chlorine nitrate with hydrogen-chloride and water at Antarctic stratospheric temperatures, Science, 238, 1258–1260, 1987.

Toon, O. B., Hamill, P., Turco, R. P., and Pinto, J.: Condensation of HNO_3 and HCl in the winter polar stratosphere, Geophysical Research Letters, 13, 1284–1287, 1986.

Traub, M.: Lagrangian transport evaluation of atmospheric chemistryin the Mediterranean region, Ph.D. thesis, Johannes Gutenberg-Universität Mainz, 2004.

Turco, R. P., Toon, O. B., and Hamill, P.: Heterogeneous Physicochemistry of the Polar Ozone Hole, Journal of Geophysical Research, 94, 16 493–16 510, 1989.

Tyndall, G. S., Cox, R. A., Granier, C., Lesclaux, R., Moortgat, G. K., Pilling, M. J., Ravishankara, A. R., and Wallington, T. J.: The atmospheric chemistry of small organic peroxy radicals, Journal of Geophysical Research, 106D, 12 157–12 182, 2001.

van Aalst, M.: Dynamics and Transport in the Stratosphere, Ph.D. thesis, Utrecht University, 2005.

van den Broek, M.: The Arctic winter stratosphere – Simulated with a 3-D Chemistry Transport Model, Ph.D. thesis, Universiteit Utrecht, 2004.

Villenave, E. and Lesclaux, R.: Kinetics of the cross reactions of CH_3O_2 and $C_2H_5O_2$ radicals with selected peroxy radicals, Journal of Physical Chemistry, 100, 14 372–14 382, 1996.

Voigt, C., Schreiner, J., Kohlmann, A., Zink, P., Mauersberger, K., Larsen, N., Deshler, T., Kröger, C., Rosen, J., Adriani, A., Cairo, F., Donfrancesco, G. D., Viterbini, M., Ovarlez, J., Ovarlez, H., David, C., and Dörnbrack, A.: Nitric Acid Trihydrate (NAT) in Polar Stratospheric Clouds, Science, 290, 1756–1758, 2000.

von Clarmann, T., Chidiezie Chineke, T., Fischer, H., Funke, B., Gil-Lopez, S., Glatthor, N., Grabowski, U., Höpfner, M., Kellmann, S., Kiefer, M., Linden, A., Lopez-Puertas, M., Mengistu Tsidu, G., Milz, M., Steck, T., and Stiller, G. P.: Remote sensing of the middle atmosphere with MIPAS, in: Remote sensing of Clouds and the Atmosphere VII, Proceedings of SPIE, edited by Schäfer, K. and Lado Bordowsky, O., vol. 4882, pp. 172–183, 2003a.

von Clarmann, T., Glatthor, N., Grabowski, U., Höpfner, M., Kellmann, S., Kiefer, M., Linden, A., Mengistu Tsidu, G., Milz, M., Steck, T., Stiller, G. P., Wang, D. Y., Fischer, H., Funke, B., Gil-Lopez, S., and Lopez-Puertas, M.: Retrieval of temperature and tangent altitude pointing from limb emission spectra recorded from space by the Michelson Interferometer for Passive Atmospheric Sounding (MIPAS), Journal of Geophysical Research, 108, doi: 10.1029/2003JD-003602, 2003b.

von Kuhlmann, R.: Tropospheric photochemistry of ozone, its precursors and the hydroxyl radical: A 3D-modeling study considering non-methane hydrocarbons, Ph.D. thesis, Johannes Gutenberg-Universität, Mainz, Germany, 2001.

von Storch, H. and Zwiers, F. W.: Statistical Analysis in Climate Research, Cambridge University Press, Cambridge, 1999.

Wahner, A., Tyndall, G. S., and Ravishankara, A. R.: Absorption cross-sections for OClO as a function of temperature in the wavelength range 240-480 nm, Journal of Physical Chemistry, 91, 2734–2738, 1987.

Waibel, A. E.: Anomalien ozonchemisch relevanter Spurengase, Ph.D. thesis, Ruprecht-Karls-Universität Heidelberg, 1997.

Waibel, A. E., Peter, T., Carslaw, K. S., Oelhaf, H., Wetzel, G., Crutzen, P. J., Pöschl, U., Tsias, A., Reimer, E., and Fischer, H.: Arctic Ozone Loss Due to Denitrification, Science, 283, 2064–2069, 1999.

Walcek, C. J.: Minor flux adjustment near mixing ratio extremes for simplified yet highly accurate monotonic calculation of tracer advection, Journal of Geophysical Research, 105, 9335–9348, 2000.

Washburn, E. W.: The Vapor Pressure of Ice and of Water Below the Freezing Point, Monthly Weather Review, 52, 488–490, 1924.

Wayne, R. P.: Chemistry of Atmospheres, Oxford University Press, New York, 3rd edn., 2000.

WMO: Scientific Assessment of Ozone Depletion: 2002, Global Ozone Research and Monitoring Project—Report No. 47, World Meteorological Organization, Geneva, 2003.

Worsnop, D. R., Fox, L. E., Zahniser, M. S., and Wofsy, S. C.: Vapor pressure of solid hydrates of nitric acid: Implications for polar stratospheric clouds, Science, 259, 71–74, 1993.

Zaveri, R. A. and Peters, L. K.: A new lumped structure photochemical mechanism for large-scale applications, Journal of Geophysical Research, 104D, 30 387–30 415, 1999.

Zubov, V., Karol, I., and Rozanov, E.: MGO/UIUC: Description of the 2-D Zonally Averaged Transient Model of Photochemical Dynamical and Radiative Processes in the Troposphere and Stratosphere, in: Models and Measurement Intercomparison II, edited by Park, J. H., Ko, M. K. W., Jackman, C. H., Plumb, R. A., Kaye, J. A., and Sage, K. H., pp. 31–37, National Aeronautics and Space Administration, Langley Research Center, Hampton, Virginia, 1999.